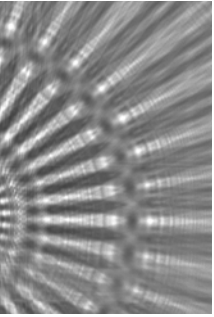


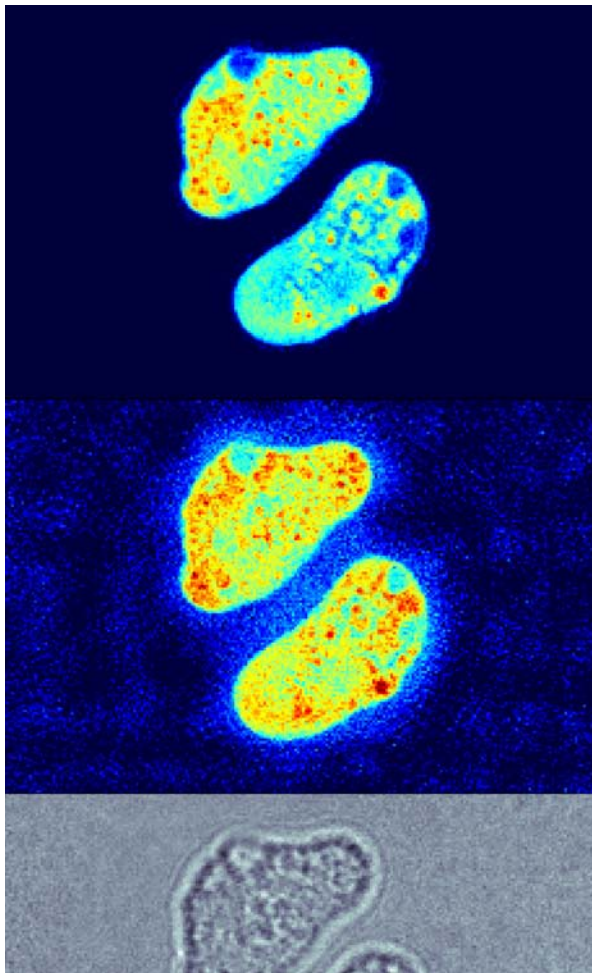


Göttingen Series in
X-ray Physics



Klaus Giewekemeyer

A study on new approaches in coherent
x-ray microscopy of biological specimens



Universitätsverlag Göttingen

Klaus Giewekemeyer

A study on new approaches in coherent
x-ray microscopy of biological specimens

This work is licensed under the
[Creative Commons](#) License 3.0 “by-nd”,
allowing you to download, distribute and print the
document in a few copies for private or educational
use, given that the document stays unchanged
and the creator is mentioned.
You are not allowed to sell copies of the free version.



Published in 2011 by Universitätsverlag Göttingen
as Volume 5 in the series „Göttingen series in x-ray physics“

Klaus Giewekemeyer

A study on new
approaches in coherent
x-ray microscopy of
biological specimens

Göttingen series in x-ray physics
Volume 5



Universitätsverlag Göttingen
2011

Bibliographische Information der Deutschen Nationalbibliothek

Die Deutsche Nationalbibliothek verzeichnet diese Publikation in der Deutschen Nationalbibliographie; detaillierte bibliographische Daten sind im Internet über <http://dnb.ddb.de> abrufbar.

This work has been supported financially by the DFG Collaborative Research Center SFB 755 "Nanoscale Photonic Imaging", the Helmholtz Society in the framework of the Virtual Institute VI-203, and the German Ministry of Education and Research under Grant No. 05KS7MGA.

Address of the Author

Dr. Klaus Giewekemeyer
Email: k.giewek@phys.uni-goettingen.de

Dissertation zur Erlangung des
mathematisch-naturwissenschaftlichen Doktorgrades
„Doctor rerum naturalium“
der Georg-August-Universität Göttingen
vorgelegt von Klaus Giewekemeyer aus Sögel
Göttingen 2011

Referent: Prof. Dr. Tim Salditt
Koreferent: Prof. Dr. Stefan W. Hell
Tag der mündlichen Prüfung: 8.2.2011

This work is protected by German Intellectual Property Right Law.
It is also available as an Open Access version through the publisher's homepage and the Online Catalogue of the State and University Library of Goettingen (<http://www.sub.uni-goettingen.de>). Users of the free online version are invited to read, download and distribute it. Users may also print a small number for educational or private use. However they may not sell print versions of the online book.

Layout: Klaus Giewekemeyer
Cover: Jutta Pabst
Cover image: Klaus Giewekemeyer

© 2011 Universitätsverlag Göttingen
<http://univerlag.uni-goettingen.de>
ISBN: 978-3-86395-023-1
ISSN: 2191-9860

Preface of the series editor

The Göttingen series in x-ray physics is intended as a collection of research monographs in x-ray science, carried out at the Institute for X-ray Physics at the Georg-August-Universität in Göttingen, and in the framework of its related research networks and collaborations.

It covers topics ranging from x-ray microscopy, nano-focusing, wave propagation, image reconstruction, tomography, short x-ray pulses to applications of nanoscale x-ray imaging and biomolecular structure analysis.

In most but not all cases, the contributions are based on Ph.D. dissertations. The individual monographs should be enhanced by putting them in the context of related work, often based on a common long term research strategy, and funded by the same research networks. We hope that the series will also help to enhance the visibility of the research carried out here and help others in the field to advance similar projects.

Prof. Dr. Tim Salditt, Editor
Göttingen February 2011

Contents

1	Introduction	1
2	Aspects of Fourier and signal theory	7
2.1	Motivation	7
2.2	From the Fourier series to the continuous Fourier transform	8
2.2.1	Important properties of the continuous Fourier transform	9
2.2.2	Fourier transforms of important functions	11
2.3	Sampling continuous functions	13
2.3.1	Definitions related to sampling	14
2.3.2	Ideal sampling and Dirac combs	16
2.4	The discrete Fourier transform	17
2.4.1	Important properties of the discrete Fourier transform	18
2.4.2	Implementation of the DFT in Matlab	22
2.4.3	Relation of the Discrete to the Continuous Fourier Transform	23
2.4.4	The sampling theorem	26
2.4.5	The sampling theorem and the discrete Fourier transform	30
3	Propagation of x-ray wave fields in matter and free space	31
3.1	Propagation of light waves in free space	31
3.1.1	Angular spectrum solution to the Helmholtz equation	33
3.1.2	Propagation within the paraxial approximation	35
3.1.3	Far field propagation within the paraxial approximation	37
3.1.4	Effective near field propagation: The Fresnel scaling theorem	38
3.1.5	Measurement of monochromatic wave fields	40
3.1.5.1	Detection statistics	42
3.1.6	Coherence of wave fields	42
3.1.6.1	Spatial coherence	45
3.1.6.2	Temporal coherence	46
3.1.7	Numerical implementation of free space propagation	46
3.1.7.1	Paraxial propagation	47
3.1.7.2	Paraxial propagation into the far field using the Fraunhofer diffraction formula	50
3.1.7.3	Exact propagation equation	50
3.1.7.4	Implementation in Matlab	50

3.1.8	Flux conservation in propagation equations	51
3.2	Propagation of x-ray wave fields in matter	53
3.2.1	Refractive index	54
3.2.2	The projection approximation	57
3.2.3	Simulation of an object transmission function	61
3.2.4	The scattering picture and the Born approximation	62
3.2.4.1	Far-field diffraction and the Born approximation	63
3.2.5	Remarks on the projection and Born approximation	65
4	Lensless x-ray microscopy of cells: From concepts to experimental realization	69
4.1	Generic setup	69
4.2	The phase problem	70
4.3	Imaging regimes	72
4.3.1	Far field	72
4.3.2	Near field	76
4.3.3	Effective near field geometry for a divergent illuminating wave field	79
4.4	Reconstruction	82
4.4.1	Reconstruction by iterative maps	83
4.4.1.1	Gerchberg-Saxton algorithm	84
4.4.1.2	Error-Reduction algorithm	85
4.4.1.3	Hybrid-Input-Output algorithm	87
4.4.1.4	Difference map algorithm	88
4.4.2	Holographic reconstruction	89
4.4.2.1	In-line holography in the near field	90
4.4.3	Iterative reconstruction in the near field	91
4.4.4	Scanning microscopy	96
4.4.5	Ptychography	97
4.4.5.1	The Ptychographic iterative engine	98
4.4.5.2	Ptychography with probe retrieval	100
4.4.6	Convergence and uniqueness	102
4.5	Resolution	103
4.6	Treatment of noise in diffraction data	106
4.7	Coherence	107
4.7.1	Far field	107
4.7.2	Near field	108
4.8	Radiation damage, Dose and resolution	110
4.9	Biological samples and their preparation	112
4.9.1	<i>Dictyostelium Discoideum</i>	112
4.9.2	<i>Deinococcus Radiodurans</i>	113
4.9.3	Fixation by rapid freezing	114
4.9.3.1	Setup and protocol for cryo-fixation	116
4.9.3.2	Sample environment for frozen hydrated samples	121
4.9.4	Freeze drying	124

5	Quantitative ptychographic coherent x-ray diffractive imaging of bacterial cells	125
5.1	Experiment	125
5.2	Simulations	127
5.3	Reconstructions	128
5.4	Results	129
5.4.1	Reconstructed phase maps	129
5.4.2	Reconstructed diffraction patterns	131
5.4.3	Reconstructed illumination	132
5.4.4	Density maps	133
5.4.5	Reconstructions from simulated data	135
5.4.6	Resolution	136
5.4.7	Experimental error	139
5.5	Discussion and Conclusion	140
6	Ptychographic soft x-ray microscopy	141
6.1	Experiment	141
6.1.1	Fossil diatom	141
6.1.2	Siemens star	144
6.2	Reconstruction	144
6.2.1	Diatom dataset	144
6.2.2	Siemens star	147
6.3	Results	149
6.3.1	Fossil diatom	149
6.3.2	Siemens star test pattern	152
6.3.3	Reconstructed illumination functions	153
6.4	Discussion	154
6.5	Conclusion	158
7	Waveguide based x-ray propagation microscopy of eukaryotic cells	159
7.1	Setup, experimental procedure and treatment of raw data	160
7.2	Simulations	166
7.2.1	Cells	168
7.2.2	High resolution test objects	169
7.2.2.1	Resolution provided by the waveguide beam	169
7.2.2.2	Test pattern simulation	170
7.3	Reconstruction	171
7.4	Results	173
7.4.1	Experimental cell dataset	173
7.4.2	Simulated cell dataset	176
7.4.3	Simulated Siemens star dataset	177
7.5	Conclusion	178
8	Summary	181

A Appendix	183
A.1 List of abbreviations	183
A.2 Graphical representation of complex-valued images	184
A.3 Kaiser-Bessel-window	186
A.4 PCDI of bacterial cells: Reconstructions for different values of the relaxation parameter	186
A.4.1 Short exposure dataset	186
A.4.2 Long exposure dataset	189
A.5 Waveguide based propagation microscopy: Near field reconstructions for different values of algorithmic parameters	192
Bibliography	197
Publications	209
Acknowledgements	211
Lebenslauf	213

1 Introduction

The aim of the present thesis was to extend new methods in coherent x-ray microscopy to single unstained biological cells. In the following we give a brief outline on the historical development that led to the methods which were applied in this work.

Over the past three decades conventional x-ray microscopy has developed into a mature technique that is now applied routinely at most of the existing synchrotron sources in the world [115]. This development has been motivated by several specific advantages of x rays as a microscopic probe, namely their small wavelength, allowing for nanoscale resolution [17], their high penetration power, allowing for the investigation of relatively thick three-dimensional specimens without the need for sectioning [78], and their relatively simple interaction process with the sample material, allowing for element specific contrast, either in transmission mode or by measuring the fluorescence signal [e.g. 156]. Until the mid-1990s, when first third generation synchrotron radiation sources started to become operational, this development was limited largely to full field and scanning transmission microscopy, mostly in the soft x-ray energy range¹ [78]. The application to cellular imaging has been a motivation for the development of the method from the early stages on [79] and has turned until today into a mature technique to image three-dimensional subcellular ultrastructure of cells in a frozen hydrated environment [81, 82, 151].

Conventional biological x-ray microscopy mostly relies on absorption contrast which is well-suited for biological applications in the so-called water window range of photon energies (between about 280 eV and 530 eV) where absorption contrast between carbon and oxygen is especially high. If an (x-ray) optical wave field leaves a sample surface, there is, however, a second quantity next to the wave's amplitude that carries information on the sample to a detector: the phase. The degree to which this phase information can be exploited, however, depends largely on the degree of coherence of the incident wave field.

With an increasing awareness of the high degree of spatial coherence that is provided by modern synchrotron radiation sources the development of propagation-based phase contrast imaging was initiated [22, 134]. For reviews on the further development of the technique see [105, 108]. One of the methods studied in the present thesis with respect to single cell imaging, is based on this technique. Here the contrast is formed not by absorption as in transmission x-ray microscopy (or radiography), but solely based on diffraction effects upon interaction of the (partially) coherent x-ray beam with a semi-transparent sample. As a result, the change in phase that is imprinted by the sample onto

¹I.e. photon energies between ca. 0.284 keV (carbon K-absorption edge) and 5 keV.

the wave field can be measured quantitatively [23]. Using hard x-ray beams², the technique has been demonstrated to be well-suited for imaging macroscopic thick samples with resolutions in the micrometer range, depending mostly on the resolution of the detection system [e.g. 25, 85, 137]. Combined with geometric magnification provided by a 'point' source, the resolution can be significantly increased [8, 48]. To provide the necessary cone beam illumination, focusing optics, such as reflective mirrors [8] or refractive lenses [128] are applied. Two-dimensional x-ray waveguides can be used to further decrease the source size [80], enabling a higher numerical aperture of the resulting divergent wave field and thus providing the potential for higher resolution [80], i.e. in the routine resolution range of current soft x-ray biological microscopy (about 40-100 nm) [81, 82, 126, 151]. Current biological applications of propagation-based x-ray phase contrast imaging and microscopy reach from in vivo studies of small vertebrate [85] and insect [85] respiratory systems to quantitative three dimensional analysis of multicellular seed structures [24].

Parallel to the development of propagation-based coherent x-ray imaging another coherent x-ray microscopy technique has evolved, now named Coherent x-ray Diffractive Imaging (CXDI) which forms the basis for the second technique studied in this thesis. For recent reviews see [105, 142]. In its original experimental realization the technique is very similar to conventional crystallography: A plane wave is used to illuminate the specimen, and a far field diffraction pattern is collected on a two-dimensional detector. Unlike in crystallography, however, the specimen is *not crystalline*. As a result, the diffraction pattern is not a collection of isolated Bragg peaks, but a continuous intensity distribution, sampled at the location of the detector pixels. As only the wave field intensity can be measured in the detector plane, a recovery of the phase information is necessary to reconstruct an image of the object in real space. The potential for a reconstruction of such a continuous intensity pattern and related sampling requirements have first been discussed in 1952 [124], and iterative algorithms to reconstruct the complex-valued wave fields from their far field intensity distributions started to evolve rather independently [45, 53]. In 1999 the first experimental demonstration of coherent x-ray diffractive imaging was achieved in the (soft) x-ray energy range [99], again enabled by the high degree of coherence provided by a synchrotron source. Largely driven by the potential to overcome technical restrictions in the fabrication of x-ray lenses, the technique has been applied successfully by now to single freeze-dried [103, 132] and frozen-hydrated [73, 86] cells, with a potential to exceed the resolution of conventional x-ray microscopy which is limited by the lenses. As a result of the Shannon theorem, for plane wave illumination sufficient sampling of the diffraction pattern and therefore reconstruction is only possible, if the object has a finite extension in real space. As a consequence, the 'classical' scheme of CXDI does not allow for the application to extended specimens, such as multicellular arrangements exceeding the cross-section of the illumination. This limitation has motivated the development of alternatives which allow for the combination of scanning microscopy with diffraction microscopy. Ptychographic coherent diffractive imaging (PCDI), a combination of iterative phase retrieval with scanning microscopy, was the first demonstrated extension of the original CXDI scheme to overcome its field of view limitation [118]. Here a localized illumination, e.g. provided by an unfocused synchrotron beam confined by a small pinhole

²I.e. photon energies above ca. 5 keV up to typically several dozen keV.

(diameter in the range of a micron), is used to probe an extended specimen at varying lateral positions. The transmission function of the extended object is then reconstructed iteratively from an ensemble of diffraction patterns, each corresponding to one sample position [118]. Originally [118], the complex-valued illumination had to be known or estimated a-priori to make the reconstruction process feasible. As a localized x-ray wave field provided e.g. by a pinhole is much more difficult to predict than the nearly plane wave used in conventional CDI, the accuracy of the method was limited to that of the predicted illumination. As a consequence, in its original scheme the method was limited in the x-ray range to strongly scattering specimens [118]. As a crucial step forward, in 2008 it was first demonstrated [141] using a nanofabricated Au test structure as an object and the focus of a Fresnel zone plate for illumination that the complex-valued illumination can be reconstructed *simultaneously* with the object transmission from the same dataset.

Goals and structure of the thesis

Within this context, the main goal of the present thesis was to apply two new variants of coherent x-ray microscopy, namely propagation-based x-ray microscopy (using waveguides) and ptychographic Coherent Diffractive Imaging to the case of weakly scattering, unstained biological cells.

To this end, it was necessary to provide a suitable sample environment for imaging of cells in a hard x-ray beam, compatible with freeze-dried, but also frozen-hydrated specimens and to implement necessary preparation techniques.

For numerical analysis and simulation, optical modeling and reconstruction routines had to be implemented, suitable for application to coherent x-ray experiments.

Within a first synchrotron experiment, then the sensitivity limits of the ptychographic imaging technique towards the application to single biological cells were to be explored. Here it was the goal to apply the recently demonstrated ptychographic reconstruction technique [141] that allows for simultaneous retrieval of the complex illumination and object.

The hard x-ray energy range is especially suited for coherent phase contrast imaging, on the other hand, the interaction of biological material with x rays in this energy range is relatively weak. An additional goal was therefore to apply ptychographic CDI also in the soft x-ray range where the scattered signal for a given incident number of photons is significantly increased.

In the second branch of activities, it was aimed to extend waveguide-based x-ray propagation microscopy [47, 48] to single biological cells. Here the goal was to use the geometry of in-line holography with cone beam illumination. For quantitative image analysis the holographic reconstruction scheme had to be replaced by a suitable iterative reconstruction scheme, similar to those applied in Coherent Diffractive Imaging.

The thesis is organized as follows. In Chapter 2 selected aspects from Fourier and signal theory are reviewed which are necessary for the theoretical description of wave field propagation. The purpose is to outline mathematical tools necessary for implementation of optical modeling techniques used throughout the thesis. Special emphasis is placed on the discrete Fourier transform (DFT) which forms the basis of all numerical propagation schemes used here. Consequences of the associated sampling of continuous

functions are discussed as well as the relation of the DFT to its continuous counterpart. As a technical, but important aspect the use of centered and non-centered sequences in the DFT is discussed. The chapter closes with a restatement of the sampling theorem and an introduction of the smallest possible sampling rate to completely characterize a continuous signal, the Nyquist rate.

In Chapter 3 selected aspects of scalar diffraction theory in free space and matter are outlined. The concepts form the basis for wave field reconstructions and simulations presented in the following chapters. Analytical expressions for the propagation equations are restated and complemented by numerical counterparts using the discrete Fourier transform. As an important theoretical prerequisite for propagation microscopy with cone-beam illumination, the Fresnel scaling theorem is restated, followed by a discussion of coherence. The interaction of wave fields with matter is described for all experiments of this thesis within the so-called projection approximation which is reviewed and discussed in terms of its validity range. For completeness, also the description within Born approximation is briefly reviewed and set into context to the projection approximation.

In Chapter 4 basic concepts of coherent x-ray microscopy are described, as needed for the later applications to biological cells. In particular, different optical imaging regimes are discussed and illustrated with numerical examples. As a first possible route to reconstruction iterative maps are reviewed and illustrated with a numerical example for classical far field CDI. Next, the principle of in-line holography is restated which can be applied in propagation-based coherent microscopy. Based on iterative reconstruction, it is shown for a numerical example how the twin-image problem of in-line holography can be circumvented for experimental parameters relevant to this thesis. Subsequently, the principle of ptychographic CDI is reviewed. Then, experimental aspects such as resolution, noise and coherence are discussed, followed by a section on radiation damage to biological samples. Finally, the sample environment, the used preparation methods and their theoretical background are described.

The experimental part of the thesis is based on three synchrotron experiments carried out (in the order of appearance) at the Swiss Light Source (Villigen, Switzerland), the synchrotron storage ring Bessy II at the Helmholtz Center Berlin, as well as the European Synchrotron Radiation Facility (Grenoble, France).

Chapter 5 presents the extension of ptychographic CDI to freeze-dried bacterial cells. Details of the reconstruction process are described, followed by an evaluation of the obtained results. Reconstructions of simulated data are shown to corroborate the experimental findings and to give an estimate of the experimental error.

Chapter 6 presents the extension of ptychographic CDI to soft x-ray wavelengths. Two samples have been imaged, namely a fossil diatom and a tantalum test structure. A detailed description of the reconstruction is followed by a presentation of the experimental results. Consequences of the low photon energy and the high phase curvature of the incident illumination are discussed.

Chapter 7 describes the extension of waveguide-based x-ray microscopy to freeze-dried eukaryotic cells. A detailed review of the necessary raw data treatment is followed by the description of simulations which are again used here to support and test the experimental results. Next, an iterative reconstruction scheme that takes into account the experimental noise and allows for the circumvention of the twin image problem is described. Subse-

quently, the results obtained on the experimental and simulated data using three different reconstruction schemes are presented, compared and evaluated. Lastly, a reconstruction for simulated data is shown that explores higher magnifications than experimentally obtained.

The thesis ends with a short summary and conclusion in Chapter 8.

2 Aspects of Fourier and signal theory

In this chapter important relations from the theory of continuous and discrete Fourier transforms are reviewed and discussed. With a wide range of applications, for which the modeling of optical wave fields is only one example, the underlying concepts are more generally covered under the term ‘signal theory’ in the physics and engineering literature. A large body of textbook literature is available on the topic from which a selection [10, 14, 16, 20, 28, 74] was used in the preparation of this chapter. The emphasis is on a self-contained presentation and discussion of concepts relevant to the topic of this thesis rather than on mathematically rigorous derivations.

2.1 Motivation

The description of light wave propagation would be impossible without the mathematical concept of Fourier transforms. Given a possibly complex-valued scalar function $f(x)$ of a real variable x (i.e. a wave field at a certain position), the Fourier transform allows to give a mathematically equivalent representation of the function in terms of its spectral or frequency components. As outlined in chapter 3, this is the basis for the mathematical description of the spatial evolution of a wave field that can be written as an infinite sum of so-called elementary waves with distinct single-frequency components.

As a consequence, many concepts from the theory of Fourier transforms are applied throughout the text, so that a commented list of them is given in this chapter. Importantly, continuous wave fields are experimentally only accessible with two main restrictions: We can only observe them at *distinct positions* in space (in fact only as a mean over a finite interval) and on a *finite amount* of these positions. In other words, we have only access to *sampled* versions of the functions and its Fourier transforms, both experimentally and in terms of numerical analysis on a computer. Such an analysis inevitably requires abandoning the concept of continuous Fourier transforms and relying on approximations of the continuous fields using a finite amount of samples at certain positions. We will follow a rather pragmatic approach here and use the mathematical tool of the discrete Fourier transform (DFT) to approximate the propagation of continuous wave fields. There are various ways to connect the discrete Fourier transform to the continuous Fourier transform [for an overview on different approaches see 10]. One very common approach is the view of the DFT as an approximation of the Fourier integral by the trapezoidal rule. However, the periodicity that is induced by the sampling process, both in real and Fourier space, and the related consequences relevant for the DFT are not reflected by this approach.

These become clear when the DFT is interpreted as the continuous Fourier transform of a continuous function, sampled by a Dirac comb.

All relations are presented here for one dimension only. For higher dimensions analogous relations exist.¹

2.2 From the Fourier series to the continuous Fourier transform

A suitably well-behaved periodic function $f_L : x \in \mathbb{R} \mapsto f(x) \in \mathbb{C}$ with finite period length $L \in \mathbb{R}$ can be expressed as a (not necessarily) infinite linear combination of elementary periodic functions with distinct frequencies $k_n = 2\pi n/L$ via its so-called **Fourier series**

$$f_L(x) = \sum_{n=-\infty}^{+\infty} C_n e^{ik_n x}. \quad (2.1)$$

The complex-valued weight factors C_n can be determined via the integrals

$$C_n = 1/L \int_{-L/2}^{L/2} f_L(x) e^{-ik_n x} dx \quad (2.2)$$

of f_L over one period length. Note that Eq. (2.1) can equivalently be given as an infinite non-negative sum over cosine- and sine-functions with non-negative angular frequencies $k_n \geq 0$. As a consequence, every frequency modulus $|k_n|$ with $n \neq 0$ is associated with two independent real coefficients, but the appearance of negative frequencies in the sum is a matter of definition here.

For this reason there is a component in the sum (2.1) with a distinct, lowest non-zero fundamental frequency $k_1 = 2\pi/L$ – or if we define the rotational frequency as $\nu_n = k_n/2\pi$ – with the fundamental $\nu_1 = 1/L$, corresponding to the period length of the function f_L . No lower-frequency components can be contained in f_L as they would have a period larger than L . In addition, no frequency components other than those with integer multiple frequencies of ν_1 can be contained as they would not be periodic with period length L . In other words, the periodicity of f_L with a finite period length L leads to its spectral decomposition into components with *discrete* frequencies k_n and spacing $\Delta k = k_1 = 2\pi/L$ in the space of all possible frequencies $k \in \mathbb{R}$. On the other hand, f_L is defined on a *continuous* real space with values $x \in \mathbb{R}$.

A full duality between the space of possible frequencies of elementary periodic functions that make up a function f and the space it is defined on is established via extending the period length L to infinity, i.e. considering a function $f(x)$ that is non-periodic.

Making this transition explicitly in Eq. (2.1) we obtain for a non-periodic function f (or f_L in the limit $L \rightarrow \infty$):

$$f(x) = \lim_{L \rightarrow \infty} \sum_{n=-\infty}^{n=+\infty} \frac{1}{L} \left(\int_{-L/2}^{L/2} f(x) e^{-ik_n x} dx \right) e^{ik_n x} \quad (2.3)$$

$$= \frac{1}{\sqrt{2\pi}} \int dk \left(\frac{1}{\sqrt{2\pi}} \int f(x) e^{-ikx} dx \right) e^{ikx}. \quad (2.4)$$

¹In particular, for the 2D discrete Fourier transform and its properties we refer the reader to refs. [10, 109].

Note that before taking the limit $L \rightarrow \infty$ we have substituted $1/L = \Delta k / (2\pi)$ and $k_n = n\Delta k$. We now define the **Fourier transform** of a function f as

$$\mathcal{F}[f](k) := \tilde{f}(k) := \frac{1}{\sqrt{2\pi}} \int f(x) e^{-ikx} dx \quad (2.5)$$

and the **Fourier back transform** of a function g as

$$\mathcal{F}^{-1}[g](x) := \hat{g}(x) := \frac{1}{\sqrt{2\pi}} \int g(k) e^{ikx} dk. \quad (2.6)$$

With these definitions we can interpret Eq. (2.4) as follows: Any suitably well-behaved function f can be decomposed into its elementary periodic spectral components e^{ikx} with angular frequencies k and weight factors which are given by the Fourier transform $\tilde{f}(k)$, evaluated at frequency k . As the spectral decomposition is defined as the inverse Fourier transform, we also have the result

$$\mathcal{F}^{-1}[\mathcal{F}[f]] = f \quad (2.7)$$

which is also denoted as the **Fourier theorem**.

It can be shown [3] that on the space $L^2(\mathbb{R})$ of square-integrable functions on \mathbb{R} the Fourier theorem (2.7) defines a bijective mapping, i.e. there is a one-to-one correspondence between a function and its Fourier transform and vice versa. We call such a tuple of functions a **Fourier pair** and denote it by

$$f(x) \leftrightarrow \tilde{f}(k). \quad (2.8)$$

2.2.1 Important properties of the continuous Fourier transform

Shifting property. The Fourier transform of a shifted function is given as the Fourier transform of the original times a complex exponential and vice versa:

$$f(x - x_0) \leftrightarrow \tilde{f}(k) e^{-ikx_0} \quad (2.9)$$

$$f(x) e^{ik_0 x} \leftrightarrow \tilde{f}(k - k_0) \quad (2.10)$$

Scaling.

$$f(\alpha x) \leftrightarrow \frac{1}{|\alpha|} \tilde{f}\left(\frac{k}{\alpha}\right) \quad (2.11)$$

for $\alpha \in \mathbb{R} \setminus \{0\}$.

Derivatives of functions. Derivatives in real space are translated into a multiplication with the reciprocal coordinate k in Fourier space:

$$\frac{d^m}{dx^m} f(x) \leftrightarrow (ik)^m \tilde{f}(k) \quad (2.12)$$

for any $m \in \mathbb{N}$.

Convolution theorem. We define the **convolution** of two functions f and g as

$$(f \otimes g)(x) := \int d\lambda f(\lambda) g(x - \lambda) = \int d\lambda f(x - \lambda) g(\lambda) = (g \otimes f)(x). \quad (2.13)$$

We then have the following Fourier pairs:

$$(f \otimes g)(x) \leftrightarrow \sqrt{2\pi} \tilde{f}(k) \tilde{g}(k) \quad (2.14)$$

$$f(x)g(x) \leftrightarrow \frac{1}{\sqrt{2\pi}} (\tilde{f} \otimes \tilde{g})(k). \quad (2.15)$$

In words, the Fourier transform of the convolution of two functions is proportional to the product of their Fourier transforms and the Fourier transform of the product of two functions is proportional to the convolution of their Fourier transforms.

Correlation theorem. We define the **cross-correlation** of two functions as

$$(f \oplus g)(x) := \int d\lambda f(\lambda) g^*(\lambda + x) = \int d\lambda f(\lambda - x) g^*(\lambda) \quad (2.16)$$

with the star $*$ denoting complex conjugation. Note that as an operator on the two functions f and g , the cross-correlation, unlike the convolution, is generally *not* commutative. We then have the Fourier pair

$$(f \oplus g)(x) \leftrightarrow \sqrt{2\pi} \tilde{f}(k) \tilde{g}^*(k). \quad (2.17)$$

We define the **autocorrelation** of a function f as

$$(f \oplus f)(x) := \int d\lambda f(\lambda) f^*(\lambda + x) = \int d\lambda f(\lambda - x) f^*(\lambda) \quad (2.18)$$

which is hermitian, i.e.

$$(f \oplus f)(-x) = (f \oplus f)^*(x) \quad (2.19)$$

as can be derived by writing out the definitions. The Fourier transform of the autocorrelation of f is related to the Fourier transform of f via

$$\mathcal{F}[(f \oplus f)](k) = \sqrt{2\pi} |\tilde{f}(k)|^2, \quad (2.20)$$

i.e. the Fourier transform of the autocorrelation of a function is proportional to the squared modulus of the function's Fourier transform. The function $|\tilde{f}(k)|^2$ is often also called the **power spectrum** or **power spectral density** of the function.

Plancherel's theorem. Fourier back transformation of Eq. (2.20) and setting $x = 0$ on both sides leads to

$$\int |f(x)|^2 dx = \int |\tilde{f}(k)|^2 dk. \quad (2.21)$$

Symmetry. An even (odd) function stays even (odd) after Fourier transforming it, i.e.

$$f(x) = f(-x) \Rightarrow \tilde{f}(k) = \tilde{f}(-k), \quad (2.22)$$

$$f(x) = -f(-x) \Rightarrow \tilde{f}(k) = -\tilde{f}(-k). \quad (2.23)$$

In addition we note that

$$f \text{ real} \Rightarrow \tilde{f}^*(k) = \tilde{f}(-k) \quad (2.24)$$

$$f \text{ imaginary} \Rightarrow \tilde{f}^*(k) = -\tilde{f}(-k). \quad (2.25)$$

This can also be formulated in the following way: The Fourier transform of a real function is hermitian, the Fourier transform of an imaginary function is anti-hermitian. By combination of the preceding properties one arrives at

$$f \text{ real and even} \Rightarrow \tilde{f} \text{ real and even.} \quad (2.26)$$

Friedel symmetry. From the definition of the autocorrelation $f \oplus f$ it follows that it is a hermitian function. This implies, firstly, that the real part of the autocorrelation function is always an even function while the imaginary part is always odd. In addition, it follows that a real function always has an even (and real) autocorrelation function, just as a purely imaginary function also has a real and even autocorrelation function. In either case, the Fourier transform of the corresponding autocorrelation function is an even function as well, so that we have

$$\begin{aligned} f(x) \in \mathbb{R} \forall x \quad \vee \quad f(x) \in \mathbb{C} \setminus \mathbb{R} \forall x \\ \Downarrow \\ (f \oplus f)(x) &= (f \oplus f)(-x) \\ \Downarrow \\ |\tilde{f}(k)| &= |\tilde{f}(-k)|. \end{aligned} \quad (2.27)$$

These relations express what is called Friedel symmetry in crystallography: A real electron density function leads to centrosymmetric diffraction patterns [2].

2.2.2 Fourier transforms of important functions

Double-sided step function. The function

$$\Pi_L(x) = \begin{cases} 1 & \text{for } -L/2 \leq x < L/2 \\ 0 & \text{else} \end{cases} \quad (2.28)$$

is sometimes also called a hat-function. In its normalized form (with unit area under the hat) it forms the following Fourier pair with the sinc-function (sinus cardinalis):

$$\frac{1}{L} \Pi_L \leftrightarrow \frac{1}{\sqrt{2\pi}} \text{sinc}(kL/2) = \frac{1}{\sqrt{2\pi}} \frac{\sin(kL/2)}{kL/2}. \quad (2.29)$$

Dirac- Δ . The “function” defined by $\delta(x) := \lim_{L \rightarrow \infty} \Pi_L(x)/L$ goes to infinity at $x = 0$ and vanishes elsewhere while maintaining a constant area of one below every function of the series, so that $\int \delta(x) dx = 1$. For any function $f(x)$

$$\int dx \delta(x - x_0) f(x) = f(x_0), \quad (2.30)$$

i.e. integration over the product of the Dirac- δ , centered at a position x_0 , with function $f(x)$ picks out the function value at that position. With the Dirac- δ one arrives at the following Fourier pairs

$$\delta(x) \leftrightarrow \frac{1}{\sqrt{2\pi}} \quad (2.31)$$

$$1 \leftrightarrow \sqrt{2\pi} \delta(k). \quad (2.32)$$

In words: One needs the whole frequency space to model an infinitely sharp peak (which can be seen by looking at the Fourier transform of the hat-function for $L \rightarrow 0$). On the other hand, a constant in real space corresponds to a single distinct frequency $\nu = 1/L = 0$. Using the shifting property of the Fourier transform we also get

$$\delta(x - x_0) \leftrightarrow \frac{1}{\sqrt{2\pi}} e^{-ikx_0} \quad (2.33)$$

$$e^{ik_0x} \leftrightarrow \sqrt{2\pi} \delta(k - k_0). \quad (2.34)$$

Fourier back transforming the right side of the Fourier pair (2.33) yields an integral representation for the Dirac- δ :

$$\delta(x - x_0) = \frac{1}{2\pi} \int e^{ik(x-x_0)} dk. \quad (2.35)$$

Gaussian function. The Fourier transform of a Gaussian function $f(x) = \exp(-\alpha x^2)$ with $\alpha > 0$ is another Gaussian [3]:

$$e^{-\alpha x^2} \leftrightarrow \frac{1}{\sqrt{2\alpha}} e^{-\frac{k^2}{4\alpha}}. \quad (2.36)$$

For $\alpha = 1/(2\sigma^2)$ the $1/\sqrt{e} \approx 0.61$ decay half width of the Gaussian function is equal to σ . One then obtains

$$e^{-\frac{x^2}{2\sigma^2}} \leftrightarrow \sigma e^{-\frac{\sigma^2 k^2}{2}}. \quad (2.37)$$

The Fourier transform of a Gaussian with $1/\sqrt{e}$ decay half width σ is thus another Gaussian with $1/\sqrt{e}$ decay half width of $1/\sigma$. If a Gaussian is given as defined above with $\alpha = 1/(2\sigma^2)$, the $1/\beta$ decay half width with $\beta > 0$ can be obtained as $\sigma \sqrt{2 \ln \beta}$. As an example, the half width at half maximum is given as $\sigma \sqrt{2 \ln 2}$.

Comb function. We can construct a periodic “comb” of Dirac- δ ’s with period length L as

$$\text{III}_L(x) := \sum_{n=-\infty}^{\infty} \delta(x - nL), \quad (2.38)$$

giving rise to the Fourier pair

$$\sum_{n=-\infty}^{\infty} \delta(x - nL) \leftrightarrow \frac{1}{\sqrt{2\pi}} \sum_{m=-\infty}^{\infty} e^{imkL}. \quad (2.39)$$

As $\text{III}_L(x)$ is a periodic function with period L , it has a Fourier series representation

$$\text{III}_L(x) = \frac{1}{L} \sum_{n=-\infty}^{\infty} e^{-i2\pi nx/L}, \quad (2.40)$$

leading to the Fourier pair

$$\frac{1}{L} \sum_{n=-\infty}^{\infty} e^{-i2\pi nx/L} \leftrightarrow \frac{\sqrt{2\pi}}{L} \sum_{m=-\infty}^{\infty} \delta\left(k - m \frac{2\pi}{L}\right). \quad (2.41)$$

As a consequence we see that the Fourier transform of an infinite train of Dirac- δ 's is another infinite train of Dirac- δ 's:

$$\sum_{n=-\infty}^{\infty} \delta(x - nL) \leftrightarrow \frac{\sqrt{2\pi}}{L} \sum_{m=-\infty}^{\infty} \delta\left(k - m\frac{2\pi}{L}\right). \quad (2.42)$$

Note that we have seen before that the Fourier transform of a *single* Dirac- δ is a finite function. Here the periodicity of the III_L -function causes the Fourier transform to be a another function with infinite values. In short we can write the above Fourier pair as

$$\text{III}_L(x) \leftrightarrow \frac{\sqrt{2\pi}}{L} \text{III}_{\frac{2\pi}{L}}(k). \quad (2.43)$$

2.3 Sampling continuous functions

As outlined in the beginning of this chapter the application of the theory of Fourier transforms to measured data suffers from several restrictions. Instead of knowing an analytical expression $f(x)$ for the function f , one can only measure a *finite* set $\{f(x_n)\}$ of *noisy*, *digitized* function values, *averaged* over a *finite* measurement interval.

Mathematically, the knowledge of exact function values at an infinite number of discrete points x_n with equal distances $\Delta x = x_{n+1} - x_n \forall n$ allows for the derivation of an exact analytical expression between the Fourier transform of an infinite sequence of sample values $(f(x_n))$ and the continuous Fourier transform of $f(x)$. This relation implies the Discrete Fourier transform and experimentally we will make an effort to work close to this 'ideal sampling' in a mathematical sense, in order to replace the continuous Fourier transform by its discrete counterpart.

We will also see that the knowledge of f at an infinite amount of discrete points $x_n = n\Delta x$ with $n \in \mathbb{Z}$ is enough to give an analytical expression for $f(x)$ at any $x \in \mathbb{R}$ with quite loose demands on f . This is the content of the sampling theorem.

At first, we take a short look on how the 'ideal' sampling process is related to the measurement process. Experimentally, it is not possible to measure the value of a function at a discrete point x_n with zero extension, as a detector will always have some finite sensitive area (and finite measurement time), over which the incoming signal has to be averaged. If the area (or in one dimension the interval $I = [x_n - \Delta x/2, x_n + \Delta x/2]$) is small and if the signal does not vary much within I the measured mean value $\langle f \rangle_I := 1/\Delta x \int_{x_n - \Delta x/2}^{x_n + \Delta x/2} f(x) dx$ will not differ a lot from any $f(x)$ for $x \in I$.² Therefore, one is tempted to choose the width Δx of the interval I as small as possible as with a smooth f one has $\langle f \rangle_I \rightarrow f(x)$ for any $x \in I$ and $\Delta x \rightarrow 0$. On the other hand, measuring light intensities inherently involves (at least) photon noise and a continuously decreasing measurement interval will lead eventually to very high relative noise values in the signal, unless a nearly infinite amount of measurement time is used. This makes the measured value $\langle f \rangle_I$ useless as a representation of $f(x_n)$. Therefore, one always has to compromise between small

²Furthermore, we note here that the detector may not have a constant sensitivity over the active area as it is implicitly assumed here. Before integration, $f(x)$ then has to be multiplied with a non-constant window function to model the detector's response.

sampling periods, i.e. measurement intervals, which are desirable in terms of close-to-ideal sampling, and the required measurement time to get a useful non-noisy signal.

To proceed further, the measured signal $\langle f \rangle_I \in \mathbb{R}$ has to be discretized in the measurement process to $D(\langle f \rangle_I) \in \mathbb{N}$ before it is fed into any numerical calculation for further analysis. Here one has to make sure that the discretization is fine enough, so that $D(\langle f \rangle_I) \simeq \langle f \rangle_I$. For measuring light intensities, this is not a restriction as there is a physical quantization of light intensity into photons.

With these restrictions in mind, in the following, we will assume that we have made our measurements careful enough so that one can always well approximate

$$D(\langle f \rangle_{I=[x_n-\Delta x, x_n+\Delta x]}) \simeq f(x_n). \quad (2.44)$$

2.3.1 Definitions related to sampling

We now give some notation conventions and definitions related to the sampling of a function. Consider the function $f : x \in \mathbb{R} \mapsto f(x) \in \mathbb{C}$. We call the infinite sequence of function values

$$\mathbf{f}_\infty := (f(x_n)) := (f_n) \quad (2.45)$$

with $n \in \mathbb{Z}$ and $x_n = n\Delta x$ the **sampled (version of the) function**, sampled at the equispaced **infinite grid**

$$\mathbf{x}_\infty := (x_n). \quad (2.46)$$

Representing a continuous function by a sampled version thus always requires two sequences, namely the sequence of function values (f_n) as well as the associated grid (x_n) . The choice of the index number $n_0 = 0$ for the value $f(x_{n_0} = 0) = f_{n_0}$ at the origin is fixed by the above definition and if not stated otherwise we will use $n_0 = 0$.

The frequency $r_{\Delta x} := 1/\Delta x$ is called the **sampling rate**. Note that an **index shift** $x_n \rightarrow x_{n+l}$ with $l \in \mathbb{Z}$ now corresponds to a **translation** by the distance $l\Delta x$, as $x_{n+l} = x_n + l\Delta x$. For the discretized sequence of function values this leads to $f(x_n) = f_n \rightarrow f_{n+l} = f(x_{n+l}) = f(x_n + l\Delta x)$.

Defined on the **finite** interval $I = [0, L[$ the sequence (f_n) of function values

$$\mathbf{f}_N := (f_0, f_1, \dots, f_{N-1}) \quad (2.47)$$

and the associated grid

$$\mathbf{x}_N := (x_0, x_1, \dots, x_{N-1}) \quad (2.48)$$

$$:= \mathbf{n}_N \Delta x \quad (2.49)$$

with the **standard index sequence**

$$\mathbf{n}_N := (0, 1, \dots, N-1) \quad (2.50)$$

become finite with N elements. Similarly, we call the finite sequences \mathbf{f}_N and \mathbf{x}_N the **standard sequences** of \mathbf{f}_∞ and \mathbf{x}_∞ , respectively. Note that with this definition the interval I is divided into N positions x_n , the first position is equal to the left limit of the interval

and the distance between the positions is $\Delta x = L/N$.

Consider now the shifted interval $I_a = [a, a + L[$, shifted by a distance $a = l\Delta x$ with $l \in \mathbb{Z}$. With the shifted standard index sequence

$$\mathbf{n}_N^{(l)} := \mathbf{n}_N + l\mathbf{1}_N \quad l \in \mathbb{Z} \quad (2.51)$$

with $\mathbf{1}_N := (1, 1, \dots, 1)$ of length N one has $\mathbf{n}_N = \mathbf{n}_N^{(0)}$ and in general $\mathbf{n}_N^{(l)} = \mathbf{n}_N^{(j)} + (l - j)\mathbf{1}_N$ for $l, j \in \mathbb{Z}$. This leads to the shifted grid

$$\mathbf{x}_N^{(l)} = \mathbf{n}_N^{(l)} \Delta x \quad (2.52)$$

defined now on the interval $I_a = [a, a + L[$. Also here the definitions yield $\Delta x = L/N$. The corresponding sequence of function values is $\mathbf{f}_N^{(l)} = (f_l, f_{l+1}, \dots, f_{l+N-1})$.

Important note on implementation in Matlab. All numerical calculations within this thesis have been carried out using the Matlab³ language. An N -tuple of real or complex numbers h_1, h_2, \dots, h_N can be defined in Matlab as a line-vector (or $(1 \times N)$ -matrix) as

$$\mathbf{h}_N := [h_1, h_2, \dots, h_N] \quad (2.53)$$

and the fields in the vector are addressed via

$$h(1) = h_1, h(2) = h_2, \dots, h_N = h(N), \quad (2.54)$$

i.e. the indexing in a Matlab-vector always starts at 1 and there is no zero index nor negative indices. As a consequence, the previously defined notation for the sampling of an interval $I = [0, L[$ has to be modified. In other words, for the index n_0 of the zero element $f_{n_0} = f(x_{n_0} = 0)$ one now has $n_0 = 1$. The standard sequences in Matlab are therefore

$$\mathbf{f}_N := [f_1, f_2, \dots, f_N] \quad (2.55)$$

and the associated grid

$$\mathbf{x}_N := [x_1, x_2, \dots, x_N] \quad (2.56)$$

$$:= (\mathbf{n}_N - \mathbf{1}_N) \Delta x. \quad (2.57)$$

Note that we have defined the standard Matlab index sequence of length N as

$$\mathbf{n}_N := [1, 2, \dots, N]. \quad (2.58)$$

We distinguish abstract sequences (f_n) from Matlab-sequences $[f_n]$ by using typewriter letters. Note that with this notation $\mathbf{x}_N = \mathbf{x}_N$, $\mathbf{f}_N = \mathbf{f}_N$ and $\mathbf{n}_N = \mathbf{n}_N - \mathbf{1}_N$. In both cases the definitions involve $\Delta x = L/N$.

³Matlab is a registered trademark of the The Mathworks Inc.

2.3.2 Ideal sampling and Dirac combs

Suppose the values of the function f are known at an infinite number of discrete points $x_n = n\Delta x$ with $n \in \mathbb{Z}$. We thus have the two infinite sequences (x_n) and (f_n) . We call the expression

$$S_{\Delta x}[f](x) := f(x)\text{III}_{\Delta x}(x) = f(x) \sum_{n=-\infty}^{\infty} \delta(x - n\Delta x) = f(n\Delta x) \sum_{n=-\infty}^{\infty} \delta(x - n\Delta x) \quad (2.59)$$

the **ideally sampled (version of the) function** f with sampling period Δx which has the property $\int S_{\Delta x}[f](x)dx = \sum_{n=-\infty}^{\infty} f_n$ which does not change if we replace $f(x)$ by the sampled values $f(n\Delta x)$ as we did on the right side of Eq. (2.59).

Furthermore, from the function f we can always uniquely construct a periodic function with period length L via

$$P_L[f](x) := f(x) \otimes \text{III}_L(x) = \sum_{n=-\infty}^{\infty} f(x - nL) \quad (2.60)$$

which we call the **periodized (version of the) function** f with period length L . It is constructed as an infinite sum of translated copies of the original function f , each translated by an integer multiple of the period length L . Suppose now that f has a bounded support⁴. Here we define the **support** of a function $f(\mathbf{x})$ with $\mathbf{x} \in \mathbb{R}^d$ and $d \in \mathbb{N}$ as the set $S := \{\mathbf{x} \mid f(\mathbf{x}) \neq 0\}$ of points where the function is non-zero. S is called bounded, if it has a finite extension with respect to a certain norm in \mathbb{R}^d . If $f(x)$ (we now return to $d = 1$) has bounded support, we can always choose an origin so that $\exists b \in \mathbb{R}$ with $f(x) = 0$ for $|x| > b$. If then $L > 2b$, then $P_L[f](x) = f(x)$ on the interval $[-L/2, L/2]$.

Summarizing, multiplication of a function with a Dirac-comb yields an ideally sampled version of the function. Convolution with a Dirac-comb leads to a periodized version of the original function which is equal to the function itself on the interval $B = [-L/2, L/2]$, if f vanishes outside $[-b, b]$ and if $L > 2b$.

We will now evaluate the Fourier transforms of ideally sampled and of periodized functions. Consider the ideally sampled function $S_{\Delta x}[f]$ with sampling period Δx . With previously stated Fourier transform relations we obtain

$$\begin{aligned} \mathcal{F}[S_{\Delta x}[f]] &= \mathcal{F}[f \cdot \text{III}_{\Delta x}] \\ &= \frac{1}{\sqrt{2\pi}} \cdot \tilde{f} \otimes \widetilde{\text{III}}_{\Delta x} \\ &= \frac{1}{\Delta x} \cdot \tilde{f} \otimes \text{III}_{\frac{2\pi}{\Delta x}} \\ &= \frac{1}{\Delta x} \cdot P_{\frac{2\pi}{\Delta x}}[\tilde{f}]. \end{aligned}$$

⁴In fact, if f has no bounded support, the existence of a finite function $P_L[f](x)$ is generally not guaranteed. One may then have to select a certain interval from the domain of f by multiplication of f with a window function $\Pi_B(x)$ with $B > 0$. Note, however, that this affects the Fourier transform of the function $P_L[f](x)$.

Consider now the periodized function $P_L[f]$ of f with period length L . For the Fourier transform we obtain

$$\begin{aligned} \mathcal{F}[P_L[f]] &= \mathcal{F}[f \otimes \text{III}_L] \\ &= \sqrt{2\pi} \cdot \tilde{f} \cdot \widetilde{\text{III}}_L \\ &= \frac{2\pi}{L} \cdot \tilde{f} \cdot \text{III}_{\frac{2\pi}{L}} \\ &= \frac{2\pi}{L} \cdot S_{\frac{2\pi}{L}}[\tilde{f}]. \end{aligned}$$

We thus arrive at the following conclusion:

(Ideal) sampling of a function f in real space with sampling period Δx is equivalent to periodizing its Fourier transform with period $2\pi/\Delta x$.

Ideal sampling of the Fourier transform \tilde{f} of a function f , with sampling period $2\pi/L$, corresponds to periodizing the function itself, with period length L .

Short: Sampling in real space corresponds to periodizing in reciprocal space and vice versa.

This can be expressed by the Fourier pairs

$\begin{aligned} S_{\Delta x}[f] &\leftrightarrow \frac{1}{\Delta x} P_{\frac{2\pi}{\Delta x}}[\tilde{f}] \\ P_L[f] &\leftrightarrow \frac{2\pi}{L} S_{\frac{2\pi}{L}}[\tilde{f}]. \end{aligned}$	(2.61)
---	--------

2.4 The discrete Fourier transform

Before we establish a connection between the continuous and the discrete Fourier transform (DFT) we will give its definition and state some of its main properties. It inherits many properties from the continuous Fourier transform.

Complex roots of unity. We define

$$\omega_N := e^{i\frac{2\pi}{N}} \tag{2.62}$$

as the N -th complex root of unity. With respect to the exponent, powers of ω_N are periodic with period N , i.e.

$$\omega_N^{l+zN} = \omega_N^l \tag{2.63}$$

for any $l, z \in \mathbb{Z}$. Furthermore,

$$\sum_{l=0}^{N-1} \omega_N^{l(n-m)} = N \cdot \delta_{nm}, \tag{2.64}$$

where δ_{nm} denotes the Kronecker- δ with the property

$$\delta_{nm} = \begin{cases} 1 & \text{for } n = m \\ 0 & \text{else.} \end{cases} \tag{2.65}$$

Eq. (2.64) can be derived by using the property that the sum is a finite geometric series [10].

Discrete Fourier transform. Consider the finite sequence $\mathbf{h}_N = (h_0, h_1, \dots, h_{N-1})$ of N complex numbers. The new sequence

$$\mathbf{DFT}[\mathbf{h}_N] := \left(\frac{1}{\sqrt{N}} \sum_{n=0}^{N-1} h_n w_N^{-nm} \right)_{m=0,1,\dots,N-1} \quad (2.66)$$

is called the **discrete Fourier transform (DFT)** of the sequence \mathbf{h}_N . The sequence

$$\mathbf{IDFT}[\mathbf{G}_N] := \left(\frac{1}{\sqrt{N}} \sum_{m=0}^{N-1} G_m w_N^{nm} \right)_{n=0,1,\dots,N-1} \quad (2.67)$$

is called the **inverse discrete Fourier transform (IDFT)** of the sequence \mathbf{G}_N .

2.4.1 Important properties of the discrete Fourier transform

Reciprocity of the DFT. By writing out the definition and using the representation of the Kronecker- δ as a sum over complex roots of unity one derives

$$\begin{aligned} \mathbf{IDFT}[\mathbf{DFT}[\mathbf{h}_N]] &= \mathbf{h}_N \\ \Leftrightarrow \text{IDFT}_n[\mathbf{DFT}[\mathbf{h}_N]] &= h_n \text{ for } n = 0, 1 \dots N-1. \end{aligned} \quad (2.68)$$

Here $\text{IDFT}_n[\cdot]$ denotes the n -th component of the inverse discrete Fourier transform. Although we have not yet established a relation to the continuous Fourier transform we can recognize this relation as the discrete analogon to the Fourier theorem (2.7). Thus, there is a one-to-one correspondence between a finite sequence \mathbf{h}_N and its DFT $\mathbf{H}_N := \mathbf{DFT}[\mathbf{h}_N]$ as a discrete Fourier pair

$$\mathbf{h}_N \leftrightarrow \mathbf{H}_N. \quad (2.69)$$

Periodicity. Due to the periodicity of the complex root of unity the discrete Fourier transform is itself periodic, i.e.

$$\mathbf{DFT}_m[\mathbf{h}_N] = \mathbf{DFT}_{m+l \cdot N}[\mathbf{h}_N] \text{ for any } m, l \in \mathbb{Z}. \quad (2.70)$$

This allows for the infinite *periodic* extension of both sequences of a discrete Fourier pair $\mathbf{h}_N \leftrightarrow \mathbf{H}_N$ to the pair of infinite sequences

$$\mathbf{h}_\infty \leftrightarrow \mathbf{H}_\infty \quad (2.71)$$

with

$$\mathbf{h}_\infty = (\dots, \mathbf{h}_N^{(-2N)}, \mathbf{h}_N^{(-N)}, \mathbf{h}_N^{(0)}, \mathbf{h}_N^{(N)}, \dots) \quad (2.72)$$

and an analogous relation for \mathbf{H}_∞ . Note that this also allows for alternative definitions of the discrete Fourier transform. In fact, it can be shown [10] that for any $P, Q \in \mathbb{Z}$ the sum

$$\frac{1}{\sqrt{N}} \left(\sum_{n=P+1}^{P+N} h_n w_N^{-nm} \right)_{m=Q+1, Q+2, \dots, Q+N} \quad (2.73)$$

yields a definition equivalent to (2.66). Here $P = Q = -1$ has been used, so that the zero element h_0 of the real space sequence is the first element in the sequence.

Note, however, that the definition of any DFT/IDFT pair also fixes the required subsequences out of \mathbf{h}_∞ and \mathbf{H}_∞ : Any element in h_n needs a unique (up to multiples of N) exponential factor w_N^{-nm} for a given m . Therefore, choosing the wrong subsequence out of \mathbf{h}_∞ for a given DFT definition will lead to an error in the result which can, however, be corrected quite easily (see below).

Centered and non-centered sequences. The periodicity of \mathbf{h}_∞ allows for the generation of any shifted subsequence $\mathbf{h}_N^{(l)}$ of length N with $l \in \mathbb{Z}$ from the standard sequence \mathbf{h}_N by a cyclic rearrangement of the elements in \mathbf{h}_N . With the subsequences $\mathbf{h}_N = (h_n)_{n=0, \dots, N-1}$ and $\mathbf{h}_N^{(l)} = (h_{n+l})_{n=0, \dots, N-1}$ of \mathbf{h}_∞ the periodicity of \mathbf{h}_∞ invokes the relation $(h_{n+l}) = (h_{(n+l) \bmod N})$ with

$$c_N^l(n) := (n + l) \bmod N \quad (2.74)$$

defining a **cyclic permutation** on the sequence $(0, 1, \dots, N)$. As a consequence, the shifted sequence $\mathbf{h}_N^{(l)} = (h_{n+l})_{n=0, \dots, N-1}$ is equal to a cyclic permutation $(h_{c_N^l(n)})_{n=0, \dots, N-1}$ of the standard sequence $\mathbf{h}_N = (h_n)_{n=0, \dots, N-1}$. As an operation on the whole sequence we define

$$\mathbf{C}^l(\mathbf{h}_N) := (h_{c_N^l(n)}) \text{ for } n = 0, 1, \dots, N-1. \quad (2.75)$$

In summary, for any shifted sequence $\mathbf{h}_N^{(l)}$ with $l \in \mathbb{Z}$ we thus have

$$\mathbf{h}_N^{(l)} = \mathbf{C}^l(\mathbf{h}_N) = (h_{c_N^l(n)}) \text{ for } n = 0, 1, \dots, N-1. \quad (2.76)$$

There are two distinct subsequences of \mathbf{h}_∞ which frequently appear in the application of the DFT. The first is the standard sequence $\mathbf{h}_N = (h_0, h_1, \dots, h_{N-1})$ as defined before, with the zero-element (corresponding to $x = 0$) at the beginning. This is often used in the context of time-dependent signals. The second type is characterized by a zero-element placed into the center of the sequence, i.e.

$$\mathbf{h}_N^{(c)} := \begin{cases} (h_{-N/2}, \dots, h_{N/2-1}) & \text{for } N \text{ even,} \\ (h_{-(N-1)/2}, \dots, h_{(N-1)/2}) & \text{for } N \text{ odd.} \end{cases} \quad (2.77)$$

The sequence $\mathbf{h}_N^{(c)}$ thus, just as \mathbf{h}_N , has N elements, with h_0 at the center if N is odd, and the center between h_{-1} and h_0 if N is even. This sequence is relevant when \mathbf{h}_N represents function values on the spatial domain such as intensities in the plane perpendicular to propagation direction of an optical system. The definition of $\mathbf{H}_N^{(c)}$ is analogous.

The centered sequence can be generated from the elements of the standard sequence via

$$\mathbf{h}_N^{(c)} = \begin{cases} \mathbf{C}^{-N/2}(\mathbf{h}_N) & \text{for } N \text{ even,} \\ \mathbf{C}^{-(N-1)/2}(\mathbf{h}_N) & \text{for } N \text{ odd.} \end{cases} \quad (2.78)$$

Inversely, one also has

$$\mathbf{h}_N = \begin{cases} \mathbf{C}^{N/2}(\mathbf{h}_N^{(c)}) & \text{for } N \text{ even,} \\ \mathbf{C}^{(N-1)/2}(\mathbf{h}_N^{(c)}) & \text{for } N \text{ odd.} \end{cases} \quad (2.79)$$

Note that $\mathbf{C}^{-N/2}(\mathbf{h}_N) = \mathbf{C}^{+N/2}(\mathbf{h}_N)$ for N even, but $\mathbf{C}^{-(N-1)/2}(\mathbf{h}_N) \neq \mathbf{C}^{+(N-1)/2}(\mathbf{h}_N)$ for N odd.

DC component of the DFT. The zero element of the DFT of a sequence \mathbf{h}_N , i.e.

$$H_0 = \frac{1}{\sqrt{N}} \sum_{n=0}^{N-1} h_n, \quad (2.80)$$

the DC (direct current) component of the DFT, has a special role in that it is just the sum over all elements of \mathbf{h}_N times $N^{-1/2}$. If the DFT is applied to a time-dependent current signal \mathbf{h}_N , H_0/\sqrt{N} corresponds to the average direct current (DC) component of the signal.

Shifting relation. Let $\mathbf{h}_\infty \leftrightarrow \mathbf{H}_\infty$ denote an infinite discrete Fourier pair and \mathbf{h}_N denote the standard subsequence of \mathbf{h}_∞ . Elementwise multiplication of \mathbf{h}_N with the complex exponential

$$e^{i\frac{2\pi}{N}\mathbf{n}_N j} := \left(e^{i\frac{2\pi}{N}j}, e^{i\frac{2\pi}{N}2j}, \dots, e^{i\frac{2\pi}{N}(N-1)j} \right) \quad (2.81)$$

with $j \in \mathbb{Z}$ corresponds to an index shift (i.e. a translation) of the transformed sequence, i.e.

$$e^{i\frac{2\pi}{N}\mathbf{n}_N j} * \mathbf{h}_N \leftrightarrow \mathbf{H}_N^{(-j)} \quad (2.82)$$

which can be derived by application of the preceding definitions. Here we have introduced the elementwise multiplication of two finite sequences of equal length as $\mathbf{h}_N * \mathbf{g}_N = (h_n g_n)$ for $n = 0, 1, \dots, N$. In other words,

$$\text{DFT}_m \left[\left(w_N^{nj} h_n \right)_{n=0,1,\dots,N-1} \right] = H_{m-j}. \quad (2.83)$$

Inversely,

$$\mathbf{h}_N^{(-j)} \leftrightarrow \mathbf{H}_N * e^{-i\frac{2\pi}{N}\mathbf{n}_N j} \quad (2.84)$$

or

$$\text{DFT}_m \left[(h_{n-j})_{n=0,1,\dots,N-1} \right] = w_N^{-mj} H_m. \quad (2.85)$$

The previously mentioned error which occurs when a given DFT definition is applied to a wrong subsequence of \mathbf{h}_∞ is thus given by an additional exponential factor in the result, so that a correction of the error is easily achieved by multiplying the result with the inverse factor, i.e. w_N^{+mj} in the present case. Due to the equality of a shifted sequence to a cyclic permutation of the standard sequence there is also another way to correct this error which is illustrated in the following example.

Example (centered real space sequence). Suppose one would like to retrieve $\mathbf{H}_N^{(c)}$ from a given $\mathbf{h}_N^{(c)}$, using the DFT as defined in Eq. (2.66), for a non-centered sequence. For the sake of simplicity we assume that N is even. The application of the non-centered DFT to the centered sequence $\mathbf{h}_N^{(c)}$ then yields

$$\text{DFT} \left[\mathbf{h}_N^{(c)} \right] = \text{DFT} \left[\mathbf{h}_N^{(-N/2)} \right] = w_N^{-\mathbf{n}_N N/2} * \mathbf{H}_N. \quad (2.86)$$

The result \mathbf{H}_N thus is non-centered and contains an incorrect factor of $w_N^{-\mathbf{n}_N N/2}$. The first error can be corrected by a cyclic rearrangement of the resulting sequence, the second error

can either be corrected by multiplying Eq. (2.86) by $w_N^{+nN/2}$ or by cyclic rearrangement of the input sequence prior to the application of the DFT. The correct application of the non-centered DFT to the centered sequence thus is given by

$$\mathbf{H}_N^{(c)} = \mathbf{C}^{-N/2} \left[\text{DFT} \left[\mathbf{C}^{N/2} \left[\mathbf{h}_N^{(c)} \right] \right] \right]. \quad (2.87)$$

We thus define for N even the **centered DFT** as

$$\text{DFT}^{(c)} \left[\mathbf{h}_N^{(c)} \right] := \mathbf{C}^{-N/2} \left[\text{DFT} \left[\mathbf{C}^{N/2} \left[\mathbf{h}_N^{(c)} \right] \right] \right] \quad (2.88)$$

and in an analogous way

$$\text{IDFT}^{(c)} \left[\mathbf{H}_N^{(c)} \right] := \mathbf{C}^{-N/2} \left[\text{IDFT} \left[\mathbf{C}^{N/2} \left[\mathbf{H}_N^{(c)} \right] \right] \right]. \quad (2.89)$$

If N is odd, $N/2$ needs to be replaced by $N/2 - 1$ in the definitions.

Discrete cyclic convolution. We define the (cyclic) convolution of two sequences \mathbf{f}_N and \mathbf{g}_N by [20]

$$\mathbf{f}_N \otimes \mathbf{g}_N := \left(\sum_{l=0}^{N-1} f_l g_{(-l+n) \bmod N} \right)_{n=0, \dots, N-1}. \quad (2.90)$$

Note that the outcome of a cyclic convolution is generally not a direct analogue to the continuous convolution of two non-periodic functions. For the discrete Fourier transform of a cyclic convolution of two sequences \mathbf{f}_N and \mathbf{g}_N one obtains in analogy to the continuous case

$$\text{DFT} [\mathbf{f}_N \otimes \mathbf{g}_N] = \sqrt{N} \mathbf{F}_N * \mathbf{G}_N, \quad (2.91)$$

for \mathbf{F}_N and \mathbf{G}_N denoting the discrete Fourier transforms of \mathbf{f}_N and \mathbf{g}_N .

Discrete correlation. We define the correlation of two sequences \mathbf{f}_N and \mathbf{g}_N by

$$\mathbf{f}_N \oplus \mathbf{g}_N := \left(\sum_{l=0}^{N-1} f_l g_{(l+n) \bmod N}^* \right)_{n=0, \dots, N-1}. \quad (2.92)$$

For the discrete Fourier transform of the correlation of two sequences \mathbf{f}_N and \mathbf{g}_N one obtains in analogy to the continuous case

$$\text{DFT} [\mathbf{f}_N \oplus \mathbf{g}_N] = \sqrt{N} \mathbf{F}_N * \mathbf{G}_N^*. \quad (2.93)$$

This implies

$$\text{DFT} [\mathbf{f}_N \oplus \mathbf{f}_N] = \sqrt{N} (|F_m|^2)_{m=0, \dots, N-1}. \quad (2.94)$$

for the autocorrelation of a sequence \mathbf{f}_N .

Discrete analogue to Plancherel's theorem. Back-transforming the last equation and evaluating the element at $n = 0$ gives

$$\sum_{l=0}^{N-1} |f_l|^2 = \sum_{l=0}^{N-1} |F_l|^2. \quad (2.95)$$

The sum over the squared modulus of all elements in the original sequence is equal to the sum over the squared modulus of all elements of the transformed sequence. Note that analogous results on cyclic convolution and correlation can be obtained for centered sequences.

2.4.2 Implementation of the DFT in Matlab

Undoubtedly, the discrete Fourier transform owes its importance to the fact that it stands as a numerical counterpart to the continuous Fourier transform (see below). However, the replacement of the continuous by the discrete Fourier transform is not entirely unproblematic and there are alternative ways to calculate a Fourier integral numerically [28]. From a practical point of view, there is, however, a very important argument in favor of the DFT, namely the very efficient and fast way in that it can be computed via the so-called fast Fourier transformation (FFT). First introduced in the 1960s [26], the FFT algorithm allows for a computation of the sum in the definition Eq. (2.66) of the DFT for all $m = 0, \dots, N-1$ in a significantly shorter time ($N \log N$ elementary operations, i.e. multiplication of a complex number with a complex root of unity and addition) than needed for a direct evaluation of the sum which requires N^2 of such operations for all $m = 0, \dots, N-1$.

As the FFT exactly performs the same calculation as defined by the DFT we do not distinguish here between the two operations in their numerical implementation. In Matlab a vector \mathbf{h}_N is transformed by the Matlab implementation of the FFT according to

$$\text{fft}(\mathbf{h}_N) := \left(\sum_{n=1}^N h_n w_N^{-(n-1)(m-1)} \right)_{m=1,2,\dots,N} \quad (2.96)$$

with the back transformation

$$\text{ifft}(\mathbf{H}_N) := \left(\frac{1}{N} \sum_{m=1}^N H_m w_N^{(n-1)(m-1)} \right)_{n=1,2,\dots,N}. \quad (2.97)$$

Therefore, with $\mathbf{h}_N = \mathbf{h}_N$ and $\mathbf{H}_N = \mathbf{H}_N$,

$$\begin{aligned} \frac{1}{\sqrt{N}} \text{fft}(\mathbf{h}_N) &= \mathbf{DFT}[\mathbf{h}_N] \\ \sqrt{N} \text{ifft}(\mathbf{H}_N) &= \mathbf{IDFT}[\mathbf{H}_N]. \end{aligned}$$

The only differences in the definitions are the indexing, i.e. $h_n = h_{n+1}$ and $h_0 = h_1$ for the zero-element, as well as the different normalization. *The Matlab-implementation of the discrete Fourier transform thus requires the first element to be the zero element of the DFT, just as in the definition (2.66).* If thus a sequence $\mathbf{h}_N^{(c)}$ has to be ‘discretely’ Fourier transformed, one has to perform the same operations as described before to avoid errors in the result. Matlab knows the function

$$\text{fftshift}(\mathbf{h}_N) = \begin{cases} \mathbf{C}^{-N/2}(\mathbf{h}_N) & \text{for } N \text{ even,} \\ \mathbf{C}^{-(N-1)/2}(\mathbf{h}_N) & \text{for } N \text{ odd} \end{cases} \quad (2.98)$$

which centers a non-centered vector and the inverse function `ifftshift` which de-centers a vector, i.e. brings it back into the Matlab system with the zero-element at the beginning of the sequence. Correct application of the Matlab-FFT function to a centered vector $\mathbf{h}_N^{(c)} = \mathbf{h}_N^{(c)}$ is thus performed via

$$\mathbf{H}_N^{(c)} = \mathbf{H}_N^{(c)} = \text{fftshift}(\text{fft}(\text{ifftshift}(\mathbf{h}_N^{(c)}))). \quad (2.99)$$

Note that

$$\text{fftshift}(\mathbf{h}_N) = \text{ifftshift}(\mathbf{h}_N), \quad (2.100)$$

if N is even, but

$$\text{fftshift}(\mathbf{h}_N) \neq \text{ifftshift}(\mathbf{h}_N), \quad (2.101)$$

if N is odd.

2.4.3 Relation of the Discrete to the Continuous Fourier Transform

In the following we would like to study how the discrete Fourier transform is related to its continuous counterpart. The derivation of Eq. (2.111) which gives such a relation is adapted from the one given in [28, pp. 89]. Based on this equation, we illustrate, why the DFT can be used to approximate the Fourier transform of a continuous function. For the connection between the DFT, sampling and periodicity in the context of optical modeling the reader is also referred to [83].

Consider the suitably well-behaved⁵ function $f(x)$ on \mathbb{R} with a Fourier transform $\tilde{f}(k)$. As we have seen above, f can be periodized with period length L via

$$P_L[f](x) := f(x) \otimes \text{III}_L(x) = \sum_{n=-\infty}^{\infty} f(x - nL). \quad (2.102)$$

We can then write the sampled values $P_L[f](x_n)$ in the interval $[-L/2, L/2[$ on the centered grid $\mathbf{x}_N^{(c)} = (x_{-N/2}, x_{-N/2+1}, \dots, x_{N/2-1}) = (n\Delta x)_{n=-N/2, -N/2+1, \dots, N/2-1}$ with $\Delta x = L/N$ as

$$P_L[f](n\Delta x) = \sum_{j=-\infty}^{\infty} f(\Delta x(n + jN)), \text{ for } n = -N/2, -N/2 + 1, \dots, N/2 - 1. \quad (2.103)$$

For the sake of simplicity we assume N to be even. The following considerations are analogous for N odd. Consider now the sampled version

$$S_{\Delta x}[f](x) = \sum_{v=-\infty}^{\infty} f(v\Delta x)\delta(x - v\Delta x) \quad (2.104)$$

of the original function f , sampled with sampling period Δx . Using the Fourier transform of the Dirac- δ its Fourier transform can be written as

$$\mathcal{F}[S_{\Delta x}[f]](k) = \frac{1}{\sqrt{2\pi}} \sum_{v=-\infty}^{\infty} f(v\Delta x)e^{-ikv\Delta x}. \quad (2.105)$$

⁵Generally, this implies $f(x)$ to possess a bounded support, as otherwise the periodization of f can lead to infinite function values. If f has no bounded support, it needs to be multiplied by a window function $\Pi_B(x)$ with $B > 0$. The Fourier transform of f is then convolved by the Fourier transform of $\Pi_B(x)$, a sinc-function. As a consequence, the DFT of a sequence of function values of f is then altered by an additional convolution with a sinc-function. This phenomenon can be kept to a minimum, if f is multiplied by an additional symmetric fast-decaying function such as a Gaussian which is adapted in width to the interval of length B . The situation is somewhat different, if f itself is periodic. If then B coincides with the period length of f , then the DFT values can *exactly* represent the corresponding values of the continuous Fourier transform of f [11].

We can divide this infinite sum into an infinite sum of finite sums with N elements each, i.e.

$$\mathcal{F}[S_{\Delta x}[f]](k) = \frac{1}{\sqrt{2\pi}} \sum_{j=-\infty}^{\infty} \sum_{v=jN-N/2}^{jN+N/2-1} f(v\Delta x) e^{-ikv\Delta x} \quad (2.106)$$

and then make the substitution $n = v - jN$. Then $n \in [-N/2, -N/2 + 1, \dots, N/2 - 1]$ always and we get

$$\mathcal{F}[S_{\Delta x}[f]](k) = \frac{1}{\sqrt{2\pi}} \sum_{n=-N/2}^{N/2-1} \sum_{j=-\infty}^{\infty} f((n+jN)\Delta x) e^{-ikn\Delta x} e^{-ijN\Delta x}. \quad (2.107)$$

Suppose now that we would like to evaluate $\mathcal{F}[S_{\Delta x}[f]]$ on the finite grid $\mathbf{k}_N^{(c)}$ with values $\mathcal{F}[S_{\Delta x}[f]](m\Delta k)$ and $m = -N/2, -N/2 + 1, \dots, N/2 - 1$. Further assume that the sampling period Δx in real space is related to the sampling period Δk in Fourier space according to

$$\Delta x \Delta k = \frac{2\pi}{N}. \quad (2.108)$$

The length of the interval $J = [-b, b]$ associated with the grid $\mathbf{k}_N^{(c)}$ is then $B = N\Delta k = 2\pi/\Delta x = 2\pi r_{\Delta x}$, i.e. 2π times the sampling rate in real space. Turning back now to Eq. (2.107), the last exponential is always 1 and we get

$$\mathcal{F}[S_{\Delta x}[f]](m\Delta k) = \frac{1}{\sqrt{2\pi}} \sum_{n=-N/2}^{N/2-1} \sum_{j=-\infty}^{\infty} f(\Delta x(n+jN)) e^{-i2\pi nm/N}. \quad (2.109)$$

We recognize the infinite sum over index j in the above expression as the periodized version of f with period length L , evaluated on each element of the finite grid $\mathbf{x}_N^{(c)}$ as given in Eq. (2.103). We can therefore reduce Eq. (2.109) to the finite sum

$$\mathcal{F}[S_{\Delta x}[f]](m\Delta k) = \sqrt{\frac{N}{2\pi}} \frac{1}{\sqrt{N}} \sum_{n=-N/2}^{N/2-1} P_L[f](n\Delta x) w_N^{-nm} \quad \text{for } m = -N/2, \dots, N/2 - 1. \quad (2.110)$$

We recognize the finite sum on the right side as the centered discrete Fourier transform (2.66) of the sequence $(P_L[f](n\Delta x))$ of function values and arrive at the following result

$$\boxed{\begin{aligned} \left(\tilde{f} \otimes \text{III}_{\frac{2\pi}{\Delta x}} \right) (m\Delta k) &= \Delta x \sqrt{\frac{N}{2\pi}} \cdot \text{DFT}_m^{(c)} \left[(f \otimes \text{III}_L) (\mathbf{x}_N^{(c)}) \right] \\ &\text{for } m = -N/2, \dots, N/2 - 1 \text{ and } \Delta k \Delta x = \frac{2\pi}{N}. \end{aligned}} \quad (2.111)$$

Eq. (2.111) relates the continuous Fourier transform \tilde{f} of a function f , the function f itself and the discrete Fourier transform in a single analytical expression. The meaning (2.111) can be formulated as follows

The m -th component of the discrete Fourier transform of a periodized version of a function f , with period length L , evaluated on the grid \mathbf{x}_N with grid spacing

Δx on the interval $I = [-L/2, L/2[$ is equal to the periodized continuous Fourier transform of f , with period length $2\pi/\Delta x$, evaluated at the position $m\Delta k$, provided that the real space grid spacing Δx is related to the frequency space grid spacing Δk via the reciprocity relation $\Delta x\Delta k = 2\pi/N$.

Discrete back-transformation of Eq. (2.111) yields

$$\boxed{\begin{aligned} (f \otimes \text{III}_L)(n\Delta x) &= \frac{1}{\Delta x} \sqrt{\frac{2\pi}{N}} \cdot \text{IDFT}_n^{(c)} \left[\left(\tilde{f} \otimes \text{III}_{\frac{2\pi}{\Delta x}} \right) (\mathbf{k}_N^{(c)}) \right] \\ &\text{for } n = -N/2, \dots, N/2 - 1 \text{ and } \Delta k\Delta x = \frac{2\pi}{N}. \end{aligned}} \quad (2.112)$$

In reviewing the preceding two equations it transpires that the discrete Fourier transform does not simply relate the sampled version of a function and the sampled version of its Fourier transform, as one would wish. *It rather relates the periodized versions of the sampled function and its Fourier transform with each other.* Under which conditions can the continuous FT, evaluated at $m\Delta k$ within a finite Fourier space interval, thus be replaced by the DFT of the original sampled function in a finite real space interval? The following conditions would be sufficient:

1. Fourier space: $\tilde{f} \stackrel{\dagger}{=} (\tilde{f} \otimes \text{III}_{2\pi/\Delta x})$ on the interval $[-\pi/\Delta x, \pi/\Delta x]$. Here the period width $2\pi/\Delta x$ is inversely proportional to the sampling period in real space.
2. Real space: $f \stackrel{\dagger}{=} (f \otimes \text{III}_{2\pi/\Delta k})$ on the interval $[-\pi/\Delta k, \pi/\Delta k]$. Here the period width $2\pi/\Delta k$ is inversely proportional to the sampling period in Fourier space.

If f was (i) band-limited *and* (ii) has a bounded support, both conditions could be met. There is, however, no function that has both properties (i) and (ii) in a strict mathematical sense [10]. If f has bounded support, it can, however, still be “essentially band-limited” [10], i.e. $\exists \beta, \mu > 0$, so that

$$|\tilde{f}(k)| \leq \frac{\beta}{(1 + |k|)^{1+\mu}}. \quad (2.113)$$

In other words, $\tilde{f}(k)$ decays faster than an exponential function.

Let us thus assume that $|f(x)| = 0$ for $|x| > S/2$ where S is the support of the function f . If in addition the sampling period Δk in Fourier space is chosen such that

$$\frac{2\pi}{\Delta k} > S \Leftrightarrow N\Delta x > S, \quad (2.114)$$

then $f(x) = (f \otimes \text{III}_{2\pi/\Delta k})(x)$ for $x \in [-\pi/\Delta k, \pi/\Delta k[$. We further assume that f is essentially band-limited in the sense as defined above. This implies that $\exists b > 0$, so that $|\tilde{f}(k)| \approx 0$ for $k \notin [-b, b]$. If then the sampling period Δx in real space is chosen such that

$$\frac{2\pi}{\Delta x} > 2b, \quad (2.115)$$

then $\tilde{f} \simeq (\tilde{f} \otimes \text{III}_{2\pi/\Delta x})$ for $k \in [-\pi/\Delta x, \pi/\Delta x[$. The Discrete Fourier transform thus becomes a good approximation to the continuous Fourier transform, i.e.

$$\tilde{f}(m\Delta k) \simeq \Delta x \sqrt{\frac{N}{2\pi}} \cdot \text{DFT}_m^{(c)} \left[f(\mathbf{x}_N^{(c)}) \right] \quad (2.116)$$

for $m = -N/2, \dots, N/2 - 1$ and

$$\frac{S}{N} < \Delta x < \frac{\pi}{b}. \quad (2.117)$$

The approximation becomes better the larger N and the smaller Δx . After this illustration of how the DFT might be used as a good approximation to the continuous Fourier transform, we do not consider further the problem of errors in the DFT. It is treated e.g. in [10].

Luckily, in the context of optical problems, i.e. when f represents a complex wave field one is often in the situation that $|f| > 0$ only close to the optical axis, so that the DFT can generally be used very well to approximate the continuous Fourier transform. In the context of spectral analysis of an image one often has to use the technique of **windowing** in real space. Here the image is multiplied with a symmetric fast-decaying function, so that the windowed image obtains a bounded support. If the spectral range of the window is chosen such that it does not interfere with the spectrum of the image, the result still gives a good representation of the image's spectrum alone. An example of such a window function is the Kaiser-Bessel window [14].

2.4.4 The sampling theorem

It was derived above (see Eq. (2.61)) that the Fourier transform of an ideally sampled function $f(x_n)$ is given by a periodization of the original function's Fourier transform \tilde{f} , with period length $2\pi/\Delta x$, i.e. one has

$$\begin{aligned} \Delta x \cdot \mathcal{F} [S_{\Delta x}[f]] &= P_{\frac{2\pi}{\Delta x}}[\tilde{f}] \\ &= \sum_{n=-\infty}^{\infty} \tilde{f} \left(k - n \frac{2\pi}{\Delta x} \right) \end{aligned}$$

with the real space sampling interval now brought to the left side of the equation. Assume now that f is **band-limited**, i.e. that its Fourier transform or frequency spectrum vanishes for frequencies $|k| > b$ with b denoting a positive real number. As illustrated in Fig. 2.1 a sufficient condition for the translated copies in the periodized version of \tilde{f} not to overlap is then given by

$$\frac{2\pi}{\Delta x} > 2b. \quad (2.118)$$

If condition Eq. (2.118) is met, $P[\tilde{f}]$ and \tilde{f} are equal on the interval $B = [-b, b]$, but also on the interval $C = [-\pi/\Delta x, \pi/\Delta x]$. We can then truncate $P[\tilde{f}]$ outside the interval C and write, now for all $k \in \mathbb{R}$,

$$\tilde{f}(k) = \Pi_{\frac{2\pi}{\Delta x}}(k) \cdot P_{\frac{2\pi}{\Delta x}}[\tilde{f}](k) = \Delta x \cdot \Pi_{\frac{2\pi}{\Delta x}}(k) \cdot \mathcal{F} [S_{\Delta x}[f]](k). \quad (2.119)$$

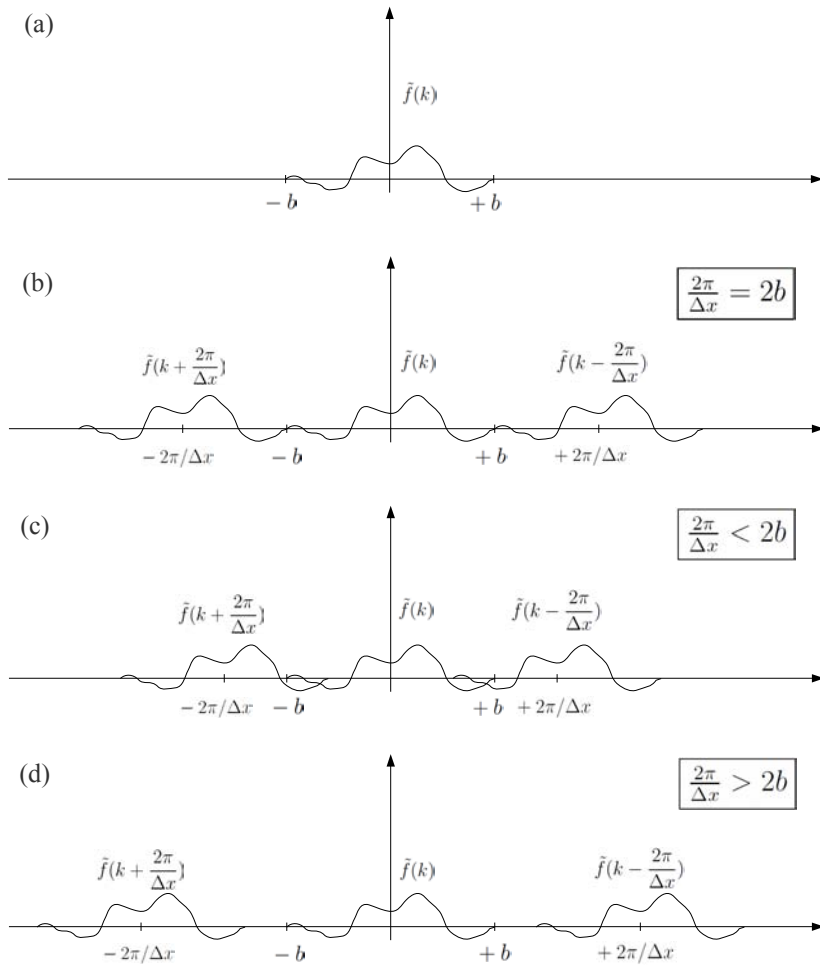


Figure 2.1: (a) A representation of the Fourier transform \tilde{f} of the band-limited function f . \tilde{f} vanishes outside the interval $[-b, b]$. Note that although the graph indicates that \tilde{f} is a real function the subsequent considerations are valid also for complex \tilde{f} and one may think of the graph also as representing the real and/or imaginary part of \tilde{f} . The Fourier transform of the ideally sampled function $f(x_n)$ is given as an infinite sum $P_{\frac{2\pi}{\Delta x}}[\tilde{f}]$ of translated copies of the Fourier transform \tilde{f} of the continuous f . Three of these translated copies are shown in (b/c/d), with different sampling periods Δx in real space. (b) For $2\pi/\Delta x < 2b$ the translated copies exactly fit next to each other and $P_{\frac{2\pi}{\Delta x}}[\tilde{f}] = \tilde{f}$ on the interval $]-\pi/\Delta x, \pi/\Delta x[$. (c) For $2\pi/\Delta x = 2b$ the translated copies overlap and $P_{\frac{2\pi}{\Delta x}}[\tilde{f}]$ differs from \tilde{f} in the interval $]-\pi/\Delta x, \pi/\Delta x[$. (d) For $2\pi/\Delta x < 2b$ one has $P_{\frac{2\pi}{\Delta x}}[\tilde{f}] = \tilde{f}$ on the interval $]-b, b[$ ($\subset]-\pi/\Delta x, \pi/\Delta x[$). In this case the function f is “oversampled”.

Note that the hat-function $\Pi_{\frac{2\pi}{\Delta x}}$ has a width of $2\pi/\Delta x$ and is zero outside the interval $C = [-\pi/\Delta x, \pi/\Delta x]$. Fourier back transformation of the above equation leaves us then with an expression for the original continuous function $f(x)$, i.e. [following 20, p. 210]

$$\begin{aligned}
 f(x) &= \Delta x \cdot \mathcal{F}^{-1} \left[\Pi_{\frac{2\pi}{\Delta x}}(k) \cdot \mathcal{F} [S_{\Delta x}[f]](k) \right] \\
 &= \Delta x \cdot \frac{1}{\sqrt{2\pi}} \mathcal{F}^{-1} \left[\Pi_{\frac{2\pi}{\Delta x}}(k) \right] \otimes S_{\Delta x}[f] \\
 &= \Delta x \frac{1}{\sqrt{2\pi}} \frac{\sqrt{2\pi}}{\Delta x} \operatorname{sinc} \left(\frac{\pi}{\Delta x} \cdot x \right) \otimes S_{\Delta x}[f] \\
 &= \sum_{n=-\infty}^{\infty} f(n\Delta x) \delta(x - n\Delta x) \otimes \operatorname{sinc} \left(\frac{\pi}{\Delta x} \cdot x \right) \\
 &= \int d\lambda \sum_{n=-\infty}^{\infty} f(n\Delta x) \delta(x - n\Delta x - \lambda) \operatorname{sinc} \left(\frac{\pi}{\Delta x} \cdot \lambda \right) \\
 &= \sum_{n=-\infty}^{\infty} f(n\Delta x) \int d\lambda \delta(\lambda - (x - n\Delta x)) \operatorname{sinc} \left(\frac{\pi}{\Delta x} \cdot \lambda \right) \\
 &= \sum_{n=-\infty}^{\infty} f(n\Delta x) \operatorname{sinc} \left(\frac{\pi}{\Delta x} \cdot (x - n\Delta x) \right),
 \end{aligned}$$

where we have used that $\mathcal{F}^{-1}[\Pi_B(k)] = B/\sqrt{2\pi} \cdot \operatorname{sinc}(Bx/2)$. We have thus derived the Whittaker-Shannon sampling theorem which we reformulate here for easy reference.

Theorem 1 (Whittaker-Shannon) Consider a band-limited, possibly complex-valued function f , i.e. $\exists b > 0$, so that $\tilde{f}(k) = 0 \forall |k| > b$, or, expressed in non-angular frequencies, $\exists \beta > 0$, so that $\tilde{f}(v) = 0, \forall |v| > \beta$. Furthermore assume that f is only known at the sampling positions $n\Delta x$ with $n \in \mathbb{Z}$. If then the sampling period Δx is chosen in such a way that

$$\frac{1}{\Delta x} \geq \frac{b}{\pi} \quad (2.120)$$

or, equivalently,

$$\frac{1}{\Delta x} \geq 2\beta \quad (2.121)$$

the continuous function f is fully determined by its sampled values $f(n\Delta x)$.⁶

The smallest sampling rate,

$$r_{\text{Ny}} := b/\pi = 2\beta, \quad (2.122)$$

which is sufficient according to the sampling theorem to fully represent the band-limited continuous function f with highest frequency $k_{\text{max}} = b$ (or $v_{\text{max}} = \beta$) is called the **Nyquist rate**.

⁶Here $\tilde{f}(k)$ denotes an alternative definition of the Fourier transform based on a non-angular variable v in frequency space. The forward Fourier transform is given then as $\tilde{f}(k) = \int dx \exp(-i2\pi vx)$. Furthermore note that the bandwidth of the band-limited function f is often referred to as b and not $2b$, the full interval on which \tilde{f} may have non-vanishing components.

We now take a closer look on the interpretation of Theorem 1. Note that in the formulation of the sampling theorem we have not given the explicit formula to calculate the continuous f from its samples, simply because we have just used the formula here to proof the theorem by explicitly giving a way to reconstruct f . For our later application of the sampling theorem it is just important *that* the information content of the sampled $f(n\Delta x)$ is sufficient to exactly represent f , not *how* this could be achieved. That a sampling rate below the Nyquist rate is generally not enough to fully represent the function is illustrated in Fig. 2.1: If the sampling rate is chosen too small the translated copies of the Fourier transform $\tilde{f}(k)$ will at least partially overlap and Eq. (2.119) becomes wrong. One can still, of course, follow the same calculations as used for proving the sampling theorem, but there will be an error in the reconstruction which is caused by the overlapping high-frequency tails of the shifted versions of \tilde{f} .

In a certain sense, we can turn the sampling theorem around and infer that given a sampling rate $r_{\Delta x} = 1/\Delta x$ at which a continuous signal is sampled, the highest frequency that the function f may have, so that it can be exactly represented by the samples, is given by

$$k_{\text{Ny}} = \pi / \Delta x, \quad (2.123)$$

or, equivalently,

$$\nu_{\text{Ny}} = 1 / (2\Delta x). \quad (2.124)$$

This frequency is then called the **Nyquist frequency**. Note that with these definitions the Nyquist frequency is a property of the sampling process and the Nyquist rate a property of the signal [see e.g. 10, 106].

To summarize the preceding considerations we can conclude: To adequately sample a given signal with highest angular spatial frequency b , we need a sampling rate $r_{\Delta x}$ higher than the Nyquist rate $r_{\text{Ny}} = b/\pi$, i.e. $r_{\Delta x} > b/\pi$. Note that this condition is equivalent to the condition expressed in Eq. (2.115) that was introduced for approximating the continuous Fourier transform by the discrete FT. On the other hand, given a sampling rate $r_{\Delta x}$ we can only adequately describe signals with a highest frequency b that is smaller than the Nyquist frequency $k_{\text{Ny}} = \pi r_{\Delta x}$, i.e. b needs to obey $b < k_{\text{Ny}}$.

As the simplest example we can think of, we take the signal $y = \sin(kx)$ with highest frequency k . To adequately sample this function we need a sampling rate $r_{\Delta x} > k/\pi \Leftrightarrow 1/\Delta x > 2/\lambda$: We need a sampling period smaller than half the wavelength $\lambda = 2\pi/k$ of the sine-signal to adequately sample it.

Note that the sampling theorem can equally be applied in the Fourier domain, leading here to a condition equivalent to Eq. (2.114).

From an information theoretical point of view the sampling theorem is quite remarkable. It allows for the complete determination of an unknown continuous function, once its values are known at discrete sample positions. However, there is still one subtlety left: For an exact reconstruction of the continuous function an *infinite* amount of samples is needed. This is a consequence of the fact that a band-limited function can never have a bounded support, or equivalently, that a function with bounded support can never be band-limited. In practice, however, the errors from finite truncation can be kept at a controllable level.

One may ask, if the sampling theorem can be generalized to functions whose Fourier transform vanishes outside the frequency bands $[-k_2, -k_1]$ and $[k_1, k_2]$ with $0 < k_1 < k_2$. Of course, one can in such a case always choose $1/\Delta x \geq k_2/\pi$, but a smaller sampling rate is actually sufficient in this case. However, such so-called non-baseband signals [see e.g. 107] are not considered within the context of this thesis.

2.4.5 The sampling theorem and the discrete Fourier transform

Let us reconsider the situation sketched at the end of section 2.4.3: We apply the discrete Fourier transform to a nearly band-limited function f with bounded support. If f is sampled with a sampling period Δx , the highest frequency it may have, if its Fourier transform is to be represented by the discrete FT, is given by the Nyquist frequency of the sampling process, i.e. $\nu_{\text{Ny}} = 1/(2\Delta x)$ or $k_{\text{Ny}} = \pi/\Delta x$. Using the reciprocity relation this leads to the highest frequency that is ‘properly’ transformed by a discrete Fourier transform, given a real space sampling period Δx , namely $k_{\text{Ny}} = (N/2)\Delta k$ (for N even). We could have seen this from the definition of the centered discrete FT, however, this is also true for any definition of the DFT, especially for the non-centered type (2.66). Here the frequency range goes to a maximum $(N-1)\Delta k$. Still, the component corresponding to the highest frequency is $(N/2)\Delta k$, the Nyquist frequency.

3 Propagation of x-ray wave fields in matter and free space

3.1 Propagation of light waves in free space

The time evolution of the electric field $\mathbf{E}(\mathbf{r}, t)$ and the magnetic induction $\mathbf{B}(\mathbf{r}, t)$ at any point $\mathbf{r} = (x, y, z)$ in real space \mathbb{R}^3 in the absence of matter is described by Maxwell's equations, given here¹ as a set of four partial differential equations for the 3-dimensional vector fields $\mathbf{E}(\mathbf{r}, t)$ and $\mathbf{B}(\mathbf{r}, t)$ [108]:

$$\nabla \cdot \mathbf{E}(\mathbf{r}, t) = 0, \quad (3.1)$$

$$\nabla \cdot \mathbf{B}(\mathbf{r}, t) = 0, \quad (3.2)$$

$$\nabla \times \mathbf{E}(\mathbf{r}, t) = -\partial_t \mathbf{B}(\mathbf{r}, t), \quad (3.3)$$

$$\nabla \times \mathbf{B}(\mathbf{r}, t) = \varepsilon_0 \mu_0 \partial_t \mathbf{E}(\mathbf{r}, t). \quad (3.4)$$

We allow the components of $\mathbf{E}(\mathbf{r}, t)$ and $\mathbf{B}(\mathbf{r}, t)$ to be complex, being aware of the fact that their physically meaningful representation is given by the real part of them. The constants $\varepsilon_0 = 8.854 \cdot 10^{-12} \text{ AsV}^{-1} \text{ m}^{-1}$ and $\mu_0 = 4\pi \cdot 10^{-7} \text{ VsA}^{-1} \text{ m}^{-1}$ are the electric and magnetic field constant, respectively. The homogeneity of equations (3.1 – 3.4) allows one to derive two independent wave equations for $\mathbf{E}(\mathbf{r}, t)$ and $\mathbf{B}(\mathbf{r}, t)$, namely [108]

$$(\varepsilon_0 \mu_0 \partial_t^2 - \nabla^2) \mathbf{E}(\mathbf{r}, t) = 0, \quad (3.5)$$

$$(\varepsilon_0 \mu_0 \partial_t^2 - \nabla^2) \mathbf{B}(\mathbf{r}, t) = 0. \quad (3.6)$$

The individual components of both $\mathbf{E}(\mathbf{r}, t)$ and $\mathbf{B}(\mathbf{r}, t)$ obey all the same scalar equation. This suggests that it is sufficient to study the 1D **scalar field** $\Psi(\mathbf{r}, t)$, obeying the scalar (D'Alambert) wave equation

$$(\varepsilon_0 \mu_0 \partial_t^2 - \nabla^2) \Psi(\mathbf{r}, t) = 0. \quad (3.7)$$

If not stated otherwise we will neglect polarization effects and describe a time-dependent **optical wave field** by the scalar function Ψ . We define $c := 1/\sqrt{\mu_0 \varepsilon_0}$ as the **vacuum phase velocity**.

Before we describe solutions to Eq. (3.7) we introduce the **time-dependent monochromatic plane wave**

$$P_{\omega, \mathbf{u}}(\mathbf{r}, t) := a \cdot \exp[i\varphi(\mathbf{r}, t)] = a \cdot \exp[i(\mathbf{u} \cdot \mathbf{r} - \omega t + \varphi_0)], \quad (3.8)$$

¹SI units are used throughout this thesis. The partial derivative with respect to a variable x is abbreviated as ∂_x .

where a is a complex, \mathbf{u} and φ_0 are real constants. $\varphi(\mathbf{r}, t)$ is called the **phase** and $a = |P_{\omega, \mathbf{u}}(\mathbf{r}, t)|$ the **amplitude** of the wave, just as for any complex number in its polar representation. At a fixed time t the term $\varphi(\mathbf{r}, t) = (\mathbf{u} \cdot \mathbf{r} - \omega t) + \varphi_0$ defines planes of constant phase, perpendicular to the **wave vector** \mathbf{u} . Without loss of generality we can choose the coordinate system so that $\mathbf{u} \parallel \mathbf{e}_z$, where \mathbf{e}_z is the unit vector in z -direction, which in the optics context is generally referred to as the **direction of the optical axis**. We then have $\varphi(\mathbf{r}, t) = (|\mathbf{u}|z - \omega t) + \varphi_0$. Holding the phase $\varphi(\mathbf{r}, t) \equiv C$ at a fixed value C , i.e. observing an arbitrary plane of constant phase evolving in space and time yields a one-dimensional equation for the location of such a plane, namely $z = \frac{\omega}{|\mathbf{u}|} \cdot t + (C - \varphi_0)/|\mathbf{u}|$. Eq. (3.8) thus describes the propagation of an infinite set of wave fronts, each characterized by a constant phase, traveling with the **phase velocity** $v := \omega/|\mathbf{u}|$ into the direction of \mathbf{u} . $|\mathbf{u}| = \omega/v$ is also called the **wave number**. The periodicity of the **phasor** $\exp(i\varphi(\mathbf{r}, t))$ with a period 2π of its phase implies a spatial distance of one wavelength $\lambda := 2\pi/|\mathbf{u}|$ and a temporal distance of one oscillation period $T := 2\pi/\omega$ between two wave fronts of equal field values. In terms of wavelength and rotational frequency $\nu = \omega/2\pi$ we can thus also write $v = \lambda\nu$.

As can be verified by insertion into the vacuum wave equation (3.7), $P_{\omega, \mathbf{u}}(\mathbf{r}, t)$ is a solution, if

$$|\mathbf{u}|^2 = \omega^2/c^2. \quad (3.9)$$

The previously defined vacuum phase velocity c is thus given as $c = \omega/|\mathbf{u}| = v$. We define $k := \omega/c$ as the **vacuum wave number**. Then $\lambda_0 := 2\pi/k$ corresponds to the **vacuum wavelength**. From now on, for a general plane wave in vacuum we therefore identify $\mathbf{u} \equiv \mathbf{k}$ with $|\mathbf{k}| = k$. A wave vector \mathbf{k} can thus always be associated with a plane wave that is a solution to the vacuum wave equation (3.7).

Note that the physical phase $\varphi(\mathbf{r}, t)$ cannot uniquely be obtained from the complex $P_{\omega, \mathbf{q}}(\mathbf{r}, t)$, but only up to integer multiples of 2π . As a consequence, $\varphi(a)$ for any complex number a is not a well-defined function. One can make it well-defined by allowing only values in the **principle value** interval $]-\pi, \pi]$. This is the output of the Matlab function $\arg(z)$ for any complex number z . Physically, however, φ is not restricted to this interval and therefore confining its values to $]-\pi, \pi]$ can lead to unphysical phase jumps. These have to be corrected in a procedure that is commonly referred to as **phase unwrapping** which is a well-known and, under certain circumstances, hard to solve mathematical problem, especially if φ is a scalar field on a 2- or 3-dimensional domain [52, 54].

Proceeding further, any solution $\Psi(\mathbf{r}, t)$ to Eq. (3.7) can be written as a spectral decomposition into monochromatic components $\psi_\omega(\mathbf{r})$ with their time-dependence separated into the factor $\exp(-i\omega t)$ [108]:

$$\psi(\mathbf{r}, t) = \frac{1}{\sqrt{2\pi}} \int_0^\infty \psi_\omega(\mathbf{r}) \exp(-i\omega t) d\omega. \quad (3.10)$$

Each **stationary monochromatic field** $\psi_\omega(\mathbf{r})$ is characterized by a single frequency ω , and with $\omega = kc$ also by a single wavelength λ_0 .

Inserting the decomposition (3.10) into Eq. (3.7) results in a time-independent equation for the monochromatic field [108]:

$$\boxed{(\nabla^2 + k^2) \psi_\omega(\mathbf{r}) = 0} \quad (3.11)$$

with $k = \omega/c$. This time-independent equation is commonly referred to as the **Helmholtz equation** and describes the spatial evolution of a scalar stationary monochromatic field in free space.

3.1.1 Angular spectrum solution to the Helmholtz equation

The standard problem of free-space diffraction can be considered as a special boundary-value problem for the Helmholtz equation (3.11) [108]: Assuming all sources of radiation to be contained in the lower half space $z < z_0$ and the stationary monochromatic field $\psi_\omega(\mathbf{r})$ to be known in the plane $z = z_0$, one asks for the field $\psi_\omega(\mathbf{r})$ anywhere in the upper half space $z > z_0$, which is free of sources and matter.

The practically most relevant approach to this problem is to study solutions on planes $z = z_1 = z_0 + \Delta z > z_0$ with any field on such a plane being the propagated version of the boundary field at $z = z_0$. The propagation direction then is along the optical axis with direction \mathbf{e}_z .²

Most commonly, a general solution to the previously stated problem is given on the basis of the Helmholtz-Kirchhoff or the Rayleigh-Sommerfeld diffraction integrals [60], which deliver the field $\psi_\omega(\mathbf{r}_Q)$ at a point Q in the upper half-space $z > 0$, given the field $\psi_\omega(\mathbf{r})$ – and, for the Helmholtz-Kirchhoff integral, also its normal derivative – on a smooth closed surface S enclosing Q . This eventually leads to diffraction formulae, relating the field at a plane $z > 0$ to the field at $z = 0$. For derivation of such a formula we will use an alternative approach which is sometimes also referred to as the *angular spectrum method*³ [108].

We first mention two very general solutions to the Helmholtz equation, which, from a conceptual point of view, represent two very important ideal wave forms: plane waves and spherical waves. A **time-independent plane wave**

$$P_{\omega, \mathbf{k}}(\mathbf{r}) := \exp[i\mathbf{k} \cdot \mathbf{r}] = \exp[i(k_x x + k_y y + k_z z)] \quad (3.12)$$

with wave vector \mathbf{k} and $k_x, k_y, k_z \in \mathbb{R}$ is a solution to the Helmholtz equation filling up the entire \mathbb{R}^3 space, provided that $(k_x^2 + k_y^2 + k_z^2) = k^2 = \omega^2/c^2$. While thus a plane wave is characterized by a distinct direction $\mathbf{k}/|\mathbf{k}|$ in space, a **time-independent spherical wave**

$$S_{\omega, \mathbf{r}_0}(\mathbf{r}) := \frac{\exp(ik|\mathbf{r} - \mathbf{r}_0|)}{|\mathbf{r} - \mathbf{r}_0|} \quad (3.13)$$

is characterized by a distinct point \mathbf{r}_0 , around which surfaces of constant phase are arranged as concentric spheres. Spheres with phase values differing by 2π are separated by one wavelength λ_0 . As before, $k = \omega/c$. Unlike the plane wave, the spherical wave has no distinct direction of propagation and is a solution for all $\mathbf{r} \in \mathbb{R}^3 \setminus \{\mathbf{r}_0\}$.

²Note that the term ‘propagation’ which one may immediately associate with the movement of a particle is partially misleading here. Eq. (3.11) delivers a stationary solution for a single monochromatic component of a general wave field and although its time evolution can be easily accounted for by multiplying $\psi_\omega(\mathbf{r})$ with the time dependent phasor $\exp(-i\omega t)$, such a monochromatic wave remains generally non-localizable in the sense of a particle. Alternatively, one could speak of the *spatial evolution instead of the propagation of the field* $\psi_\omega(\mathbf{r})$ along the optical axis.

³It can be shown that the so-called ‘Rayleigh-Sommerfeld diffraction integral of the first kind’ yields equivalent results to the angular spectrum approach outlined here [108, p. 25].

We would now like to derive a general solution to the Helmholtz equation based on the angular spectrum method. The following line of arguments can be found e.g. in [60]. Let us consider again the typical ‘propagation’ problem, in which a solution $\psi_\omega(\mathbf{r}_\perp; z_0)$ to the Helmholtz equation is given at plane $z = z_0$ and we would like to derive from it a solution $\psi_\omega(\mathbf{r}_\perp; z_1)$ at a plane $z = z_1 > z_0$.⁴ According to the Fourier theorem Eq. (2.7), $\psi_\omega(\mathbf{r}_\perp, z)$ in any plane can be decomposed laterally into its spectral components as

$$\psi_\omega(\mathbf{r}_\perp, z) = \frac{1}{2\pi} \int \tilde{\psi}_\omega(\mathbf{k}_\perp, z) \exp[i(\mathbf{k}_\perp \cdot \mathbf{r}_\perp)] d\mathbf{k}_\perp. \quad (3.14)$$

As $\psi_\omega(\mathbf{r}_\perp, z)$ has to obey the Helmholtz equation, one obtains by inserting the decomposition above into Eq. (3.11)

$$\frac{1}{2\pi} \int [\partial_z^2 \tilde{\psi}_\omega(\mathbf{k}_\perp, z) + (k^2 - k_\perp^2) \tilde{\psi}_\omega(\mathbf{k}_\perp, z)] \exp(i\mathbf{k}_\perp \cdot \mathbf{r}_\perp) d\mathbf{k}_\perp = 0. \quad (3.15)$$

The only Fourier transform of the zero-function is the zero-function, so that the above expression is equivalent to the following differential equation for $\tilde{\psi}_\omega(\mathbf{k}_\perp, z)$:

$$\partial_z^2 \tilde{\psi}_\omega(\mathbf{k}_\perp, z) = -(k^2 - k_\perp^2) \tilde{\psi}_\omega(\mathbf{k}_\perp, z). \quad (3.16)$$

If $\psi_\omega(\mathbf{k}_\perp; z_0)$ is known in a plane z_0 , a general solution (excluding backward propagation) for $z > z_0$ is given as

$$\tilde{\psi}_\omega(\mathbf{k}_\perp; z) = \tilde{\psi}_\omega(\mathbf{k}_\perp; z_0) \exp\left(i\Delta z \sqrt{k^2 - k_\perp^2}\right) \quad (3.17)$$

with $\Delta z = z - z_0$. There are two fundamentally different classes of solutions. For $k_\perp^2 > k^2$, the exponential term becomes real and decays to zero within a few wavelengths. This is the non-propagating solution that is also called an **evanescent wave**. It is only relevant, if we are considering propagation effects on the length scale of the wavelength. For $k_\perp^2 < k^2$ the exponential term oscillates and insertion of Eq. (3.17) into the spectral decomposition Eq. (3.14) at a fixed plane $z = z_1 = z_0 + \Delta z$ yields

$$\psi_\omega(\mathbf{r}_\perp; z_1) = \frac{1}{2\pi} \int \tilde{\psi}_\omega(\mathbf{k}_\perp; z_0) \exp\left(i\Delta z \sqrt{k^2 - k_\perp^2}\right) \exp[i(\mathbf{k}_\perp \cdot \mathbf{r}_\perp)] d\mathbf{k}_\perp. \quad (3.18)$$

This ‘propagation integral’ provides the field at plane $z = z_1 = z_0 + \Delta z$, given the initial field $\tilde{\psi}_\omega(\mathbf{k}_\perp; z_0)$ in its (lateral) Fourier representation. Eq. (3.18) has two different interpretations. First of all, it is a true Fourier integral with an integration range $k_{x,y} \in \mathbb{R}$. However, if $\Delta z \gg \lambda_0$, the exponential factor $\exp\left(i\Delta z \sqrt{k^2 - k_\perp^2}\right)$ is practically zero for $k_\perp^2 > k^2$, so that only components $\tilde{\psi}_\omega(\mathbf{k}_\perp; z_0)$ with $k_\perp^2 \leq k^2$ contribute (non-evanescent waves). Note that, once the initial field $\psi_\omega(\mathbf{r}_\perp; z_0)$ is known, the field in plane $z = z_1 = z_0 + \Delta z$ does *not* depend on the *absolute* location of the plane $z = z_1$ any more, but just on the *relative distance* to

⁴We introduce some notational conventions here. If a wave field is considered in a fixed plane, the z -coordinate becomes a constant, which is then separated by a semicolon. Lateral coordinates (x, y) in a plane perpendicular to the optical axis are summarized as $\mathbf{r}_\perp := (x, y)$. $\tilde{\psi}$ may denote the 1D, 2D or 3D Fourier transform of ψ , depending on the context. If it denotes the 2D transform, it is taken with respect to the lateral coordinates.

the plane of the initial field. The second interpretation of Eq. (3.18) can be seen by writing its integrand as

$$\left[\tilde{\psi}_\omega(\mathbf{k}_\perp; z_0) \exp\left(-iz_0\sqrt{k^2 - k_\perp^2}\right) \right] \exp\left(iz_1\sqrt{k^2 - k_\perp^2}\right) \exp[i(\mathbf{k}_\perp \cdot \mathbf{r}_\perp)]. \quad (3.19)$$

For $\Delta z \gg \lambda_0$ Eq. (3.18) thus represents a decomposition of the propagated field at plane $z = z_1$ into plane waves propagating into directions $(\mathbf{k}_\perp, \sqrt{k^2 - k_\perp^2})$, evaluated at $z = z_1$. As all plane wave components are characterized by a certain direction \mathbf{k} , limited by $k_\perp^2 < k^2$, the decomposition (3.14) may also be called an **angular spectrum** of plane waves.

For notational convenience henceforth we set $z_0 = 0$ and $z_1 = z = \text{const.} > 0$ in the propagation equations, well aware that on the left side z in the propagated field $\psi_\omega(\mathbf{r}_\perp; z)$ denotes a field at a plane $z = \text{const.} > 0$, at distance z from the initial plane at $z = 0$. Contrarily, on the right side of the propagation equations z may rather be interpreted as a distance $\Delta z = z_1 - z_0 = z - 0$ between the initial and the final plane of the propagation process, rather than a constant spatial coordinate. Eq. (3.18) can thus be written as a general propagation equation for wave fields in planes $z = 0$ and a second plane at distance z :

$$\psi_\omega(\mathbf{r}_\perp; z) = \mathcal{F}_\perp^{-1} \left[\exp\left[iz\sqrt{k^2 - k_\perp^2}\right] \mathcal{F}_\perp [\psi_\omega(\mathbf{r}_\perp; 0)] \right]. \quad (3.20)$$

with \mathcal{F}_\perp and \mathcal{F}_\perp^{-1} denoting the 2D Fourier transform and Fourier back transform with respect to the x - and y -coordinates. Note that all following propagation equations could also be written as equations relating wave fields between planes $z = z_0$ and $z = z_1 > 0$.

3.1.2 Propagation within the paraxial approximation

Although Eq. (3.20) allows for an exact propagation of a general monochromatic two-dimensional wave field from plane $z = 0$ to a plane $z = \text{const.} > 0$ in a closed form, analytical solutions to the integrals involved in Eq. (3.20) are rare. It can therefore be very useful, if certain approximations can be applied to the above equation. The most prominent ones are the paraxial (Fresnel or small-angle) approximation and the far field (Fraunhofer) approximation which will be introduced in the following two subsections.

Consider again the problem of propagating a monochromatic wave field $\psi_\omega(\mathbf{r}_\perp; 0)$ from plane $z = 0$ into a plane $z = \text{const.} > 0$. Let us now assume that the original field $\psi_\omega(\mathbf{r}_\perp; 0)$ is **paraxial**, i.e. [108]

$$|\tilde{\psi}_\omega(\mathbf{k}_\perp; 0)| > 0 \text{ only for } k_\perp^2 \ll k^2. \quad (3.21)$$

As a consequence, the plane wave components in the integrand of Eq. (3.18) will contribute to the propagated field only, if their wave vector $(\mathbf{k}_\perp, \sqrt{k^2 - k_\perp^2})$ makes a small angle with respect to the optical axis. The paraxial requirement thus amounts to the condition that the largest value k_\perp^2 , for which the amplitude $|\tilde{\psi}_\omega(\mathbf{k}_\perp, 0)|$ is non-negligible, needs to obey $k_\perp^2 \ll k^2$ [108].⁵ Equivalently, the smallest lateral length scale a_{\min} , over which the non-propagated field varies considerably in any direction perpendicular to the optical axis,

⁵The weaker condition $k_\perp^2 < k^2$ is usually already assumed, if evanescent wave effects and therefore any Fourier components higher than k can be neglected.

needs to obey $(2\pi/a_{\min})^2 \ll k^2$, or

$$a_{\min} \gg \lambda_0 \Leftrightarrow k_{\perp}^2 \ll k^2. \quad (3.22)$$

If the above sufficient [108] condition is met, we can approximate the argument of the exponential function in the propagation factor as

$$\begin{aligned} \sqrt{k^2 - k_{\perp}^2} &= k - \frac{k_{\perp}^2}{2k} + \mathcal{O}(k_{\perp}^4) \\ &\simeq k - \frac{k_{\perp}^2}{2k}. \end{aligned} \quad (3.23)$$

Using this approximation, the expression for the propagation of a monochromatic wave field $\psi_{\omega}(\mathbf{r}_{\perp}; 0)$ at plane $z = 0$ to a plane $z = \text{const.} > 0$ becomes

$$\boxed{\psi_{\omega}(\mathbf{r}_{\perp}; z) \simeq \exp(ikz) \mathcal{F}_{\perp}^{-1} \left[\exp \left[\frac{-izk_{\perp}^2}{2k} \right] \mathcal{F}_{\perp} [\psi_{\omega}(\mathbf{r}_{\perp}; 0)] \right]}. \quad (3.24)$$

We call this approximation, for reasons which become clear when studying the numerical implementation of the propagation, the **near field formulation of Fresnel propagation**. Alternatively, instead of the term ‘Fresnel approximation’ the terms ‘small-angle’ or ‘paraxial approximation’ of free-space propagation may be used here.

There is an equivalent formulation of the above approximation with only one Fourier transform involved. In order to derive this form we rewrite Eq. (3.24) as

$$\psi_{\omega}(\mathbf{r}_{\perp}; z) \simeq \exp(ikz) \mathcal{F}_{\perp}^{-1} \left[\mathcal{F}_{\perp} \mathcal{F}_{\perp}^{-1} \left[\exp \left[\frac{-izk_{\perp}^2}{2k} \right] \right] \mathcal{F}_{\perp} [\psi_{\omega}(\mathbf{r}_{\perp}; 0)] \right]. \quad (3.25)$$

and apply the 2D analogue of the convolution theorem (2.14) to yield

$$\psi_{\omega}(\mathbf{r}_{\perp}; z) \simeq \psi_{\omega}(\mathbf{r}_{\perp}; 0) \otimes P(\mathbf{r}_{\perp}, z) \quad (3.26)$$

with the operator

$$P(\mathbf{r}_{\perp}, z) := \frac{\exp(ikz)}{2\pi} \mathcal{F}_{\perp}^{-1} \left[\exp \left[\frac{-izk_{\perp}^2}{2k} \right] \right]. \quad (3.27)$$

Hence, we have obtained a convolution formulation of the Fresnel propagation formula [108]. Using complex analysis one can derive an explicit form of the convolution operator $P(\mathbf{r}_{\perp}, z)$ as [108]

$$P(\mathbf{r}_{\perp}, z) = -\frac{ik \exp(ikz)}{2\pi z} \exp \left[\frac{ikr_{\perp}^2}{2z} \right] \quad (3.28)$$

with $r_{\perp}^2 := x^2 + y^2$. Consider now the phase of the spherical wave $S_{\omega,0}(\mathbf{r}_{\perp}; z)$, emanating from $\mathbf{r}_0 = 0$, observed at a plane $z = \text{const.} > 0$:

$$\varphi(S_{\omega,0}(x, y; z)) = ik \sqrt{z^2 + r_{\perp}^2}. \quad (3.29)$$

In the small-angle approximation $r_{\perp}^2 \ll z^2$ we can approximate

$$\begin{aligned}\varphi(S_{\omega,0}(x, y; z)) &= ikz + \frac{ikr_{\perp}^2}{2z} + \mathcal{O}(r_{\perp}^4) \\ &\simeq ikz + \frac{ikr_{\perp}^2}{2z}.\end{aligned}\quad (3.30)$$

The Fresnel convolution operator $P(\mathbf{r}_{\perp}, z)$ is thus proportional to a spherical wave, emanating from the origin, with its phase approximated to first order in r_{\perp}^2 . This gives us a new interpretation of the convolution formulation of Fresnel propagation, as described by Eq. (3.26): The propagation of a monochromatic wave field $\psi_{\omega}(\mathbf{r}_{\perp}; 0)$ in plane $z = 0$ (in the small-angle approximation) to a plane $z = \text{const.} > 0$ can be described by a summation over all spherical waves emanating from each point $(\mathbf{r}_{\perp}, 0)$ in the original plane, with amplitude $\psi_{\omega}(\mathbf{r}_{\perp}; 0)$. Hence we have obtained a reformulation of Huygens' principle for the description of diffraction. Eq. (3.26) thus provides us with an alternative formula to propagate a monochromatic field $\psi_{\omega}(\mathbf{r}_{\perp}; 0)$ at plane $z = 0$ to another plane $z = \text{const.} > 0$ within the small-angle-approximation, namely

$$\psi_{\omega}(\mathbf{r}_{\perp}; z) \simeq -\frac{ik \exp(ikz)}{2\pi z} \exp\left[\frac{ikr_{\perp}^2}{2z}\right] \int \psi_{\omega}(\mathbf{r}'_{\perp}; 0) \exp\left[\frac{ikr'_{\perp}{}^2}{2z}\right] \exp\left[-ik \frac{\mathbf{r}_{\perp} \cdot \mathbf{r}'_{\perp}}{z}\right] d\mathbf{r}'_{\perp}.\quad (3.31)$$

Note that the above integral is actually a two-dimensional Fourier transform of the modified incident field with spatial coordinates (x, y) transformed into Fourier space with coordinates $(k_x, k_y) := (kx/z, ky/z)$. We can thus write

$$\boxed{\psi_{\omega}(\mathbf{r}'_{\perp}; z) \simeq -\frac{ik \exp(ikz)}{z} \exp\left[\frac{ikr'_{\perp}{}^2}{2z}\right] \mathcal{F}_{\perp} \left[\psi_{\omega}(\mathbf{r}_{\perp}; 0) \exp\left[\frac{ikr_{\perp}^2}{2z}\right] \right]_{\mathbf{k}_{\perp} = \frac{k\mathbf{r}'_{\perp}}{z}}.}\quad (3.32)$$

Note that we have switched the notation here for later convenience, so that \mathbf{r}'_{\perp} now denotes the spatial coordinates in plane $z = \text{const.} > 0$ and \mathbf{r}_{\perp} those in plane $z = 0$. Summarizing, we have reduced the problem of calculating a convolution integral to a simple Fourier transform which is advantageous for a numerical implementation of the integral. We call Eq. (3.32) the **far field formulation of Fresnel propagation**. Note that unlike in the near field formulation (see Eq. 3.24), here the real-space coordinate systems of the incident and the propagated field are not the same.

3.1.3 Far field propagation within the paraxial approximation

Let D_{\max} denote the diameter of the largest area, within which the non-propagated wave field $\psi(\mathbf{r}_{\perp}; 0)$ in plane $z = 0$ varies significantly. We then call the dimensionless number

$$F := \frac{D_{\max}^2}{\lambda_0 z}\quad (3.33)$$

the **Fresnel number** of our optical setup (including the incident wave field) [108]. If now the propagation distance z is much larger than the diameter of the non-vanishing region

of the non-propagated wave field, i.e. if

$$F \ll 1 \quad (3.34)$$

we can omit the spherical phase term *inside* the integrand of Eq. (3.32) and obtain the propagated field at plane $z > 0$ as a simple Fourier transform of the incident wave field, modulated by a spherical phase term [108]:

$$\psi_{\omega}(\mathbf{r}'_{\perp}; z) \simeq -\frac{ik \exp(ikz)}{z} \exp\left[\frac{ikr_{\perp}'^2}{2z}\right] \mathcal{F}_{\perp} [\psi_{\omega}(\mathbf{r}_{\perp}; 0)]_{\mathbf{k}_{\perp} = \frac{k\mathbf{r}'_{\perp}}{z}}. \quad (3.35)$$

We call this equation the (small-angle) **far field or Fraunhofer diffraction formula**. Working in the validity range of this equation significantly simplifies the analysis of diffraction experiments, due to the relatively simple Fourier transform relation between the field in the incident and final plane.

Note that both the condition of the small-angle approximation *and* far field diffraction were assumed for the validity of Eq. (3.35). In other words, Fraunhofer diffraction is presented here as a limiting case of Fresnel diffraction which remains valid in the range of $F \ll 1$.⁶ Note, however, that both conditions are sufficient, but not necessary conditions for Fraunhofer diffraction to be valid [108].

Note that in the Fresnel and Fraunhofer diffraction formulas we have always used ' \simeq ' to stress that these equations are approximations to the exact diffraction formula Eq. (3.20). We have seen that both formulations of Fresnel-diffraction rely on an approximation which is accurate up to second order in r_{\perp} with the next correction term of order 4. If paraxiality can be assumed, the Fresnel diffraction equations are thus usually very good approximations.

Lastly, we note that the transition to Fraunhofer diffraction relies on an approximation accurate to first order in r_{\perp} . Luckily, a large body of experimental setups can be designed both in the optical and x-ray regime, where this approximation is very well justified.

3.1.4 Effective near field propagation: The Fresnel scaling theorem

It has been shown above that the Fresnel convolution operator $P(\mathbf{r}_{\perp}, z)$ is proportional to the paraxial approximation of a spherical wave with its dependence on lateral coordinates contained in the 'chirp' [149] factor $\exp(ikr_{\perp}^2/(2z))$. This raises the question, if any simplifications in the propagation equation can be obtained, if the wave field to be propagated is itself (nearly) spherical.

Consider a complex wave field $\psi_{\omega}(\mathbf{r}_{\perp}; 0)$ at plane $z = 0$ which is to be propagated within the small-angle approximation to a plane $z = \text{const.} > 0$. If $\psi_{\omega}(\mathbf{r}_{\perp}; 0)$ is nearly spherical with radius of curvature R and with a nearly planar complex envelope $\psi_{\omega}^{(P)}(\mathbf{r}_{\perp}; 0)$ it is useful to separate the spherical part, i.e. write

$$\psi_{\omega}(\mathbf{r}; 0) = \psi_{\omega}^{(P)}(\mathbf{r}_{\perp}; 0) \exp\left(\frac{ikr_{\perp}^2}{2R}\right). \quad (3.36)$$

⁶Note that one often finds the term 'Fresnel diffraction' or 'Fresnel propagation' used as a representation of the case $F \gtrsim 1$, although, from a systematic point of view, the term refers to all F , as long as the small-angle approximation is valid.

As an example consider an ideal point source emanating a spherical wave from a point on the optical axis, at distance R upstream of the plane $z = 0$. Within the small-angle approximation the resulting wave field at plane $z = 0$ has the form

$$S_{\omega,(0,0,-R)}(\mathbf{r}; 0) \simeq \frac{\exp(ikR)}{R} \exp\left(\frac{ikr_{\perp}^2}{2R}\right). \quad (3.37)$$

Inserting the ansatz (3.36) as an incident field into the propagation equation (3.31) and denoting the lateral coordinates at plane $z = \text{const.} > 0$ by \mathbf{r}'_{\perp} and those at plane $z = 0$ by \mathbf{r}_{\perp} , one obtains

$$\psi_{\omega}(\mathbf{r}'_{\perp}; z) = A(z) \exp\left[\frac{ikr_{\perp}'^2}{2z}\right] \int \psi_{\omega}^{(P)}(\mathbf{r}_{\perp}; 0) \exp\left[\frac{ikr_{\perp}^2}{2}\left(\frac{1}{R} + \frac{1}{z}\right)\right] \exp\left[-ik\frac{\mathbf{r}'_{\perp} \cdot \mathbf{r}_{\perp}}{z}\right] d\mathbf{r}_{\perp} \quad (3.38)$$

with $A(z) = -ik \exp(ikz)/(2\pi z)$. We introduce the geometrical magnification factor

$$M := \frac{R+z}{R} = 1 + \frac{z}{R} = \frac{\frac{R}{z} + 1}{\frac{R}{z}} \quad (3.39)$$

due to the spherical illumination, and the effective propagation distance

$$z_{\text{eff}} := \frac{z}{M} = \frac{R}{\frac{R}{z} + 1} = \frac{z}{1 + \frac{z}{R}}. \quad (3.40)$$

The different forms are useful for limiting cases $R \gg z$ and $R \ll z$. The amplitude of the field ψ_{ω} at a plane $z > 0$, can then be written as

$$|\psi_{\omega}(\mathbf{r}'_{\perp}; z)| = \frac{|A(z_{\text{eff}})|}{M} \left| \int \psi_{\omega}^{(P)}(\mathbf{r}_{\perp}; 0) \exp\left[\frac{ikr_{\perp}^2}{2z_{\text{eff}}}\right] \exp\left[-ik\frac{(\mathbf{r}'_{\perp}/M) \cdot \mathbf{r}_{\perp}}{z_{\text{eff}}}\right] d\mathbf{r}_{\perp} \right| \quad (3.41)$$

Consider now for comparison the amplitude of the planar part $\psi^{(P)}$, propagated according to Eq. (3.32) from plane $z = 0$ to a plane $z = z_{\text{eff}}$, evaluated at lateral position \mathbf{r}'/M :

$$|\psi_{\omega}^{(P)}(\mathbf{r}'_{\perp}/M; z_{\text{eff}})| = |A(z_{\text{eff}})| \left| \int \psi_{\omega}^{(P)}(\mathbf{r}_{\perp}; 0) \exp\left[\frac{ikr_{\perp}^2}{2z_{\text{eff}}}\right] \exp\left[-ik\frac{(\mathbf{r}'_{\perp}/M) \cdot \mathbf{r}_{\perp}}{z_{\text{eff}}}\right] d\mathbf{r}_{\perp} \right|. \quad (3.42)$$

By comparison of the two equations above one obtains

$$\boxed{|\psi_{\omega}(\mathbf{r}'_{\perp}; z)| = \frac{1}{M} |\psi_{\omega}^{(P)}(\mathbf{r}'_{\perp}/M; z_{\text{eff}})|.} \quad (3.43)$$

Thus the amplitude of the field ψ_{ω} , propagated from plane $z = 0$ to plane $z = \text{const.} > 0$, at lateral position \mathbf{r}'_{\perp} , is equal to the amplitude of the field $\psi^{(P)}$, propagated from plane $z = 0$ to plane $z = z_{\text{eff}}$, at lateral position \mathbf{r}'/M . Here ψ_{ω} is related to $\psi_{\omega}^{(P)}$ via $\psi_{\omega}^{(P)}(\mathbf{r}_{\perp}; 0) = \psi_{\omega}(\mathbf{r}_{\perp}; 0) \exp(-ikr_{\perp}^2/(2R))$. Note that this relation is given in plane $z = 0$. A similar derivation is given in [108]. There, however, it is explicitly assumed that ψ is generated by an ideal point source, so that —apart from possible contributions of a sample

in the beam— $\psi_\omega^{(P)}$ is a true plane wave. Relation (3.43) then represents what is sometimes also called the **Fresnel scaling theorem**. To our knowledge and according to the above considerations such a restriction to an ideal point source does not seem to be necessary to arrive at Eq. (3.43).⁷

3.1.5 Measurement of monochromatic wave fields

Consider a scalar monochromatic wave field

$$\Psi_\omega(\mathbf{r}, t) = \psi_\omega(\mathbf{r}) \exp(-i\omega t). \quad (3.44)$$

Note again that the abstract scalar field $\Psi_\omega(\mathbf{r}, t)$ was introduced as a representation⁸ of e.g. the electrical field $E_\omega(\mathbf{r}, t)$ in a certain direction perpendicular to the optical axis. As $E_\omega(\mathbf{r}, t)$ is allowed to be complex, the physical quantity is obtained by forming the real part $\text{Re}[E_\omega(\mathbf{r}, t) = E_0(\mathbf{r}) \exp(-i\omega t)]$. As long as only linear operations on $E_\omega(\mathbf{r}, t)$ are performed, one can do calculations on the complex $E_\omega(\mathbf{r}, t)$ and afterwards form the real part [9]. As soon as non-linear operations, such as squaring is to be performed, one generally has to form the real part first. It turns out, however, that time averaging can relax this condition [9].

In the x-ray regime the frequency $\omega = 2\pi\nu$ is on the order 10^{19} s^{-1} , so that $E_\omega(\mathbf{r}, t)$ cannot be measured directly. Instead, only the time average of physical quantities derived from $E_\omega(\mathbf{r}, t)$ over a time span much larger than a single period $T = 2\pi/\omega$ can be measured [9]. The time averaged optical power flow density (energy per area per time) incident on a detector pixel with a certain surface area and center \mathbf{r}_p is given as

$$p(\mathbf{r}_p) = \frac{|E_0(\mathbf{r}_p)|^2}{2\eta} \quad (3.45)$$

with $\eta = \sqrt{\mu_0/\epsilon_0}$ [60]. Here $E_0(\mathbf{r}_p)$ is the complex amplitude of the electrical field that can locally be described as a plane wave with the wave vector perpendicular to the detector surface [60]. $p(\mathbf{r}_p)$ can be obtained from $E_\omega(\mathbf{r}_p, t)$ as the time average

$$p(\mathbf{r}_p) = \left\langle \frac{\text{Re}[E_\omega(\mathbf{r}_p, t)]^2}{\eta} \right\rangle = \frac{1}{\eta} \lim_{T' \rightarrow \infty} \frac{1}{T'} \int_{-T'/2}^{T'/2} \text{Re}[E_\omega(\mathbf{r}_p, t)]^2 dt. \quad (3.46)$$

using a derivation similar to that described in [9, p. 34]. In particular, the above equations state that

$$\left\langle \text{Re}[E_\omega(\mathbf{r}_p, t)]^2 \right\rangle = \frac{1}{2} |E_0(\mathbf{r}_p)|^2, \quad (3.47)$$

i.e. for a monochromatic wave field the physically meaningful *averaged squared real part* of the time-varying complex field $E_\omega(\mathbf{r}, t)$ is proportional to the squared modulus of its amplitude.

⁷Nevertheless, henceforth Eq. (3.43) will be referred to as the Fresnel scaling theorem.

⁸In other words $\Psi_\omega(\mathbf{r}, t) \propto E_\omega(\mathbf{r}, t)$.

For $E_\omega(\mathbf{r}, t)$ propagating locally in a direction normal to the detection surface the total power incident on a pixel with area A_p and center location \mathbf{r}_p is then given as

$$P_p = \int_{A_p} p(x, y) dx dy \approx p(\mathbf{r}_p) A_p, \quad (3.48)$$

assuming that the pixel is small enough so that one can replace the integral by a multiplication. The total optical power incident on the pixel is thus

$$P_p = A_p \frac{|E_0(\mathbf{r}_p)|^2}{2\eta}. \quad (3.49)$$

Optical power is delivered in particles (photons) of constant energy $\hbar\omega$ for monochromatic radiation, with $\hbar = h/2\pi = 6.626 \cdot 10^{-34} / 2\pi$ Js denoting Planck's constant. The **signal** N_p or **integrated count rate** of an ideal detector at a given pixel p with center location \mathbf{r}_p is equal to the incident number of photons integrated over measurement time T and pixel area A_p . For a monochromatic field the average optical power is constant, so that the **integrated signal** S_p is given as

$$S_p = \frac{q_{qe} T P_p}{\hbar\omega}, \quad (3.50)$$

where $0 \leq q_{qe} \leq 1$ relates one detector unit to the corresponding number of photons. For an ideal detector $q_{qe} = 1$ and thus $S_p = N_p$. For simplicity we will now assume $q_{qe} = 1$. We get

$$N_p = T A_p \frac{|E_0(\mathbf{r}_p)|^2}{2\eta\hbar\omega}. \quad (3.51)$$

The **photon flux density** is then given as

$$I_{\text{ph}}(\mathbf{r}_p) = \frac{p(\mathbf{r}_p)}{\hbar\omega} = \frac{N_p}{T A_p}, \quad (3.52)$$

with units often expressed as $\text{ph}\mu\text{m}^{-2}\text{s}^{-1}$, where 'ph' stands for 'number of photons'. Note that this equation is only valid if the pixel is small enough so that the spatial mean of the flux density over the pixel can be replaced by the flux density at the center of the pixel. We will sometimes refer to this quantity also as the **(physical) intensity** of the wave field.

We define the **photon fluence** $F_{\text{ph}}(\mathbf{r}_p)$ as the intensity integrated over the whole measurement time, i.e.

$$F_{\text{ph}}(\mathbf{r}_p) = \frac{N_p}{A_p}. \quad (3.53)$$

We define the **photon flux** $\Phi_A(\mathbf{r})$ through area A as the intensity integrated over the surface area the photons are passing, i.e. for a single pixel

$$\Phi_{\text{ph}}(\mathbf{r}_p) = \frac{N_p}{T}. \quad (3.54)$$

$\Phi_{\text{ph}}(\mathbf{r})\hbar\omega$ thus denotes the power that is incident on a surface with area A_p .

How do these physical quantities relate to the abstract complex scalar fields $\Psi_\omega(\mathbf{r}_p, t)$ and $\psi_\omega(\mathbf{r}_p, t)$? After all, these are the quantities that are used in all calculations. Analogous to Eq. (3.47) one can derive

$$\left\langle \text{Re} [\Psi_\omega(\mathbf{r}_p, t)]^2 \right\rangle = \frac{1}{2} |\Psi_\omega(\mathbf{r}_p, t)|^2 = \frac{1}{2} |\psi_\omega(\mathbf{r}_p)|^2 \quad (3.55)$$

for any monochromatic x-ray wave field $\Psi_\omega(\mathbf{r}_p, t)$ with a harmonic time dependence $\exp(-i\omega t)$. If the scalar field $\Psi_\omega(\mathbf{r}_p, t)$ thus is assumed to be proportional to a certain component of the electric field, then the **(abstract) intensity** defined as

$$I(\mathbf{r}_p) := |\psi_\omega(\mathbf{r}_p)|^2 \quad (3.56)$$

is *proportional* to the physically meaningful and measurable photon flux density $I_{\text{ph}}(\mathbf{r}_p)$ as defined above. For a simulation or an experiment, the measurement time and pixel area are fixed quantities, so that, in addition, $|\psi_\omega(\mathbf{r}_p)|^2$ becomes proportional to the photon flux $\Phi_{\text{ph}}(\mathbf{r}_p)$ integrated over the pixel area, the photon fluence $F_{\text{ph}}(\mathbf{r}_p)$ integrated over the measurement time, and the total integrated photon number N_p per pixel. We will allow a certain freedom here in the definition of ψ_ω , so that, depending on the context, $|\psi_\omega|^2$ may denote a photon flux density, a fluence, etc.

3.1.5.1 Detection statistics

Due to the quantum nature of light, the detector signal S is a non-deterministic quantity, even for strictly monochromatic radiation. Its randomness is actually different from the stochastic nature of wave fields in the classical picture that is described below. As a consequence, the integrated photon count rate N_p follows Poisson statistics with the probability distribution

$$p(N_p) = \frac{\langle N_p \rangle^{N_p} \exp(-\langle N_p \rangle)}{N_p!} \quad (3.57)$$

with expectation value $\langle N_p \rangle$, standard deviation $\sigma = \sqrt{\langle N_p \rangle}$ and relative error $\sigma / \langle N_p \rangle = 1 / \sqrt{\langle N_p \rangle}$. The signal-to-noise ratio of a given photon count is defined as the inverse relative error

$$\text{SNR} := \sqrt{\langle N_p \rangle}. \quad (3.58)$$

3.1.6 Coherence of wave fields

The **coherence** of the involved wave fields is an essential prerequisite to all experiments that are presented within this thesis. More precisely, it is the high *degree of coherence* of the wave field that is required for lensless imaging experiments. Here the term ‘coherence’ can be interpreted as the self-correlation of a wave field $\Psi(\mathbf{r}, t)$ in space and time, which is directly related to the strength of interference effects that can be observed for a given $\Psi(\mathbf{r}, t)$.

Only the **mean intensity**

$$I(\mathbf{r}) := \lim_{T \rightarrow \infty} \langle |\Psi(\mathbf{r}, t)|^2 \rangle_T = 1/T \int_{-T/2}^{T/2} \Psi(\mathbf{r}, t) \Psi^*(\mathbf{r}, t) dt,$$

i.e. the time-averaged squared modulus of an x-ray wave field is accessible experimentally. Thus, in deducing information on some material in a scattering experiment, e.g. by application of Eq. (3.155), one has to rely on the assumption that the scattered intensity is the modulus squared of a (deterministic) sum of elementary complex scattered fields and we have implicitly relied on this assumption so far.

Due to the generally non-deterministic creation process of x rays, which is intrinsically random due to quantum mechanical and thermal effects that influence the emission of photons from an atom (or a relativistic bunch of electrons), the wave field $\Psi(\mathbf{r}, t)$ is rather a stochastic process than a deterministic scalar field in space and time. Measuring $\Psi(\mathbf{r}, t)$ in an experiment for all \mathbf{r} and t then would amount to the determination of a certain realization of such a process. The assumption of ergodicity allows us to replace the ensemble average $\langle \dots \rangle_{\mathcal{E}}$ over all possible realizations of a wave field by the time average over a single realization, $\lim_{T \rightarrow \infty} \langle \dots \rangle_T$ [108, 155]. Although we cannot obtain any of the two quantities in a strict sense, we can come much closer to the second one in an experiment. Due to the assumption of ergodicity, henceforth we leave out the index of the braces.

The correlation at two spacetime points of a given realization $\Psi(\mathbf{r}, t)$ of a general wave field can be described by the two-point correlation function

$$\Gamma(\mathbf{r}_1, \mathbf{r}_2, \tau) := \Gamma_{12}(\tau) := \langle \Psi(\mathbf{r}_1, t + \tau) \Psi^*(\mathbf{r}_2, t) \rangle \quad (3.59)$$

which is also called the **mutual coherence function (MCF)** [108]. The mean intensity

$$I(\mathbf{r}_1) = \Gamma(\mathbf{r}_1, \mathbf{r}_1, \tau = 0) \quad (3.60)$$

is thus a special case of the MCF. Likewise, the time-averaged **autocorrelation function** of $\Psi(\mathbf{r}, t)$ at \mathbf{r} is also a special form of the MCF, namely $\Gamma_{11}(\tau)$. The case $J(\mathbf{r}_1, \mathbf{r}_2) := \Gamma(\mathbf{r}_1, \mathbf{r}_2, \tau = 0)$ defines the **mutual intensity** [108]. As a result $\Gamma_{12}(0) = J(\mathbf{r}_1, \mathbf{r}_2)$ embodies only spatial correlations, while $\Gamma_{11}(\tau)$ embodies only time correlations.

The above definitions imply that $I(\mathbf{r}_1)$ is independent of t and $\Gamma_{12}(\tau)$ only depends on the difference of two points in time, not on their absolute location.⁹ The normalized version

$$\gamma(\mathbf{r}_1, \mathbf{r}_2, \tau) := \gamma_{12}(\tau) := \frac{\Gamma(\mathbf{r}_1, \mathbf{r}_2, \tau)}{\sqrt{\Gamma(\mathbf{r}_1, \mathbf{r}_1, 0)\Gamma(\mathbf{r}_2, \mathbf{r}_2, 0)}} = \frac{\Gamma(\mathbf{r}_1, \mathbf{r}_2, \tau)}{\sqrt{I(\mathbf{r}_1)I(\mathbf{r}_2)}} \quad (3.61)$$

of the mutual coherence function is called the **complex degree of coherence** [108]. The normalization is such that $\gamma_{11}(0) = 1$.¹⁰

A **strictly monochromatic wave field** is characterized by a fully deterministic realization

$$\Psi(\mathbf{r}) = \sqrt{I(\mathbf{x})} \exp[i(\varphi(\mathbf{r}) - \omega t)]. \quad (3.62)$$

⁹A field $\Psi(\mathbf{r}, t)$, for which these prerequisites are given, is called stationary (in the wide sense) [108].

¹⁰Of course, higher order correlation functions can be studied. For synchrotron and tube sources, however, it suffices to study $\gamma_{12}(\tau)$ [105]. The situation is different for a free-electron laser source [105].

Its complex degree of coherence [108]

$$\gamma_{12}(\tau) = \exp[i(\varphi(\mathbf{r}_1) - \varphi(\mathbf{r}_2) - \omega\tau)] \quad (3.63)$$

has a unit modulus $|\gamma_{12}(\tau)| = 1$ for all space-time points and hence represents an optimal degree of coherence.

The opposite extreme, a wave field with zero degree of coherence, i.e. $\gamma_{12}(\tau) = 0$ except $\mathbf{r}_1 = \mathbf{r}_2$ and $\tau = 0$, then corresponds to no correlation at all between (wave field values at) any two spacetime points.

A realistic wave field that is used in a lensless imaging experiment can be modeled as a so-called **quasi-monochromatic** wave field [108, 155]. Its frequency spectrum $\psi_\omega(\mathbf{r})$ is negligible outside a narrow band $\Omega = [\bar{\omega} - \Delta\omega/2, \bar{\omega} + \Delta\omega/2]$ of frequencies ω with $\Delta\omega \ll \bar{\omega}$. It is therefore meaningful to extract a ‘mean’ or dominating deterministic time dependence $\exp(-i\bar{\omega}t)$ and write a given quasi-monochromatic wave field realization as [108]

$$\Psi(\mathbf{r}, t) = \exp(-i\bar{\omega}t)\mathcal{A}(\mathbf{r}, t) \quad (3.64)$$

with

$$\mathcal{A}(\mathbf{r}, t) = \frac{1}{\sqrt{2\pi}} \int_{\Omega - \bar{\omega}} \psi_{\bar{\omega} + \varepsilon}(\mathbf{r}) \exp(-i\varepsilon t) d\varepsilon. \quad (3.65)$$

The envelope $\mathcal{A}(\mathbf{r}, t)$ still exhibits a random time dependence due to the spectral amplitudes $\psi_{\bar{\omega} + \varepsilon}(\mathbf{r})$ which inherit a small randomness with respect to their frequency index, however, the variation will be much slower, because $\varepsilon \ll \bar{\omega}$. By inserting Eq. (3.64) into Eq. (3.59) one finds for a quasi-monochromatic wave field [108]

$$\Gamma(\mathbf{r}_1, \mathbf{r}_2, \tau) = \exp(-i\bar{\omega}\tau) \langle \mathcal{A}(\mathbf{r}_1, t + \tau) \mathcal{A}^*(\mathbf{r}_2, t) \rangle \quad (3.66)$$

One can show [108] that for quasi-monochromatic wave fields

$$|\gamma(\mathbf{r}_1, \mathbf{r}_2, \tau)| \leq 1. \quad (3.67)$$

In practice, one will always encounter wave fields with

$$0 < |\gamma(\mathbf{r}_1, \mathbf{r}_2, \tau)| < 1 \quad (3.68)$$

with the cases $|\gamma(\mathbf{r}_1, \mathbf{r}_2, \tau)| = 0$ (complete incoherence) and $|\gamma(\mathbf{r}_1, \mathbf{r}_2, \tau)| = 1$ (full coherence) only being theoretical idealizations.

Having shortly studied the previous examples, it becomes clear that the ‘coherence of a wave field’ corresponds to a rather information-rich quantity. Fortunately, it is often possible to model $|\gamma(\mathbf{r}_1, \mathbf{r}_2, \tau)|$ with some functional form. In such a case the model parameters will then give a simple measure for the degree of coherence. For a realistic wave field we expect $|\gamma(\mathbf{r}_1, \mathbf{r}_2, \tau)|$ to be a function that decays with increasing spatial separation $|\mathbf{r}_1 - \mathbf{r}_2|$ and temporal separation τ of the spacetime points to be correlated. In other words, the degree of correlation between to points in space and time decreases in a predictable manner as their distance increases.

3.1.6.1 Spatial coherence

Let us first consider the spatial correlations. In the following, we assume quasi-monochromatic radiation. A central general result from the theory of coherence is the dependence of the degree of spatial correlation on the propagation of a partially coherent wave field. More precisely, it can be shown [4, 108, 155] that a wave field with $|\gamma_{12}(\tau)| = 0$ for all $\mathbf{r}_{\perp,1} \neq \mathbf{r}_{\perp,2}$ in a plane perpendicular to the optical axis, the source plane, shows non-vanishing spatial correlations in a plane in the far field of the source. This effect is quantified by the van Cittert - Zernike theorem [4, 108, 155] which relates the intensity distribution $I(s_x, s_y)$ in the source plane of a small quasi-monochromatic two-dimensional source with zero spatial correlation to the mutual intensity function $J(\mathbf{r}_{\perp,1}, \mathbf{r}_{\perp,2})$ in an observation plane at a distance z in the far field of the source, i.e. for $z \gg d_s$ where d_s denotes the largest lateral extension of the source. The theorem can be written as [105]:

$$J(\mathbf{r}_{\perp,1}, \mathbf{r}_{\perp,2}) \propto \exp(i\varphi) \int I(\mathbf{s}_{\perp}) \exp \left[-i \frac{\bar{k}(\mathbf{r}_{\perp,1} - \mathbf{r}_{\perp,2}) \cdot \mathbf{s}_{\perp}}{z} \right] ds_x ds_y \quad (3.69)$$

$$\propto \exp(i\varphi) \mathcal{F}_{\perp} [I(\mathbf{s}_{\perp})] (\mathbf{k}_{\perp} = \bar{k}(\mathbf{r}_{\perp,1} - \mathbf{r}_{\perp,2})/z) \quad (3.70)$$

with φ being a real number dependent on z , $\mathbf{r}_{\perp,1}$ and $\mathbf{r}_{\perp,2}$. $\bar{k} = \bar{\omega}/c$ here denotes the mean wave number [108]. The essential message of the van Cittert - Zernike theorem thus is that far away from a small, spatially incoherent quasi-monochromatic source the modulus of the mutual intensity is given as (up to prefactors constant in lateral variables) the Fourier transform of the lateral intensity distribution in the source plane. For a synchrotron source one can model the essentially incoherent intensity distribution emitted from the relativistic electron bunch at the source plane as [147]

$$I(\mathbf{s}_{\perp}) = \frac{I_0}{2\pi\sigma_x\sigma_y} \exp \left[-\frac{1}{2} \left(\frac{s_x^2}{\sigma_x^2} + \frac{s_y^2}{\sigma_y^2} \right) \right]. \quad (3.71)$$

with the lateral $1/\sqrt{e}$ -intensity-decay (half-) lengths σ_x and σ_y . The van Cittert - Zernike theorem (3.70) here leads to

$$|J(\mathbf{r}_{\perp,1}, \mathbf{r}_{\perp,2})| \propto I_0 \exp \left[-\frac{1}{2} \frac{\bar{k}^2}{z^2} \left((x_1 - x_2)^2 \sigma_x^2 + (y_1 - y_2)^2 \sigma_y^2 \right) \right]. \quad (3.72)$$

With the definition of the **spatial coherence length** ℓ_c as *the $1/\sqrt{e}$ -decay half length of the modulus of the mutual intensity function for quasi-monochromatic light* this leads to the horizontal (vertical) coherence length of

$$\ell_{c,x(y)} = \frac{1}{2\pi} \cdot \frac{\bar{\lambda}_0 z}{\sigma_{x(y)}} \simeq 0.159 \cdot \frac{\bar{\lambda}_0 z}{\sigma_{x(y)}} \quad (3.73)$$

for an undulator synchrotron source at a distance z from the source with lateral $1/\sqrt{e}$ -mutual intensity decay half length $\sigma_{x(y)}$ in the source plane. The prefactors are rather arbitrary given various used definitions of the characteristic decay length. Note that the spatial coherence length is sometimes also denoted the *lateral* coherence length as it refers to correlations with planes perpendicular to the optical axis.

We give an example here for the spatial coherence length of an undulator synchrotron beamline, the coherent Small Angle Scattering (cSAXS) beamline at the Swiss Light Source (SLS) [29]. With a source-to-sample distance of about 34 m and source dimensions (FWHM) of $202 \times 18 \mu\text{m}^2$ (horz. \times vert.), one obtains at a photon energy of 6.2 keV coherence lengths of $\ell_{c,x} \approx 12.6 \mu\text{m}$ and $\ell_{c,y} \approx 141.6 \mu\text{m}$, using Eq. (3.73) and the relation $\text{FWHM} = 2\sqrt{2\ln 2}\sigma$.

In principle, it is possible to build a full theory of the propagation of wave fields in terms of their correlation functions [9, 108] and a full quantification of all effects due to partial coherence requires such a treatment. *Within this thesis the effects of partial coherence are not considered explicitly.* As a consequence, one has to make sure by choosing proper experimental conditions that effects of partial coherence can be neglected.

3.1.6.2 Temporal coherence

For quasi-monochromatic light, the time correlation is encoded in the autocorrelation function $\Gamma_{11}(\tau)$ which has a Fourier transform (the power spectral density) that is sharply peaked around a mean frequency $\bar{\omega}$. Using a Lorentzian function with a bandwidth $\Delta\omega$ to model the spectral density of a synchrotron source, the autocorrelation function has an exponential lag-time dependence $\Gamma_{11}(\tau) \propto \exp(-\tau/\tau_c)$ [147]. A **coherence time** τ_c may be defined as the $1/e$ -decay length of the autocorrelation function of a quasi-monochromatic wave field [147]. The value $\Gamma_{11}(\tau_c)$ thus corresponds to the degree of correlation between two points in a wave field which are separated, in the direction of propagation, by a distance $\ell_t := c\tau$. We have thus defined a second **temporal or longitudinal coherence length** ℓ_t . For a quasi-monochromatic wave field with mean wavelength $\bar{\lambda}_0$ and a Lorentzian power spectral density with bandwidth $\Delta\omega$ one obtains [147]

$$\ell_t = \frac{2}{\pi} \left(\frac{\bar{\lambda}_0^2}{\Delta\lambda_0} \right). \quad (3.74)$$

Again the pre-factors are subject to the definitions used.

A typical bandwidth $\Delta\bar{\lambda}_0/\bar{\lambda}_0$ of undulator radiation, monochromatized by a crystal monochromator is on the order of 0.02%, the value for the cSAXS beamline. For a mean photon energy of 6.2 keV, this yields a longitudinal coherence length of $\ell_t = 0.6 \mu\text{m}$.

The validity of data analysis under the assumption of full spatial and temporal coherence will be discussed in Chapter 4.

3.1.7 Numerical implementation of free space propagation

We are equipped with four different analytical expressions for the free-space propagation of a stationary monochromatic wave $\psi_\omega(\mathbf{r}_\perp; 0)$ from plane $z = 0$ to a plane $z = \text{const.} > 0$, one of them being an exact expression (Eq. (3.20)), the others being approximations in the case that only paraxial fields are studied, either in the near field (see Eq. (3.24)) or far field (see Eqs. (3.32) and (3.35)). Although these are approximative equations, there are still quite few analytical solutions, giving an explicit expression for $\psi_\omega(\mathbf{r}_\perp; z)$, once $\psi_\omega(\mathbf{r}_\perp; 0)$ is known. We therefore need a numerical implementation of free-space propagation which

within this thesis is solely based on the discrete Fourier transform approximation to the derived propagation equations. Note that there are various alternative ways to carry out free-space propagation numerically and that so far no method has been found which can be regarded as being the best in terms of criteria such as accuracy, computational speed, geometrical range of validity etc. In other words, numerical free-space propagation of wave fields is still an area of active research [see e.g. 95].

DFT-based methods for numerical free-space diffraction allow for very fast computations using the fast Fourier transform, but suffer from artifacts, if the input array is sampled with a non-sufficient sampling rate.

3.1.7.1 Paraxial propagation

Let us first consider the Fresnel propagation equations (3.24) and (3.32). For reasons of simplicity, in the following we assume the total number of sampling points in x and y direction, N_x and N_y , to be even. We therefore define a real space grid by

$$\begin{aligned}\mathbf{x}_N^{(c)} &= \left(-\frac{N_x}{2}\Delta x, \dots, \left(\frac{N_x}{2}-1\right)\Delta x \right), \\ \mathbf{y}_N^{(c)} &= \left(-\frac{N_y}{2}\Delta y, \dots, \left(\frac{N_y}{2}-1\right)\Delta y \right),\end{aligned}\quad (3.75)$$

and a reciprocal space grid by

$$\begin{aligned}\mathbf{k}_{xN}^{(c)} &= \left(-\frac{N_x}{2}\Delta k_x, \dots, \left(\frac{N_x}{2}-1\right)\Delta k_x \right), \\ \mathbf{k}_{yN}^{(c)} &= \left(-\frac{N_y}{2}\Delta k_y, \dots, \left(\frac{N_y}{2}-1\right)\Delta k_y \right).\end{aligned}\quad (3.76)$$

We have omitted here the indication ‘ \perp ’ that \mathbf{k}_N is only defined in planes perpendicular to the optical axis. The reciprocity relations of the discrete Fourier Transform establish a connection between the grids, i.e.

$$\Delta x \Delta k_x = \frac{2\pi}{N_x}, \quad (3.77)$$

$$\Delta y \Delta k_y = \frac{2\pi}{N_y}. \quad (3.78)$$

The discrete version of the near field Fresnel propagation equation (3.24), using a 2D generalization of Eq. (2.116), then reads

$$\begin{aligned}\psi_\omega(\mathbf{x}_N^{(c)}, \mathbf{y}_N^{(c)}; z) &= \exp(ikz) \\ &\times \text{IDFT}^{(c)} \left[\left(\exp \left[-\frac{iz(m_x^2 \Delta k_x^2 + m_y^2 \Delta k_y^2)}{2k} \right] \text{DFT}_{m_x, m_y}^{(c)} \left[\psi_\omega(\mathbf{x}_N^{(c)}, \mathbf{y}_N^{(c)}; 0) \right] \right) \right]\end{aligned}\quad (3.79)$$

with $m_x, m_y = -N_{x,y}/2 \dots, N_{x,y}/2 - 1$ in the argument of the inverse discrete FT. Evidently, the phase term in the argument of the inverse DFT causes very steep phase gradients for

large propagation distances z . A given sampling period Δk (in either coordinate direction) will thus become insufficiently small for large z . Therefore, Eq. (3.24) is also referred to as the near field Fresnel-propagation equation.

The far field Fresnel propagation equation (3.32) contains spherical phase terms, both in planes $z = 0$ and $z = \text{const.} > 0$. In this case, however, the real-space coordinate system undergoes a linear scaling which depends on the propagation distance. With $\Delta x'$ denoting the real-space sampling period in plane $z = \text{const.} > 0$, the Fourier space sampling period is given as $\Delta k_x = \Delta x' \cdot k/z$. In addition, with the reciprocity relation of the DFT Δk_x is related to the real space sampling period Δx in plane $z = 0$ via $\Delta k_x \Delta x = 2\pi/N_x$. As a consequence we have a sampling period of

$$\Delta x' = \frac{\lambda z}{N_x \Delta x} \quad (3.80)$$

in plane $z = \text{const.} > 0$, given a sampling period Δx in a plane $z = 0$ upstream, if the far field version of the Fresnel propagator is used. Note that this scaling also applies to the Fraunhofer diffraction equation (3.35) and implies that once the far field condition $F \ll 1$ is met, further propagation just corresponds to a geometric magnification of the diffracted wave field, as $\Delta x' \propto z$. With these considerations the far field Fresnel propagation equation (3.32) may be discretized with a 2D generalization of Eq. (2.116) to

$$\begin{aligned} \psi_\omega(m_x \Delta x', m_y \Delta y'; z) &= -\frac{\Delta x \Delta y \sqrt{N_x N_y}}{2\pi} \frac{ik \exp(ikz)}{z} \times \exp \left[\frac{ik(m_x^2 \Delta x'^2 + m_y^2 \Delta y'^2)}{2z} \right] \\ &\times \text{DFT}_{m_x, m_y}^{(c)} \left[\left(\psi_\omega(n_x \Delta x, n_y \Delta y; 0) \exp \left[\frac{ik(n_x^2 \Delta x^2 + n_y^2 \Delta y^2)}{2z} \right] \right) \right] \end{aligned}$$

with $n_x, n_y = -N_{x,y}/2, \dots, N_{x,y}/2 - 1$ and $m_x, m_y = -N_{x,y}/2, \dots, N_{x,y}/2 - 1$. Note that with above relations

$$\frac{k}{z} = \frac{2\pi}{N_x \Delta x \Delta x'} = \frac{2\pi}{N_y \Delta y \Delta y'}. \quad (3.81)$$

With the pixel area size $A_p := \Delta x \Delta y$ in plane $z = 0$ and $A'_p := \Delta x' \Delta y'$ in plane $z = \text{const.} > 0$ one can considerably condense the prefactors and obtains

$$\begin{aligned} \psi_\omega(m_x \Delta x', m_y \Delta y'; z) &= -i \sqrt{\frac{A_p}{A'_p}} \exp(ikz) \times \exp \left[\frac{ik(m_x^2 \Delta x'^2 + m_y^2 \Delta y'^2)}{2z} \right] \\ &\times \text{DFT}_{m_x, m_y}^{(c)} \left[\left(\psi_\omega(n_x \Delta x, n_y \Delta y; 0) \exp \left[\frac{ik(n_x^2 \Delta x^2 + n_y^2 \Delta y^2)}{2z} \right] \right) \right] \end{aligned} \quad (3.82)$$

In contrast to Eq. (3.79) here the phase term in the argument of the DFT exhibits steepest gradients for small z . For a given sampling period Δx (or Δy) sufficient sampling is therefore only ensured for large z , therefore Eq. (3.32) is also referred to as the far field Fresnel propagation equation.

Beyond these qualitative considerations on the validity regimes of the Eqs. (3.79) and (3.82), is it possible to give more accurate conditions when to choose which equation? In principle, for the replacement of any Fourier transform by its discrete analogon, the

sampling condition expressed in Eq. (2.117) needs to be fulfilled. As propagation over increasing distances leads to a broadening of the input field distribution, this requires larger and larger fields of view as the propagation distance increases. However, due to an infinite variety of possible input fields, it is difficult to give a general criterion which always ensures adequate sampling.

On the other hand, regarding the Fresnel propagators (Eqs. (3.24/3.79) and (3.32/3.82)) one can give a simple criterion for the involved spherical phase terms to be adequately sampled [50, 94, 149]. For a modestly distorted incident wave field $\psi_\omega(\mathbf{r}_\perp)$ they will actually be the terms which limit the sampling process as they possess the steepest phase gradients. For simplicity, the following considerations are only presented for one coordinate direction (for the other one the reasoning is analogous).

For the near field case consider Eq. (3.79). The local phase gradient with respect to the frequency variable $k_x = m\Delta x$ is given as

$$\frac{\partial\varphi}{\partial k_x} = -\frac{zk_x}{k}. \quad (3.83)$$

It can be interpreted as a ‘frequency’ in Fourier space. (Better than) Nyquist sampling in Fourier space then requires [149]

$$2 \left| \frac{\partial\varphi}{\partial k_x} \right|_{\max} \leq \frac{2\pi}{\Delta k}. \quad (3.84)$$

with $\left| \partial\varphi/\partial k_x \right|_{\max} = N_x \Delta k z / (2k) = \lambda_0 z / (2\Delta x)$, i.e.

$$\frac{\lambda_0 z}{N_x \Delta x^2} \leq 1. \quad (3.85)$$

The reciprocity relation $\Delta x \Delta k = 2\pi / N_x$ has been used several times here. Note that Eq. (3.84) is equivalent to the condition that the largest phase difference between two sampling points may not be larger than π .

For the far field case consider Eq. (3.82). The local phase gradient with respect to the spatial variable $x = n_x \Delta x$ is given as

$$\frac{\partial\varphi}{\partial x} = \frac{kx}{z}. \quad (3.86)$$

(Better than) Nyquist sampling in real space then requires [149]

$$2 \left| \frac{\partial\varphi}{\partial x} \right|_{\max} \leq \frac{2\pi}{\Delta x}. \quad (3.87)$$

with $\left| \partial\varphi/\partial x \right|_{\max} = N_x k \Delta x / (2z) = N_x \pi \Delta x / (\lambda_0 z)$, i.e.

$$\frac{\lambda_0 z}{N_x \Delta x^2} \geq 1 \quad (3.88)$$

which is just the complementary condition to the near field sampling condition (3.85). Note that the leading spherical phase term outside the DFT in Eq. (3.82) is generally not sampled according to the Nyquist criterion, if condition (3.88) is met. However, as this term is outside the discrete Fourier transform and its analytical expression is known, this is generally not a problem as long as no further propagation step and thus at least one discrete Fourier transform is involved.

3.1.7.2 Paraxial propagation into the far field using the Fraunhofer diffraction formula

The numerical implementation of the Fraunhofer diffraction formula (3.35) is analogous to the numerical implementation of far field Fresnel propagation as expressed in Eq. (3.82). The only difference is the neglect of the phase term within the argument of the DFT. The numerical version of Eq. (3.35) thus reads

$$\begin{aligned} \psi_\omega(m_x \Delta x', m_y \Delta y'; z) &= -i \sqrt{\frac{A_p}{A'_p}} \exp(ikz) \times \exp \left[\frac{ik(m_x^2 \Delta x'^2 + m_y^2 \Delta y'^2)}{2z} \right] \\ &\times \text{DFT}_{m_x, m_y}^{(c)} [\psi_\omega(n_x \Delta x, n_y \Delta y; 0)] \end{aligned} \quad (3.89)$$

with $m_x, m_y = -N_{x,y}/2, \dots, N_{x,y}/2 - 1$ and the scaling relations

$$\Delta x' = \frac{\lambda z}{N_x \Delta x}, \quad \Delta y' = \frac{\lambda z}{N_y \Delta y}. \quad (3.90)$$

3.1.7.3 Exact propagation equation

As long as the small-angle approximation is met, Eq. (3.85) is also a good sampling criterion for the numerical implementation of the exact propagation equation (3.20). Its numerical implementation is completely analogous to the numerical near field propagation equation (3.82).

3.1.7.4 Implementation in Matlab

Note on the pixel entries in numerical calculations. It is convenient to do numerical propagation calculations directly with the integrated count rate or signal N_p that has been collected over the area A_p of the pixel within some measurement time T . In other words, numerical propagation is directly performed on fields $\psi'(\mathbf{r}_p)$ with $|\psi'(\mathbf{r}_p)|^2 = N_p$ with integrated photon count N_p as entries. In fact, it can be shown (see Section 3.1.8) by using the discretized versions of the propagation equations that generally only the sum over the number of photons in all pixels is conserved, not the sum over all intensities in an array. This corresponds to the fact that the total photon flux through any plane of propagation needs to be conserved. In the Matlab code representation we will still use the symbol `psi` for the complex field quantity, whose squared modulus, however, does not directly denote intensity but integrated intensity per pixel and a certain measurement time. Note that, as the propagation equations are time-independent, they are equal for the flux in a pixel and the total number of photons in a pixel acquired over some measurement time.

We define the $N_y \times N_x$ matrices

$$\mathbf{K}_{\mathbf{x}N}^{(c)} := \begin{pmatrix} \mathbf{k}_{\mathbf{x}N}^{(c)} \\ \vdots \\ \mathbf{k}_{\mathbf{x}N}^{(c)} \end{pmatrix} \quad (3.91)$$

and

$$\mathbf{K}_{\mathbf{y}N}^{(c)} := \left(\mathbf{k}_{\mathbf{y}N}^{\top(c)} \cdots \mathbf{k}_{\mathbf{y}N}^{\top(c)} \right), \quad (3.92)$$

with 'T' denoting transposition and use the elementwise multiplication '*' of two matrices. We can then write the discretized near field Fresnel propagation formula expressed in Eq. (3.79) in index-free notation, namely

$$\begin{aligned} \psi_\omega(\mathbf{x}_N^{(c)}, \mathbf{y}_N^{(c)}; z) &= \exp(ikz) \\ &\times \text{IDFT}^{(c)} \left[\exp \left[-\frac{iz(\mathbf{K}_{\mathbf{x}_N}^{(c)2} + \mathbf{K}_{\mathbf{y}_N}^{(c)2})}{2k} \right] * \text{DFT}^{(c)} \left[\psi_\omega(\mathbf{x}_N^{(c)}, \mathbf{y}_N^{(c)}; 0) \right] \right]. \end{aligned} \quad (3.93)$$

Note that here $\mathbf{K}_{\mathbf{x}, \mathbf{y}_N}^{(c)2} := \mathbf{K}_{\mathbf{x}, \mathbf{y}_N}^{(c)} * \mathbf{K}_{\mathbf{x}, \mathbf{y}_N}^{(c)}$. In Matlab the definition of the vectors $\mathbf{K}_{\mathbf{x}, \mathbf{y}_N}^{(c)}$ is obtained via the command

$$[K_x, K_y] = \text{meshgrid}(\Delta k_x * (-N_x/2 : N_x/2 - 1), \Delta k_y * (-N_y/2 : N_y/2 - 1))$$

with an analogue definition of matrices X and Y. A possible numerical implementation in Matlab of Eq. (3.79) thus could read

$$\begin{aligned} \text{Psi} &= \exp(1i * k * z) \\ &* (\text{ifft2c}(\exp(-1i * z * (K_x.^2 + K_y.^2)/(2 * k)). * (\text{fft2c}(\text{psi})))) \end{aligned} \quad (3.94)$$

with the user-defined functions

$$\text{fft2c}(\dots) = \text{fftshift}(\text{fft2}(\text{ifftshift}(\dots))) \quad (3.95)$$

$$\text{ifft2c}(\dots) = \text{fftshift}(\text{ifft2}(\text{ifftshift}(\dots))). \quad (3.96)$$

fft2 and ifft2 are the built-in Matlab implementations for the 2D fast Fourier transformation (FFT). Note that the normalization factors $N_{x,y}^{\pm 1/2}$ for the FFT/IFFT cancel out in this propagation equation, so that they are not needed.

For the Matlab implementation of the discrete Fraunhofer propagation equation (3.89) we need the vector

$$[X, Y] = \text{meshgrid}(\Delta X * (-N_x/2 : N_x/2 - 1), \Delta Y * (-N_y/2 : N_y/2 - 1))$$

in the propagated plane. The Matlab implementation of Eq. (3.89) thus reads

$$\begin{aligned} \text{Psi} &= -1i * \exp(1i * k * z) * \exp(1i * k * (X.^2 + Y.^2)/(2 * z)) \\ &* 1/\text{sqrt}(N_x * N_y) * \text{fft2c}(\text{psi}). \end{aligned} \quad (3.97)$$

Note that with respect to Eq. (3.89) here the pixel area has been absorbed into Psi and psi as described above.

3.1.8 Flux conservation in propagation equations

Continuous case. The propagation equations should all be defined such that the energy flow per unit time (or the photon flux) through any plane should be constant for a time-independent field.

Lateral Fourier transformation of the paraxial near field propagation equation (3.24) yields

$$\mathcal{F}_\perp [\psi_\omega(\mathbf{r}_\perp; z)] = \exp(ikz) \exp \left[\frac{-izk_\perp^2}{2k} \right] \mathcal{F}_\perp [\psi_\omega(\mathbf{r}_\perp; 0)]. \quad (3.98)$$

After application of Plancherel's theorem (see Eq. (2.21) for a 1D analogue) on both sides one obtains

$$\int |\psi_\omega(\mathbf{r}_\perp; z)|^2 d\mathbf{r}_\perp = \int |\psi_\omega(\mathbf{r}_\perp; 0)|^2 d\mathbf{r}_\perp. \quad (3.99)$$

The same strategy can be applied to the exact propagation equation (3.20). The paraxial far field propagation equation (3.32) can be written as

$$-\frac{z \exp(-ikz)}{ik} \exp\left[-\frac{ikr_\perp'^2}{2z}\right] \psi_\omega(\mathbf{r}'_\perp; z) = \mathcal{F}_\perp \left[\psi_\omega(\mathbf{r}_\perp; 0) \exp\left[\frac{ikr_\perp^2}{2z}\right] \right]_{\mathbf{k}_\perp = \frac{k\mathbf{r}'_\perp}{z}}. \quad (3.100)$$

The application of Plancherel's theorem to this equation yields

$$\int |\psi_\omega(\mathbf{r}'_\perp; z)|^2 \left|\frac{z}{k}\right|^2 dk_x dk_y = \int |\psi_\omega(\mathbf{r}_\perp; 0)|^2 d\mathbf{r}_\perp. \quad (3.101)$$

$$\int |\psi_\omega(\mathbf{r}'_\perp; z)|^2 d\mathbf{r}'_\perp = \int |\psi_\omega(\mathbf{r}_\perp; 0)|^2 d\mathbf{r}_\perp. \quad (3.102)$$

The same can be applied to the paraxial Fraunhofer propagation equation (3.35). We thus see that the total power that impinges on the infinitely extended plane $z = 0$ stays constant under propagation.

Discrete case. The discrete paraxial near field propagation equation (3.79) can be treated with the same strategy as the continuous analogue. Discrete Fourier transformation of the equation yields

$$\begin{aligned} & \text{DFT}_{m_x, m_y}^{(c)} \left[\psi_\omega(\mathbf{x}_N^{(c)}, \mathbf{y}_N^{(c)}; z) \right] = \\ & \exp(ikz) \left(\exp\left[-\frac{iz(m_x^2 \Delta k_x^2 + m_y^2 \Delta k_y^2)}{2k}\right] \text{DFT}_{m_x, m_y}^{(c)} \left[\psi_\omega(\mathbf{x}_N^{(c)}, \mathbf{y}_N^{(c)}; 0) \right] \right). \end{aligned} \quad (3.103)$$

The discrete Plancherel theorem applied to both discrete Fourier transforms, together with this equation then yields

$$\sum_{n_x, n_y} |\psi_{n_x, n_y}^{(z)}|^2 = \sum_{n_x, n_y} |\psi_{n_x, n_y}^{(0)}|^2 \quad (3.104)$$

with $\psi_{n_x, n_y}^{(z')} := \psi_\omega(n_x \Delta x, n_y \Delta y; z')$ for $z' = z$ and $z' = 0$.

On the other hand, Plancherel's theorem applied to the discrete paraxial Fraunhofer propagation equation (3.89) then yields

$$\sum_{n_x, n_y} A'_p |\psi_{n_x, n_y}^{(z)}|^2 = \sum_{n_x, n_y} A_p |\psi_{n_x, n_y}^{(0)}|^2 \quad (3.105)$$

Due to the change in the pixel size, Eq. (3.104) would be wrong in this case. We thus see that *generally the summed photon flux through all pixels is conserved, not the intensity (photons per area and unit time), summed over all pixels.*

Remarks

Obviously, the need for different numerical propagation equations for different imaging regimes is not very satisfying, even more, if the criterion for selecting the correct one does not take into account the structure of the wave field itself that needs to be propagated. Alternative numerical propagators which can be used for all Fresnel numbers have been suggested, e.g. based on the fractional Fourier transform [94]. An alternative approach is to limit the bandwidth of the spherical phase term for large z in Eq. (3.82) by multiplication with a hat-function [95]. Another problem is the sampling of the exact propagation equation (3.20) for high-numerical aperture beams. Also here, an alternative propagation scheme has been suggested [42].

For the sake of simplicity we have used only the previously presented well-established propagation equations. Fortunately, especially in the hard x-ray regime, the small angle-approximation is usually fulfilled very well. Therefore one can either use the near field Fresnel or exact propagation equation with sampling criterion (3.85) in the near field and the far field Fresnel propagation equation with sampling criterion (3.88) in the far field. Due to the change in sampling period needed for the application of the far field equation, we usually tried to avoid the far field equation while maintaining the validity of the near field criterion (3.85) by embedding the numerical field into a larger field of view, if necessary.

3.2 Propagation of x-ray wave fields in matter

The interaction of magnetic and electric fields with matter is fully described by Maxwell's equations [108], which provide a continuum picture on matter. Here the electrical and magnetic properties of a linear isotropic material are entirely described by two scalar continuous functions of space and time, namely the electrical permittivity $\varepsilon(\mathbf{r}, t)$ and the magnetic permeability $\mu(\mathbf{r}, t)$. In vacuum these quantities reduce to the electric field constant $\varepsilon_0 = 8.854 \cdot 10^{-12} \text{ AsV}^{-1} \text{ m}^{-1}$ and the magnetic field constant $\mu_0 = 4\pi \cdot 10^{-7} \text{ VsA}^{-1} \text{ m}^{-1}$. Most biological materials of interest are non-magnetic on length-scales relevant for this thesis, i.e. larger than tens of nanometers. Therefore $\mu(\mathbf{r}, t) = \mu_0$ can be assumed. In addition, we will restrict ourselves to static materials, i.e. $\varepsilon(\mathbf{r}, t) = \varepsilon(\mathbf{r})$. If we assume in addition that no net-charge or current densities are present in the samples under study the Maxwell equations simplify to [108]

$$\nabla \cdot [\varepsilon(\mathbf{r})\mathbf{E}(\mathbf{r}, t)] = 0, \quad (3.106)$$

$$\nabla \cdot \mathbf{B}(\mathbf{r}, t) = 0, \quad (3.107)$$

$$\nabla \times \mathbf{E}(\mathbf{r}, t) = -\partial_t \mathbf{B}(\mathbf{r}, t), \quad (3.108)$$

$$\nabla \times \mathbf{B}(\mathbf{r}, t) = \mu_0 \varepsilon(\mathbf{r}) \partial_t \mathbf{E}(\mathbf{r}, t). \quad (3.109)$$

With the further assumption that $\varepsilon(\mathbf{r})$ varies slowly on length scales comparable to the wavelength of the wave fields one can derive a pair of wave equations for the magnetic induction and the electric field [108]. One can thus make the transition to a scalar wave equation in the presence of matter with electric permittivity $\varepsilon(\mathbf{r})$, namely [108]

$$(\mu_0 \varepsilon(\mathbf{r}) \partial_t^2 - \nabla^2) \Psi(\mathbf{r}, t) = 0. \quad (3.110)$$

All material properties relevant for diffractive imaging of biological samples (with the exception of magnetic materials) are encoded in $\varepsilon(\mathbf{r})$. With the definition

$$n_\omega(\mathbf{r}) := \sqrt{\frac{\varepsilon(\mathbf{r})}{\varepsilon_0}} \quad (3.111)$$

the wave equation becomes

$$\left(\frac{n_\omega^2(\mathbf{r})}{c^2} \partial_t^2 - \nabla^2 \right) \Psi(\mathbf{r}, t) = 0 \quad (3.112)$$

and the ansatz of a time-dependent plane wave $P_{\omega, \mathbf{u}}(\mathbf{r}, t)$ now leads to the condition

$$|\mathbf{u}|^2 = n_\omega^2(\mathbf{r}) \frac{\omega^2}{c^2} = n_\omega^2(\mathbf{r}) k^2. \quad (3.113)$$

As a consequence, the wavelength $\lambda = 2\pi/|\mathbf{u}| = \lambda_0/n_\omega(\mathbf{r})$ is altered within the medium with respect to vacuum, just as the phase velocity $v = \omega/|\mathbf{u}| = c/n_\omega(\mathbf{r})$.

With the same reasoning as for the matter-free case one can decompose the time-dependent scalar wave field $\Psi(\mathbf{r}, t)$ into monochromatic components $\psi_\omega(\mathbf{r})$, each with the simple time dependence $\exp(-i\omega t)$. Substituting an infinite sum over monochromatic waves into the time-dependent wave equation then yields the scalar **Helmholtz equation in the presence of a medium** with refractive index $n_\omega(\mathbf{r})$ [108]:

$$\boxed{(\nabla^2 + n_\omega^2(\mathbf{r}) k^2) \psi_\omega(\mathbf{r}) = 0.} \quad (3.114)$$

3.2.1 Refractive index

The refractive index for X-rays is very close to unity and is commonly written in the form [4]

$$n_\omega(\mathbf{r}) := 1 - \delta_\omega(\mathbf{r}) + i\beta_\omega(\mathbf{r}) \quad (3.115)$$

with both $\delta_\omega(\mathbf{r})$ and $\beta_\omega(\mathbf{r})$ being real numbers much less than unity in magnitude. We further define¹¹

$$\Delta n_\omega(\mathbf{r}) := \delta_\omega(\mathbf{r}) - i\beta_\omega(\mathbf{r}). \quad (3.116)$$

To first order in $\delta_\omega(\mathbf{r})$ and $\beta_\omega(\mathbf{r})$ we thus obtain [108]

$$n_\omega^2(\mathbf{r}) - 1 \simeq -2\Delta n_\omega(\mathbf{r}). \quad (3.117)$$

As the interaction of the x-ray photons is primarily with the electrons in the atomic shells, the deviation of the refractive index from unity is proportional to the electron density in the material.

¹¹Note that the sign in front of the imaginary part, β_ω , of the index of refraction $n_\omega = 1 - \delta_\omega + i\beta_\omega$ is connected to the fact that we have defined a plane wave of the form $\exp(i(kz - \omega t))$ as traveling into the positive z direction [see also 4, p. 20]. As β_ω accounts for an exponential damping of a wave field in matter, i.e. absorption, this definition also fixes the sign of β_ω in the definition of the refractive index. Alternatively one can define a plane wave as $\exp(-i(kz - \omega t))$ which also travels into positive z -direction. This in turn influences the angular spectrum representation of a forward propagated wave, which leads, for example, to the modeling of forward propagation into the far field by an inverse Fourier transform. Therefore, within our definitions, a sample always leads to a negative phase with respect to vacuum.

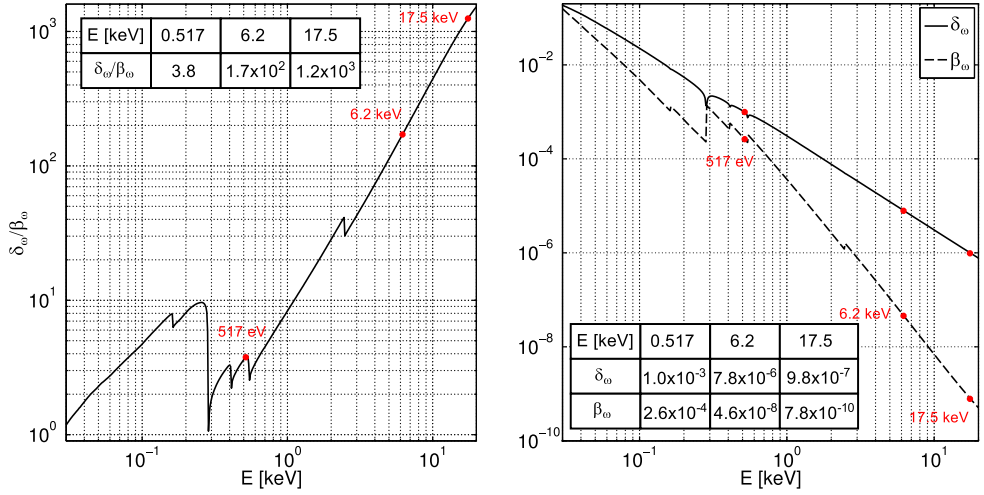


Figure 3.1: (Left) Ratio of the real to the imaginary part of the refractive index for a model biological substance with empirical formula $H_{50}C_{30}N_9O_{10}S_1$ and mass density 1.35 gcm^{-3} [71]. Numerical data was obtained from [67]. Values at energies that were used for experiments within this thesis are indicated on the curve and given in the table. (Right) Absolute values of δ_ω and β_ω , corresponding to the ratio on the left.

The real and imaginary part of the refractive index of a non-magnetic, isotropic material composed of a single type of atoms can be related to the atomic scattering factor as [2]

$$\delta_\omega(\mathbf{r}) = \frac{r_e \lambda_0^2}{2\pi} \rho_a(\mathbf{r}) [Z + f'(\omega)] \quad (3.118)$$

$$\beta_\omega(\mathbf{r}) = \frac{r_e \lambda_0^2}{2\pi} \rho_a(\mathbf{r}) f''(\omega) \quad (3.119)$$

where r_e denotes the classical electron radius, $\rho_a(\mathbf{r})$ the atomic number density and $f(\mathbf{q}) = f^0(\mathbf{q}) + f'(\omega) - i f''(\omega)$ the atomic scattering factor with its energy-dependent dispersion corrections $f'(\omega)$ and $f''(\omega)$ [2].¹² $f(\mathbf{q})$ determines the interaction strength of the photons with the electron shell of an atom. In the limit of forward scattering ($\mathbf{q} \approx \mathbf{0}$), which can safely be assumed in the context of this thesis, $f^0(\mathbf{q} \approx \mathbf{0}) = Z$ corresponds to the number of electrons in a single atom. The dispersion corrections $f'(\omega)$ and $f''(\omega)$ account for the fact that the wave field interacts with bound electrons which thus possess certain resonance energies (binding energies) where the interaction is particularly strong. Close to resonance edges f' and f'' depend on the local environment of the atoms and one usually has to rely on measurements rather than theoretical predictions [2]. Once, either f' or f'' is known, however, the missing quantity can be calculated [2]. For most abundant atoms in biological material (H, C, N, O, P, S) none of these resonance energies lies in between photon energies

¹²Note that with above definitions $f''(\omega) \geq 0$.

of $E = 5$ keV and $E = 20$ keV [67], and within this range $f(0) + f'(\omega) \approx Z$ holds to a very good approximation¹³ for these materials. We refer to the range of photon energies above 5 keV as the **hard x-ray range**.

For a multi-element biological material contained in a scattering volume V , with N_j atoms of element j exposed to photons in the energy range given above, $\delta_\omega(\mathbf{r})$ is thus proportional to the electron density in the material to a very good approximation [21]:

$$\delta_\omega(\mathbf{r}) = \frac{r_e \lambda_0^2}{2\pi} \frac{\sum_j N_j (Z_j + f'_j)}{V} \quad (3.120)$$

$$= \frac{r_e \lambda_0^2}{2\pi} \left[\rho_e(\mathbf{r}) + \frac{\sum_j N_j f'_j}{V} \right] \quad (3.121)$$

$$= \frac{r_e \lambda_0^2}{2\pi} \left[\rho_e(\mathbf{r}) + \rho_a(\mathbf{r}) \sum_j p_j f'_j \right] \quad (3.122)$$

$$\approx \frac{r_e \lambda_0^2}{2\pi} \rho_e(\mathbf{r}). \quad (3.123)$$

Here p_j denotes the molar fraction of element j . In terms of the mass density $\rho_m(\mathbf{r})$, one finds

$$\delta(\mathbf{r}) = \frac{r_e \lambda_0^2}{2\pi u} \rho_m(\mathbf{r}) \sum_j \frac{Z_j + f'_j}{A_j} q_j \quad (3.124)$$

with mass fraction q_j and relative atomic weight A_j of element j , in units of the atomic mass unit $1 u \approx 1.661 \cdot 10^{-27}$ kg. Alternatively, this can be written as

$$\delta(\mathbf{r}) = \frac{r_e \lambda_0^2}{2\pi u} \rho_m(\mathbf{r}) \frac{\sum_j p_j (Z_j + f'_j)}{\sum_j p_j A_j} \quad (3.125)$$

with molar fractions p_j . Note that, as the mass fraction of hydrogen in biological matter is very low and as $Z_j/A_j \approx 1/2$ for other low- Z elements, one can in the energy range given above also approximate [21]

$$\delta(\mathbf{r}) \approx \frac{r_e \lambda_0^2}{4\pi u} \rho_m(\mathbf{r}). \quad (3.126)$$

$$= 1.3 \times 10^{-6} \lambda_0^2 [\text{\AA}^2] \rho_m [\text{g/cm}^3]. \quad (3.127)$$

However, this approximation is not as good as for the electron density, as expressed in Eq. (3.123). For the imaginary part $\beta_\omega(\mathbf{r})$ there is no such simple relation to the material's electron (mass) density. In general, the λ_0^2 -dependence of δ , together with the linear dependence of the phase on the wavenumber k (see below), induces a decay of scattering effects with increasing photon energy.

It will be seen below (see Eq. (3.134)) that $\delta_\omega(\mathbf{r})$ is relevant for a change in the phase of the object transmission function, while $\beta_\omega(\mathbf{r})$ accounts for absorption. To estimate scattering effects at different photon energies as well as phase against absorption effects, it

¹³The maximum relative deviation in this range is below 3% [67].

E [keV]	$ O = \exp(-k\beta_\omega t)$	$-\varphi(O) = k\delta_\omega t$ [rad]
0.517	0.2524	5.19
6.2	0.9971	0.49
17.5	0.9999	0.17

Table 3.1: Amplitude decrement and phase of the object transmission function for a generic biological material ($\text{H}_{50}\text{C}_{30}\text{N}_9\text{O}_{10}\text{S}_1$, $\rho_m = 1.35 \text{ gcm}^{-3}$, $t = 2 \text{ }\mu\text{m}$, as used for Fig. 3.1).

is useful to plot the ratio $\delta_\omega/\beta_\omega$ with respect to the photon energy $E_{\text{ph}} = \hbar\omega$ for a generic biological material ($\text{H}_{50}\text{C}_{30}\text{N}_9\text{O}_{10}\text{S}_1$ and mass density 1.35 gcm^{-3} , as used in [71]). Such a plot is depicted in Fig. 3.1 (left). Evidently, phase effects are always stronger than absorption effects. However, for soft x-ray wavelengths around 517 eV, the absorption due to $t = 2 \text{ }\mu\text{m}$ generic biological material already induces a decrease in intensity by a factor $\exp(-2k\beta_\omega t) \approx 0.06$ (see also Table 3.1). Consequently, a few microns of biological material are enough at $E = 517 \text{ eV}$ to almost completely annihilate an incoming x-ray beam, which makes a quantitative phase measurement very difficult, if not impossible. On the other hand, at hard x-ray wavelengths ($E_{\text{ph}} \gtrsim 5 \text{ keV}$), the (intensity) absorption for the same material and thickness is less than 1%, making them almost pure **phase objects**.

3.2.2 The projection approximation

Let us consider the general situation of a medium with refractive index $n_\omega(\mathbf{r})$, localized in an infinite slab between the **entrance plane** $z = 0$ and the **exit plane** $z = \Delta z$. Given the time-independent monochromatic wave field $\psi_\omega(\mathbf{r}_\perp; 0)$, the **entrance field**, we would like to know the **exit field** $\psi_\omega(\mathbf{r}_\perp; \Delta z)$. As a further assumption we demand that the entrance field can be described by the small-angle approximation, i.e. has only non-negligible lateral Fourier components $\tilde{\psi}_\omega(\mathbf{k}_\perp; 0)$ for $k_\perp^2 \ll k^2$ (on length scales k considerably larger than the wavelength).

Note that, according to the angular spectrum decomposition, a paraxial wave field with a mean wave vector $\langle \mathbf{k} \rangle$ parallel to \mathbf{e}_z is characterized in free space by a rapidly oscillating z -dependence on the order of

$$\exp\left(i\sqrt{k^2 - k_\perp^2} z\right) \approx \exp(ikz) \exp\left(-i\frac{k_\perp^2}{2k} z\right). \quad (3.128)$$

Apart from the rapidly oscillating $\exp(ikz)$ term, however, the paraxial beam varies much more slowly in z -direction ($\propto k_\perp/(2k) \cdot k_\perp$) than in perpendicular direction ($\propto k_\perp$).

If we thus assume that the small angle-approximation *remains* valid within the medium, we can factor out the rapidly oscillating z -dependence and make the ansatz [108]

$$\psi_\omega(\mathbf{r}) = \Lambda_\omega(\mathbf{r}) \exp(ikz) \quad (3.129)$$

for $z > 0$ with $k = \omega/c$ denoting the vacuum wave number of a plane wave traveling in direction \mathbf{e}_z with wave vector $\mathbf{k} = k\mathbf{e}_z$. $\Lambda_\omega(\mathbf{r})$ will then be a function that varies much more slowly in z -direction than in lateral direction.

Inserting the ansatz Eq. (3.129) into Eq. (3.114) yields a new differential equation for the envelope field $\Lambda_\omega(\mathbf{r})$ [108]:

$$[\nabla_\perp^2 + \partial_z^2 + 2ik\partial_z + k^2(n_\omega^2(\mathbf{r}) - 1)]\Lambda_\omega(\mathbf{r}) = 0 \quad (3.130)$$

with $\nabla_\perp^2 := \partial_x^2 + \partial_y^2$. With the approximation (3.117), which is well-justified for x rays, we can further write

$$\left[\frac{1}{k^2}\nabla_\perp^2 + \frac{1}{k^2}\partial_z^2 + \frac{2i}{k}\partial_z \right]\Lambda_\omega(\mathbf{r}) = 2\Delta n_\omega(\mathbf{r})\Lambda_\omega(\mathbf{r}) \quad (3.131)$$

It is now assumed that the incident wave field $\Lambda_\omega(\mathbf{r})$ is paraxial and that the disturbance of $\Lambda_\omega(\mathbf{r})$ by the object is sufficiently weak, so that the exit field at each lateral position is “entirely determined by the phase and amplitude shifts that are accumulated along streamlines of the unscattered beam” [108], i.e. rays parallel to the optical axis. The second derivatives in Eq. (3.131) may then be neglected [108], and one obtains the relatively simple boundary value problem

$$\partial_z\Lambda_\omega(\mathbf{r}) = -ik\Delta n_\omega(\mathbf{r})\Lambda_\omega(\mathbf{r}). \quad (3.132)$$

With a known entrance field $\Lambda_\omega(\mathbf{r}_\perp, 0)$ a solution in plane $z = \Delta z$ is given as [108]

$$\Lambda_\omega(\mathbf{r}_\perp, \Delta z) = \Lambda_\omega(\mathbf{r}_\perp, 0) \exp\left[-ik \int_0^{\Delta z} \Delta n_\omega(\mathbf{r}) dz\right]. \quad (3.133)$$

Back-substitution of the ansatz Eq. (3.129) then yields

$$\boxed{\psi_\omega(\mathbf{r}_\perp; \Delta z) \simeq \exp(ik\Delta z)\psi_\omega(\mathbf{r}_\perp, 0) \exp\left[-ik \int_0^{\Delta z} \Delta n_\omega(\mathbf{r}) dz\right]}. \quad (3.134)$$

The integration corresponds to a geometrical projection of the material properties along the direction that the undiffracted beam would take, if no material was present. We therefore call Eq. (3.134) the **projection approximation** [108]. It corresponds to the limit of geometrical optics where the propagation of light can be described along straight rays and where diffraction effects can be neglected. Note that, if no material is present, Eq. (3.134) reduces to

$$\psi_\omega(\mathbf{r}_\perp; \Delta z) \simeq \exp(ik\Delta z)\psi_\omega(\mathbf{r}_\perp, 0). \quad (3.135)$$

Thus, as a *necessary condition for the validity of the projection approximation*, the incident wave field stays unchanged upon propagation through the sample, apart from a global complex factor.

As a condition¹⁴ for the validity of the projection approximation one finds [e.g. 15, 21]

$$\boxed{\Delta r_\perp > \sqrt{\Delta z \lambda_0}} \quad (3.136)$$

or

$$\boxed{\Delta z < \frac{\Delta r_\perp^2}{\lambda_0}}. \quad (3.137)$$

¹⁴Note that these conditions should be interpreted as reference points, but not as strict laws. Therefore, conditions given in the literature [e.g. 15, 21] vary within a small range of prefactors.

Here Δr_{\perp} denotes the smallest non-negligible lateral length scale of the object (the resolution) and Δz the extension of the object along the optical axis, i.e. the propagation direction.

Conditions (3.136) and (3.137) can be interpreted as follows. Consider propagation of a wave field within a sample as described above. Condition (3.136) implies that diffraction effects can be neglected for lateral length scales larger than $\sqrt{\Delta z \lambda_0}$: The projection of optical properties along rays parallel to the optical axis, as described by Eq. (3.134), allows no interaction of neighboring ray paths. As a consequence no diffraction within the distance Δz occurs when the projection approximation is valid.

Equivalently, if Eq. (3.137) is obeyed, diffraction effects can be neglected for propagation distances smaller than Δz . Within this propagation distance the propagated field appears 'in focus'. Therefore, the quantity $\Delta r_{\perp}^2 / \lambda$ can also be defined as a **depth of focus** for paraxial propagation through a sample.

In the following, we would like to briefly discuss, how condition (3.136) (or, equivalently, (3.137)) may be related to the approximation of Eq. (3.131) by Eq. (3.132) which leads to the projection approximation. The Fourier transform of Eq. (3.131) is given as

$$\left[\frac{k_{\perp}^2}{k^2} + \frac{k_z^2}{k^2} + 2 \frac{k_z}{k} \right] \tilde{\Lambda}_{\omega}(\mathbf{k}) = -\frac{2}{(2\pi)^{3/2}} [\tilde{\Delta n}_{\omega} \otimes \tilde{\Lambda}_{\omega}](\mathbf{k}). \quad (3.138)$$

Due to the paraxiality of the entrance field $\tilde{\Lambda}_{\omega}(\mathbf{k})$, is non-negligible only, if $k_{\perp}^2 \ll k^2$. As $|\Delta n_{\omega}| \ll 1$, the influence of the sample on the wave field is small and the paraxiality is conserved within the sample. Due to the chosen ansatz, $\Lambda_{\omega}(\mathbf{r})$ varies much more slowly along the optical axis compared to the lateral direction, so that $\tilde{\Lambda}_{\omega}(\mathbf{k})$ is non-negligible only for $k_z < k_{\perp} \Rightarrow k_z^2 \ll k_{\perp}^2$. The term proportional to k_z^2 can therefore be neglected as a result of paraxiality [108] and the weak effect of the sample. To neglect the term proportional to k_{\perp}^2 it is necessary to demand

$$\frac{k_{\perp}^2}{k^2} < 2 \frac{k_z}{k}. \quad (3.139)$$

The largest length scale of the problem in longitudinal direction is the propagation distance Δz , corresponding to the smallest non-negligible k_z of $\Delta n_{\omega}(\mathbf{r})$ and $\Lambda_{\omega}(\mathbf{r})$. On the other hand, the largest non-negligible k_{\perp} corresponds to the smallest non-negligible lateral length, the resolution Δr_{\perp} . In real space one thus obtains the equivalent demands Eq. (3.136) and (3.137).

It is convenient to define the **illumination or probe function**

$$P(x, y) := \psi_{\omega}(x, y; 0) \quad (3.140)$$

as the wave incident on the specimen at the entrance plane $z = 0$, and the **object transmission function** at the exit plane $z = \Delta z$ as

$$O(x, y) := \exp \left[-ik \int_0^{\Delta z} \Delta n_{\omega}(\mathbf{r}) dz \right]. \quad (3.141)$$

The exit wave in plane $z = \Delta z$ can then be written in the projection approximation as

$$\psi_{\omega}(x, y; 0) \simeq \exp(ik\Delta z) P(x, y) O(x, y). \quad (3.142)$$

Note that O and P have been defined here in different planes, in accordance with [119]. As shown above, the illumination in plane $z = \Delta z$, however, is equal to that in $z = \Delta z$, apart from a global phase factor.

For notational convenience we define

$$\bar{\delta}(x, y) := \int_0^{\Delta z} \delta_\omega(\mathbf{r}) dz \quad (3.143)$$

$$\bar{\beta}(x, y) := \int_0^{\Delta z} \beta_\omega(\mathbf{r}) dz \quad (3.144)$$

$$\overline{\Delta n}(x, y) := \bar{\delta}(x, y) - i\bar{\beta}(x, y), \quad (3.145)$$

so that the object transmission function reads

$$O(x, y) = \exp(-k\bar{\beta}(x, y)) \exp(-ik\bar{\delta}(x, y)). \quad (3.146)$$

We have also dropped here the index ω . The amplitude of the object transmission function is thus related to the projected imaginary part of the refractive index as

$$a(x, y) = |O(x, y)| = \exp(-k\bar{\beta}(x, y)) \quad (3.147)$$

with the phase given as

$$\varphi(O(x, y)) = -k\bar{\delta}(x, y). \quad (3.148)$$

If thus the complex exit wave behind a sample can be obtained in a measurement and if the projection approximation is valid, one can derive the 2D distribution of the real and imaginary part of the object's index of refraction, projected along the propagation direction, via

$$\bar{\beta}(x, y) = -\frac{\lambda_0}{2\pi} \ln(|O(x, y)|) \quad (3.149)$$

$$\bar{\delta}(x, y) = -\frac{\lambda_0}{2\pi} \varphi(O(x, y)). \quad (3.150)$$

For sufficiently weak and/or thin objects $\varphi(O(x, y)) \in [-\pi, \pi]$, so that

$$\varphi(O(x, y)) = \arg[O(x, y)].$$

Otherwise, phase unwrapping methods have to be used. Note that for an experimentally obtained object function errors in retrieving $\bar{\beta}(x, y)$ are amplified by the logarithmic dependence in Eq. (3.149). Therefore, for $\varphi(O(x, y)) \in [-\pi, \pi]$, the phase, only linearly dependent on $\bar{\delta}(x, y)$, can be obtained from $O(x, y)$ with much smaller experimental error.

If the specimen becomes too thick, the resolution too high, or the wavelength too large, conditions (3.136) and (3.137) are not obeyed any more and the projection approximation becomes invalid. In other words, diffraction effects will distort the projection of the sample transmission function, it gets 'out of focus'. To obtain the wave field at distance Δz within the sample, once the incident field at plane $z = 0$ is known, one has to use other methods of finding a solution to the inhomogeneous Helmholtz equation (3.114). One possibility

are so-called multislice methods [see e.g. 138], in which the propagation is divided into elementary propagations within small intervals along the distance Δz . Another possibility is to solve Eq. (3.114) by a finite difference scheme [see e.g. 47].

Note that the projection approximation is a special case of the so-called **product approximation** [e.g. 141]. This states that the product of two independently propagated wave fields (e.g. an illumination function and an object function) equals the propagated product of the two wave fields over a certain distance along the optical axis.

A derivation for such a condition has been given in [141]. There it is studied what limits the assumption that an object transmission function $T(\mathbf{r})$ alone can obey the inhomogeneous wave equation within the specimen, once $T(\mathbf{r})\Psi_0(\mathbf{r})$ is a solution to the inhomogeneous wave equation with a function $\Psi_0(\mathbf{r})$ that is a solution to the free-space wave equation. Defining $P(x, y) := \Psi_0(x, y, \Delta z)$ and $O(x, y) := T(x, y, \Delta z)$ the exit wave is then given as $\psi(x, y) = P(x, y)O(x, y)$. One obtains the condition

$$\Delta z < \frac{\Delta r_{\perp} a}{\lambda_0}, \quad (3.151)$$

where Δr_{\perp} is the lateral resolution of the experiment and a is the lateral extent of the illumination in the sample plane. The experiment presented in [141] uses the focus of a Fresnel zone plate as the illumination wave field on the sample. Such an illumination wave field can be well-approximated by an essentially featureless Gaussian beam with only one parameter a describing the lateral extent of that beam. If instead the Fresnel propagated exit field from a circular mask is used for illumination, there are smaller non-negligible lateral length scales present in the sample than its mere linear extent. Condition (3.151) might then have to be restricted by letting a denote the smallest lateral length scale in the illumination.

3.2.3 Simulation of an object transmission function

For a homogeneous object with mean refractive index $n = 1 - \delta_{\omega} + i\beta_{\omega}$ the object transmission function can be written as

$$O(x, y) = \exp(-k\beta_{\omega}\Delta z(x, y)) \exp(-ik\delta_{\omega}\Delta z(x, y)) \quad (3.152)$$

with the lateral thickness profile function $\Delta z(x, y)$. If the maximum thickness is denoted as Δz_{\max} , then $O(x, y)$ can be written as

$$O(x, y) = \exp(-\alpha_{\max}T(x, y)) \exp(-i\varphi_{\max}T(x, y)) \quad (3.153)$$

with the relative height profile $T(x, y) = \Delta z(x, y)/\Delta z_{\max}$ varying between 0 and 1 and the constants $\alpha_{\max} = k\beta_{\omega}\Delta z_{\max}$ and $\varphi_{\max} = k\delta_{\omega}\Delta z_{\max}$. φ_{\max} is the maximum phase change due to the sample, whereas $\exp(-\alpha_{\max})$ is the minimum transmission.

To simulate the diffraction signal from complex objects such as cells within this thesis, a gray level phantom image with values between 0 and 1 was used as a model for $T(x, y)$ with the constants φ_{\max} and α_{\max} generated from tabulated values [67]. Usually, a thickness of several microns was assumed. Note that for cells at photon energies above ca. 5 keV the absorption is very small (see Tb. 3.1), so that one can approximate the transmissive factor

as $1 - \alpha_{\max} T(x, y)$, which then also scales linearly with T , just as the phase. Note that in the case of hard x-rays, where the absorptive part can often be neglected, $T(x, y)$ can also be interpreted as a relative profile of the optical thickness $|k\overline{\Delta n_\omega}(x, y)| \approx |k\overline{\delta_\omega}(x, y)|$ of a generally non-homogeneous biological material.

3.2.4 The scattering picture and the Born approximation

In this section the formulation of matter-wave interaction in the language of scattering shall be outlined. This leads to the (first order) Born approximation of scattering, an important concept in coherent diffraction microscopy [19].

Using the formalism of Green's functions one can derive [108] the following integral equation for a monochromatic solution $\psi_\omega(\mathbf{r})$ to the Helmholtz equation in matter, Eq. (3.114):

$$\psi_\omega(\mathbf{r}) = \psi_\omega^{(0)}(\mathbf{r}) + \frac{k^2}{4\pi} \int_{\mathcal{D}} d^3\mathbf{r}' (n_\omega^2(\mathbf{r}') - 1) \psi_\omega(\mathbf{r}') S_{\omega, \mathbf{r}'}(\mathbf{r}), \quad (3.154)$$

where $\psi_\omega^{(0)}(\mathbf{r})$ is a solution to the free-space Helmholtz equation (3.11), with $S_{\omega, \mathbf{r}'}(\mathbf{r})$ denoting a spherical wave as defined in Eq. (3.13). For a refractive index distribution $n_\omega(\mathbf{r})$ with bounded support, i.e. a medium contained within a finite domain \mathcal{D} , the physical interpretation of this equation is as follows: The total field $\psi_\omega(\mathbf{r})$ at an observation point \mathbf{r} is given as the sum of the field $\psi_\omega^{(0)}(\mathbf{r})$, which would have been present without the material, and an infinite sum over spherical waves emanating from all points \mathbf{r}' within the material, each with an amplitude equal to the total field $\psi_\omega(\mathbf{r}')$ at \mathbf{r}' , times the local scattering strength $n_\omega^2(\mathbf{r}') - 1$ of the medium. In this picture all points within the material are centers, from which **scattered** spherical fields emanate within an amplitude proportional to the local field amplitude and scattering power. $\psi_\omega^{(0)}(\mathbf{r})$ is then called the **unscattered** field, while the integral term represents the scattered field. **Elastic** scattering is assumed here, i.e. the frequency ω of the scattered wave field is unchanged upon scattering. Unfortunately, Eq. (3.154) is only an integral equation for the total field $\psi_\omega(\mathbf{r})$ as this appears also as part of the amplitude of the scattered field at each scattering center \mathbf{r}' .

Under the assumption that the magnitude of scattering term is very small compared to the unscattered field, which can be the case, if the scattering volume \mathcal{D} is small and we are working in the hard x-ray regime, where $|n_\omega^2(\mathbf{r}') - 1| \lesssim 10^{-6}$, one can replace the total wave field ψ_ω within the integral by the unscattered field $\psi_\omega^{(0)}$. In the scattering picture this amounts to considering just single-scattering and the approximative solution can then be re-inserted into the integral to account for double scattering etc. This eventually leads to an infinite sum, the so-called **Born series**, and the truncation after the first series element is then referred to as the first-order **Born approximation**:

$$\psi_\omega(\mathbf{r}) \approx \psi_\omega^{(0)}(\mathbf{r}) + \frac{k^2}{4\pi} \int_{\mathcal{D}} d^3\mathbf{r}' (n_\omega^2(\mathbf{r}') - 1) \psi_\omega^{(0)}(\mathbf{r}') S_{\omega, \mathbf{r}'}(\mathbf{r}). \quad (3.155)$$

The approximation of single-scattering is often also named **kinematical scattering**, while the consideration of higher-order terms of the Born series is referred to as **dynamical scattering**.

As the Born approximation neglects multiple scattering effects, it is clear that its validity depends on the density of scatterers, expressed in $\Delta n_\omega(\mathbf{r})$, as well as the sample volume. There appears to be no unique criterion for the validity of the Born approximation in the literature. Bearing in mind the connection of the projection and Born approximation (see below), one could give a criterion, for a sample with average refractive index $\langle \Delta n_\omega \rangle$ and thickness Δz , based on the approximation of the exponential in the object transmission function. If we approximate the exponential $\exp(i\varphi) \approx 1 - i\varphi$ for $|\varphi| < 0.1$ we obtain with $\varphi = k\Delta z \langle \Delta n_\omega \rangle$ the criterion

$$\Delta z |\langle \Delta n_\omega \rangle| < 0.02\lambda_0. \quad (3.156)$$

Other criteria such as [138]

$$\Delta z |\langle \Delta n_\omega \rangle| < 0.10\lambda_0 \quad (3.157)$$

and [19]

$$\Delta z |\langle \Delta n_\omega \rangle| < 1.3\lambda_0 \quad (3.158)$$

can be found in the literature on diffraction microscopy. Within this thesis we will solely use the projection approximation to derive optical properties of the studied materials.

3.2.4.1 Far-field diffraction and the Born approximation

Consider the case of a small scatterer contained within a finite domain \mathcal{D} which is located between two planes $z = 0$ and $z = \Delta z > 0$ with Δz being the smallest distance to contain the whole domain \mathcal{D} and the origin of coordinates placed close to the scatterer, so that for an observation point \mathbf{r} far away from the scatterer $|\mathbf{r}'| \ll |\mathbf{r}|$ for all $\mathbf{r}' \in \mathcal{D}$. The spherical waves emanating from any scattering center \mathbf{r}' can then be approximated as [108]

$$S_{\omega, \mathbf{r}'}(\mathbf{r}) = \frac{\exp(-ik|\mathbf{r} - \mathbf{r}'|)}{|\mathbf{r} - \mathbf{r}'|} \simeq \frac{\exp(ikr)}{r} \exp(-ik\hat{\mathbf{r}} \cdot \mathbf{r}') \quad (3.159)$$

with $r = |\mathbf{r}|$ and $\hat{\mathbf{r}} = \mathbf{r}/r$. The far field approximation thus amounts to a product of a spherical wave emanating from the origin and an outgoing plane wave

$$\exp[-\mathbf{k} \cdot \mathbf{r}'] \quad (3.160)$$

propagating into the direction of the observer with $\mathbf{k} = k\hat{\mathbf{r}}$. After insertion of this equation into the first Born approximation (3.155) and without loss of generality assuming a planar unscattered (incident) wave field $\exp(ikz)$ traveling in direction \mathbf{e}_z , one obtains [108]

$$\psi_\omega(\mathbf{r}) \simeq \exp(ikz) - \frac{k^2}{2\pi} \frac{\exp(ikr)}{r} \int_{\mathcal{D}} d^3\mathbf{r}' \Delta n_\omega(\mathbf{r}') \exp(-i\mathbf{q} \cdot \mathbf{r}') \quad (3.161)$$

with

$$\mathbf{q} =: \mathbf{k} - \mathbf{k}_i = k(\hat{\mathbf{r}} - \mathbf{e}_z). \quad (3.162)$$

Note that Eq. (3.162) implies that all possible **scattering vectors** \mathbf{q} are limited to a two-dimensional surface of spherical shape, the so-called **Ewald sphere** with radius k and, both, the outgoing wave vector \mathbf{k} as well as the incident wave vector $k\mathbf{e}_z$ pointing out from the center of the sphere. The first Born approximation expressed in Eq. (3.161) thus has the following very important interpretation:

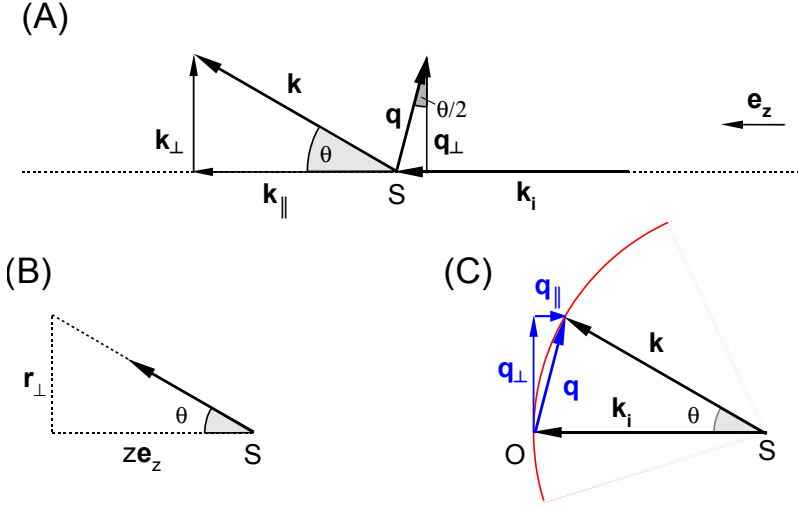


Figure 3.2: (A) Geometry of an elastic scattering experiment. Consider an incident plane wave with wave vector \mathbf{k}_i and a scattered wave with wave vector \mathbf{k} . The diameter of the sample placed close to the point S is very small compared to the distance to the observation point. The scattering vector $\mathbf{q} := \mathbf{k} - \mathbf{k}_i$ then fully describes the scattering experiment. Note that the scattering plane defined by the scattering triangle $(\mathbf{k}_i, \mathbf{q}, \mathbf{k})$ can make any angle with respect to the y - z - or x - z -plane. (B) If an area detector is placed at a distance z from the sample with z being much larger than the sample dimensions, $z\mathbf{e}_z$ and the detector coordinate vector $\mathbf{r}_\perp = (x, y)$ define a rectangular triangle mathematically similar to the one defined by \mathbf{k}_\parallel and \mathbf{k}_\perp . (C) In the Born approximation the three-dimensional Fourier space coordinate \mathbf{q} (i.e. the scattering vector) of the scattered wave in the far field is restricted to points on the Ewald sphere (red) in Fourier space. In this picture, the point, where \mathbf{k}_i pierces the Ewald sphere, is the origin of Fourier space.

In the weak scattering limit (Born approximation) the scattered wave in the far field of a small scattering volume is given as the three-dimensional Fourier transform of the three-dimensional refractive index distribution Δn_ω inside the scatterer. Notably, the scattered wave is limited in three-dimensional Fourier space to a 2-dimensional subspace, the surface of the Ewald sphere.

As only elastic scattering is considered here, the z -component of the outgoing wave vector obeys $k_z = \sqrt{k^2 - k_\perp^2}$ and we can write the scattering vector as

$$\mathbf{q} = \left(\mathbf{q}_\perp, \sqrt{k^2 - q_\perp^2} - k \right). \quad (3.163)$$

In particular note that $\mathbf{q}_\perp = \mathbf{k}_\perp$. The scattering geometry (see Fig. 3.2) allows us to relate the scattering vector coordinates (q_x, q_y, q_z) to the coordinates (x, y, z) on a plane

perpendicular to the optical axis at distance z from the scatterer [19]:

$$q_x = k \cdot \frac{x}{\sqrt{r_{\perp}^2 + z^2}} \quad (3.164)$$

$$q_y = k \cdot \frac{y}{\sqrt{r_{\perp}^2 + z^2}} \quad (3.165)$$

$$q_z = k \cdot \left(\frac{z}{\sqrt{r_{\perp}^2 + z^2}} - 1 \right) \quad (3.166)$$

with $r_{\perp} = \sqrt{x^2 + y^2}$. This is the typical geometry as encountered when using an area detector at distance z . As a consequence, *all* \mathbf{q} -coordinates are coupled with *all* \mathbf{r} -coordinates in the general case. Two other useful relations that can be derived from the scattering geometry are

$$|\mathbf{q}_{\perp}| = q_{\perp} = |\mathbf{k}_{\perp}| = k_{\perp} = k \sin \theta \quad (3.167)$$

and

$$|\mathbf{q}| = q = 2k \sin(\theta/2). \quad (3.168)$$

In the small-angle approximation the coordinates of the momentum transfer vector simplify to

$$q_x \simeq k \cdot \frac{x}{z} \quad (3.169)$$

$$q_y \simeq k \cdot \frac{y}{z} \quad (3.170)$$

$$q_z \simeq 0. \quad (3.171)$$

By changing the Ewald sphere, e.g. by rotating the sample or changing the wavelength of the incident radiation, one can in principle probe the full Fourier space with a scattering experiment. The scattering geometry and the Ewald sphere are illustrated in Fig. 3.2.

3.2.5 Remarks on the projection and Born approximation

Within the projection approximation, the exit wave behind a sample of thickness Δz in the exit plane $z = 0$ is given according to Eq. (3.134) as

$$\psi_{\omega}(\mathbf{r}_{\perp}; 0) = P(x, y)O(x, y) \quad (3.172)$$

with the illumination (probe) function P and object transmission function O . For reasons of simplicity, we have dropped the global phase factor $\exp(ik\Delta z)$ here.

This exit wave field can be propagated to any plane downstream ($z > \Delta z$) by the angular spectrum representation Eq. (3.18), yielding

$$\psi_{\omega}(\mathbf{r}_{\perp}; z) = \int \mathcal{F}_{\perp} [\psi_{\omega}(\mathbf{r}_{\perp}; 0)] \exp\left(iz\sqrt{k^2 - k_{\perp}^2}\right) \exp[i(\mathbf{k}_{\perp} \cdot \mathbf{r}_{\perp})] d\mathbf{k}_{\perp}. \quad (3.173)$$

If we neglect evanescent waves (which only travel for a few wavelengths due to their exponential damping) as well as back-scattering, the diffracted field is given as a continuous sum over plane wave components with their wave vectors $(\mathbf{k}_\perp, \sqrt{k^2 - k_\perp^2})$ pointing away from the origin onto a two-dimensional surface. This is again the Ewald sphere, encountered here in the context of free-space diffraction [see e.g. 138].

Under given approximations we can replace the exact propagation equation (3.173) by one of the approximation Eqs. (3.24), (3.32) and (3.35) discussed above and obtain the general propagation equation

$$\psi_\omega(\mathbf{r}'_\perp; z) = D_z [\psi_\omega(\mathbf{r}_\perp; 0)], \quad (3.174)$$

where D_z embodies the used free-space propagation equation. \mathbf{r}'_\perp denotes a possible change in lateral coordinates between the initial and final plane of the propagation process. If the diffracted wave field $\psi_\omega(\mathbf{r}'_\perp; z)$ was known, the exit wave field $\psi_\omega(\mathbf{r}_\perp; 0) = P(x, y)O(x, y)$ could be obtained via simple inversion of the above equation,

$$P(x, y)O(x, y) = D_z^{-1} [\psi_\omega(\mathbf{r}'_\perp; z)]. \quad (3.175)$$

If, in addition, the complex illumination $P(x, y)$ is known, one can derive the projected index of refraction $\Delta n_\omega(x, y)$ from the knowledge of the object transmission function via Eqs. (3.149) and (3.150). A three-dimensional reconstruction of $\Delta n_\omega(\mathbf{r})$ then becomes possible by obtaining many projections $\Delta n_\omega(x, y, \varphi)$, each obtained for a certain rotation angle φ with respect to an axis perpendicular to the propagation direction. The resulting set of projections can then be reconstructed into a three-dimensional refractive index distribution $\Delta n_\omega(x, y, z)$ with mathematical tools of computerized tomography [see e.g. 68].

We would now like to establish a connection between the picture of an exit wave that undergoes free space diffraction as described above and the scattering picture of the Born approximation. The Born approximation expressed in Eq. (3.155) delivers, apart from constant factors, a relation between the scattered field and the three-dimensional refractive index distribution $\Delta n_\omega(\mathbf{r})$ as a simple three-dimensional Fourier transform. However, also here the scattered field is located in Fourier space on a two-dimensional plane (the Ewald sphere). With different orientations of the sample in the beam, one can sweep a certain subspace of the total Fourier space and obtain enough information to reconstruct $\Delta n_\omega(\mathbf{r})$. This process is then named diffraction tomography [see e.g. 19] and is conceptually different from a tomography by projections which was mentioned above.

Let us now consider the limit of the Born approximation within the small-angle approximation. In this case one may approximate [108]

$$\exp(ikr)/r \simeq \exp(ikz) \exp(ikr_\perp^2/2z)/z, \quad (3.176)$$

so that Eq. (3.161) can then be written as¹⁵

$$\begin{aligned} \psi_\omega(\mathbf{r}'_\perp; z) &\simeq \exp(ikz) - \frac{ik \exp(ikz)}{2\pi z} \exp\left[\frac{ikr'^2_\perp}{2z}\right] \\ &\times \int_{\mathcal{D}} d^2\mathbf{r}_\perp \left[-ik \int_0^{\Delta z} d\bar{z} \Delta n_\omega(\mathbf{r}_\perp, \bar{z}) \exp(-iq_z \bar{z}) \right] \exp(-i\mathbf{k}_\perp \cdot \mathbf{r}_\perp). \end{aligned} \quad (3.177)$$

Within the paraxial approximation one may approximate

$$q_z = \sqrt{k^2 - q_\perp^2} - k \simeq -\frac{k_\perp^2}{2k}. \quad (3.178)$$

In the direction of the optical axis, the domain \mathcal{D} is limited by the thickness Δz of the sample. The largest relevant $k_\perp = k_{\perp, \max}$ is determined by the resolution Δr_R of the experiment via $\Delta r_R = \pi / k_{\perp, \max}$ (see Section 4.5). If thus the sample is thin enough, such that

$$\frac{k_{\perp, \max}^2 \Delta z}{2k} \ll 1 \Leftrightarrow \frac{\pi}{4} \lambda_0 \Delta z \ll \Delta r_R^2 \quad (3.179)$$

the exponential factor in the inner integral, along the \bar{z} -direction, can be approximated as 1 and one obtains

$$\psi_\omega(\mathbf{r}'_\perp; z) \simeq \exp(ikz) - \frac{k^2 \exp(ikz)}{2\pi z} \exp\left[\frac{ikr'^2_\perp}{2z}\right] \mathcal{F}_\perp \left[\overline{\Delta n_\omega}(\mathbf{r}_\perp) \right]_{\mathbf{k}_\perp = \frac{k}{z} \mathbf{r}'_\perp}. \quad (3.180)$$

Here $\overline{\Delta n_\omega}(\mathbf{r}_\perp)$ denotes the projection of the refractive index in \bar{z} -direction, as defined before. As a result, within the small-angle approximation and for sufficiently thin objects the Born approximation delivers the scattered field, apart from constant factors and a spherical curvature term, as a two-dimensional Fourier transform of the refractive index distribution of the sample, projected into the mean direction of scattering, i.e. along the optical axis. Interestingly, Eq. (3.179) is approximately the same condition as that for the validity of the projection approximation as outlined in Section 3.2.2. For similar considerations regarding the validity of the projection approximation in the context of the Born approximation see also [19].

We now return to the diffraction picture within the projection approximation. Let us assume the probe function to be a plane wave $\exp(ikz)$ with wave vector $\mathbf{k} = k\mathbf{e}_z$. For a weak object (e.g. $k|\overline{\Delta n_\omega}| \leq 0.1$) the exponential term in the projection approximation Eq. (3.134) can be linearized. The exit wave is then given as

$$\psi_\omega(\mathbf{r}_\perp; 0) \simeq \left(1 - ik \overline{\Delta n_\omega}(\mathbf{r}_\perp) \right). \quad (3.181)$$

Here we can interpret the left term as the undiffracted and the right term as the diffracted exit wave.

¹⁵The real space coordinate system in the far field plane now is (x', y') .

Consider now the propagation of this wave field into the far field at plane $z = \text{const.} \gg 0$ and within the small-angle approximation. The propagated plane wave is then given as $\exp(ikz)$ and for the right-hand side expression within braces one can apply the Fraunhofer diffraction formula Eq. (3.35), yielding

$$\psi_{\omega}(\mathbf{r}'_{\perp}, z) \simeq \exp(ikz) - \frac{k^2 \exp(ikz)}{2\pi z} \exp\left[\frac{ikr'^2_{\perp}}{2z}\right] \mathcal{F}_{\perp} \left[\overline{\Delta n_{\omega}}(\mathbf{r}_{\perp}) \right]_{\mathbf{k}_{\perp} = \frac{k}{z} \mathbf{r}'_{\perp}}. \quad (3.182)$$

The projection and the Born approximation thus lead to the same result, once the object is thin, a weak scatterer and the paraxial approximation can be assumed. Here the diffracted amplitude is observed in the far field with the sample being illuminated by a plane wave.

4 Lensless x-ray microscopy of cells: From concepts to experimental realization

In a general sense, the goal of **coherent (lensless) x-ray microscopy**¹ (XM) is to obtain a magnified image of an object by illumination with a sufficiently coherent beam, utilizing free-space propagation between sample and detector as well as, in most cases, subsequent numerical inversion of the recorded diffraction pattern on the detector. It is important to note here that this reconstruction scheme does not involve the refinement of any parametrized model of the object, as it is sometimes used in other diffraction techniques such as x-ray reflectivity of thin films [e.g. 58]. Therefore, it may still be called an imaging technique [142]. The main characteristics of the technique are thus the absence of any optical element, in particular a lens, between the sample and the detector and the use of a computer to generate an ‘image’ of the object from the measured diffraction pattern which in practice may have little or no resemblance with the object itself.

There are at least two fundamental prospects of such an approach: Firstly, as there is no optical element between the sample and the detector, there can be no degradation of the image due to such a device, which could manifest itself in the form of aberrations or limited resolution. Secondly, as the technique uses a numerical reconstruction scheme, its implementation requires a very precise definition of what is considered as an ‘image’ here (see below). It will be shown below, how these efforts in precise definitions later result in quantitative contrast values.

4.1 Generic setup

A generic setup for coherent x-ray microscopy, as it has been applied here, is depicted in Fig. 4.1. Within the projection approximation and using the notation that has been introduced in the previous chapter, the experiment can be described as follows: An incoming illumination (or probe) field $P(x, y)$ impinges onto a sample with object transmission function $O(x, y)$ which is thin enough, so that the exit wave $\psi(x, y; 0) = P(x, y)O(x, y)$ at the exit plane ($z = 0$) directly behind the sample is given as a product of $O(x, y)$ and $P(x, y)$. If not stated otherwise, we assume a strictly monochromatic, fully coherent incident wave field, so that from now on we omit the index ω at the exit wave field. A planar two-dimensional pixelated detector is placed at a distance z from the exit plane to measure the intensity of the diffracted field. We assume the detector area to be small and the propagation distance

¹We exclude interferometric methods here, which use no lenses, but optical grids between sample and detector.

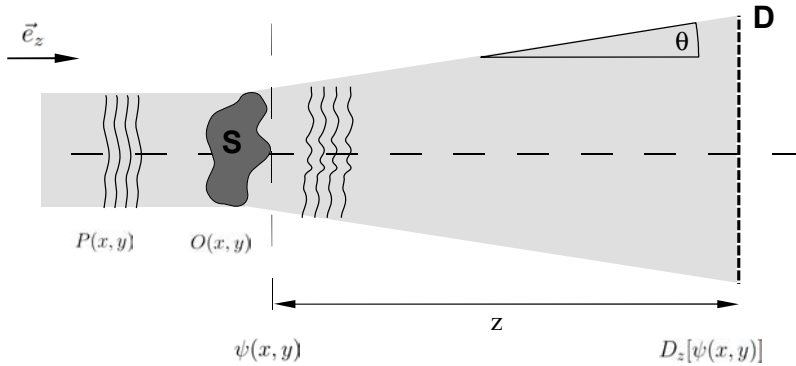


Figure 4.1: A generic setup for a coherent lensless x-ray microscopy experiment as applied within this thesis, i.e. within the small-angle and projection approximation: An incoming, not necessarily planar wave or probe field $P(x, y)$ illuminates a sufficiently thin sample S with object transmission function $O(x, y)$. The exit wave $\psi(x, y; 0) = P(x, y)O(x, y)$ at the exit plane directly behind the sample is observed at a pixelated detector D at a distance z from the exit plane. The detector area covers only those diffracted rays which make a small angle θ with respect to the optical axis with direction \mathbf{e}_z . The field at the detection plane can be obtained from the exit wave using a free space propagation operator, denoted as D_z . As a main characteristic of this type of experiment, there are no optical elements between the sample and the detector.

z to be large enough for the small-angle approximation to be valid. The diffracted field at the detector at location (x', y') is thus given as

$$\psi(x', y', z) = D_z[\psi(x, y, 0)] = D_z[P(x, y)O(x, y)]. \quad (4.1)$$

Here D_z is a symbolic notation for one of the previously derived propagation operations, expressed in Eqs. (3.24), (3.32) and (3.35), which are chosen according to the geometry of the experiment. Note that the lateral coordinate systems $\mathbf{r}_\perp = (x, y)$ and $\mathbf{r}'_\perp = (x', y')$ can be different in the exit and detection plane, depending on the used propagation equation.

4.2 The phase problem

The experimental goal is to obtain a quantitative image of the object, i.e. its complex-valued object transmission function $O(x, y)$. It is therefore necessary, to obtain first the exit wave $\psi(x, y, 0)$ in the sample plane and in a second step, with the knowledge of the illumination function $P(x, y)$ the object transmission $O(x, y)$.

If the complex field $\psi(x', y', z)$ at the detector could be measured directly, $\psi(\mathbf{r}_\perp, 0) = P(\mathbf{r}_\perp)O(\mathbf{r}_\perp)$ could be simply obtained via numerical back-propagation. Unfortunately, only the intensity $|\psi(x', y', z)|^2$ at the detector can be measured, not the complex wave field itself. One is thus faced with the problem to reconstruct the complex exit wave at the sample plane from the measured intensity at the detector plane. Expressed in symbolic

notation this reads

$$\boxed{|D_z[\psi(\mathbf{r}_\perp; 0)]|^2 \rightarrow \psi(\mathbf{r}_\perp; 0)}. \quad (4.2)$$

Equivalently, one could formulate that one needs to obtain the phase of the propagated $\psi(\mathbf{r}_\perp; z)$ which is lost during a measurement. Therefore the problem (4.2) may also be viewed as a variant of the famous **phase problem**, as it is encountered in many fields of science, and very prominently in crystallography [125]. But unlike in crystallography, in the present context the sample is not crystalline and therefore the problem (4.2) is also referred to as the ‘non-crystallographic phase problem’ [108]. As a consequence, reconstruction techniques quite different from those used in crystallography have to be used. One way is to use iterative reconstruction schemes, which start with a certain initial guess of the exit wave $\psi(\mathbf{r}_\perp, 0)$ in the sample plane, and iteratively find a solution that is consistent with the measured intensity in the detector plane and with certain a-priori-information on the sample such as a finite extension. It is this a-priori information which generally makes a solution to the phase problem feasible.

Note further that the propagated exit wave intensity $|D_z[\psi(\mathbf{r}_\perp; 0)]|^2$ can only be measured on a finite grid. This discretization has certain consequences on the measurement and reconstruction process (see below).

As outlined above, it is generally not sufficient to reconstruct the exit wave field $\psi(\mathbf{r}_\perp; z)$ in order to obtain the object transmission function. It is further necessary to know the complex illumination $P(x, y)$. It turns out that this can be a major experimental challenge in coherent x-ray microscopy, for which several solutions have been devised. The first is to to prepare the experiment in such way, that $P(x, y)$ can be assumed to have an ideal form, i.e. being planar [e.g. 99] or spherical [e.g. 152]. A variant of this method, which can be used in near field propagation-based XM, is to obtain an empty image, which under certain conditions may be used to normalize out the effects of the incoming beam on the sample diffraction pattern by division with the empty beam intensity. The second approach is to obtain both, $P(x, y)$ and $O(x, y)$ individually, from a lensless XM experiment, either by solving the phase problem separately for the empty beam and the sample beam [113, 154], or by simultaneous iterative inversion of multiple diffraction patterns obtained by laterally scanning an extended sample through a constant illumination [141], a technique which is called **ptychography**.

Even within the restrictions stated above (small-angle and projection approximation) a rather large variety of different techniques can be summarized under the term ‘coherent lensless x-ray microscopy’ [105]. They all rely on a considerable degree of spatial (and longitudinal) coherence of the incident wave field. For a recent overview on all of these techniques see [105].

Two main criteria are used here to characterize the used variants of coherent XM, namely the optical regime in which the wave fields are recorded and the method that is used to solve the phase problem. Naturally, the optical regime is not truly independent of the chosen inversion method, however, there is a considerable amount of cases where, e.g. the same inversion method can be used for both, near field and far field experiments. Within this work several different combinations of both, geometry and inversion method, are used.

4.3 Imaging regimes

Coherent x-ray microscopy can be performed in the optical near and far field. In the following we will discuss general aspects of the quite different diffraction patterns which arise in these two different optical regimes, as well as consequences for the measurement and reconstruction process.

4.3.1 Far field

If the diffraction pattern is recorded in the far field regime, i.e. for Fresnel numbers $F \ll 1$, there is a simple Fourier transform relation between the exit wave behind the sample and the diffracted field at the detection plane. This important variant of coherent x-ray microscopy is commonly also referred to as **coherent x-ray diffractive imaging** (CDI, or CXDI) [105] or simply **x-ray diffraction microscopy** [142]. Within the paraxial approximation ($k_{\perp}^2 \ll k^2$ for all relevant inverse length scales k_{\perp} in the exit wave), the recorded intensity at the detector is given as (see Eq. (3.35))

$$|\psi(\mathbf{r}'_{\perp}; z)|^2 = \alpha |\mathcal{F}_{\perp} [\psi(\mathbf{r}_{\perp}; 0)]_{\mathbf{k}_{\perp} = \frac{k\mathbf{r}'_{\perp}}{z}}|^2 = \alpha |\tilde{\psi}(\mathbf{k}_{\perp})|^2 \quad (4.3)$$

where $\psi(\mathbf{r}_{\perp}; 0) = P(\mathbf{r}_{\perp})O(\mathbf{r}_{\perp})$ denotes the exit wave behind the sample and $\tilde{\psi}(\mathbf{k}_{\perp})$ its two-dimensional Fourier transform with respect to x and y . α is a scalar factor containing experimental parameters. As a result, the diffraction pattern is a true 2D frequency spectrum of exit wave. In fact, the measured diffraction pattern is proportional to the **power spectral density (PSD)** $|\tilde{\psi}|^2$ of the exit wave field. With a plane wave illumination pointing into direction \mathbf{e}_z , $P(x, y)$ simplifies to a complex constant. Consequently, the diffracted intensity at the detector plane is directly proportional to $|\tilde{O}(\mathbf{k}_{\perp})|^2$, i.e. the squared modulus of the Fourier transform of the object function.

If the Born approximation holds (see Eq. (3.180)) and the object is sufficiently thin, there is an alternative to this optical point of view. To simplify notations we define a generalized complex electron density $\rho(\mathbf{r}) := \rho_a(\mathbf{r})f_{\omega}$ where $f_{\omega} = Z + f'(\omega) - i f''(\omega)$ is the energy dependent form factor for scattering in forward direction. According to Eq. (3.181) the object wave can then be approximated as

$$O(\mathbf{r}_{\perp}) \simeq (1 - i r_e \lambda_0 \rho(\mathbf{r}_{\perp})). \quad (4.4)$$

For simplicity we have assumed the object to be two-dimensional. The far field diffraction pattern of this function is the same as that of $1 - O(\mathbf{r}_{\perp})$ [146], apart from the center, where the empty beam is located (Babinet's principle). In an experiment, the direct beam is blocked by a beam stop so that the recorded intensity distribution $I(\mathbf{k}_{\perp})$, apart from constant factors, is equal to the squared modulus of the Fourier transformed electron density distribution:

$$I(\mathbf{k}_{\perp}) = |\tilde{\rho}(\mathbf{k}_{\perp})|^2. \quad (4.5)$$

This picture is the same as in conventional crystallography and also very common in the CDI literature [see e.g. 92, 101, 146]).

In an experiment one can only measure $I(\mathbf{k}_\perp)$ on a finite grid with a certain sampling period Δk . We now discuss how this affects the phase problem (4.2) and how fine the sampling grid has to be.

In crystallography, the far field intensity distribution is characterized by distinct Bragg peaks of finite area and practically no intensity in between [146]. For illustration and following ref. [146] let us consider an infinite periodic 1D density function $P_L[\rho](x) = \rho(x) \otimes \text{III}_L(x)$ with period L in real space and nomenclature as introduced in Chapter 2. Here the function $\rho(x)$ is the unit cell density distribution with $\rho(x) = 0$ outside the interval $[-L/2, L/2]$. Ignoring global factors, the measured diffraction pattern

$$I(k_x) = |S_{2\pi/L}[\tilde{\rho}](k_x)|^2 \quad (4.6)$$

is then given as the sampled Fourier transform of the unit cell density with Bragg peaks separated by a distance $2\pi/L$ in Fourier space and zero intensity in between [146]. It is therefore sufficient to measure the intensity distribution at the Bragg peaks, and no information is gained, if additional sampling points are added. This has also been called the ‘intensity problem’ of crystallography [142].

The situation is fundamentally different, if there is only one unit cell with finite extension L , i.e. if $\rho(x)$ is non-periodic and has a bounded support. In this case the diffraction pattern $\tilde{\rho}(k)$ is a continuous function in reciprocal space:

$$I(k_x) = |\tilde{\rho}(k_x)|^2. \quad (4.7)$$

The question arises, how fine this continuous pattern has to be sampled, so that all information is contained in the sampled values. Due to the bounded support of $\rho(x)$ with diameter L in real space, the associated diffraction pattern is characterized by smallest features of size $2\pi/L$, which are also referred to as **speckles** [146]. Therefore, it seems intuitively reasonable that a certain smallest sampling period is sufficient to encode all information of the continuous intensity distribution in the sampled (measured) diffraction pattern. This notion is firmly established and quantified by the sampling theorem (see section 2.4.4). It can be applied here to the intensity $I(k_x)$ in Fourier space, as this is ‘band’-limited in real space (i.e. it has bounded support). According to Eq. (2.20) its inverse Fourier transform yields the density autocorrelation, i.e. (apart from constant factors)

$$\mathcal{F}^{-1}[I(k_x)] = (\rho \oplus \rho)(x), \quad (4.8)$$

which has a bounded support on the interval $[-L, L]$ of width $2L$. As a consequence, a sampling period of $\Delta k_a = \pi/L$ in Fourier space, corresponding to the inverse Nyquist rate of the sampling process, is sufficient to encode all information contained in the continuous diffraction pattern $I(k_x)$ [146]. Higher sampling does not add information, but due to experimental noise and the non-ideal experimental sampling process, higher than Nyquist sampling of the intensity is very advisable [146] (see also Section 2.3).

If the full complex field at the detector could be measured, the Nyquist sampling period would be increased by a factor of two to $\Delta k_B = 2\pi/L$, as the density itself is limited to the interval $[-L/2, L/2]$ in real space. As Δk_B is equal to the distance of Bragg peaks due to the corresponding periodic real space density with unit cell width L , sampling with width Δk_B

is sometimes also referred to as sampling “at Bragg density” [101]. The factor

$$\sigma_j := \Delta k_B / \Delta k_j \quad (4.9)$$

with Δk_j denoting experimental sampling period along dimension j is also referred to as the **(Shannon) oversampling factor** along dimension $j = x, y, z$. As a speckle in the diffraction pattern has a width of roughly $2\pi/L$ [146] sampling at twice the Bragg density corresponds to two sampling points per speckle, on average. Extending the previous analysis to two (and possibly three) dimensions, the Shannon theorem requires an oversampling of the diffraction pattern by a factor of $\sigma_j = 2$ in each direction. This value is also referred to as Shannon oversampling [138].

It has been shown [101] that under ideal conditions oversampling by a factor of only $\sigma_j = 2^{1/N_d}$ along each dimension is necessary, given a problem with N_d dimensions. To see this, consider the discrete version of Eq. (4.7), sampled at Bragg density, i.e. $\Delta k_x = \Delta k_B = 2\pi/L$:

$$I(m_x \Delta k_x) = |\text{DFT}_{m_x}^{(c)} [\rho(\mathbf{x}_N^{(c)})]|^2. \quad (4.10)$$

Here $m_x = -N/2, \dots, N/2 - 1$ and $\mathbf{x}_N^{(c)} = (-N/2, \dots, N/2 - 1)\Delta x$. For simplicity, we assume N to be even. Eq. (4.10) is a system of N equations with $2N$ unknowns, namely the real and imaginary part of $\rho(\mathbf{x}_N^{(c)})$. Consider now the sampling at twice the Bragg density, i.e. $\Delta k_x = \pi/L$, leading to $2N$ sampling points in Fourier space and $2N$ equations. The real space “field of view” (FOV) increases from $N\Delta x = N2\pi/(N\Delta k_B) = 2\pi/(2\pi)L = L$ to $2N\Delta x = 2L$. As $\rho(x)$ has a bounded support in the interval $[-L/2, L/2]$, $\rho(x) = 0$ for $|x| > L/2$. As a consequence, N values out of the $2N$ complex unknowns $\rho(\mathbf{x}_{2N}^{(c)})$ are known to be zero. We are left with N complex unknowns and $2N$ equations. Thus, the problem is fully determined for $\sigma_j = 2$. The same analysis can be applied to the case of two and three dimensions, leading to a requirement of only $\sigma_j = 2^{1/2}$ and $2^{1/3}$, respectively, to obtain N density values that are known to be zero in real space. Combined with the $2N$ equations, this makes the problem with $2N$ variables fully determined. One can define an alternative oversampling ratio

$$\sigma := \frac{\text{Total number of density sampling points}}{\text{Number of unknown density points}}. \quad (4.11)$$

This definition is dimension independent, and the previous analysis indicates that $\sigma \geq 2$ suffices to completely determine the discrete phase problem in the far field, independent of the dimensionality of the problem. The observation that an increase in the sampling rate beyond the Bragg sampling causes a zero density region outside the known support of the object [101] is a very important ingredient to reconstruction algorithms (see below). To avoid confusion with the (Shannon) oversampling ratio σ_j we call σ as defined in Eq. (4.11) the **generalized oversampling ratio**.

Experimentally, oversampling the diffraction pattern of a non-periodic object with extension L_j by a factor of σ_j along dimension j requires a certain physical detector pixel width $\Delta j'$ along that direction. Using Eqs. (3.80), (4.9) and the reciprocity relation of the DFT one obtains

$$\Delta j' = \frac{\lambda_0 z}{\sigma_j L_j}. \quad (4.12)$$

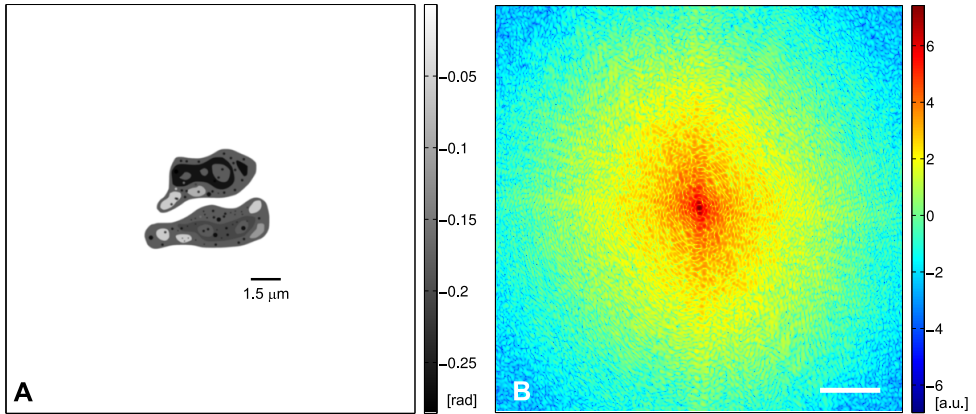


Figure 4.2: (A) Simulated object transmission function (phase). At the simulated photon energy of 8 keV the absorption due to the object is negligible. (B) Corresponding simulated, non-noisy intensity distribution in the far field, shown on logarithmic scale, covering many orders of magnitude. The intensity distribution shows speckles which are sampled on average with more than two pixels per speckle along each dimension. The scale bar corresponds to a distance of 1 mm on a detector at a distance 3.5 m away from the sample. For further simulation parameters see main text.

For illustration, a phantom object function was simulated as described in Section 3.2.3. The object here resembles two unstained biological cells, illuminated by a coherent x-ray beam with a photon energy of 8 keV. The object refractive index was obtained from tabulated data [67], assuming a stoichiometry of $\text{H}_{50}\text{C}_{30}\text{N}_9\text{O}_{10}\text{S}_1$ and mass density of 1.35 g/cm^3 , as used in the literature to simulate a typical protein density [71]. The maximum thickness of the cells was assumed to be $1.5 \mu\text{m}$. With $\beta/\delta \approx 0.004$ at these experimental parameters, the absorption due to the sample is negligible with respect to the phase change on the incident wave field. The resulting phase distribution of the simulated object function $O(\mathbf{r}_\perp)$ is shown in Fig. 4.2A. The corresponding diffraction pattern (see Fig. 4.2B) was simulated by numerical propagation into the Fraunhofer plane, as given in Eq. (3.89). The detector was assumed to be placed at a distance of 3.5 m away from the sample. With a maximum linear extension of the sample of about $6.6 \mu\text{m}$ this corresponds to a Fresnel number of $F \approx 0.08$.

Note that the diffraction pattern shown in Fig. 4.2B covers many orders of magnitude. To measure such a diffraction pattern poses a great experimental challenge, and a quite usual detector dynamic range of 16 bit, allowing to discriminate $65536 \approx 10^{4.8}$ intensity values, is generally not enough to record a diffraction pattern that is sufficient for a good reconstruction. Often many exposures have to be combined to increase the dynamic range of the diffraction pattern [see e.g. 135].

4.3.2 Near field

If a semi-transparent sample is illuminated by a coherent plane wave and the diffraction pattern is observed at a distance z in the optical near field, there is a significant resemblance between the transmitted intensity at the exit plane and the recorded diffraction pattern. Roughly speaking, only length scales $d \lesssim \sqrt{\lambda_0 z}$ are subject to diffraction (see Eq. (3.136)) and on length scales $d \gg \sqrt{\lambda_0 z}$ the diffraction pattern appears as a blurred version of the original object. An interesting property of near field diffraction patterns can be observed for objects with unit transmittance in the exit plane. Although no structure of the object can be observed directly in the exit plane, near field propagation reveals the features of the object. The ideal of such purely phase shifting objects is well-met by single unstained cells illuminated by a hard x-ray beam.

Simulated near field diffraction patterns of a pure amplitude ('A') and phase object ('P') are shown in in Fig. 4.3 (left). The corresponding complex exit wave field is illustrated in Fig. A.1. Even though the phase object has a unit amplitude transmittance in the exit plane, the near field diffraction pattern reveals the presence of the object. This is an example of the transfer of phase into amplitude contrast. As outlined above, there is a strong resemblance of the diffraction pattern with the original object for both the amplitude and the phase object on length scales $d \gg \sqrt{\lambda_0 z} \approx 0.25 \mu\text{m}$. Further propagation (right side) leads to complete distortion of the original transmission function.

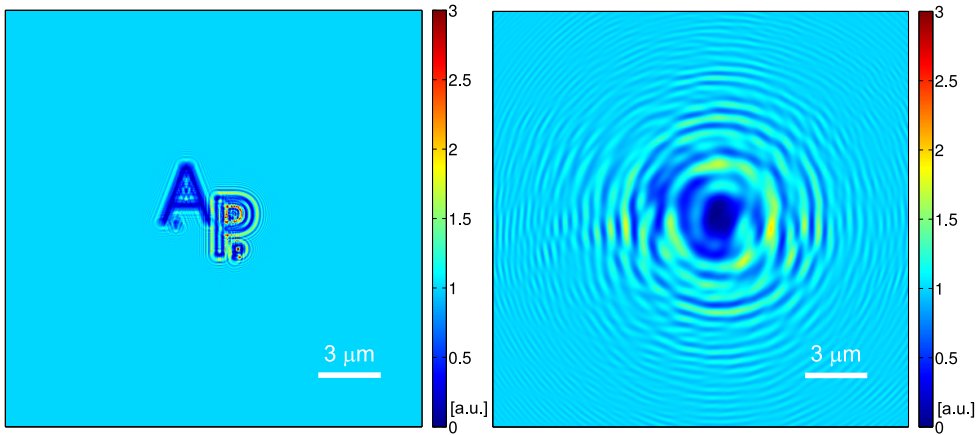


Figure 4.3: Simulated near field intensity distribution due to the sample transmission function shown in Figs. A.1 and A.2. The simulated propagation distance corresponding to the diffraction pattern on the left was $z = 0.4 \text{ mm}$, corresponding to a Fresnel number $F \approx 470$. The simulated propagation distance corresponding to the pattern on the right was $z = 30 \text{ mm}$, corresponding to a Fresnel number $F \approx 9$.

The contrast transfer in the optical near field can be quantified in the **phase and amplitude contrast transfer functions (PCTF and ACTF)**. For a weak object the complex

transmission function (3.146) can be written as

$$O(\mathbf{r}) \approx 1 - k\bar{\beta}(\mathbf{r}_\perp) - ik\bar{\delta}(\mathbf{r}_\perp) \quad (4.13)$$

$$= 1 - a(\mathbf{r}_\perp) - i\varphi(\mathbf{r}_\perp). \quad (4.14)$$

The amplitude and phase change due to the sample have been captured here in the functions $a(\mathbf{r}_\perp)$ and $\varphi(\mathbf{r}_\perp)$.

Assuming a plane wave illumination with unit amplitude and neglecting global phase factors, the near field propagated exit wave due to transmission $O(\mathbf{r})$ becomes with Eq. (3.24), apart from a global phase factor:

$$\psi(\mathbf{r}_\perp; z) = 1 - \mathcal{F}^{-1} \left[[\bar{a}(\mathbf{k}_\perp) - i\bar{\varphi}(\mathbf{k}_\perp)] \exp\left(\frac{-izk_\perp^2}{2k}\right) \right]. \quad (4.15)$$

It can be shown [96, 110] that, to first order in $\bar{\varphi}$ and \bar{a} , the 2D Fourier transform of the propagated intensity, $I(\mathbf{r}_\perp; z) = |\psi(\mathbf{r}_\perp; z)|^2$, is given as

$$\tilde{I}(\mathbf{k}_\perp; z) \approx 2\pi\delta(\mathbf{k}_\perp) + 2\bar{a}(\mathbf{k}_\perp) \cos[\chi(\mathbf{k}_\perp)] + 2\bar{\varphi}(\mathbf{k}_\perp) \sin[\chi(\mathbf{k}_\perp)] \quad (4.16)$$

with $\chi(\mathbf{k}_\perp) = zk_\perp^2/2k$. It is convenient to express Eq. (4.16) in terms of rotational frequencies $(\nu_x, \nu_y) = (k_x, k_y)/(2\pi)$, so that $\chi = \pi z\lambda_0\nu^2$ with $\nu := (\nu_x^2 + \nu_y^2)^{1/2}$. Eq. (4.16) then becomes²

$$\tilde{I}(\nu_x, \nu_y; z) \approx \delta(\nu_x, \nu_y) + 2\bar{a}(\nu_x, \nu_y) \cos[\chi(\nu)] + 2\bar{\varphi}(\nu_x, \nu_y) \sin[\chi(\nu)]. \quad (4.17)$$

Note that the amplitude and phase contribution of the intensity spectrum $\tilde{I}(\nu_x, \nu_y; z)$, i.e. the second and third term on the right side of Eq. (4.17), become zero at certain spatial frequencies. This is a consequence of the filtering properties of the free-space Fresnel operator, expressed in Eq. (3.27). If the near field intensity is thus measured at a certain distance z , there is zero amplitude contrast for radial spatial frequencies

$$\nu_n := \sqrt{\frac{n+1/2}{\lambda_0 z}} \quad (4.18)$$

and zero phase contrast for

$$\nu_n := \sqrt{\frac{n}{\lambda_0 z}} \quad (4.19)$$

with $n \in \mathbb{N}^0$. The functions $\cos(\chi)$ and $\sin(\chi)$ are also referred to as the **amplitude and phase contrast transfer functions**, respectively. For a graphical representation of the amplitude and phase contrast transfer function for a weak object see Fig. 4.4. Here the contrast transfer functions are shown with respect to the normalized radial frequency $\sqrt{\lambda_0 z}\nu$.

A simulated near field diffraction pattern of phantom cell objects is depicted in Fig. 4.5. The simulated diffracted intensity is shown here normalized by the intensity of the

²The symbol $\tilde{\cdot}$ here denotes a slightly modified Fourier transform definition with respect to that introduced in Chapter 2. Here the reciprocal coordinates are (ν_x, ν_y) , instead of (k_x, k_y) .

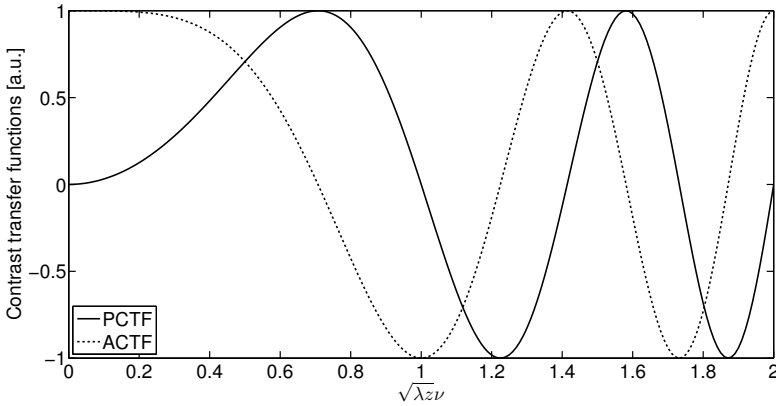


Figure 4.4: Amplitude contrast transfer function (ACTF) and phase contrast transfer function (PCTF) against normalized radial frequency.

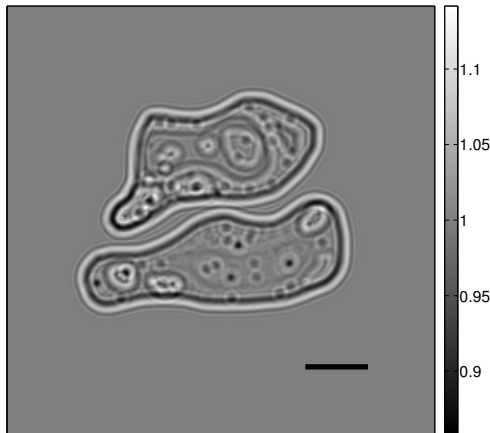


Figure 4.5: Simulated near field diffraction pattern of biological cells (see Fig. 4.2A), normalized by the diffraction pattern of the illumination function, here a plane wave. The scale bar indicates a distance of 1.5 μm .

propagated empty beam, in this case an ideal plane wave. The physical parameters of the cell phantom are the same as used for the simulation of the far field diffraction pattern shown in Fig. 4.2, except the neglect of any absorption in the present example.³ The simulated sample exit wave was propagated here over a distance of 0.2 mm, the pixel width of the simulation array was 40 nm in horizontal and vertical direction.

³This assumption was necessary to make the reconstruction of the non-noisy diffraction pattern converge (see Section 4.4.3). For the reconstruction of simulated noisy diffraction patterns this assumption was not necessary.

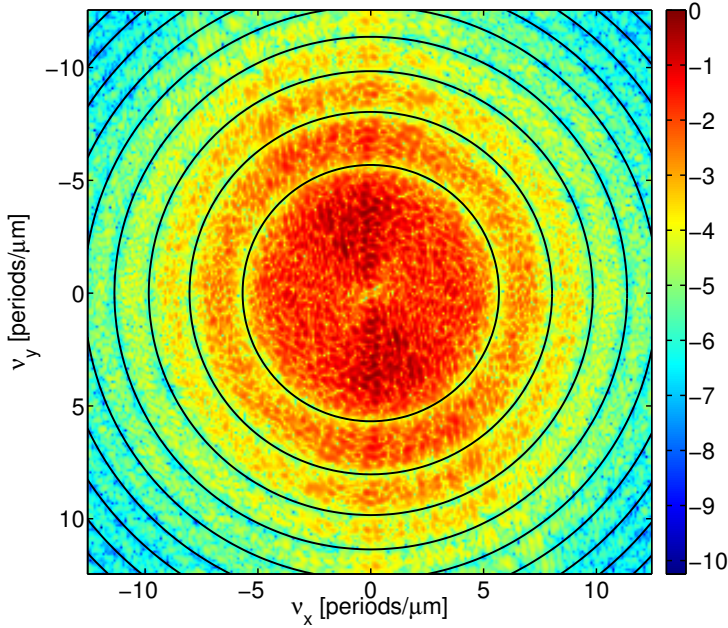


Figure 4.6: Normalized power spectral density (on a logarithmic scale) of the diffraction pattern shown in Fig. 4.5. The black rings indicate the zeros of the phase contrast transfer function at $v_n = \sqrt{n/\lambda_0 z}$ with $n \in \mathbb{N}$. Note also the minimum of the PSD at the center ($n = 0$). The colorbar indicates the PSD in units of its maximum value, on a logarithmic scale. A Kaiser-Bessel window was applied prior to calculation of the PSD. For a definition of the used Kaiser-Bessel-window see Section A.3.

To illustrate the effect of the phase contrast transfer function on the information content of the diffraction pattern, the PSD of the normalized near field diffraction pattern (see Fig. 4.5) is shown in Fig. 4.6. Characteristic minima can be observed at radial frequencies where the PCTF becomes zero. As a consequence, no or very little information is encoded in the diffraction pattern at these frequencies.

4.3.3 Effective near field geometry for a divergent illuminating wave field

Using plane wave illumination, the observation of near field diffraction patterns is limited to the *physical* near field of the sample. A near field observation of samples as small as biological cells with a diameter on the order of $10 \mu\text{m}$ therefore seems to be impossible: The observation would require detector pixel sizes on the order of the required resolution in the experiment, i.e. 100 nm and substantially further below. Indeed, in near field propagation imaging using plane wave illumination, the resolution (for a proper definition see below) is usually limited to the physical pixel width of the detector [105], i.e. down to about $0.3 \mu\text{m}$ for systems with an x-ray/visible light converter [24] and to about $10 - 20 \mu\text{m}$ for direct illuminated CCD's [e.g. 48, 121]. On the other hand, the Fresnel scaling theorem expressed

in Eq. (3.43) allows for the observation of an *effective* near field diffraction pattern, if the microscopic sample is illuminated by a paraxial spherical wave field and the diffracted intensity observed at a macroscopically large distance away from the sample. As the diffraction pattern is, apart from geometrical magnification, *identical* to one that would have been observed at a very small distance from the sample with plane wave illumination, the analysis is the *same* as for near field imaging with plane waves. Using a divergent wave field as an illumination thus largely expands the resolution of near field propagation-based imaging, keeping the analysis of the experiment the same as for illumination with a plane wave.

To produce a spherical illumination with high enough flux at a synchrotron source focusing devices are needed. In the hard x-ray regime e.g. Kirkpatrick-Baez (KB) mirrors [8] are used to provide the illumination for effective near field propagation-based imaging. In the laboratory high-power conventional solid anode [152] as well as liquid jet anode sources [145] can be used for the same application. A key requirement here is a small source size, to provide (i) a nearly point source and (ii) high enough spatial coherence at the sample. A further diminution of the source can be obtained by the use of 2D x-ray waveguides [75, 80].

The general experimental setup of effective near field propagation imaging is sketched in Fig. 4.7. A highly confined x-ray wave field $S(r_0)$ has non-negligible amplitude only within a maximum linear extension of D in the source plane Σ_0 at $z = -z_{01}$.⁴ The exit plane behind the sample is defined to be at $z = 0$. Let us further assume the wave front in the source plane to be nearly planar. Such a wave field can be found in the focal plane of an x-ray focusing device, such as KB-mirrors, but also in the exit plane of a 2D x-ray waveguide system. Equally, the source spot of a laboratory source produces a divergent beam. If a sample with thickness Δz is placed at a distance $z_{01} \gg \Delta z$ into the far zone of the source field ($F_S = D^2/(\lambda_0 z_{01}) \ll 1$), it is illuminated by a probe field

$$P(r_1; -\Delta z) = A(z_{01} - \Delta z) \exp\left(\frac{ikr_1^2}{2(z_{01} - \Delta z)}\right) \tilde{S}\left(\mathbf{k}_\perp = \frac{k}{z_{01} - \Delta z} r_1\right), \quad (4.20)$$

in plane $z = -\Delta z$, where \tilde{S} denotes the two-dimensional Fourier transform of the source field S along its lateral dimensions and $A(z) = -ik \exp(ikz)/z$ (see Eq. 3.32). We assume the sample to be thin enough for the projection approximation to be valid, in other words, Δz has to obey Eq. (3.136), $\Delta z < \Delta r_1^2/\lambda_0$ with the smallest non-negligible lateral length scale Δr_1 in the sample exit plane. Then

$$P(r_1; -\Delta z) \simeq P(r_1; 0) \quad (4.21)$$

and the exit wave $\psi(r_1; 0)$ in plane Σ_1 is given as

$$\psi(r_1; 0) = P(r_1; 0)O(r_1; 0) \quad (4.22)$$

⁴Note that in the present section we use $r_i := \mathbf{r}_\perp^{(i)} = (x_i, y_i)$ and thus $(r_i, z) = (\mathbf{r}_\perp^{(i)}, z)$ here to assign lateral coordinates in plane Σ_i .

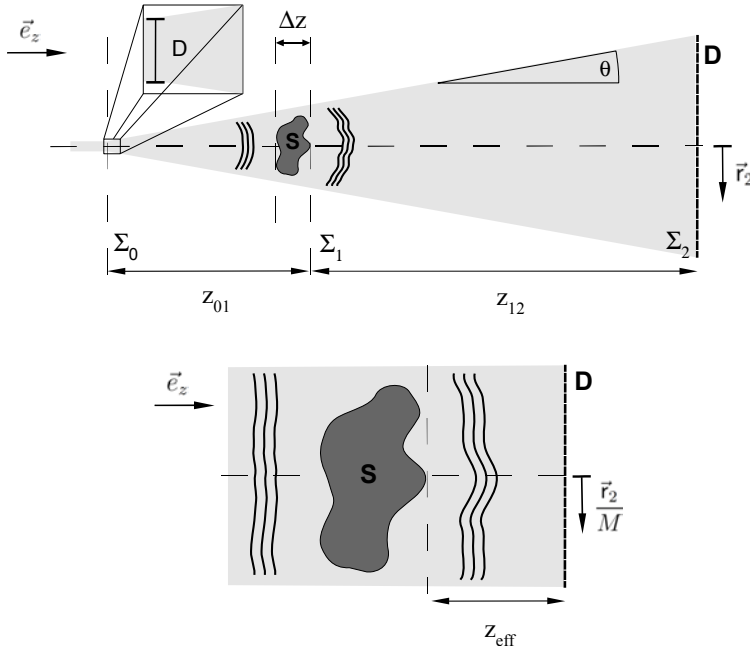


Figure 4.7: (Top) A divergent-beam setup for (effective) near field imaging (side view). A highly confined beam of lateral extension D in plane Σ_0 propagates onto a sample of thickness Δz over distance $z_{01} - \Delta z$ with $\Delta z \ll z_{01}$. The sample here is placed into the far field with respect to the field in the source plane Σ_0 , so that $D^2/(\lambda_0 z_{01}) \ll 1$. The exit wave behind the sample then impinges onto a planar pixelated area detector at distance $z_{12} \gg z_{01}$ from the exit plane Σ_1 directly behind the sample. (Bottom) Within the small-angle and projection approximation the wave field amplitude at the detector at lateral position r_2 , normalized by the amplitude measured without a sample, is equal to the amplitude of the object transmission function O , propagated by an effective distance z_{eff} , and observed at lateral position r_2/M .

with the sample transmission function $O(r_1; 0)$. The planar part of the exit wave is given as

$$\psi^{(P)}(r_1; 0) = P^{(P)}(r_1; 0)O(r_1; 0) \quad (4.23)$$

$$\Leftrightarrow \psi^{(P)}\left(\frac{r_2}{M}; 0\right) = P^{(P)}\left(\frac{r_2}{M}; 0\right)O\left(\frac{r_2}{M}; 0\right). \quad (4.24)$$

The equivalence follows as the first equation is true for any lateral position in plane $z = 0$. One now needs to make the transition to the plane at distance z_{eff} downstream of the exit plane, i.e.

$$\left| \psi^{(P)}\left(\frac{r_2}{M}; z_{\text{eff}}\right) \right| = \left| P^{(P)}\left(\frac{r_2}{M}; z_{\text{eff}}\right) \right| \left| O\left(\frac{r_2}{M}; z_{\text{eff}}\right) \right|. \quad (4.25)$$

The transition is true, if the fields $P^{(P)}(\mathbf{r})$ and $O(\mathbf{r})$ obey the product approximation within the propagation distance z_{eff} . This amounts to the assumption that the product of the propagated fields is equal to the propagated product of the fields. A similar situation has

been considered in [141] and a criterion for the validity of Eq. (4.25) might be derived along the same line of arguments. Eq. (4.25) is certainly true, if $P^{(P)}$ is a true plane wave, and it can be expected that if the lateral variations in $P^{(P)}$ are small in amplitude and on a large length scale Eq. (4.25) is still true.

One can then apply the Fresnel scaling theorem (3.43) to the exit and the illumination wave field, i.e.

$$|\psi(r_2; z_{12})| = \frac{1}{M} \left| \psi^{(P)} \left(\frac{r_2}{M}; z_{\text{eff}} \right) \right|, \quad (4.26)$$

and

$$|P(r_2; z_{12})| = \frac{1}{M} \left| P^{(P)} \left(\frac{r_2}{M}; z_{\text{eff}} \right) \right|, \quad (4.27)$$

As a consequence, one obtains

$$M |\psi(r_2; z_{12})| = M |P(r_2; z_{12})| \left| O \left(\frac{r_2}{M}, z_{\text{eff}} \right) \right|, \quad (4.28)$$

or equivalently,

$$\left| O \left(\frac{r_2}{M}; z_{\text{eff}} \right) \right|^2 = \frac{|\psi(r_2; z_{12})|^2}{|P(r_2; z_{12})|^2}. \quad (4.29)$$

The quantities on the right side of the equation can be obtained in a measurement. Eq. (4.29) thus allows for an experimental determination of the geometrically magnified amplitude of the object transmission function (as if illuminated by a plane wave), propagated over an effective distance z_{eff} away from the exit plane. For this reason the geometry sketched in the bottom part of Fig. 4.7 is sometimes also called effective plane wave geometry.

4.4 Reconstruction

Many different ways to solve the non-crystallographic phase problem (4.2) have been demonstrated over the past decades [105].

Within this thesis, two alternative reconstruction approaches have been followed. The first is based on the iterative refinement of a guessed initial exit wave (or object density) ψ_0 by repeated numerical forward and backward propagation between the exit plane and the detector plane and the iterated application of known constraints to ψ_0 in either plane. This widely used scheme can often be formulated in the language of projections onto constraint sets in the search space [92, 138]. More generally, one can speak of iterated maps on the search space [138].

The second approach that has been followed is the concept of **(in-line) holography** [49, 60, 108]. Here an image of the object can be obtained by a single numerical operation. The result, however, is spoiled by the so-called twin image (see below) and therefore not suitable for quantitative analysis.

The third approach can be interpreted as a scanning extension of diffraction microscopy [141]: Here a localized illumination wave field is applied to a sample that is

laterally scanned through the beam, while at each scan position a two-dimensional diffraction pattern of the propagated sample exit wave is recorded. The resulting ensemble of diffraction patterns is then used to iteratively reconstruct the object transmission function and the illumination simultaneously. It can be shown [141] that this approach can still be formulated in the language of iterated maps onto constraint sets, with now a much more complicated search space.

4.4.1 Reconstruction by iterative maps

For this section, let ψ denote an element of \mathcal{E} , the space of two-dimensional complex matrices with N_p entries, corresponding to sampled 2D wave fields. $\psi(\mathbf{r})$ then denotes a (complex) entry of ψ , corresponding to the pixel with location $\mathbf{r} = (x, y)$ in the plane perpendicular to the propagation direction. $|\psi(\mathbf{r})|^2$ is proportional to the time-integrated flux through the pixel area A_p . This notation slightly differs from that used in Chapter 3, but it allows to write the algorithms in simple notation. Note that the factor $\sqrt{A_p}$ present in propagation equations on discrete fields is now absorbed into ψ . As a consequence, the elements $I(\mathbf{r})$ of the matrix I , which usually refers to the experimental data, denote the time-integrated flux in each pixel with area A_p . Nevertheless, I might sometimes still be referred to as the ‘intensity’ which is proportional to the integrated flux for a given measurement. $\mathbf{k} = (k_x, k_y)$ corresponds to the 2D reciprocal space coordinate.

As noted above, the algorithms which are outlined in the following can be interpreted as iterative maps onto constraint sets. A general description of phase retrieval within this language can be found e.g. in [38]. A **constraint set** is a subspace \mathcal{C} of \mathcal{E} which contains only elements which obey a certain constraint. As an example,

$$\mathcal{C}_M := \{\psi \in \mathcal{E} \mid |\tilde{\psi}| = \sqrt{I}\}. \quad (4.30)$$

is the set of all elements in \mathcal{E} whose Fourier transform has an amplitude equal to \sqrt{I} . In the far field geometry of lensless microscopy this corresponds to all elements of ψ which are compatible with the experimental data. Additional knowledge about the object can be formulated in another constraint set \mathcal{C}' . A solution must then be an element of the intersection $\mathcal{C}_\cap = \mathcal{C} \cap \mathcal{C}'$.

If only one constraint set is given, it is very simple to find a solution that obeys this constraint [38], one only needs a **constraint map** on \mathcal{E} that maps any element of \mathcal{E} onto an element of \mathcal{C} . For the constraint set \mathcal{C} this is, for example, the constraint map

$$P_M : \mathcal{E} \setminus \{0\} \rightarrow \mathcal{C}_M : \psi \mapsto \mathcal{F}^{-1} \left[\sqrt{I} \frac{\tilde{\psi}}{|\tilde{\psi}|} \right]. \quad (4.31)$$

It can be shown that for this example the map also has the properties of a **projection**, i.e. it finds the element of the constraint set that is *closest* to the original ψ , with respect to a certain distance defined on \mathcal{E} [38]. In other words, the original ψ undergoes a *minimum* change to obey the constraint.

Due to the usually rather complex structure of the constraint sets [138], finding a member of \mathcal{C}_\cap is not an easy task, starting at any $\psi \in \mathcal{E}$. On the other hand, it turns out [38] that the iterated application of constraint maps or combinations of them on an element of \mathcal{E} can lead to a possible solution in \mathcal{C}_\cap .

4.4.1.1 Gerchberg-Saxton algorithm

To our knowledge, the so-called **Gerchberg-Saxton (GS) algorithm** [53] was the first iterative propagation algorithm used in the imaging community. It is designed to solve the problem of complex wave field reconstruction when the field amplitude is known in two planes which are separated by a distance z . In this setting the number of independent equations ($2N_P$ for an image with N_P pixels) is equal to the number of independent unknowns ($2N_P$ real and imaginary pixel values).

An implementation of the algorithm proceeds as follows: Start e.g. with an initial guess ψ_1 of random phase and amplitude values in the near plane.⁵

(i) Forward propagate to $\Psi_1 = D_z[\psi_1]$. D_z here denotes forward propagation by a distance z .

(ii) Replace the calculated amplitude $|\Psi_1|$ by the known amplitude $\sqrt{I_F}$ in the far plane and retain the phase part:

$$\Psi_1' = \sqrt{I_F} \frac{\Psi_1}{|\Psi_1|}. \quad (4.32)$$

(iii) Back propagate to obtain $\psi_1' = D_z^{-1}[\Psi_1']$.

(iv) Replace the calculated amplitude $|\psi_1'|$ by the known amplitude $\sqrt{I_N}$ in the near plane and retain the phase part to obtain the new estimate

$$\psi_2 = \sqrt{I_N} \frac{\psi_1'}{|\psi_1'|}. \quad (4.33)$$

Afterwards, steps (i)-(iv), which represent one **iteration** of the algorithm, are repeated until a pre-set number of iterations is reached or a stopping criterion is met. Steps (i)-(iii) are often also summarized as the so-called **modulus constraint operation** $P_M[\psi_1] := \psi_1'$ which defines a map on the search space \mathcal{E} . ψ is said to fulfill the modulus constraint P_M , if it is invariant under application of P_M . The propagation method used here to obtain Ψ_j from ψ_j depends on the geometry of the experiment.

To define a reconstruction error we use the norm on \mathcal{E} defined as

$$\|\psi\| := \sqrt{\frac{1}{N_P} \sum_{\mathbf{r}} |\psi(\mathbf{r})|^2} \quad (4.34)$$

for any $\psi \in \mathcal{E}$. The squared error at iteration j can then be defined as [92]

$$\varepsilon_{M,j}^2 := \|\psi_j - P_M[\psi_j]\|^2. \quad (4.35)$$

$\varepsilon_{M,j}^2 = d^2(\psi_j, P_M[\psi_j])$ also defines the distance between ψ_j and its image under the map P_M with respect to the metric d that is induced by the norm defined in Eq. (4.34).

⁵The probably most common approach [see e.g. 108, p. 292], however, is to choose the phases randomly in the interval $[-\pi, \pi]$ and set the amplitudes as measured or known in the near plane.

Plancherel's theorem (see Section 3.1.8) states the conservation of the integrated flux with respect to any of the discussed propagation operations, so that

$$\varepsilon_{M,j}^2 = \|D_z[\psi_j] - D_z[P_M[\psi_j]]\|^2. \quad (4.36)$$

$$= \|\Psi_j \exp(i\varphi(\Psi_j)) - \sqrt{I_F} \exp(i\varphi(\Psi_j))\|^2 \quad (4.37)$$

$$= \|\Psi_j - \sqrt{I_F}\|^2. \quad (4.38)$$

$\varepsilon_{M,j}$ is thus equal to the root mean square (RMS) deviation of the known amplitude $\sqrt{I_F}$ and the amplitude of the current estimate in the same plane.

If the algorithm reaches a **fixed point** ψ^* , i.e. if another iteration will have no effect on ψ^* any more, **convergence** has been achieved [138]. $\varepsilon_{M,j}$ will then stay at a constant level, ideally at zero. In practice, convergence may take a very large or even infinite number of iterations, especially for experimental, i.e. noisy data $\sqrt{I_N}$ and $\sqrt{I_F}$ [132]. One may therefore stop the algorithm once ε_j has gone below a certain threshold. For the GS algorithm it can be shown that the error decreases monotonically [53]. As a consequence, ψ_{j+1} will always be an estimate equal to or better than ψ_j , with respect to the error ε_j . Note, however, that convergence of the algorithm does not generally guarantee that the algorithm has found the correct solution. In other words, there may be many different fixed points which are not the desired solution. For further details see the Section on uniqueness below.

The GS algorithm is a good candidate for imaging pure phase objects. In this case the amplitude in the exit plane is equal to unity $\sqrt{I_N} = 1$ and only one intensity measurement is required.

4.4.1.2 Error-Reduction algorithm

If only one intensity measurement is available and if the object function is characterized by a distortion in phase and amplitude, the GS algorithm is not applicable. With additional constraints in the near plane the problem can still be solved in many cases.

Consider the case of far field diffraction with plane wave illumination as described above. Except at the center ($\mathbf{k} = 0$), the far field diffraction pattern of the exit wave O is the same as that of $\psi := 1 - O$. As noted above, oversampling of a far field diffraction pattern beyond the Bragg density induces regions of zero density outside the support \mathcal{S} of the object (for a definition of support see Section 2.3.2). Here the support of the object corresponds to the support of ψ . In other words $\psi(\mathbf{r}) = 0$ for all $\mathbf{r} \notin \mathcal{S}$. This allows for the construction of the so-called **support constraint operation**. For an incident complex field ψ it can be defined as

$$P_S[\psi(\mathbf{r}_\perp)] := \begin{cases} \psi(\mathbf{r}_\perp) & \text{for } \mathbf{x} \in \mathcal{S} \\ 0 & \text{otherwise.} \end{cases} \quad (4.39)$$

If the Born approximation and thus Eq. (4.4) holds, the algorithm can directly be applied to the complex electron density $\rho(\mathbf{r})$ of the object, integrated along the propagation direction. If absorption can be neglected, $\rho(\mathbf{r})$ is real and positive, so that the support constraint can be extended by the **positivity constraint** which, in the case of negligible absorption, also

implies ρ to be real [92, 100]:

$$P_{S^+}[\rho(\mathbf{r})] := \begin{cases} \text{Re}[\rho(\mathbf{r})] & \text{for } \mathbf{x} \in S \text{ and } \text{Re}[\rho(\mathbf{r})] > 0 \\ 0 & \text{otherwise.} \end{cases} \quad (4.40)$$

These operators can now be used to construct a new algorithm [44] which is referred to as the **Error Reduction (ER) algorithm**. For a general complex array ψ_j (this may also be the density) the j th iteration reads as follows:

- (i) Apply the modulus constraint as defined above to the j th iterate ψ_j :

$$\psi'_j = P_M[\psi_j]. \quad (4.41)$$

- (ii) Apply the support constraint:

$$\psi_{j+1} = P_S[\psi'_j]. \quad (4.42)$$

The final result is obtained by a last evaluation of the modulus constraint. If the error has not decreased to 0, this last operation makes the solution fully consistent with the experimental data which is usually known better than the support of the object. If ψ_j can be replaced by the object density and absorption is negligible, one may also replace P_S by P_{S^+} in the algorithm.

The estimation of the correct support from a diffraction pattern alone is not an easy task and in general the diffraction pattern or, equivalently, the autocorrelation function, does not uniquely determine the object support [46]. On the other hand, it is known that a tight support enhances the quality of reconstructions, especially for object functions with both, a phase and amplitude shift [19].

An empiric method to define a tight support dynamically during the process of an iterative propagation algorithm is the so-called **Shrink-Wrap (SW)** method [93]. Initially, the support is defined by thresholding the amplitude of the autocorrelation function. After a few iterations of the reconstruction algorithm the same thresholding operation is performed on the amplitude of the current iterate. To prevent the support from shrinking to an area smaller than the physical support of the object, the amplitude is blurred with a Gaussian filter before the thresholding operation.

Just as for the GS algorithm the error $\varepsilon_{M,j}$ decreases monotonically [45] with the number of iterations in the ER algorithm, hence the naming of the algorithm. Note that another error can be defined which can also be referred to as the real space error. It can be defined as [92]

$$\varepsilon_{S,j}^2 := \|\psi_j - P_S[\psi_j]\|^2 \quad (4.43)$$

$$= \frac{1}{N_P} \sum_{\mathbf{r} \notin S} |\psi_j(\mathbf{r})|^2 \quad (4.44)$$

and counts the total integrated fluence in the area outside the support.⁶

⁶Note that for the ER algorithm $\varepsilon_{S,j}$ should be applied to the updated quantity, ψ'_j , in each iteration, as at the beginning of each iteration, as defined here, ψ_j obeys the support constraint via construction.

The monotonic decrease of the error often causes the GS and the ER algorithm to be trapped in local minima of the complex error landscape defined e.g. by $\varepsilon_{M,j}$ as a function of ψ_j . As a consequence, both algorithms are generally rather strongly dependent on the initial conditions.

4.4.1.3 Hybrid-Input-Output algorithm

The stagnation problems of the GS and ER algorithms are overcome by the so-called **Hybrid Input-Output (HIO)** algorithm [44]. It is based on the interpretation of the modulus constraint as a nonlinear system with input ψ_j and output ψ'_j at iteration j [44]. The new iterate ψ_{j+1} is now formed not by (minimally) modifying ψ'_j in order to obey the support constraint as it is done in the ER algorithm. Instead, ψ_{j+1} is formed as a linear combination of the input and output of the modulus constraint system [38]. Hence, the j th iteration can be formulated as follows:

- (i) Apply the modulus constraint on the 'input' ψ_j to obtain the output ψ'_j :

$$\psi'_j = P_M[\psi_j]. \quad (4.45)$$

- (ii) Generate the new iterate as a linear combination of input and output under consideration of the support area:

$$\psi_{j+1}(\mathbf{r}) = \begin{cases} \psi'_j(\mathbf{r}) & \text{if } \mathbf{r} \in \mathcal{S} \\ \psi_j(\mathbf{r}) - \beta\psi'_j(\mathbf{r}) & \text{otherwise.} \end{cases} \quad (4.46)$$

Here the parameter $\beta \leq 1$ is typically chosen to be close to 1. It gradually moves $\psi(\mathbf{r})$ to zero at points \mathbf{r} outside the support region. This makes the HIO algorithm robust to stagnation in local minima of the error metric. Instead, it is often able to escape local minima and find a global solution of the problem [92]. In other words, the error usually decreases globally but may increase locally.

Note that $\psi_{j+1}(\mathbf{r})$ now generally does neither exactly satisfy the support nor the modulus constraint any more [38]. To reach an estimate of the object, after a predefined number of iterations has been performed or after the algorithm has reached a fixed point, a last application of the modulus constraint operation makes the updated last iterate consistent with the experimental data [19, 38]. Alternatively, one can take the last output of the modulus constraint operation as the final object estimate.

In Fig. 4.8 a reconstruction based on the HIO algorithm with support constraint P_S is shown. The corresponding diffraction pattern is shown in Fig. 4.2B. The reconstruction was obtained after 10000 iterations, starting with a random complex field in real space.⁷ As the support constraint moves the amplitude outside the support to zero, the algorithm cannot reconstruct the exit wave O directly, but only $1 - O$. As noted above, the field $1 - O$ gives rise to the same diffraction pattern as O , except at the center. In this example

⁷Note that the 'canonical' way to initialize the HIO algorithm is to use random phases and a known amplitude in Fourier space and then back-transform to real-space [108]. A random complex field in real space, as used here, however, also leads to the correct solution in the present case.

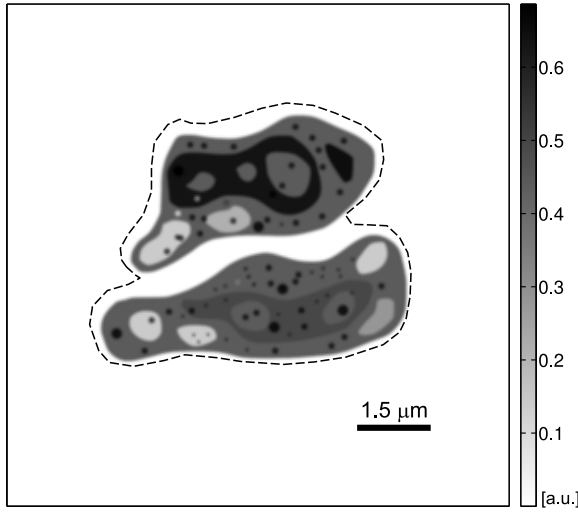


Figure 4.8: HIO reconstruction (amplitude) of the diffraction pattern shown in Fig. 4.2B. The dashed line indicates the boundary of the support area used for the reconstruction. The amplitude reconstruction shown here is proportional to the phase map of the original, essentially pure phase object. For further explanation, see the main text.

the propagation is modeled by a discrete Fourier transform. The diffraction patterns of O and $1 - O$ thus only differ in the center pixel. If this is excluded from the modulus constraint map, the HIO algorithm can be applied to the diffraction pattern due to O . As the conservation of the total integrated flux in the array is destroyed by exclusion of the central pixel, one generally reconstructs only an exit wave proportional to $1 - O$. Note that $1 - O(\mathbf{r}) \approx 1 - (1 - i\varphi(\mathbf{r})) = i\varphi(\mathbf{r})$ with the real phase distribution $\varphi(\mathbf{r})$. As a consequence, $|\hat{\varphi}(\mathbf{k})|$ well approximates the diffraction pattern. Therefore, the HIO algorithm actually reconstructs a field whose amplitude is proportional to the phase distribution (or the projected electron density) of the original phantom. One could also apply a positivity constraint in this case which was, however, not applied here.

4.4.1.4 Difference map algorithm

We briefly mention another very general global optimization algorithm with applications beyond imaging problems, the **Difference map (DM)** [38]. Assume we would like to find a solution in the intersection of two constraint sets \mathcal{C}_A and \mathcal{C}_B . Given iterate ψ_j , the new iterate is found by adding a small difference $D(\psi_j) = B(\psi_j) - A(\psi_j)$:

$$\psi_{j+1} = \psi_j + \beta D(\psi_j) \quad (4.47)$$

with scalar parameter β . Usually β is a real number, but may be complex. $A(\psi_j)$ and $B(\psi_j)$ are maps on \mathcal{E} which are formed by a linear combination of projections onto the two constraint sets of the problem. Here these might be the modulus projection P_M and

the support projection P_S . A and B are designed in such a way that A is a constraint map on C_A and B is one on C_B . We refer the reader to the literature [38] on how A and B can be constructed in detail.

Two things are to be considered from a practical point of view. The DM algorithm has found a fixed point ψ^* , if $D(\psi^*) = 0$. Then

$$A(\psi^*) = B(\psi^*). \quad (4.48)$$

Note, however that the fixed point ψ^* itself generally is not a member of the intersection of the constraint sets [38]. One needs to apply either A or B on it to find the correct solution. This requirement is similar to the last added iteration step needed for the HIO algorithm.

Convergence of the algorithm can be followed simply by monitoring the **difference map error** [138], namely the distance

$$d(\psi_{j+1}, \psi_j) = \|\psi_{j+1} - \psi_j\| \quad (4.49)$$

between two subsequent iterates.

4.4.2 Holographic reconstruction

Under ideal experimental situations the method of holography [49, 60] allows for the full reconstruction of a wave field scattered by a sample from an interference pattern that is produced by the coherent superposition of the scattered wave with a reference wave. It's invention and first demonstration is due to Gabor [49]. Today different variants of the original form exist [60].

The general principle can be described in symbolic notation as follows [47]: A reference wave R and a sample wave S are coherently superimposed and the resulting intensity

$$I = |R + S|^2 = |R|^2 + R^*S + RS^* + |S|^2 \quad (4.50)$$

is recorded on a planar screen, e.g. a glass plate with some holographic emulsion. The transmittance of the developed image then is proportional to the recorded intensity. If this is illuminated with the same reference wave at the same position as in the original setup, one obtains a wave field H proportional to

$$H \propto R|R|^2 + |R|^2S + R^2S^* + R|S|^2. \quad (4.51)$$

The second term in this sum is thus proportional to the complex sample wave field. If R is a plane wave and if one can prepare an experimental situation, where all other components of the sum are negligible or spatially separated in the plane at which the reconstruction field H is observed, the same sample field S is present at this location as if the sample was still present.

4.4.2.1 In-line holography in the near field

In the original scheme proposed by Gabor [49], now also referred to as in-line or Gabor holography, the scattered wave is produced by the reference wave itself. Consider the experimental situation depicted in Fig. 4.1 and assume a (nearly) plane wave $P(\mathbf{r})$ as the illuminating wave field (the reference wave).⁸ Let us further assume that the detector is placed into the optical near field of the sample with transmission function $O(x, y; 0) \simeq \bar{O} + \delta O(x, y; 0)$ in the sample exit plane. Here \bar{O} denotes the mean transmission function of the object. Let us assume that the object obeys $|\delta O(x, y; 0)| \ll |\bar{O}|$. This, for example, allows the case of strong, but isolated absorption objects in an otherwise transparent background as an object, but not small holes in an otherwise nearly opaque background [60]. With the exit wave $\psi(x, y; 0) \simeq P(x, y; 0)O(x, y; 0)$ we write the wave field between planes $z = 0$ and $z = z_D$ as the sum

$$\psi(\mathbf{r}) = P(\mathbf{r})\bar{O} + P(\mathbf{r})\delta O(\mathbf{r}) = \psi_0(\mathbf{r}) + \psi_s(\mathbf{r}), \quad (4.52)$$

i.e. the superposition of a reference wave $\psi_0(\mathbf{r}) = P(\mathbf{r})\bar{O}$ and a scattered wave $\psi_s(\mathbf{r}) = P(\mathbf{r})\delta O(\mathbf{r})$, proportional to the reference wave, but much weaker, i.e. $|P(\mathbf{r})\delta O(\mathbf{r})| \ll |\bar{O}P(\mathbf{r})|$. We have assumed here that the scattered wave $\psi_s(x, y; z' > 0)$, propagated to any plane $0 < z < z_D$, can be written as a product of the propagated reference wave $P(\mathbf{r}_\perp; z')$ and the propagated sample contribution $\delta O(\mathbf{r}_\perp; z')$. This is certainly true for a perfect plane wave illumination. The intensity at the detector is then given as

$$\begin{aligned} I_D(\mathbf{r}_\perp; z_D) &\simeq |\psi_0(\mathbf{r}_\perp; z_D)|^2 + \psi_0^*(\mathbf{r}_\perp; z_D)\psi_s(\mathbf{r}_\perp; z_D) + \psi_0(\mathbf{r}_\perp; z_D)\psi_s^*(\mathbf{r}_\perp; z_D) + |\psi_s(\mathbf{r}_\perp; z_D)|^2 \\ &= |P(\mathbf{r}_\perp; z_D)|^2 (|\bar{O}|^2 + \bar{O}^* \delta O(\mathbf{r}_\perp; z_D) + \bar{O} \delta O^*(\mathbf{r}_\perp; z_D) + |\delta O(\mathbf{r}_\perp; z_D)|^2) \\ &\simeq |P(\mathbf{r}_\perp; z_D)|^2 (|\bar{O}|^2 + \bar{O}^* \delta O(\mathbf{r}_\perp; z_D) + \bar{O} \delta O^*(\mathbf{r}_\perp; z_D)). \end{aligned} \quad (4.53)$$

$|P(\mathbf{r}_\perp; z_D)|^2$ is the intensity of the empty beam which can be obtained in a separate measurement without the sample and can then be used to obtain the normalized detector intensity $\bar{I}_D(\mathbf{r}_\perp; z_D) := I_D(\mathbf{r}_\perp; z_D)/|P(\mathbf{r}_\perp; z_D)|^2$. Due to the assumption $|\delta O| \ll |\bar{O}|$ the last term proportional to $|\delta O|^2$ can be neglected. In an ideal in-line holography experiment the illumination is a perfect plane wave, so that $|P(\mathbf{r}_\perp; z_D)|^2 = \text{const}$. The product assumption is then always possible and the normalization step is not needed. Biological cells for hard x-rays are essentially pure phase objects, so that henceforth we set $\bar{O} = 1$.

Historically, the intensity $I_D(\mathbf{r}_\perp; z_D)$ was recorded on a transparent screen (e.g. a glass plate) covered with a photographic emulsion [60]. The optical reconstruction of the hologram was then obtained by illumination of the developed glass plate image, i.e. the intensity distribution $I_D(\mathbf{r}_\perp; z_D)$, with a plane wave and observation of the resulting intensity in a plane $z = 2z_D$, or if backwards illuminated, in plane $z = 0$. As nowadays the intensity is usually recorded on a CCD, we perform a numerical reconstruction of Eq. (4.53), i.e. we back-propagate the intensity $\bar{I}_D(\mathbf{r}_\perp; z_D)$ with the near field propagator D_z over a distance $z = -z_D$. The resulting field (with $\bar{O} = 1$) is given as

$$D_{-z_D}[\bar{I}_D(\mathbf{r}_\perp; z_D)] = \exp(-ikz_D) + \delta O(\mathbf{r}_\perp; 0) + D_{-z_D}[\delta O^*(\mathbf{r}_\perp; z_D)]. \quad (4.54)$$

⁸For a treatment of in-line holography within the x-ray context see also [108].

In lateral direction the first term is a constant, the second term is a focused ‘image’ of the object function $\delta O(\mathbf{r}_\perp; 0)$ in the sample exit plane. The third term gives rise to an unwanted ‘twin image’ which spoils the reconstruction.⁹

As a consequence, there are two drawbacks of conventional in-line holography [60]. First, the object needs to be a weak scatterer or sufficiently sparse (i.e. weak in the mean), so that the self-term $|\delta O|^2$ can be neglected. A second more fundamental problem is the defocused twin image that distorts the reconstructed object wave. While the assumption of a weak scatterer is valid for the illumination of single cells with a hard-x-ray beam, the twin image problem persists. Nevertheless, the possibility to obtain an image instantaneously from the recorded diffraction pattern with no restrictions on the lateral sample size is very valuable, especially, if further phase retrieval methods can be applied to the measured intensity distribution (see below). In this respect the holographic reconstruction may be compared to an optical microscopy image, obtained with a certain contrast enhancing method, such as differential interference contrast (DIC). A DIC image does not produce a quantitative phase map of the specimen, however, it very accurately reproduces the spatial features of the object. Finally, the holographic reconstruction is very sensitive to the back-propagation distance z_D , so that for a sparse three dimensional object it becomes possible to bring sample features at different depths into focus and thus measure their separation parallel to the optical axis [see e.g. 69].

Alternative holographic methods, such as off-axis holography [48] or Fourier transform holography [37], have been implemented for the x-ray case. Here the reference wave is prepared in such a way that the two twin image terms, which still exist, are laterally separated in the reconstruction plane. In the case of off-axis holography the reference and object wave reach the detection plane under different angles of incidence. As it is experimentally very difficult to produce two identical x-ray beams with high angular separation from the same synchrotron beam, this setup requires a free space close to the sample for the reference wave to freely propagate to the detector, so that the sample dimensions become limited.

4.4.3 Iterative reconstruction in the near field

The reconstruction of near field diffraction patterns is influenced by the oscillating contrast transfer functions discussed in Section 4.3.2: If the reconstruction is based on iterative maps as described above, and if a modulus constraint operator is used to make the data consistent with the measured diffraction pattern, the reconstructed object function remains unconstrained at the zero frequencies of the contrast transfer function. As a consequence, the reconstruction is unconstrained by the data for certain frequency components, similar to reconstructions from far field diffraction patterns, if there is missing information in the diffraction pattern due to the use of a beamstop [138, 143].

One way to circumvent this problem is to measure the near field diffraction pattern at multiple distances from the sample and using the obtained set of diffraction patterns for reconstructions [21, 23, 24]. The whole ensemble of diffraction patterns then constrains the

⁹In the optics literature the digital reconstruction process is mainly described by numerical forward propagation [see e.g. 108]. The second term in Eq. (4.54) then again becomes a focused object wave, whereas the last term gives rise to a defocused twin image.

reconstruction at all spatial frequencies, up to the resolution of the experiment. Another possibility, applicable in the case of spherical wave illumination which leads to *'effective'* near field diffraction patterns (see Section 4.3.3), is to work in the 'real' geometry of the experiment and use the illumination with high phase curvature explicitly in the algorithmic reconstruction. This is done in a technique named 'Fresnel Coherent Diffractive Imaging' [154]. It has been shown that high-curvature beams can strongly facilitate the reconstruction process [112]. For experimental realization, however, the complex illumination has to be known [113] which itself has to be recovered in a separate measurement and numerical reconstruction.

In the following we would like to study for an example, in how far it is possible to reconstruct *single* near field diffraction patterns in the (effective) plane wave geometry, without artifacts due to unconstrained frequencies. After all, the reconstruction is unconstrained only at distinct spatial frequencies. Mathematically, it might thus be possible to continue the reconstruction, a scalar complex function in 2D frequency space, also to these frequencies. Note that in the context of bandwidth extrapolation it is known that analytic continuation in principle allows for the recovery of the entire (complex) object spectrum, once it is known exactly on a finite domain in frequency space [60].

To this end, the simulated near field diffraction pattern shown in Fig. 4.5 was reconstructed using the Gerchberg-Saxton algorithm (see Section 4.4.1.2). It can be applied here, as with a *single* measurement the amplitude of the object wave is known in *two* planes: The measurement itself yields the amplitude in the detection plane, whereas in the sample exit plane the amplitude of a pure phase object is known to be one. For unstained, several microns thick biological material this assumption is usually well met (see Table 3.1) in case of illumination with hard x rays. The reconstruction was initialized here with a field of unit amplitude and zero phase. The propagation operator D_z in this case is the near field Fresnel propagator defined in Eq. (3.24) or, for practical implementations, its numerical counterpart expressed in Eq. (3.79). The reconstructed phase after 30000 iterations is shown in Fig. 4.9(c).

For comparison, the original simulated phase distribution is shown in Fig. 4.9(a), along with the phase of the holographic reconstruction that is obtained by a single-step back propagation of the normalized diffraction pattern (Fig. 4.9(b)). Evidently, the holographic reconstruction is distorted by the defocused twin image which manifests itself here as a bright halo around the cell boundaries. The reconstruction is not quantitative, but details of the cell appear in the reconstruction.

In order to assess the results with respect to the unconstrained frequencies in the reconstruction, the power spectral densities of the reconstructed phase maps are shown in comparison to the PSD of the simulated phase distribution in Fig. 4.10. The zeros in the PCTF appear as minima in the PSD of the holographic reconstruction, explaining some of the artifacts in the holographic reconstruction. In the GS reconstruction all of these minima have been removed, except the minimum at zero spatial frequency. This zero appears as a global modulation of the reconstructed phase distribution which hence does not give a quantitative representation of the original object phase. The GS-reconstruction, however, is already much closer to the true solution than the holographic reconstruction.

Unconstrained frequency components in the data can thus indeed be reconstructed correctly, at least partially. For the present example non-noisy, ideal data was assumed. The

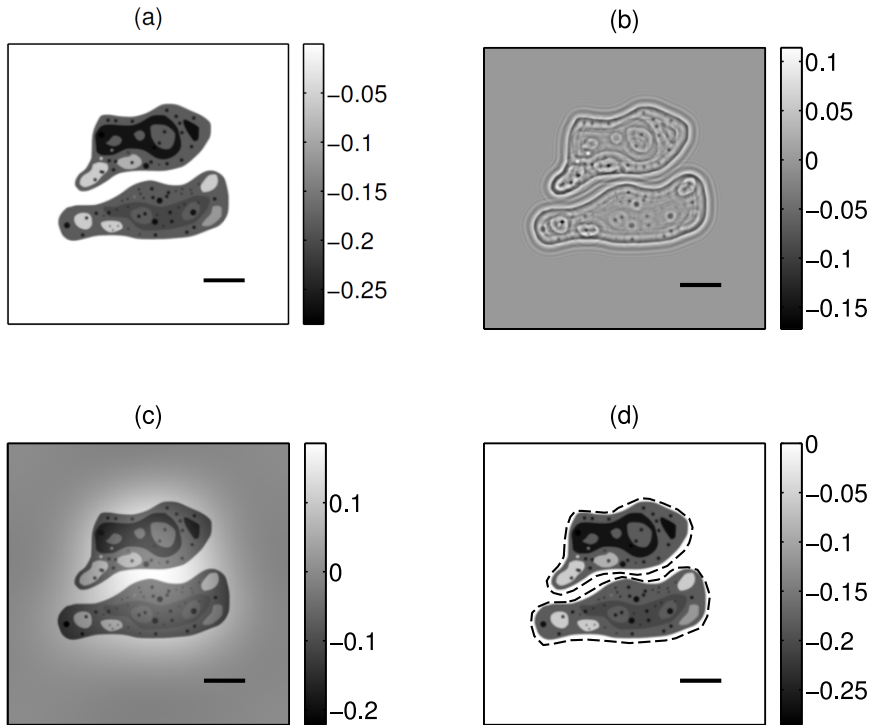


Figure 4.9: Comparison of different reconstruction schemes applied to a near field diffraction pattern. (a) Simulated phase distortion due to a phantom cell object (see also Fig. 4.2A), illuminated at 8 keV photon energy. For the corresponding near field diffraction pattern see Fig. 4.5. (b) Phase of the holographic reconstruction, obtained by simple back propagation of the diffraction pattern. (c) Reconstruction using the Gerchberg-Saxton algorithm. (d) Reconstruction using a modified Hybrid-Input-Output algorithm for pure phase objects (see main text). The support area used for the reconstruction is indicated by the dashed black lines around the cells. Colorbars indicate phase in rad, scalebars a distance of $1.5 \mu\text{m}$.

ability, however, of an iterative algorithm to fill the unconstrained frequency components with correct information can be expected to depend on the quality of the data.

An even better reconstruction becomes possible by using a reconstruction algorithm that is not subject to stagnation in local minima as the GS algorithm. For pure phase objects and near field diffraction patterns a real space¹⁰ constraint has been suggested [63] that forms the new exit plane amplitude as a linear combination of the current guess of the amplitude and the amplitude that has been updated by the detection plane modulus constraint operator. In this respect the update resembles the real space update of the HIO

¹⁰The term ‘real space’ here refers to the exit plane.

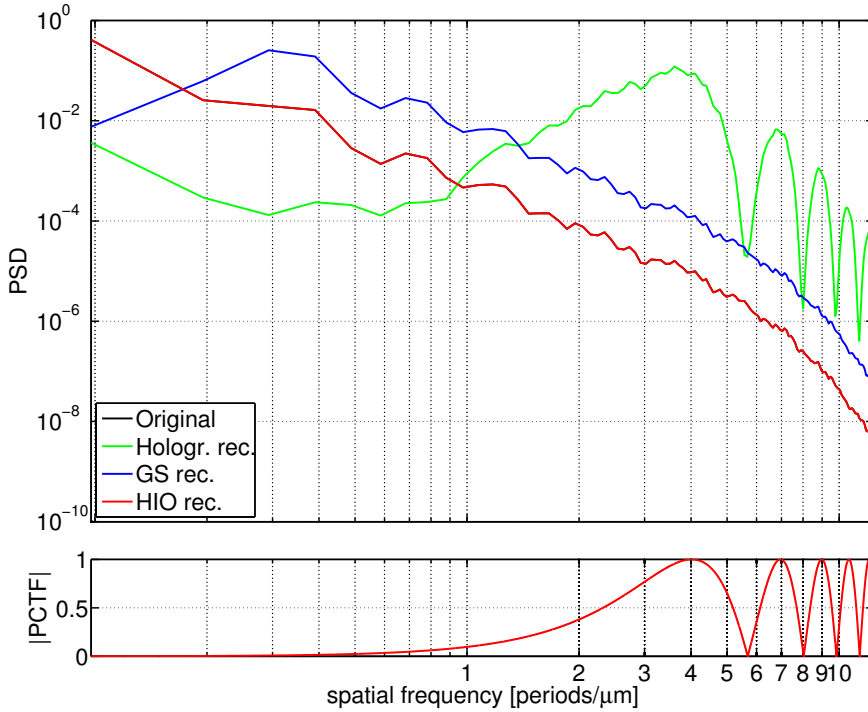


Figure 4.10: (Upper graph) Angular averaged power spectral densities (PSDs) of the reconstructed phase distributions shown in Fig. 4.9. The PSD of the phantom phase distribution is reproduced by the PSD of the HIO reconstruction. (Lower graph) Modulus of the corresponding phase contrast transfer function with characteristic zeros at distinct spatial frequencies.

algorithm. It is given here as

$$|O_{n+1}| = |O_n| - \beta \cdot (|O'_n| - 1), \quad (4.55)$$

where O_n and O'_n denote the n -th iterate of the object transmission function before and after application of the detection plane modulus constraint

$$O'_n := D_{-z} \left[\sqrt{\bar{I}} \cdot \frac{\tilde{O}_n}{|\tilde{O}_n|} \right]. \quad (4.56)$$

Here \bar{I} denotes the near field diffraction pattern of the object, normalized by the diffraction pattern of the empty beam and $\tilde{O}_n = D_z[O_n]$ denotes O_n , propagated into the near field over a distance z . The update (4.55) removes from the amplitude $|O_n|$ of the n -th iterate the difference between the amplitude of the updated iterate and the expectation value 1. β is a parameter controlling the feedback of the update. If $|O'_n|$ obeys the sample plane constraint, i.e. if $|O'_n| = 1$, the difference is zero and the update has no effect.

In the present numerical example there is a large empty region surrounding the cells where amplitude and phase are known to be uniform. Often this is also experimentally the

case. For the phase $\varphi(O)$ of the object function one expects a constant value in this region. As $\varphi(O)$ is only unique up to addition of a constant, one can freely chose the value to which the phase should be restricted outside the cellular area, e.g. to 0, just as in the simulated phase distribution. An additional update that exploits the knowledge of the phase and amplitude values in empty regions of the object function, is thus formulated here as

$$\begin{aligned} & \varphi(O_{n+1}(x, y)) \\ &= \begin{cases} \varphi(O_n(x, y)) - \gamma \cdot \varphi(O'_n(x, y)) \quad \forall (x, y) \notin S \\ \min\{\varphi(O'_n(x, y)), 0\} \quad \forall (x, y) \in S. \end{cases} \end{aligned} \quad (4.57)$$

Here S denotes the support area of the object. $\gamma \in [0, 1]$ is a feedback parameter that controls the gradual decrease of the phase outside the support region. Inside the support area the phase is restricted to negative values. This restriction amounts to the assumption that the object adds material to a substrate. For an object containing cavities in the substrate the phase should be left untouched in the support area. The restriction to negative values should also be avoided if the object is thick enough to induce phase jumps in the arg-function which is used in each iteration to determine the phase of the current iterate.

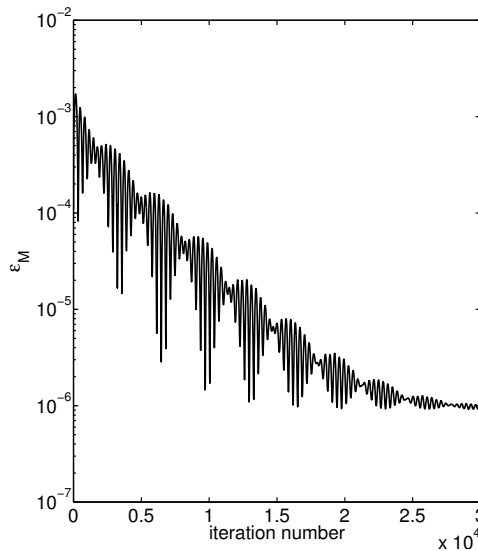


Figure 4.11: Reconstruction error ε_M with respect to iteration number, shown here for the reconstruction depicted in Fig. 4.9(d). The algorithm is an HIO type adapted for pure phase objects.

The reconstructed phase after 30000 iterations is shown in Fig. 4.9(d). The support area was determined from the holographic reconstruction shown in Fig. 4.9(b). The algorithm was initialized with an object function O_0 of unit amplitude and zero phase. In the implementation used here the real space constraints (4.55) and (4.57) were applied before the modulus replacement operation (4.56) during each iteration. As a consequence,

the algorithm ends with the modulus replacement operation and the last object estimate is consistent with the experimental data. To apply the first real space constraint, a first O'_0 is required. It was set here equal to O_0 . The algorithm can, however, also be used with iterations in the usual sequence of modulus replacement and exit plane constraints. The high number of iterations was required here to reach a region where variations in the error $\varepsilon_{M,n} = \|\tilde{O}_n - \sqrt{\tilde{I}}\|$ become small. The evolution of the error corresponding to the reconstruction depicted in Fig. 4.9(d) is shown in Fig. 4.11.

The final reconstructed phase map shown in Fig. 4.9(d) gives a very accurate, quantitative representation of the original phase distribution (cf. 4.9(a)). The accuracy of the reconstruction is also represented by its power spectral density shown in Fig. 4.10 which fully reproduces the PSD of the simulated phase map.

For the application to noisy data the HIO variant described here can also be combined with the modified modulus replacement operator defined in Section 4.6. A variant of this modified operator that has been applied to experimental data, is described in Chapter 7.

4.4.4 Scanning microscopy

So far only reconstruction procedures involving the measurement of a single diffraction pattern have been considered, if we exclude the Gerchberg-Saxton case of two intensity measurements, made at different planes downstream of the object. Nevertheless, the geometry of the illumination with respect to the object is always the same in all reconstruction schemes discussed so far.

The generalized oversampling ratio, discussed above for the case of far field diffraction with plane wave illumination, requires the area (volume), where the object function is known to be at least half as large as the total density area. For practical applications this requires the object to be isolated. Theoretically, one can generate an isolated exit wave field by using a sharp-edged illumination function. This would enable to apply the far field CDI technique also to extended specimens. Experimentally, it turns out, however, that any confined illumination will have more or less soft edges due to diffraction effects [139], unless an opaque mask is placed directly onto the extended specimen.

These limitations call for an extension of coherent microscopy techniques to the concept of scanning microscopy. It has been applied in lens-based incoherent x-ray microscopy for a long time [79]. In the simplest mode, where only the total absorption by the sample is measured, an x-ray focusing device (a Fresnel zone plate, a mirror, etc.) is used to provide a confined illumination at the sample, and the transmitted photons are collected on a (not necessarily) 2D detector. If a coherent beam is used for illumination and a 2D pixelated detector for recording the diffraction pattern in the far field of the exit wave, a phase contrast mode is added to the transmission mode. In simple terms, a linear lateral phase gradient $\partial\varphi/\partial x$ due to the sample, e.g. in x -direction will lead to the deflection of the incident beam by an angle $\Delta\alpha$ [21, 30]:

$$\Delta\alpha = -\frac{1}{k} \frac{\partial\varphi}{\partial x}. \quad (4.58)$$

This refraction phenomenon gives rise to a coarse-grained measure for the differential phase contrast in x -direction, namely the displacement of the beam center of a refracted

beam with respect to the center of the unrefracted beam. Let \mathbf{r}_j denote the j -th scan position in the sample plane. More precisely, \mathbf{r}_j denotes the position of the beam center at the sample in this position. The DPC signal in x -direction can then be calculated as the ‘center of mass’ of the diffracted intensity distribution [43]:

$$\text{DPC}_x(\mathbf{r}_j) = \frac{\sum_{\mathbf{r}'} x' I_j(\mathbf{r}')}{\sum_{\mathbf{r}'} I_j(\mathbf{r}')}. \quad (4.59)$$

The expression for the y -direction is analogous. $\mathbf{r}' = (x', y')$ here denotes the real space coordinates of the detector pixels and I_j the recorded intensity distribution for the j th scan point.

A dark field mode can be added by summing over the diffracted signal outside an area A in the center of the diffraction pattern. At scan point \mathbf{r}_j this reads

$$\text{DF}(\mathbf{r}_j) = \sum_{\mathbf{r}' \notin A} I_j(\mathbf{r}'). \quad (4.60)$$

Above concepts can be driven towards fully quantitative scanning phase contrast microscopy [30, 98, 140]. The finest lateral structures that can be imaged in the specimen are, however, limited by the lateral extent of the illumination in the sample plane.

4.4.5 Ptychography

An alternative is opened up by the so-called **ptychography** technique which combines scanning microscopy with diffraction microscopy [141]. Often the method is now also referred to as **Ptychographic Coherent X-ray Diffractive Imaging (PCDI)**. For a recent review see [117]. Here the diffraction patterns collected at each scan point are used simultaneously for iterative phase retrieval, using the same type of algorithms as described above.

The naming “ptychography” (Greek ‘ $\pi\tau\nu\zeta$ ’ for ‘(the) fold’) goes back to a concept devised around 1970 [66, 70] to solve the crystallographic phase problem in diffractive electron microscopy. If a crystalline object of infinite lateral extension is illuminated by a plane wave, the diffraction pattern will consist of distinct Bragg peaks with no intensity in between. If the illumination has a finite lateral extent, the Bragg peaks become translated copies of the illumination far field diffraction pattern. In other words, the far field of the crystal is convoluted (“folded”) with the far field of the illumination. Hence, the diffraction patterns of neighboring Bragg peaks start to overlap. It is then possible [70, 117] to retrieve the phase values at the Bragg peaks and in the overlap region up to a simple sign ambiguity for the imaginary part of the complex field at the Bragg positions. This ambiguity can further be resolved by obtaining a second diffraction pattern with the sample laterally shifted by a small distance with respect to the illumination [70, 117]. The convolution property of the far field diffraction pattern thus can be used for the reconstruction of the unknown phases at the Bragg peaks [70]. Hence the name ‘ptychography’. Mainly due to technical limitations of the available electron microscopes there was a time span of more than 20 years between these theoretical considerations and the first experimental short-wavelength demonstration “closest to classical STEM [Scanning transmission electron microscopy] ptychography” [102, 117].

4.4.5.1 The Ptychographic iterative engine

The crucial step for the application to non-crystalline samples was then the implementation of concepts from iterative phase retrieval (see above) for the analysis of a ptychographic dataset into an algorithm that was named the ‘‘Ptychographic Iterative Engine’’ (PIE) [119]. We briefly describe this first iterative non-crystallographic ptychography algorithm here.

The goal of the reconstruction is to obtain the extended 2D complex object transmission function $O(\mathbf{r})$. Here¹¹ $\mathbf{r} = (x, y)$ denotes the Cartesian real space coordinate in the plane perpendicular to the propagation direction. At the j th scan point the exit wave $\psi_j(\mathbf{r}) = O(\mathbf{r})P(\mathbf{r} - \mathbf{r}_j)$ behind the sample can be described by a product of the object function $O(\mathbf{r})$ and the complex illumination $P_j(\mathbf{r}) = P(\mathbf{r} - \mathbf{r}_j)$ where \mathbf{r}_j corresponds to a lateral shift of P with respect to a certain reference position, e.g. the center of the illumination field at the first scan position. As only the relative shift between the object and the illumination matters for the reconstruction, this description is equivalent to the experimentally more common case of a fixed illumination and a movable object. Let us assume that the experiment comprises a total number of N_S scan positions.

At each scan point a 2D diffraction pattern is collected, usually in the far field of the exit wave ψ_j , so that the intensity distribution in the detector plane for the j th scan point can be described as $I_j(\mathbf{q}) = |\tilde{\psi}_j(\mathbf{q})|^2$ with $\tilde{\psi}_j$ denoting the 2D Fourier transform of ψ_j . Here $\mathbf{q} = (q_x, q_y)$ denotes the 2D reciprocal space coordinate. Sufficient sampling of the far field diffraction pattern can be guaranteed by a sharply confined illumination function with a support that fills up to half the domain of P_j . Using a pinhole to confine an incident wave field, this can approximately be achieved. Due to diffraction effects within the pinhole and on the short propagation distance between the pinhole exit plane and the sample, the illumination is never sharply confined. This poses no difficulty experimentally, as long as the illumination is ‘‘substantially’’ localized [118].

In the original PIE algorithm [119] the complex illumination $P(\mathbf{r})$ is assumed to be known in advance. The estimated object function at iteration n is denoted as $O_n(\mathbf{r})$. As an initial guess a random field may be chosen, while a unit array $O(\mathbf{r}) = 1$ is a ‘‘usual’’ guess [117]. The first iteration ($n = 1$) proceeds as follows [13, 119]:

- (i) The current estimate of the exit wave at the j th scan point is generated via $\psi_{n,j}(\mathbf{r}) = P(\mathbf{r} - \mathbf{r}_j)O_n(\mathbf{r})$. The iteration starts with $j = 1$.
- (ii) The exit wave is updated by the Fourier constraint map as defined before, i.e. $\psi'_{n,j} = P_M(\psi_{n,j})$.
- (iii) The next step is the crucial ingredient of the PIE algorithm. The object function in the illuminated area at the current position is updated according to

$$O_{n+1}(\mathbf{r}) = O_n(\mathbf{r}) + \beta U(\mathbf{r})(\psi'_{n,j}(\mathbf{r}) - \psi_{n,j}(\mathbf{r})) \quad (4.61)$$

with the update function

$$U(\mathbf{r}) = \frac{|P(\mathbf{r} - \mathbf{r}_j)|}{\max(|P(\mathbf{r} - \mathbf{r}_j)|)} \frac{P^*(\mathbf{r} - \mathbf{r}_j)}{(|P(\mathbf{r} - \mathbf{r}_j)|^2 + \alpha)}. \quad (4.62)$$

¹¹Note that we have dropped the \perp -sign now.

Afterwards, steps (i)-(iii) are repeated for all remaining $N_S - 1$ scan positions, so that a new estimate $O_{n+1}(\mathbf{r})$ is obtained in the entire domain of the object function. Afterwards, one full iteration is completed.

The algorithm proceeds in a serial processing of iteration steps (i)-(iii) at each scan point. The object update in step (iii) is reminiscent of the real space update in the HIO algorithm. The scalar parameter β , usually chosen between 0.5 and 1, controls the feedback of the update. Unlike in the HIO algorithm, the updated object function is no longer a simple linear combination of input and output of the Fourier constraint map, as step (iii) involves the multiplication of the difference between output and input with the complex field $U(\mathbf{r})$. The 2D factor $|P(\mathbf{r} - \mathbf{r}_j)| / \max(|P(\mathbf{r} - \mathbf{r}_j)|)$ accounts for a stronger weight of regions where $P(\mathbf{r})$ is large [120]. Multiplication with $P^*(\mathbf{r} - \mathbf{r}_j) / |P(\mathbf{r} - \mathbf{r}_j)|^2$ can be interpreted as the removal of the probe function from the difference of input and output exit waves, so that only a difference of object functions remains [13]. α is a small positive number that prevents singularities due to zeros in the illumination function.

A critical ingredient which is not explicitly enforced in the algorithm is a significant amount of overlap between illuminated areas of neighboring scan positions on the object. Consider the update of the object function, step (iii), in iteration n at scan point j . When the algorithm proceeds to scan point $j + 1$ and if the illuminated regions of scan points j and $j + 1$ overlap, the object update at position $j + 1$ will profit in the overlap region from the update of the object function at position j . This redundancy greatly increases the speed of convergence, so that after as little as 30 PIE iterations good reconstruction results can be obtained for experimental data [13].

For an illumination that is confined by a circular pinhole of diameter $2r$, a relative overlap between two scan positions has been defined as [13]

$$o = 1 - \frac{a}{2r}, \quad (4.63)$$

i.e. $o \in [0, 1]$. Here a denotes the distance between the centers of the illuminated areas of the two scan positions. A value of $o = 0.6$ has been identified [13] as a very good compromise between invested scan time and reconstruction quality. Neither for $o \rightarrow 0$ nor for $o \rightarrow 1$ good reconstruction results are achieved. In those cases the PIE algorithm reduces to an HIO algorithm with the support constraint being replaced by a known illumination constraint [13].

Shortly after its introduction, the PIE reconstruction scheme was experimentally demonstrated for both, visible light [118] and hard x-ray [120] photons used for illumination. It was the latter experiment which initiated a large interest in ptychographic reconstruction in the field of coherent x-ray microscopy.

4.4.5.2 Ptychography with probe retrieval

A considerable experimental drawback of the original PIE scheme is the requirement of an *a priori* known complex illumination or probe function. With this requirement the quality of the object function can never exceed the quality of the guessed illumination. Practical experience shows, however, that an experimental illumination field, especially in the case of hard x rays, usually substantially differs from ideal assumptions. In the case of pinhole illumination the limits are clearly given by the fabrication process of pinholes with high aspect ratios on the order of $d : t \simeq 10$, where d denotes the diameter and t the depth of the pinhole.

A major improvement was thus given by ptychographic reconstruction schemes which allow for the *simultaneous* reconstruction of both the complex illumination and the object function. Three rather independent methods exist at the moment [62, 90, 141]. The method demonstrated in [90] is an extension of the PIE technique, whereas the scheme described in [62] is based on non-linear optimization along “the gradient of a squared-error metric with respect to the object, illumination and translations”.

This first scheme to be experimentally demonstrated for hard x rays was the one by THIBAULT and coworkers [141]. It is based on the difference map algorithm and can be completely explained [139, 141] in the language of projections onto constraint sets as outlined above. This is the reconstruction scheme which was used for all ptychographic reconstructions obtained for this thesis.¹² The algorithm and its theoretical foundations are outlined in the following.

The “ptychographic problem” can be formulated [139] as the problem to find single functions $P(\mathbf{r})$ and $O(\mathbf{r})$, so that

$$I_j(\mathbf{q}) = |\mathcal{F}[P(\mathbf{r} - \mathbf{r}_j)O(\mathbf{r})]|^2 \quad \text{for } j = 1 \dots N_S \quad (4.64)$$

$$= |\tilde{\psi}_j(\mathbf{q})|^2 \quad \text{for } j = 1 \dots N_S \quad (4.65)$$

with symbols as defined above. As before, a single exit wave or “view” [141] is a vector in the space \mathcal{E} of all complex arrays with N_P pixels, where N_P is the number of pixels in the recorded diffraction pattern. The exit waves ψ_j at all scan points can then be written as a vector

$$\Psi := (\psi_1, \psi_2, \dots, \psi_{N_S}) \quad (4.66)$$

in the product \mathcal{E}^{N_S} of spaces \mathcal{E} of each individual view [141]. Two constraint sets \mathcal{C}_M and \mathcal{C}_O can be defined in \mathcal{E}^{N_S} . \mathcal{C}_M is given by all Ψ whose elements ψ_j obey Eq. (4.65). \mathcal{C}_O is given by all Ψ whose elements can be written as the product of two functions $P(\mathbf{r})$ and $O(\mathbf{r})$, so that

$$\psi_j(\mathbf{r}) = P(\mathbf{r} - \mathbf{r}_j)O(\mathbf{r}) \quad \text{for } j = 1 \dots N_S. \quad (4.67)$$

A projection onto \mathcal{C}_M can be defined as [139]

$$\Pi_M : \psi_j \mapsto P_M(\psi_j) \quad \text{for } j = 1 \dots N_S \quad (4.68)$$

¹²I am thankful to Pierre Thibault for providing an example version of the implemented Matlab software code.

where P_M is the usual modulus constraint map as defined before. The projection onto \mathcal{C}_O is defined as [139]¹³

$$\Pi_O : \psi_j \mapsto \hat{\psi}_j^O(\mathbf{r}) := \hat{P}(\mathbf{r} - \mathbf{r}_j) \hat{O}(\mathbf{r}) \quad \text{for } j = 1 \dots N_S. \quad (4.69)$$

\hat{O} and \hat{P} are fields that minimize the distance of Ψ to an element Ψ^O of the constraint set \mathcal{C}_O . The minimized distance can be written as [139]

$$\|\Psi - \hat{\Psi}^O\|^2 = \frac{1}{N_S N_P} \sum_j \sum_{\mathbf{r}} |\psi_j(\mathbf{r}) - \hat{P}(\mathbf{r} - \mathbf{r}_j) \hat{O}(\mathbf{r})|^2. \quad (4.70)$$

The prefactor $(N_S N_P)^{-1}$ has been introduced here to make the norm consistent with the one defined before. A solution to Eq. (4.70) is not possible in a closed form [139]. Setting the derivative of $\|\Psi - \hat{\Psi}^O\|^2$ to zero with respect to \hat{O} and \hat{P} , however, yields a system of coupled equations for \hat{O} and \hat{P} . It is given as [139, 141]

$$\hat{O}(\mathbf{r}) = \frac{\sum_j \hat{P}^*(\mathbf{r} - \mathbf{r}_j) \psi_j(\mathbf{r})}{\sum_j |\hat{P}(\mathbf{r} - \mathbf{r}_j)|^2}, \quad (4.71)$$

$$\hat{P}(\mathbf{r}) = \frac{\sum_j \hat{O}^*(\mathbf{r} + \mathbf{r}_j) \psi_j(\mathbf{r} + \mathbf{r}_j)}{\sum_j |\hat{O}(\mathbf{r} + \mathbf{r}_j)|^2}. \quad (4.72)$$

The argument $\mathbf{r} + \mathbf{r}_j$ here compensates the shift of the probe function at each scan point by shifting the exit wave and the object function in the reverse direction, as generally

$$\psi_j(\mathbf{r}) = P(\mathbf{r} - \mathbf{r}_j) O(\mathbf{r}) \quad (4.73)$$

$$\Leftrightarrow \psi_j(\mathbf{r} + \mathbf{r}_j) = P(\mathbf{r}) O(\mathbf{r} + \mathbf{r}_j). \quad (4.74)$$

The distance as defined in Eq. (4.70) is observed to be effectively minimized by a sequential iteration of the system (4.71-4.72) for a small number of iterations [139].

Once the projections have been defined, the iteration procedure of the algorithm can be described as follows. Given the n th iterate Ψ_n , the new global iterate Ψ_{n+1} is formed according to the difference map update with [139]

$$\Psi_{n+1} = \Psi_n + D(\Psi_n) = \Psi_n + B(\Psi_n) - A(\Psi_n) \quad (4.75)$$

and

$$A(\Psi_n) := \Pi_O(\Psi_n), \quad (4.76)$$

$$B(\Psi_n) := \Pi_M(2\Pi_O(\Psi_n) - \Psi_n). \quad (4.77)$$

For initialization, one needs a first guess for the illumination wave field P which can usually be prepared based on the knowledge about the experiment's geometry. The initial vector Ψ_1 can be generated as a collection of random fields ψ_j , but may also be set equal

¹³There is a minor difference in the notation used here compared to that used in [139]: The quantity $\Psi^O = (\psi_j^O)$ that minimizes the distance as defined in Eq. (4.70) is also denoted with a $\hat{\cdot}$ here, just as P and O are.

to the first guess of the illumination function [139]. As a first operation the projection $\Pi_O(\Psi_1)$ is evaluated. To this end the system of equations (4.71-4.72) is iterated for a few times (object and illumination constraint loop). Usually, the probe is held fixed during the first global iterations, so that only Eq. (4.71) is iterated for $n = 1, \dots, 10$, say. Subsequently, every view ψ_j is updated according to the modulus constraint map P_M and the new “state vector” [139] is formed according to Eq. (4.75). Note that Eq. (4.75) decouples [141] into N_P equations for each element ψ_j of Ψ (modulus constraint loop), once the object update $P_O(\Psi_n)$ has been calculated. Once this step is finished, a complete new state vector has been generated and one global iteration has been completed. The reconstruction progress is observed by the difference map error¹⁴

$$\|\Psi_{n+1} - \Psi_n\|^2 = \|D(\Psi_n)\|^2. \quad (4.78)$$

Again, the algorithm profits from the redundant information in overlap regions of neighboring illuminated areas. Again, this consistency is not explicitly enforced but naturally flows into Eqs. (4.71-4.72). Once the difference map error has reached a steady state, a solution is found by application of a A or B to the last iterate $\Psi_{N_{it}}$ after N_{it} iterations. Usually, the final solution is found by complex averaging over an ensemble of iterates in the steady state [132].

4.4.6 Convergence and uniqueness

Ideal convergence of an iterative reconstruction algorithm is achieved, if the solution ψ^* is invariant under further iteration and if the error has decreased to zero. In practical applications this as good as never the case [19, 132, 138] due to noise in the diffraction data, possibly missing data regions in the diffraction pattern, systematic errors in the data such as the averaging over pixel areas instead of sampling the intensity at a certain point, or, quite generally, due to the “incompatibility in the constraints” which may be caused by the noise in the data, for example [143].

The HIO and DM algorithms are known [92] to be global reconstruction schemes in the sense that they do not get trapped in local minima of the error landscape. Therefore, they are usually favored with respect to the ER algorithm which may easily be trapped in a local minimum far away from the global solution. The closest case to convergence one can achieve by application of a global reconstruction scheme to noisy data is thus a steady state in the algorithmic dynamics which is indicated by an error that weakly fluctuates around an otherwise very small, but constant mean value [138]. This situation may then also be referred to as ‘convergence’ (in a practical sense) which is, for the HIO and DM algorithm, known to be a sign of being close to the true solution [139]. As a consequence of the remaining dynamics in the algorithm, even in this steady state, subsequent iterates will differ from each other. To still achieve a reproducible solution, it is common practice to average over many complex iterates. This can be implemented either by averaging over all final complex iterates that have been obtained by starting from individual random initial guesses [19], or by averaging over many complex iterates from the same algorithmic run,

¹⁴With D defined as $D^2(\Psi) := 1/(N_S N_P) \sum_j \sum_r |\psi_j(\mathbf{r})|^2$.

after the reconstruction has reached a steady state [132]. Obviously, the second method has the advantage of being much faster.

The uniqueness of the obtained result is another issue. First of all, a solution is usually unique only up to a global phase factor $\exp(i\varphi)$ with $\varphi \in \mathbb{R}$, either in the near or far field geometry.

Further examples of such ambiguities can be given especially in the far field geometry where a simple Fourier transform relates the exit wave and the wave in the detection plane. It follows from the properties of the Fourier transform that if $f(\mathbf{r})$ is a solution, then also $f(\mathbf{r} + \mathbf{r}_0)$ and $f^*(-\mathbf{r} + \mathbf{r}_0)$ are solutions with \mathbf{r}_0 denoting a constant translation vector [101]. It is intuitively clear that this ‘twin-image’ ambiguity is especially critical, if the object is highly symmetric and both solutions are consistent with the applied support constraint [129]. Apart from these ‘trivial’ ambiguities other may exist, but are very unlikely in more than one dimension, at least in the simple far field geometry [5].

In the (effective) near field geometry ambiguities may arise from the unconstrained frequencies due to the quadratic phase term in the Fresnel propagator. On the other hand and unlike in the far field case, an inversion with respect to the origin usually is not compatible with the diffraction pattern and convergence properties have been observed to be superior to the far field case [104]. Intuitively, this becomes clear as the diffracted intensity itself has strong similarity with the object.

Ptychography involves the simultaneous reconstruction of multiple diffraction patterns. If, as it is always the case within this thesis, these diffraction patterns are recorded in the far field of the exit wave, the same considerations apply in principle to the uniqueness of each of the reconstructed views as for the case of a single far field diffraction pattern [139]. Additional ambiguities are enabled [139] by the separation of the exit waves into a product of the object function $O(\mathbf{r})$ and a laterally translated illumination function $P(\mathbf{r} - \mathbf{r}_j)$: If $O(\mathbf{r})$ and $P(\mathbf{r})$ are solutions, then also $f(\mathbf{r})O(\mathbf{r})$ and $f^{-1}(\mathbf{r})P(\mathbf{r})$ will be a solution, if

$$f(\mathbf{r}) = f(\mathbf{r} - \mathbf{r}_j) \quad \forall \mathbf{r}_j. \quad (4.79)$$

For the scan points located on a Cartesian grid, $f(\mathbf{r})$ may be any periodic function of that grid [139]. For strong objects this usually poses no difficulty. For weak objects, however, it can be advantageous to use a non-Cartesian grid for the scan positions [34]. Practical experience shows that in the case of large overlap regions and therefore strong overdetermination a stable reconstruction can be obtained after relatively few iterations [13, 139].

4.5 Resolution

For the definition of **resolution** it is important to note whether it is defined as a function of the apparatus or a function of the specimen [142]. In diffraction microscopy, the latter definition is usually followed [142]. Note that, for example, a strongly scattering sample (e.g. a nanostructured sample made of heavy elements) allows to collect much more scattered photons from a certain subvolume than a weakly scattering sample (i.e. a biological cell), given the same incident photon fluence and setup. From an information theoretical point of view it is thus intuitively clear that higher resolutions can be obtained for the first group

of samples compared to the latter, under equivalent experimental conditions and using the same setup.

The following derivation of a Rayleigh resolution of a square detector placed into the far field is adapted from [105]. Consider again the basic setup of a coherent XM experiment as depicted in Fig. 4.1. If the detector is placed into the far field of the sample, the wave field at the detector is given by Eq. (3.35), i.e. the measured amplitude will be simply proportional to the modulus $|\tilde{\psi}(\mathbf{k}_\perp)|$ of the Fourier transform of the exit wave. For the recording of the diffraction pattern usually a detector with a squared detection area of sidelength L is used, so that the measured amplitude in the small-angle approximation is given as

$$\frac{1}{L^2} \Pi_L\left(x' = \frac{z}{k} k_x\right) \Pi_L\left(y' = \frac{z}{k} k_y\right) |\tilde{\psi}(k_x, k_y)| = \frac{z^2}{L^2 k^2} \Pi_{\frac{Lk}{z}}(k_x) \Pi_{\frac{Lk}{z}}(k_y) |\tilde{\psi}(k_x, k_y)| \quad (4.80)$$

with Π_L as defined in Eq. (2.28). A reconstructed exit wave field $\psi_r(x, y)$ will thus always be convoluted with the Fourier back transform of the hat-function [105]. A point source $\delta(x, y)$ will be reconstructed as a wave proportional to

$$\text{sinc}\left(\frac{Lk}{2z} x\right) \text{sinc}\left(\frac{Lk}{2z} y\right). \quad (4.81)$$

The Rayleigh criterion suggests that the resolution is defined by the smallest distance Δr_R between the images of two ideal point sources, under which the images can still be recognized as originating from two laterally separated sources. This smallest distance is reached when the maximum of one point source image coincides with the first minimum of the second one, i.e. [105]

$$\Delta r_R = \pi \frac{2z}{Lk} = \frac{\lambda z}{L} \simeq \frac{\lambda}{2\text{NA}} \quad (4.82)$$

where the **numerical aperture** is defined as $\text{NA} = \sin(\theta_{\max})$. Here θ_{\max} denotes the maximum scattering angle, under which a signal can be collected by a detector with its center placed on the optical axis. For all experiments in this thesis we can approximate $\text{NA} \simeq L/(2z)$.

According to the properties of the DFT and the sampling theorem (see Chapter 2), the maximum frequency k_{\max} measurable with a detector containing N pixels along the x -direction is given as $k_{\max} = N/2\Delta k$. With the scaling relation $\mathbf{k}_\perp = k/z\mathbf{r}'_\perp$ between the Fourier space and real space variables in the detector plane, valid in the small angle approximation, one also obtains $\Delta k = k/z\Delta x'$. As a consequence, $\Delta k = Nk\Delta x'/(2z) = Lk/(2z) = L\pi/(\lambda z)$ for a detector pixel width $\Delta x'$. The corresponding Nyquist rate in real space is $1/\Delta x = k_{\max}/\pi$ with pixel width Δx . With the previous equation one thus obtains $1/\Delta x = L/(\lambda z)$, so that

$$\Delta x = \Delta r_R. \quad (4.83)$$

In other words, the required Nyquist sampling period to sample a reconstruction containing measured Fourier components up to a frequency k_{\max} is equal to the Rayleigh resolution of the imaging experiment. As sampling with width Δx allows for the representation of signals with smallest period $2\Delta x$, one often refers to Δx as the half-period resolution of the experiment.

Δr_R , as determined from the detector and experiment geometry alone is usually not referred to as the resolution in coherent XM [142]: In many experimental situations the detected signal has decreased to zero at the edge of the detector, so that no signal from the sample has been collected that corresponds to the highest spatial frequency components which can be collected by the apparatus. Alternatively, one could give a resolution estimation based on the scattering angle, below which the scattered signal exceeds a certain signal-to-noise ratio (SNR) [19]. This quantification, however, would be solely based on the recorded data and would not account for the significant step of phase retrieval in diffraction microscopy during which additional image degradation can take place [19, 142]. A commonly accepted procedure for far field CDI goes slightly further, similar to the procedure of finding a reproducible solution from a complex average over many solution candidates as described above. One defines the so-called **phase retrieval transfer function (PRTF)** [19]

$$\text{PRTF}(\mathbf{k}_\perp) := \frac{|\mathcal{F}[\overline{\psi}](\mathbf{k}_\perp)|}{\sqrt{I(\mathbf{k}_\perp)}}. \quad (4.84)$$

$\overline{\psi}$ here denotes the complex average

$$\overline{\psi} := \frac{\sum_j \psi_j}{\sum_j j}. \quad (4.85)$$

The ψ_j can be selected iterates from a single reconstruction run, once the algorithm has reached a steady state [132], i.e. $\overline{\psi}$ is usually the ‘solution’ of the reconstruction and therefore has already been computed. Due to the linearity of the Fourier transform this complex averaging can be exchanged with the Fourier transformation. If the phases of $\mathcal{F}[\overline{\psi}](\mathbf{k}_\perp)$ are reconstructed consistently for a certain value \mathbf{k}_\perp , the amplitude $|\mathcal{F}[\overline{\psi}](\mathbf{k}_\perp)|$ has a finite non-zero value. If the phases add randomly, the averaged Fourier amplitude decreases to zero. Therefore, the PRTF is equal to 1 at spatial frequencies \mathbf{k}_\perp , for which a reliable reconstruction has been obtained. For increasing $|\mathbf{k}_\perp|$ the experimental signal decreases rapidly, the reconstruction becomes non-reliable and the PRTF eventually decreases to zero. For biological samples with globally isotropic diffraction patterns, the PRTF is also isotropic, to that it is usually averaged over all diffraction angles. A remaining ambiguity in the definition of resolution based on the PRTF is then given by the decay value of the PRTF, which is used to define the highest spatial frequency that can ‘reliably’ phased.

Note that the PRTF definition is not directly applicable to near field diffraction patterns, as those do not correspond to a frequency spectrum of the sample.

An independent determination of resolution is possible, if the sample is a test structure with lithographically fabricated patterns such as ‘lines and spaces’ in a defined frequency range. Here the smallest line/space period which can still clearly be recognized, gives a measure of resolution. Note, however, that the so obtained resolution still depends on the scattering power of the (test) specimen.

A similar measure of resolution can be given by the line spread function of the (coherent) imaging process. In incoherent imaging applications this can be obtained by scanning a sharp absorbing edge through the beam whose width is to be determined. Similar to this measurement process one may consider the amplitude or phase profile perpendicular to a sharp edge in a reconstruction from a coherent XM experiment. If this profile is fitted by a

sigmoidal function, e.g. a Gaussian error function, the FWHM of the associated Gaussian function is a measure of resolution [1]¹⁵.

4.6 Treatment of noise in diffraction data

As outlined in Section 3.1.5 any experimental diffraction pattern is spoiled by Poissonian noise. In the iterative reconstruction algorithms discussed so far as well as in the direct holographic reconstruction, noise has not been taken into account. On the other hand, it is known [153] that e.g. for iterative reconstruction algorithms as described above noise in the diffraction pattern usually distorts the reconstruction result.

In iterative propagation schemes as described above the essential operation introducing the experimental data and therefore also its noise to the reconstruction process is the (Fourier) modulus constraint operation. Let us assume for a moment the diffraction pattern $I(\mathbf{k}_\perp)$ has been recorded in the far field of the sample exit wave. The modulus replacement operation for ideal data is then given by Eq. (4.31), i.e.

$$\tilde{\psi}'(\mathbf{k}_\perp) = \sqrt{I(\mathbf{k}_\perp)} \frac{\tilde{\psi}(\mathbf{k}_\perp)}{|\tilde{\psi}(\mathbf{k}_\perp)|}. \quad (4.86)$$

Here $\tilde{\psi}'(\mathbf{k}_\perp)$ denotes the Fourier transformed exit wave after the update. To account for noise in an experimental diffraction pattern the so-called annulus projection has been devised [19, 92]. For any \mathbf{k}_\perp the old amplitude $|\tilde{\psi}(\mathbf{k}_\perp)|$ is mapped into the annulus

$$\{z \in \mathbb{C} \mid |z| \in [|\tilde{\psi}(\mathbf{k}_\perp)| - \sigma(\mathbf{k}_\perp), |\tilde{\psi}(\mathbf{k}_\perp)| + \sigma(\mathbf{k}_\perp)]\}.$$

$\sigma(\mathbf{k}_\perp)$ is the standard deviation of the experimental amplitude $\sqrt{I(\mathbf{k}_\perp)}$, as estimated from the noise statistics. Numerically, this projection is rather expensive, as at every \mathbf{k}_\perp , i.e. for every pixel in the diffraction pattern, the current estimate of the Fourier amplitude has to be compared to a certain value before the map can be applied.

A simple and computationally efficient alternative is given by¹⁶

$$|\tilde{\psi}'_{\text{rel}}(\mathbf{k}_\perp)| := \begin{cases} (1 - \frac{d}{D}) \sqrt{I(\mathbf{k}_\perp)} + \frac{d}{D} |\tilde{\psi}(\mathbf{k}_\perp)| & \text{if } d > D, \\ |\tilde{\psi}(\mathbf{k}_\perp)| & \text{if } d \leq D. \end{cases} \quad (4.87)$$

Here d is the summed deviation

$$d = \left(\frac{1}{N} \sum_{\mathbf{k}_\perp} \left| |\tilde{\psi}(\mathbf{k}_\perp)| - \sqrt{I(\mathbf{k}_\perp)} \right|^2 \right)^{1/2} \quad (4.88)$$

between the Fourier amplitude of the estimate before the update and the measured amplitude. Note that d is equal to the distance $d(\psi, \psi')$ of the initial, ψ , and conventionally updated estimate, ψ' , with respect to the metric that is induced by the norm defined in Eq.

¹⁵Note that here the reconstructed amplitude has been used.

¹⁶This modified propagator was devised by P. Thibault and is described in the supporting online material of [59].

(4.34). In other words, d gives the distance of the current estimate ψ to the closest element in the constraint set \mathcal{C}_M as defined in Eq. (4.30). D is a real parameter which should be chosen close to the experimental expectation value $\sqrt{\langle d^2 \rangle}$. With the Poissonian statistics of the measurement process one obtains the remarkable result $\sqrt{\langle d^2 \rangle} \simeq 1/2$.¹⁷

The effect of the ‘relaxed’ Fourier constraint operator is thus as follows: If the current estimate ψ has a larger distance d from the ideal constraint set than experimentally expected, it is updated such that the new estimate $\tilde{\psi}'_{\text{rel}}$ will have exactly that distance. If the current estimate already has a distance smaller or equal to the experimentally expected, then nothing is changed.

4.7 Coherence

A full consideration of partial coherence in coherent lensless imaging involves the transition from a description in terms of the propagation of wave fields to one in terms of the propagation of complex coherence functions [see 105, 108, and references therein]. Such a treatment goes beyond the scope of this thesis. Nevertheless, it is important to know under which physical conditions the effects of limited spatial and temporal coherence on recorded diffraction patterns can be neglected. The conditions are different for near field and far field diffraction patterns and shall be briefly outlined in the following.

4.7.1 Far field

The effect of limited spatial coherence in the sample plane on far field diffraction patterns is that of blurring the intensity distribution [129, 138]. This blurring is caused by the finite lateral extension of the source that is used to define the illumination on the sample [129]. If the spatial coherence length in the sample plane is large enough, so that the intensity blur in the far field has no effect on length scales comparable to or larger than the speckle size, effects of partial coherence can be neglected. As a rule of thumb [138], one demands that the spatial coherence length ℓ_c in the sample plane, e.g. as given by Eq. (3.73), is larger than the largest dimension of the sample autocorrelation. For the ptychography experiments described in Chapters 5 and 6 this roughly amounts to the requirement $\ell_c > 2D$, where D is the diameter of the pinholes used for illumination.

With spatial coherence lengths of $\ell_{c,x} \simeq 12.6 \mu\text{m}$ and $\ell_{c,y} \simeq 141.6 \mu\text{m}$ and a pinhole diameter of about $1.4 \mu\text{m}$ this condition is well obeyed for the experiment carried out at the cSAXS beamline (see Chapter 5). For the ptychographic experiment carried out at the Bessy synchrotron (see Chapter 6) the exact source parameters could not be identified. It can, however, be assumed that they are in the same order of magnitude or better as those for the experiment at the cSAXS beamline. With an increase in wavelength by a factor of about 10 and a similar source-to-sample distance Eq. (3.73) leads to an increased spatial coherence length in the sample plane. With a pinhole diameter between 1.5 and $2 \mu\text{m}$ a neglect of partial coherence effects is justified also in this experiment.

¹⁷P. Thibault, personal communication. This result has also been stated in the supporting material of reference [59].

In contrast to partial spatial coherence which affects the whole diffraction pattern, partial temporal coherence limits only the maximum obtainable resolution from a far field diffraction pattern [138]. As outlined in Section 4.5 the experiment resolution is directly related to the highest observed scattering angle. The highest path length difference between ray paths reaching the detector can be observed under this angle. The temporal coherence length ℓ_t can be regarded as sufficient, if the maximum path length difference between ray paths reaching the detector from any two points in the sample is smaller than ℓ_t [146]. For points laterally separated by the sample diameter the maximum path length difference is given in the paraxial approximation as $D \sin \theta_{\max}$ [argument adapted from 146] with θ_{\max} denoting the maximum scattering angle. This scattering angle corresponds to the highest lateral spatial frequency $k_{\perp, \max} = k \sin \theta_{\max}$ which is related to the Rayleigh resolution Δr_R via $\Delta r_R = \pi / k_{\perp, \max}$. As a consequence, the maximum path length difference of two laterally separated points in the sample is given as $D \lambda_0 / (2 \Delta r_R)$. Requiring ℓ_t to be larger than this value leads to

$$\Delta r_R > \frac{D \lambda_0}{2 \ell_t}. \quad (4.89)$$

As the path length difference of two longitudinally separated points in the sample is approximately proportional to $k_{\perp, \max}^2 / k^2$ [146], the lateral path length difference is usually the limiting one. With $\ell_t \approx 0.6 \mu\text{m}$ at the cSAXS beamline and a pinhole diameter of about $1.5 \mu\text{m}$ Eq. (4.89) leads to a resolution limit below 1 nm. Note, however, that it is rather the dimension of the near field propagated pinhole exit wave in the sample plane than the pinhole diameter which yields the maximum relevant path length difference here. For a substantially localized illumination at the sample plane the above resolution limit, however, will generally be still well below the experimentally obtained resolution.

Summarizing, the low bandwidth of $\Delta \lambda / \lambda$ obtained with the help of modern crystal monochromators makes effects of limited temporal coherence negligible in most cases. The situation is different, if pink beam radiation is used which is not monochromatized by a crystal monochromator (see below).

4.7.2 Near field

The requirements for spatial coherence are less stringent for observation in near field geometry compared to the far field geometry. As a rule of thumb, diffraction effects do only affect lateral distances below $\sqrt{\lambda_0 z}$ with z denoting the propagation distance between sample and detector. As a consequence, a spatial coherence length in that range is required as a minimum [21]. For a waveguide imaging experiment the distance z becomes the effective propagation distance z_{eff} . Modeling the waveguide exit wave as a Gaussian beam let us estimate the coherence length at the sample. We assume the beam waist to be located at the WG exit plane. If the sample is placed at a distance z_{01} from this plane and if z_{01} is much larger than the Rayleigh length $z_R = \pi w_0^2 / \lambda_0$ of the Gaussian beam, the $1/e$ decay half width of the Gaussian beam amplitude is given as [133]

$$w(z_{01}) = \frac{\lambda_0 z_{01}}{\pi w_0}. \quad (4.90)$$

w_0 here denotes the $1/e$ decay half width of the waist amplitude. As a consequence, the $1/\sqrt{e}$ decay half width of the beam intensity at distance z_{01} from the waist is given as

$$w'(z_{01}) = \frac{\lambda_0 z_{01}}{4\pi\sigma_0} \quad (4.91)$$

with the $1/\sqrt{e}$ intensity decay half width σ_0 in the exit plane. In Section 3.1.6 the spatial coherence length in the far field (at distance z) of a spatially incoherent source with a Gaussian lateral intensity distribution has been determined to

$$\ell_c = \frac{1}{2\pi} \frac{\lambda_0 z}{\sigma}. \quad (4.92)$$

Here σ denotes the $1/\sqrt{e}$ decay half width of the intensity in the source plane. Identifying z with z_{01} and σ_0 with σ one obtains

$$\ell_c = 2w'(z_{01}). \quad (4.93)$$

As a result, the spatial coherence length of a (quasimonochromatic) source with a Gaussian intensity distribution and arbitrary spatial coherence properties is equal to the full width of a fully coherent ideal Gaussian beam with the same intensity distribution in the source plane. Consequently, the lateral coherence length in the far field of a waveguide beam does not depend on its spatial coherence properties in the source plane, as long as the intensity distribution in that plane has a Gaussian shape. However, as the ideal (diffraction-limited) Gaussian beam has the smallest possible divergence for a given lateral waist size [4], the full width of the waveguide beam can be larger than the lateral coherence length, if the wave field in the source plane is laterally not fully coherent.

To determine the requirements for longitudinal coherence in coherent near field imaging consider again the intensity spectrum expressed in Eq. (4.16) due to a weak semi-transparent object in the beam. We assume an incident wave with a wavelength spread of $\Delta\lambda_0$. Let further $\Delta\chi = \pi$ in Eq. (4.16) denote the difference in χ for two wavelengths at the lower and upper end of the wavelength interval with spread $\Delta\lambda_0$, so that $\Delta\chi = \pi z \Delta\lambda_0 v^2$. The wave at the lower end of the wavelength interval will then cause an intensity maximum, when the wave at the upper end causes a minimum and vice versa [123]. For the wavelength spread $\Delta\lambda_0$ to be negligible, it thus must be small enough such that [21, 22, 123]

$$\Delta\lambda_0 z v_{\max}^2 \ll 1 \quad (4.94)$$

with v_{\max} denoting the maximum spatial frequency in the sample. In waveguide-based propagation imaging with geometrical magnification z becomes the effective propagation distance z_{eff} . With Δ denoting the real space pixel width, the maximum resolved full-period spatial frequency is $1/(2\Delta)$, so that the requirement becomes

$$\frac{\Delta\lambda_0}{\lambda_0} \frac{\lambda_0 z_{\text{eff}}}{4\Delta^2} \ll 1, \quad (4.95)$$

here expressed in terms of the bandpass $\Delta\lambda_0/\lambda_0$. If the actual resolution Δr is larger than the pixel size Δ , Δ has to be replaced by Δr in Eq. (4.95). For the parameters of the waveguide experiment presented in Chapter 7 one obtains a value of 0.13 for the left side of Eq. (4.95), assuming a band pass of $\Delta\lambda_0/\lambda_0 = 0.02$. As a result, the given longitudinal coherence is sufficient.

4.8 Radiation damage, Dose and resolution

Radiation damage reveals itself as a structural distortion of a biological object (e.g. a cell or a protein crystal) with respect to its native structure in a beam of ionizing radiation (x-ray photons, electrons etc.). As outlined in Sections 3.2.1 and 3.2.2 the interaction of x rays with a (biological) sample is accompanied by an attenuation as well as a phase distortion of the incident beam. While the total photon flux is conserved with respect to the phase distortion, it is decreased by the attenuation process. This can be understood in view of the underlying interaction processes on the atomic level. Whereas the phase distortion is caused by collective elastic scattering processes of x-ray photons from the electrons in the atomic shell, the beam attenuation is caused by photoelectric absorption [4]. Here the energy of an incident photon is transferred largely into the kinetic energy of a core shell electron which, as a result of the increased kinetic energy, is expelled from its bound state in the atom. The absorbed energy is quantified in the **dose** D which is defined as the absorbed energy per unit mass.

In the context of radiation damage the photoelectric absorption process is also referred to as the ‘primary damage’ process [116]. If the sample is a protein crystal (or a biological cell), the expelled electron then loses its energy by a cascade of inelastic scattering events in the sample [51] which lead to the formation of radicals, such as protons or hydrated electrons. Thermal motion leads to the diffusion of the highly reactive radicals within their local vicinity before they recombine with other chemical species along their diffusion path. The recombination processes cause the so-called secondary damage which manifests itself in bond breakage and the generation of new radicals [116]. Although individual damage events are statistical in nature [116], radiation damage is known [71] to set in at interatomic length scales and then proceeds further to higher length scales with increasing integrated incident photon flux. With the resolution of (coherent and incoherent) biological x-ray microscopy approaching the range between 10 and 50 nm this structural change becomes a considerable limit to the maximum obtainable resolution [71]. More precisely, the *required dose for imaging* D_{req} of a certain structural feature in the sample may not exceed the *maximum tolerable dose* D_{tol} to visualize a certain detail in a biological sample without distortion by radiation damage [71]. Whereas D_{req} can be assessed by calculations, D_{tol} depends on the detailed nature of the radiation damage process and can usually only be assessed by experiments [71]. D_{tol} can be determined as the integrated dose, at which the far field diffraction pattern of a sample starts to deviate from the initial pattern at a given spatial frequency [71]. Importantly, D_{tol} can be largely increased, if the sample is fixated, i.e. if the diffusion of photoelectric absorption products can be suppressed. Obviously, a fixation process is needed which has no or little structural effects on the length scale of the resolution. Two very common techniques are freeze-drying and cryo-fixation (see below). The latter allows for the higher tolerable doses [73].

From experiments with protein crystals and chemically similar biological materials the maximum tolerable dose for a given resolution between 0.1 and 10 nm is empirically given as [71]

$$D_{\text{tol}} [\text{Gy}] \approx 10^8 \times \Delta r [\text{nm}]. \quad (4.96)$$

Thus, the tolerable dose increases approximately linearly with the requested resolution.

The required imaging dose D_{req} , on the other hand, can be estimated [71] based on the (integrated) scattering cross section σ_s of a single cubic volume element (voxel) of sidelength d . If the material in the voxel has an amplitude transmission of T , the diffraction pattern of the voxel against vacuum is the same (except at the center) as that of a voxel with transmittance $1 - T$ in an opaque background. The scattering cross-section of this voxel is given as [71]

$$\sigma_s = r_e^2 \lambda_0^2 d^4 |\rho|^2 \quad (4.97)$$

where r_e is the classical electron radius, λ_0 the photon wavelength and $\rho = k(\beta + i\delta)/(r_e \lambda_0)$ the complex electron density of the material in the voxel. The solid angle corresponding to the cross-section σ_s here is assumed to be equal to that required for a resolution d in the reconstruction of a diffraction pattern that has been recorded in the far field on a 2D detector. The reconstruction is thus assumed to be 2D, but the depth of the voxel comes in as a thickness parameter. Due to the dose fractionation theorem, it can be expected that the dose to image a cubic voxel with volume d^3 with a given statistical accuracy is the same as that of a two-dimensional squared 'voxel' [71]. If N_d denotes the number of photons scattered into this solid angle, the scattering cross section can be written as [71]

$$\sigma_s = \frac{N_d}{F_{\text{ph}}}. \quad (4.98)$$

Here F_{ph} denotes the incident photon fluence as defined before. The Rose criterion requires the particle count in the detector to have an SNR of 5, so that N_d can be set to 25 for photon shot noise [71]. The required incident photon fluence to obtain a resolution d in a diffraction microscopy experiment is thus given as

$$F_{\text{ph}}(d) = \frac{5^2}{r_e^2 \lambda_0^2 |\rho|^2 d^4}. \quad (4.99)$$

The decrease in fluence due to the voxel is given by Lambert-Beer's law, i.e. $F(d) = F_{\text{ph}} \exp(-\mu d)$ with absorption coefficient μ . The deposited energy per unit volume after propagation over depth Δt is thus given as [71]

$$\frac{\Delta F h\nu}{\Delta t} \rightarrow \frac{\partial F}{\partial t} h\nu, \quad (4.100)$$

where $h\nu$ is the photon energy. The deposited energy density at the surface is thus given with Lambert-Beer's law as

$$\mu h\nu F_{\text{ph}}. \quad (4.101)$$

The dose absorbed at the surface is thus given as [71]

$$D = \frac{\mu h\nu F_0}{\rho_m} \quad (4.102)$$

where ρ_m is the mass density of the material. The required imaging dose to image down to a resolution d is thus obtained with Eq. (4.99) as

$$D_{\text{req}}(d) = \frac{5^2 \mu h\nu}{\rho_m} \frac{1}{r_e^2 \lambda_0^2 |\rho|^2 d^4}. \quad (4.103)$$

$D_{\text{req}}(d) \propto d^{-4}$ as well as $F_0(d) \propto d^{-4}$ are thus very rapidly decaying functions of the resolution. In essence, this states that, *for an improvement of the resolution by one order of magnitude, four orders of magnitude increase in dose or fluence are needed.*

From the previous considerations on the maximum tolerable dose it follows that the best (smallest) resolution Δr^* that can be achieved on a biological sample is given for $D_{\text{req}}(\Delta r) = D_{\text{tol}}(\Delta r)$. For $\Delta r < \Delta r^*$ one then has $D_{\text{req}} > D_{\text{tol}}$, so that no successful imaging is possible any more. For typical biological material and best fixation techniques (cryo-fixation) Δr^* is currently [71] estimated as

$$\Delta r^* \simeq 10 \text{ nm}, \quad (4.104)$$

based on above estimations for $D_{\text{req}}(\Delta r)$ and empirical estimates of $D_{\text{tol}}(\Delta r)$.

4.9 Biological samples and their preparation

In this section, the preparation of the cell samples used in the synchrotron experiments is described.¹⁸ This does not refer to the diatom sample used for the experiment described in Chapter 6.

4.9.1 *Dictyostelium Discoideum*

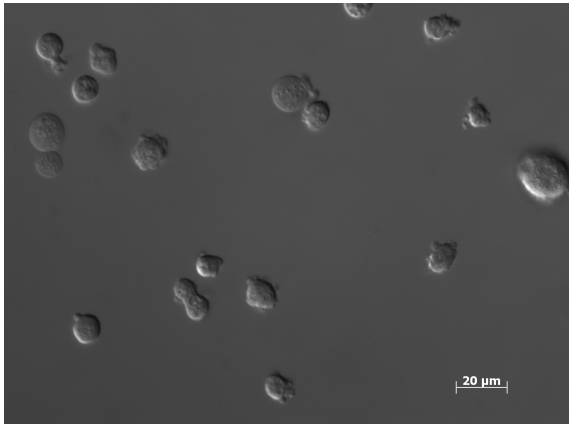


Figure 4.12: *Dictyostelium discoideum* cells observed *in vivo* in optical differential phase contrast.

Dictyostelium Discoideum is a well-studied species belonging to the so-called social amoebae [76]. Naturally, the eukaryotic *D. Discoideum* cells live in the ground and feed on bacteria. In case of starvation, the cells can start to aggregate, eventually forming stable and resistant multicellular spores. The collective behavior is enabled by the cells' ability to perform chemotaxis, i.e. to move along a concentration gradient of an external

¹⁸Parts of the work presented here have been published previously in [56, 57, 59].

chemical component, here cyclic AMP¹⁹ [76, 87]. The cell locomotion itself is associated with a constant reformation of the actin cytoskeleton. For this reason, *D. Discoideum* is a well-suited model organism to study the properties of the actin network in eukaryotes [97]. Chemotactic *D. Discoideum* cells are shown in Fig. 4.12.²⁰

For preparation²¹ cells of the wild-type strain AX2-214 were used. The cells were cultivated in shaking suspension of HL5 nutrient medium (7 g/L yeast extract, 14 g/L peptone, 0.5 g/L KH₂PO₄, 0.5 g/L Na₂HPO₄). Prior to preparation, cells were transferred to a Petri dish for transport, after which they were allowed to attach to the bottom surface of the Petri dish for at least 1h. Before transfer to the sample holder (see below) the supernatant nutrient solution was removed and cells were resuspended in 1-2 ml phosphate buffer solution (2 g/L KH₂PO₄, 0.36 g/L Na₂HPO₄ · 2H₂O, pH 6.0).

4.9.2 *Deinococcus Radiodurans*

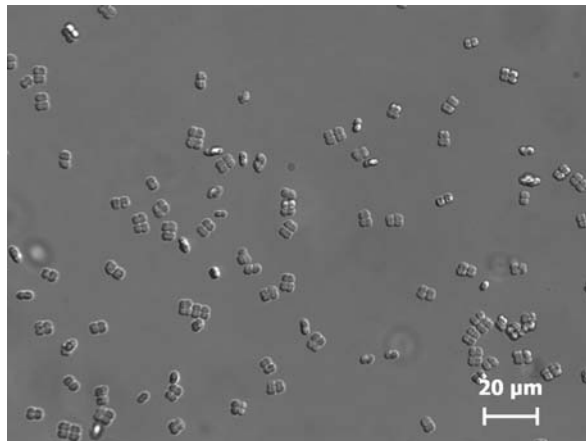


Figure 4.13: *Deinococcus radiodurans* cells observed in optical differential phase contrast.

*Deinococcus radiodurans*²² is a non-motile, non-spore forming bacterium that can be observed in single, nearly spherical form, but often also appears in pairs and tetrads with a very characteristic shape [27]. The bacterium has gained a lot of scientific interest over the past decades due to its extraordinary resistance to ionizing radiation [27]: Doses as high as 10000 Gy can be survived by 10% of an actively growing and oxygenated population [27]. It is assumed that the high radiation resistance is enabled by very effective repair mechanisms which remain not completely understood. Based on electron microscopic images of stained sections, a possible link between radioresistance and the structure of the bacterium's

¹⁹Adenosine Monophosphate, a molecule important in biological signal transduction pathways.

²⁰Cells shown here are non-wild type cells where actin has been labeled with a fluorescent protein. The overall appearance of the cells, however, is the same as that of wild-type ones used for the x-ray imaging experiments.

²¹Cell cultivation was carried by the group of Prof. C. Beta and Prof. E. Bodenschatz at the Max-Planck-Institute for Biophysical Chemistry, Göttingen, Germany. The preparation process has also been described in [56].

²²A translation of this name can be given as 'strange coccus that resists (ionizing) radiation'.

nucleoid has been suggested [84] and was subsequently strongly debated, based on other results by cryo electron microscopy of vitrified sections [39–41]. *D. radiodurans* can thus be seen as a good model organism which can be used in the development of complementary techniques such as (coherent) x-ray microscopy. Importantly, here the sample does not have to be sectioned to be imaged.

For preparation, cells of the *Deinococcus radiodurans* wild-type strain NCIB 9279 were cultivated from freeze-dried cultures (German Collection of Microorganisms and Cell Cultures, Braunschweig, Germany) for one day at 30°C on petri dishes covered with nutrient medium (corynebacterium agar: 10 g/l casein peptone, 5 g/L yeast extract, 5 g/l glucose, 5 g/l NaCl, 15 g/l agar). Prior to the transfer onto the sample support (see below) the actively growing cells were washed off the culturing medium with ca. 1.5 ml phosphate buffer solution (2 g/l KH₂PO₄, 0.36 g/L Na₂HPO₄·2H₂O, pH ca. 6.0). The resulting cell suspension was then diluted (dilution factors between 1:10 and 1:100 were used), before it was placed onto the sample support foils (see below). An optical micrograph of *D. radiodurans* bacteria is shown in Fig. 4.13.

4.9.3 Fixation by rapid freezing

Ideally, biological cells should be observed in their natural aqueous environment. Electron microscopy (EM) and soft x-ray microscopy require a vacuum sample environment due to the very small pathlength of electrons and soft x-ray photons in air. Using these techniques, a fixation of the sample is a necessary prerequisite. The situation is different in the hard x-ray range. Due to the relatively high transmission of air under ambient conditions for a hard x-ray beam (97.5% transmission per 1 cm pathlength for an x-ray beam with a photon energy of 6.2 keV [67]), it is possible to observe the specimen under ambient conditions.

As outlined above, radiation damage, to a large extent caused by recombination of freely diffusing radicals, nevertheless necessitates the fixation of the biological sample. The technique of cryo-fixation, introduced in electron microscopy in the 1980s [36], combines at the same time the maximization of the tolerable dose and an optimum preservation of the native structure. This structure preservation is enabled by an amorphous phase state that water can adopt at temperatures below the glass transition temperature $T_g \approx 136 \text{ K} = -137.15 \text{ °C}$ [88].

Solid water in general exhibits an enormously complex phase structure which can mainly be attributed to its ability to form hydrogen bonds between hydrogen and oxygen atoms of neighboring molecules [31, 88]. Upon freezing under ambient pressure water normally forms a stable crystalline phase, hexagonal ice I_h [36]. In simple terms, crystallization starts whenever a crystal nucleus is formed with a diameter large enough so that a further increase in size lowers the total free energy of the crystal. This so-called nucleation event is only possible above a certain critical crystal size. If the crystal is smaller than critical, the total free energy *increases* with the size of the crystal. This non-monotonic dependence of the total free-energy is caused by the interplay of the surface and volume contributions to the total free energy of the crystal [36]. Once the crystal size has exceeded the critical value, further crystal growth is energetically favored and appears very rapidly [36]. As the formation of crystalline ice causes irreversible structural damage to biological cells [36], observation in this phase is not an option. If, however, water is cooled so

rapidly that the immobilization of water molecules prevents nucleation events, which are intrinsically dependent on statistical density fluctuations in the liquid, liquid water can be transformed into an amorphous state with a structure very similar to that of the liquid [36]. This process is also referred to as **vitrification**. Several different forms of amorphous water exist, which can be reached by various temperature-pressure-trajectories [31, 88]. These pathways and the the final amorphous structures are an area of active research [31, 88]. The amorphous phase that is obtained by rapid freezing under ambient pressure, is also referred to as *hyperquenched glassy water (HWG)* [31]. The necessary cooling rate below T_g to reach the HWG phase is around 10^6 K/s for pure water [31]. With $T_g \approx 136$ K the necessary cooling time is thus on the order of 0.1 ms. For the cytosol and the aqueous solution surrounding the cells the required cooling rate is expected to be slightly smaller, as it is known [36] that e.g. sugars can act as a cryoprotectant. Such substances increase the viscosity in a fluid leading to a decrease in the crystal nucleation rate. A very popular cryoprotectant, glycerol, is commonly used [51] in protein crystallography to reduce necessary cooling rates. For cellular samples the addition of a cryoprotectant is usually not an option as the induced osmotic stress leads to a distortion of the native structure or even destruction of the cells by disruption of the cell membrane.

One way to achieve vitrification is the injection of a thin layer of material into a cryogenic liquid, the so-called plunge-freezing technique [36, 122]. It has been devised for sample preparation in electron microscopy. Here the specimens such as cells, viruses, macromolecules etc. are deposited within a thin aqueous film onto a flat sample holder and then injected into the coolant in such a way that the flat surface of the sample holder is oriented parallel to the direction of injection. Cooling is mainly caused by convection when the sample penetrates the coolant [122] and becomes the more effective the larger the surface area of the film is. In most plunging devices injection is simply driven by gravitational acceleration. The home-built device fabricated and used for sample preparation within this thesis is depicted in Fig. 4.15.

Liquid ethane²³ is preferred to liquid nitrogen²⁴ (LN2) as a coolant due to the absence of calefaction [36], i.e. the formation of a gas layer in between the liquid coolant and the specimen as it can be observed with LN2. The absence of this effect for liquid ethane is mainly due to the large temperature difference between LN2 temperature and the boiling point of the ethane.

Evidently, the experimentally achieved cooling time of the specimen below T_g largely depends on the specimen volume and free surface area in contact with the coolant [35, 150]. As the rapid cooling is mainly caused by convection when the specimen glides through the liquid coolant [122], injection speed is also an important parameter. As a rule of thumb the maximum thickness of a pure water film to be vitrified by immersion in to a cryogenic coolant is $1 \mu\text{m}$ [35]. Due to solutes present in the aqueous environment of biological material the vitrification depth can be increased by an order of magnitude in tissue samples [35].

²³Boiling point -89°C (184 K), melting point -183°C (90 K) under ambient pressure.

²⁴Boiling point -196°C (77 K), melting point -210°C (63 K) under ambient pressure.

4.9.3.1 Setup and protocol for cryo-fixation

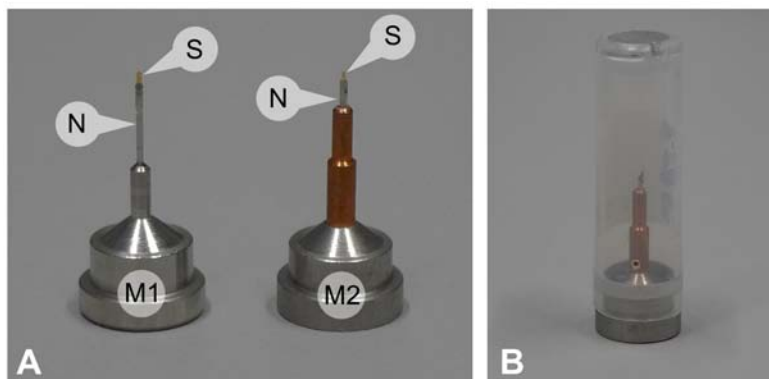


Figure 4.14: (A) Used sample mountings. The polyimide foil to which the cells are attached during the imaging experiment is the actual sample support (S). The foil is fixed to a steel needle (N) which is glued into the magnetic mount (M1, M2). Whereas the mount design M1 is recommended for room temperature applications (freeze-dried samples), the second design (M2) is equipped with a copper shield around the steel needle for use under cryogenic temperatures in a stream of cold nitrogen gas. (B) For storage and short-term transport under cryogenic temperatures the mount is covered by a plastic cap which can hold a small amount of LN₂. Unlike in this picture the mounts are stored and transported upside down when the cap is filled with LN₂. The cap is equipped with a magnetic ring so that it stays attached to the mount when turned around.

The setup and protocol used for cryo-fixation within this thesis work is very similar to standard protocols used in cellular cryo electron microscopy [36, 122].²⁵ The sample support and mounting, on the other hand, is based on a design [144] that has been devised for cryo protein crystallography and profits from the well-developed technical tools and infrastructure in this field [51].

For the actual sample support a thin microfabricated polyimide foil²⁶ was used, mounted onto a stainless steel pin with a diameter of 0.64 mm (MiTeGen, USA), see Figs. 4.14 and 4.18. The foil itself is fixed with a plastic sleeve around the steel needle, resulting in a minute curvature of the polyimide film. Several foil sizes²⁷ and thicknesses (12.5 μm and 18 μm) have been used. The polyimide itself is well suited as a sample support for hard x-ray imaging due to its relatively small absorption (98.1% per 10 μm thickness [67]) and low scattering signal with a main correlation peak around 1.2 \AA^{-1} , corresponding to a

²⁵I am thankful to Prof. H. Stark of the Max-Planck-Institute for Biophysical Chemistry, Göttingen, for an introduction to the plunge freezing technique and the advice in the design of a freezing device. The plunge freezing setup and protocol that is described here has been devised at the beginning of this thesis work and has been further refined and well documented in [64] as part of a Bachelor thesis project by M. Hantke that was supervised by the author and Prof. Dr. Tim Salditt. Figs. 4.17 and 4.18 were kindly provided by M. Hantke.

²⁶The readily mounted foils were obtained from Mitegen (USA) and are sold under the product name MicroSpoons[®].

²⁷Lateral usable foil areas varied between 400 (height) \times 300 (width) μm^2 and 1000 (height) \times 500 (width) μm^2 .

real space correlation length of 5.3 Å [144]. The needle itself is held by magnetic mounts (Mitegen, USA) that are commonly used in protein crystallography (see Fig. 4.14).

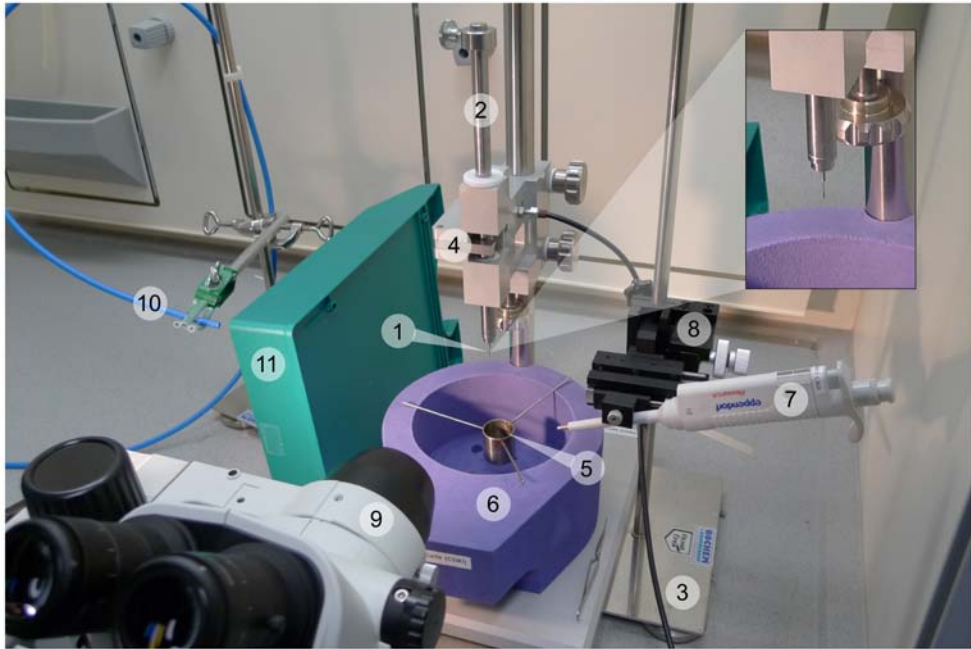


Figure 4.15: Home-built plunge-freezing device. The sample holder (1, see also zoomed-in inset in the upper right) is magnetically attached to an aluminum rod (2) which is clamped at the beginning of the preparation process in a fixed position. Upon release of the rod by a foot pedal connected mechanically (3) to the clamping device (4), the sample holder is accelerated downwards into the coolant container (5). The container itself which contains liquid ethane during the preparation process is cooled in a bath of liquid nitrogen within a foam Dewar (6). The cell suspension is deposited onto the polyimide foil attached to the sample holder using a pipette (7) that is attached to a micromanipulator (8). Due to the small size of the sample holder this process has to be observed in a long-distance optical microscope (9). As an option during the preparation process a stream of dry air (10) can be pointed onto the ethane surface immediately before the plunging process (see main text). To prevent warming the ethane during other preparation steps the air stream needs to be shielded, if not used (11). The whole setup is placed in a fume hood to prevent any danger from the highly inflammable ethane.

The setup for cryo fixation as it was used here is depicted in Fig. 4.15. The whole preparation process has to take place under a fume hood to minimize the risk of inflammation of evaporating ethane gas. The injection is propelled by gravity with an acceleration distance of about 20 cm, leading to an injection speed of 2 m/s at the ethane surface.

It has been reported [150] that cold gas layers above the liquid ethane can lead to a significant decrease in the cooling rate upon injection of the sample into the cryogenic coolant. The problem was circumvented [150] by application of a stream of dry gas (nitrogen, air) onto the coolant surface immediately before the injection of the sample. This

procedure was used for part of the samples that were prepared for this study.²⁸

The detailed protocol for the cryo-preparation process is illustrated in Fig. 4.17 and will be described in the following. Note that steps 4-6 are also depicted in microscopic photographs in Fig. 4.18. The description has been adapted from [64].

1. **Cleaning.** At the beginning the polyimide foils (attached to the steel needle) are cleaned for 15 to 20 minutes in an ultrasonic bath²⁹ to remove remaining particles (dust etc.) from the production process and transport. The needle holder that was used during the cleaning process is depicted in Fig. 4.16A. After rinsing thoroughly with ultrapure water the foils are air dried. This process can be accelerated by gently warming the foils in an oven at around 50 °C.

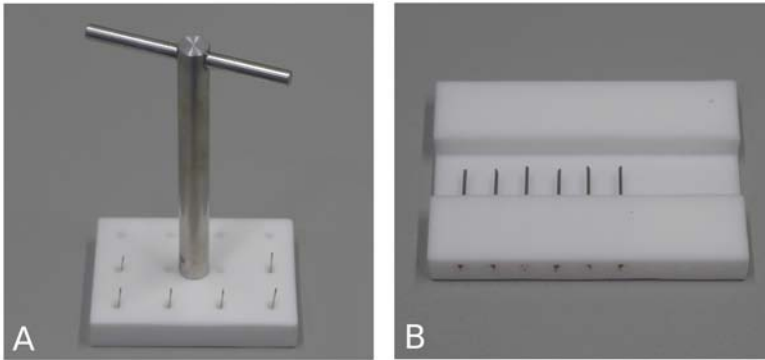


Figure 4.16: Needle holders used for ultrasonic cleaning (A) and hydrophilization in a plasma cleaner (B).

2. **Hydrophilization.** To allow for the required short cooling times the preparation of a very thin layer of cell suspension is crucial. As a prerequisite, the polyimide foil has to be rendered highly hydrophilic before application of the cell suspension. Hydrophilization is obtained by placing the foils into a plasma cleaner (Harrick Plasma, USA) for several minutes. To prevent wetting of the whole steel needle and associated dehydration of the polyimide foil the needle has to be protected from contact with the plasma during the hydrophilization process. A special Teflon sample holder was fabricated for this purpose, see Fig. 4.16B. It is noted that the hydrophilic nature of the polyimide foil strongly degrades after several hours of direct contact with air under ambient pressure. Therefore the subsequent preparation steps have to follow immediately.

²⁸It has been used for the preparation of the freeze-dried *D. radiodurans* cells used for the experiment described in Chapter 5, but not for the *D. Discoideum* cells used for the experiment described in Chapter 7. It is expected, however, that possible preparation artifacts in the freeze-dried cells are likely to be caused mainly by the freeze-drying step rather than by omitting the additional step described here.

²⁹Iso-propanol or methanol can be used as cleaning agents.

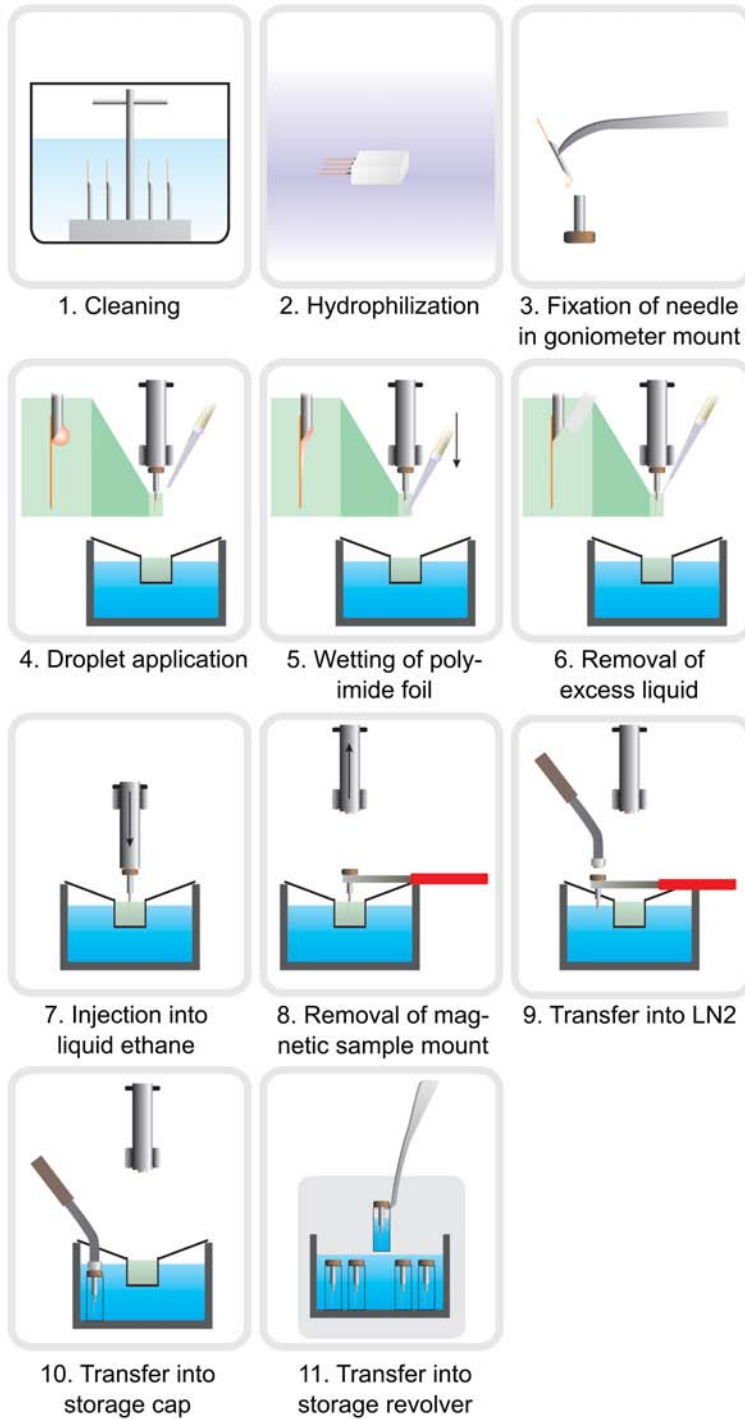


Figure 4.17: *The plunge freezing technique. For description see text. Figure adapted from [64].*

3. **Fixation of needle in goniometer mount.** After hydrophilization, the needle is placed into the magnetic goniometer mount (see Fig. 4.14). To prevent the needle from falling out of the mount it fixed within the mount by a two-component epoxy glue (Devcon, USA) which hardens within several minutes.
4. **Droplet application.** Steps 4-6 are very delicate, yet crucial to the success of the preparation and have to be performed under observation through a long-distance microscope. The droplet of cell suspension ($1-2\ \mu\text{l}$) is placed onto the polyimide foil using a micropipette that is attached to a micromanipulator. A major challenge here is to prevent the liquid from attaching on both sides of the foil. One very successful pathway is to place the whole droplet first onto the beveled edge of the steel pin and immediately afterwards ...
5. **Wetting of polyimide foil.** ... use the pipette tip to spread it downwards on the polyimide foil. An ideal spreading result is depicted in Fig. 4.18B. Now the cells are allowed to adhere to the polyimide foil for about 0.5 to 3 minutes. One has to be careful that the sample is not dehydrated during this time as evaporation of the small droplet volume can happen on similar timescales.



Figure 4.18: Application of cell suspension to sample support. (A) A small volume of cell suspension (between 1 and $2\ \mu\text{l}$) is placed onto one side of the hydrophilized polyimide foil. (B) Ideal wetting result after application of the droplet. (C) Removal of excess liquid using a paper wick immediately before the sample is injected into liquid ethane. Figure adapted from [56].

6. **Removal of excess liquid.** Immediately before the plunging process the excess liquid is carefully soaked away using a paper wick (Mitegen, USA) that is attached to the micropipette and can therefore also be controlled with the micromanipulator. Due to hydrodynamic forces the soaking process appears very rapidly, on the timescale of a second. To prevent dehydration of the foil and associated disruption of the cell samples the injection process has to be initialized immediately after most of the liquid except a very thin layer has been removed. Plunging is initialized with the help of a foot pedal by releasing the aluminum rod to which the goniometer mount is attached. At the same time the shield is removed from the dry air flow which is pointed now onto the ethane surface to remove the cold gas layer on top of the liquid. After injection the shield is put back in place to prevent warming of the injected sample and the surrounding ethane.

7. **Injection into liquid ethane.** The ethane that is filled in the gaseous phase into a small metal container prior to preparation becomes fluid in contact with the cold metal of the container that is kept at LN2 temperature at all times. As the melting point of ethane ($-183\text{ }^{\circ}\text{C} = 90\text{ K}$) is above the boiling point of LN2 ($-196\text{ }^{\circ}\text{C} = 77\text{ K}$) the liquid adopts a milky appearance after several minutes and usually freezes at the bottom of the metal container. As ethane liquefies already at $-89\text{ }^{\circ}\text{C} = 184\text{ K}$ one may not start injection immediately after filling the metal container. The solidification and milky appearance which usually sets in after several minutes is a necessary visual sign that the remaining liquid is below the water glass transition temperature $T_g = -137\text{ }^{\circ}\text{C} = 136\text{ K}$ needed for vitrification. On the other hand, the solid ethane at the bottom of the container represents a danger to the injected sample. Therefore one always has to make sure that there is remaining liquid above the solid phase to allow for injection of the sample holder. Usually, it has been injected here to a depth, so that the foil is fully covered by ethane.
8. **Removal of magnetic sample mount.** The magnetic sample mount is removed from the aluminum rod it was connected to during the injection. A tong is used to keep the foil in the liquid ethane during this process.
9. **Transfer into LN2.** Even though liquid ethane is used for the actual rapid freezing process, LN2 is used to keep the sample at cryogenic temperatures, i.e. well below T_g . Therefore the sample has to be transferred in a quick move into the LN2 bath.
10. **Transfer into storage cap.** The sample holder is then gently transferred into the storage cap (see Fig. 4.14B) that has been placed into a recess at the bottom of the foam Dewar (Molecular Dimensions, UK) before the plunging process.
11. **Transfer into storage revolver.** The sample holder including the cap which contains several milliliters of LN2 is then transferred into a storage revolver (Molecular Dimensions, UK). The LN2 reservoir assures that the sample is kept at LN2 temperature during the transfer. The whole revolver is then placed into a large LN2 Dewar where the samples can be stored *ad infinitum*.

4.9.3.2 Sample environment for frozen hydrated samples

The observation of frozen hydrated samples at cryogenic temperatures (below T_g) represents a significant technical challenge, especially in an environment suitable for x-ray imaging. To keep the sample at low temperature, several techniques are presently used. One possibility that is also used in EM is to transfer the frozen hydrated sample into a vacuum environment where an LN2 driven cryostat keeps the sample at low temperature. An instrument specifically designed for x-ray diffraction microscopy of frozen-hydrated specimens at the Advanced Light Source (Berkeley, USA) is based on this cooling technique [6]. Another possibility is opened up by a technique that is used routinely in cryocrystallography of proteins, namely the cooling of the sample by a stream of nitrogen gas at cryogenic temperatures [51]. The technique works at ambient pressure and thus greatly simplifies instrumentation demands. The optical images of frozen hydrated specimens shown below have been obtained using this technique.

The corresponding sample environment is depicted in Fig. 4.19. The cooling apparatus used in the present work was a *Cryostream 700 Series* system (Oxford Cryosystems, UK). Here a core stream of nitrogen gas at temperatures below T_g is circumvented by a stream of dry air to prevent ice contamination from moisture in the surrounding air. A long distance optical microscope³⁰ (Accel, Germany) specifically designed for the operation with the cold stream was used to produce *in situ* optical micrographs of the sample and for positioning control. The small depth of focus of the optical microscope allows for a very accurate relative positioning of the sample in the direction of the optical axis. This becomes important for an accurate measurement of distances between the sample and other optical elements along the beam path. To avoid warming of the sample and ice contamination, the transfer of the cryogenically cooled sample mounts onto the sample stage has to be performed very quickly, with the cold stream pre-aligned to the position of the polyimide foil.

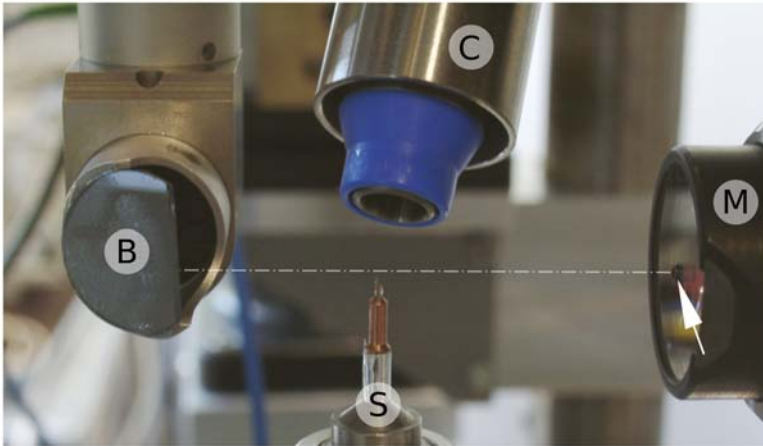


Figure 4.19: Sample environment for optical and x-ray based lensless microscopy of frozen hydrated specimens at cryogenic temperatures. A stream of cold nitrogen gas is directed onto the sample from the nozzle of the cooling apparatus (C). A long-distance optical microscope (M) is used to generate moderate resolution optical images of the sample that is held by a magnetic goniometer mount (S). A mirror (B) directs light on the back-illuminated sample. A channel drilled into the microscope lens (indicated by the white arrow) allows for the passage of an x-ray beam which can be aligned parallax free with the optical axis of the microscope (dashed line). The lens can be mounted both down- and upstream of the sample.

Optical micrographs of preparation results for both, *D. discoideum* and *D. radiodurans* are depicted in Fig. 4.20. The frozen hydrated cells compare well with those ones observed *in vivo* (see Figs. 4.12 and 4.13), indicating a successful preparation.

Are the samples truly vitrified? From the optical images it cannot be deduced with certainty that this is the case. Estimations of the heat transfer through convection while

³⁰Working distance 31.5 mm, NA = 0.28.

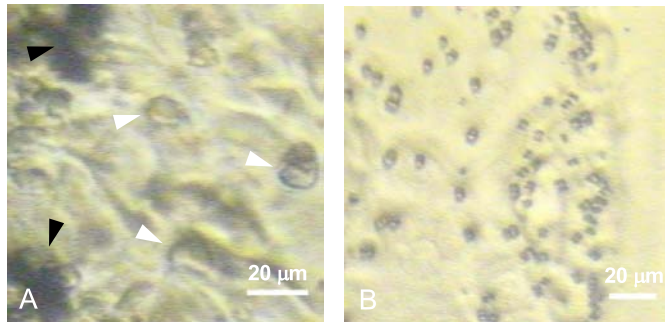


Figure 4.20: Frozen hydrated cells under cryogenic conditions in a cold stream (temperature $-173\text{ }^{\circ}\text{C}$). (A) *D. discoideum* cells (white markers). Dark regions (dark markers) can be most probably attributed to polycrystalline ice that has contaminated the specimen during preparation or transfer. (B) *D. radiodurans* cells.

the sample is traveling in the liquid ethane yield cooling rates in the required range for the present setup and sample holders [64]. To a limited extent observation between two cross polarizers can help to identify larger monocrystalline regions [64]. A certain identification of the amorphous water phase is only possible in an additional x-ray diffraction experiment. Due to the small correlation lengths of amorphous water as well as the small Bragg distances in crystalline ice rather large diffraction angles have to be covered by the detector. Therefore, a simultaneous measurement of the water diffraction signal and the coherent small angle scattering signal would require two detectors, one close to the sample for high diffraction angles (water structure) and one far away for the coherent small angle scattering signal. In addition, a very small and intensive synchrotron beam is required with a lateral size on the order of $10\text{ }\mu\text{m}$ at the sample surface. Within this thesis no such test could be performed.

Another difficulty that arises using the cryostream are sample vibrations with standard deviations between 200 and 500 nm [64]. Such vibrations are rather non-critical in diffraction imaging with plane wave illumination. With a typical beam diameter on the order of 20 to $30\text{ }\mu\text{m}$ in these experiments the small vibrational translations disappear in the Fraunhofer diffraction pattern which for an laterally infinitely extended plane wave translates translations into a phase shift in the far field (see Eq. 2.10). For the diffractive imaging methods that were used here (ptychographic CDI and effective near field microscopy) sample vibrations are rather critical.

For these reasons, experiments reported within this thesis (i.e. those ones presented in Chapters 5 and 7) were carried out with freeze-dried samples which can be observed at room temperature.

4.9.4 Freeze drying

Just as vitrification by rapid freezing, freeze-drying is a preparation method that is routinely used in electron microscopy [65]. Here the frozen water in the sample is extracted by sublimation at pressures/temperatures below the triple point of water. A cold condenser is used for solidification of the water vapor that leaves the sample, if the mean free path of water molecules in the freeze-drying chamber is long enough to reach the condenser [65].

For the present experiments a commercial freeze-drying system was used³¹ (Christ, Germany). At the beginning of the freeze-drying process the frozen hydrated samples (mount and cap, see Fig. 4.14) were placed into a metal cup filled with LN2 and transferred into the freeze-dryer. Immediately afterwards, the drying process was initiated by evacuating the reaction drying chamber at an initial condenser temperature of ca. $-60\text{ }^{\circ}\text{C}$ and a pressure reaching lowest values in between 10^{-3} to 10^{-2} mbar after several minutes. The system was then run for 40 hours, keeping pressure/condenser temperature values in the above range. After initialization of the drying process the samples are slowly warmed up, mainly due to heat transfer by radiation from the surrounding. The water in the sample can only sublime, if the pressure decreases below the temperature dependent sublimation pressure. The minimum achievable pressure thus limits the sample temperature at which sublimation can take place. The vacuum pump of the used freeze-drying system allows for a minimum nominal pressure of 10^{-3} mbar, corresponding to a sublimation temperature of $-76\text{ }^{\circ}\text{C}$ ³². It can thus be expected that the cell samples were warmed up to a temperature around this value before sublimation started (the magnetic mounts and the metal cup initially are at LN2 temperature and may thus initially act as a condenser).

The critical temperature for devitrification of biological specimens has been estimated to be around -100 up to $-80\text{ }^{\circ}\text{C}$ [114]. Although this is significantly higher than the devitrification temperature of pure water, it cannot be excluded that devitrification artifacts are present in the samples. Note, however, that the experiments described in the following chapters yield resolutions in the range of $100 - 300\text{ nm}$. As a consequence, the demand for structure preservation is not as high as that for electron microscopy. In the meantime, an updated setup has been put into operation for freeze-drying preparation, in which a massive copper block cooled to LN2 temperature works as a condenser, with pressures in the range of 10^{-5} mbar, using an UHV chamber and pump system.

³¹Model *Alpha 1-2 LDplus*.

³²Reference manual *Alpha 1-2 LDplus*, Martin Christ Gefriertrocknungsanlagen GmbH, Germany.

5 Quantitative ptychographic coherent x-ray diffractive imaging of bacterial cells

In the first experimental demonstration [120] of Ptychographic Coherent X-ray Diffractive Imaging (PCDI) the complex illumination function was included as *a priori* information into the iterative reconstruction process. As a consequence, the reconstructed sample transmission function was limited by the accuracy to which the illumination function was known. ‘Guessing’ the illumination function can work for a strongly scattering object such as a lithographically fabricated gold test object [120]. For weakly scattering objects such as unstained biological cells this procedure is usually unsuccessful, as the errors in estimating the illumination function are generally larger than effects due to sample scattering.

The introduction and first experimental demonstration [141] of PCDI with simultaneous illumination (or probe) retrieval can thus be regarded as a pre-requisite for an application of the technique to weakly scattering specimens. In the following we will describe the extension of PCDI with probe retrieval to unstained, freeze-dried bacterial cells.¹ The experimental setup used here is very simple, just using a pinhole to confine the monochromatic hard x-ray beam on the sample.

5.1 Experiment

The experiment was performed at the coherent Small Angle X-ray Scattering (cSAXS) beamline of the Swiss Light Source (Villigen, Switzerland). A schematic of the setup is depicted in Fig. 5.1. A pinhole 1.4 μm in diameter was illuminated by a coherent undulator beam monochromatized to a photon energy of 6.2 keV using a silicon (111) monochromator. Slight focusing was applied both horizontally (monochromator crystal) and vertically (bendable mirror) to increase the intensity of the beam. The pinhole was milled into a 20 μm thick tungsten foil with a focused ion beam (Swiss Federal Laboratories for Materials Testing and Research, Duebendorf, Switzerland). The nearly circular shape of the pinhole allowed for a rather accurate initial guess of the illumination function. It had been observed before that pinholes produced by e.g. laser ablation, generally produce scattering patterns which are much more difficult to predict. If the sample is a weak scatterer, it can then be difficult to obtain a correct reconstruction result.

¹The results presented in this chapter are largely based on a previously published report [59]. For the preparation of this thesis the data has been recalculated using latest versions of analysis routines. The applied changes are very small, and general reconstruction results are unaffected. If changes are of relevance, they are mentioned in the text.

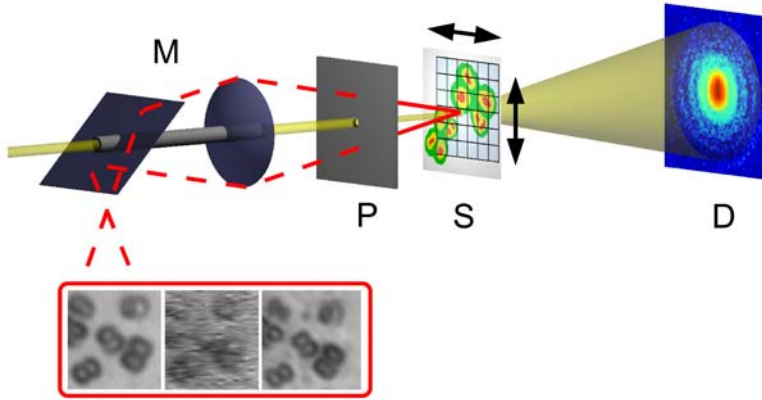


Figure 5.1: Experimental setup. The monochromatic x-ray beam (light yellow) passes through the Molybdenum-shielded channel of the on-axis microscope (M) and the probe defining pinhole (P). After short propagation the pinhole beam impinges on the sample (S) which is translated in horizontal and vertical direction between exposures, so that the illuminated spots are distributed on a 2D Cartesian grid. Via a drilled lens and mirror the optical microscope (red light path) allows for a parallax-free observation of the sample, if the pinhole is moved to the side. By subsequently translating the pinhole and sample into the fixed focal plane of the microscope the propagation distance between pinhole and sample can be measured accurately. The 2D pixel detector (D) is placed into the far field of the sample exit wave to collect the experimental diffraction patterns corresponding to each scan position on the grid. (Inset) Optical images of the freeze-dried *D. radiodurans* cells imaged in the experiment: Left, conventional bright field microscopic image before the experiment (Z1 Observer, Zeiss, Germany), middle, optical image from the in-situ-microscope at the end of the experiment, right, conventional bright field microscopic image after the experiment (Z1 Observer). The reconstruction shown in Fig. 5.3 corresponds to the same region of interest (ca. $14 \times 14 \mu\text{m}^2$). Figure from [59].

Freeze-dried, unstained cells of the bacterium *D. radiodurans* on a thin polyimide film were placed 1.4 mm downstream of the pinhole (for the preparation process and sample mounting see Sec. 4.9). The diffracted intensity was measured at a distance of 7.22 m from the sample using a single-photon counting PILATUS 2M array [12] with a pixel width of $172 \mu\text{m}$ in horizontal and vertical direction. Importantly, this detector has negligible readout noise and its high dynamic range of 20 bit $\approx 10^6$ allowed for a recording of the full diffraction pattern without using a beamstop. Given a Fresnel number $F \approx 7$ of the illumination wave field at the sample, the exit field was confined enough in lateral direction to allow for sufficient sampling of the diffraction pattern in the far field: With an exit field diameter of about $1.4 \mu\text{m}$ Eq. (4.12) yields a Shannon oversampling factor of $\sigma_{x,y} \approx 6$. A 7-m-long flight tube filled with helium was placed between sample and detector in order to minimize absorption by air and background scatter. An on-axis optical microscope (Accel, Germany; see also Fig. 4.19) with a lateral optical resolution of ca. $1 \mu\text{m}$ was placed a few centimeters upstream of the pinhole and the sample for accurate and parallax-free positioning control. Using the well-defined focal plane of the microscope as a reference, a very precise measurement of the distance between pinhole and sample was possible.

Ptychographic datasets were collected by translating the sample through the pinhole beam in a plane perpendicular to the optical axis. Sample positions were located on a Cartesian grid with a spacing of 400 nm in horizontal and vertical direction. For positioning control closed-loop high precision stages were used (Micos, Germany). Physical scanning stage positions were measured with optical encoders during the scanning process and recorded for each scan point.

In a first scan, diffraction data was collected by illuminating the sample at 51×51 positions. The exposure time at each sample position was 1 second with an average photon flux of $\Phi_{\text{ph}} \approx 1.5 \times 10^5$ ph/s at the detector. For reconstruction, a subset of 35×35 diffraction patterns was selected using the central 128×128 pixels of each diffraction pattern. Henceforth, this dataset is referred to as the short-exposure dataset. With Eq. (3.80) the corresponding real space pixel width is thus 66 nm. The average fluence applied to the sample during this scan was $F_1 \approx 10^6$ ph/ μm^2 .

Subsequently, a small region of interest was selected out of the previous scan area and scanned at 11×11 positions with the same grid spacing, but an exposure time of 60 seconds per scan point, leading to an average fluence of $F_2 \approx 6.6 \times 10^7$ ph/ μm^2 . Here a central region of 180×180 was selected from each diffraction pattern for reconstruction, leading to a real space pixel width of 47 nm. This dataset will be referred to as the long-exposure dataset.

5.2 Simulations

To validate the experimental reconstructions, to optimize the algorithmic reconstruction parameters (see below) and to give an estimate on the experimental error, two ptychographic datasets were simulated, corresponding to the two experimental datasets.

The maximum phase change and amplitude absorption due to one-micron thick cellular material at a photon energy of 6.2 keV are around 0.25 rad and 1.2×10^{-3} , respectively. As a consequence, absorption effects are generally negligible for the present experiment. The material was assumed here to be a model protein with mass density 1.35 g/cm^3 and molar fractions 48.6%H, 32.9%C, 8.9%N, 8.9%O, 0.6%S [143]. Instead of a $1 \mu\text{m}$ thick object, one can think of a freeze-dried cell of e.g. $3 \mu\text{m}$ thickness with 33 vol. % filled with protein. Other experimental parameters such as the integrated photon fluence as well as the experiment geometry, scanning parameters etc. were assumed to be the same as in the experiment.

Object transmission functions were generated here as described in Sec. 3.2.3, using preliminary experimental object reconstructions to generate the phantom images.² Substrate areas were assumed to be perfectly flat to test the algorithm's response to regions without structure. The effect of the pinhole on the planar incident field was modeled as that of an opaque mask with transmission 1 in a circular region with a diameter of $1.4 \mu\text{m}$. After numerical propagation to the sample plane, the illumination was normalized to an integrated photon flux corresponding to the mean experimental integrated photon flux collected at each scan position. The exit wave field was formed then as a product of

²The simulated phase maps used here differ from those used in [59] mainly in the sign of the phase which, however, does not affect the simulated scattering behavior and, after all, is a matter of convention.

the object transmission and the laterally translated illumination function at each scan point. Propagation of the exit field to the detector plane in the far field region was modeled as discrete Fourier transform operation (see also Eq. (3.97); the leading phase term can be omitted as it cancels out by alternating forward and backward propagations). After calculating the squared modulus of the propagated exit wave field, Poissonian noise was added to the diffraction pattern.³

5.3 Reconstructions

For reconstruction the algorithm first demonstrated in [141] and described here in Sec. 4.4.5.2 was used. The initial guess for the illumination function was generated in the same way that was used to model the illumination as described above. A random array of the form $[(T_{\max} - T_{\min})Z(x, y) + T_{\min}] \times \exp[i\pi(2Z(x, y) - 1)/20]$ with a size equal to that of the illumination was multiplied with the initial guess of the illumination, and this exit wave array was then used for all exit waves as an initial guess. $Z(x, y)$ here denotes a pseudo random number between 0 and 1. T_{\min} and T_{\max} were set to 0.5 and 1.0, respectively. To account for deviations from the ideal Cartesian positioning grid the measured scanning stage positions at each scan point were used in the algorithm. Positions were rounded [139] to the real space pixel size of the corresponding dataset (see above).

It was found that in the present case of a weakly scattering object the treatment of noise in the diffraction data played an essential role in the reconstruction process. To account for the noise in the measured data the modified propagator described in Sec. 4.6 and given by Eq. (4.87) was applied which allows for a finite mean square deviation d^2 between the measured and the updated Fourier amplitudes at each scan position. As noted earlier, Poissonian noise statistics yields an expected deviation of $\langle d^2 \rangle = D_{\text{th}}^2 = 1/4$. Although a value $D = D_{\text{th}}$ is the optimum choice according to the noise model, the final value of the relaxation parameter D had to be determined from numerical experiments, based on reconstructions of simulated as well as experimental data. This procedure was necessary to compromise between two extreme cases: A too tight constraint (small values of D) introduces too much noise from the experimental data into the reconstruction process. The complex averaging applied at the end of the reconstruction process to make the result more reproducible then leads to rather low resolution reconstructions. On the other hand, a too loose constraint (large values of D) can lead to stagnation. It has been noted [139] that especially for weakly scattering objects a remaining ambiguity in the reconstruction of the object and illumination function can lead to a “raster grid pathology”, if the sample is translated on a Cartesian grid. Such a grid pathology could be observed here mainly for too loose constraints, i.e. large values of D .

Reconstruction results for different values of the relaxation parameter D are shown in Sec. A.4 for simulated and experimental data. Based on these numerical experiments, the relaxation parameter was optimized.

³Here the Matlab-routine *imnoise.m* with an option for the generation of Poissonian noise was used.

5.4 Results

5.4.1 Reconstructed phase maps

As a first analysis step, which can even be performed during the experimental data collection process, conventional transmission, differential phase contrast and dark-field images can be generated (see Fig. 5.2 for images corresponding to the short-exposure dataset). These micrographs have a pixel size equal to the grid spacing of the raster scan, and their resolution is limited to the diameter of the illumination (about $1.4 \mu\text{m}$).

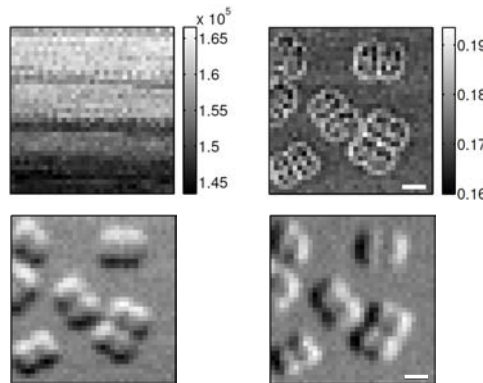


Figure 5.2: Scanning micrographs generated from the short exposure dataset. Each pixel corresponds to one scan point. Scale bars indicate a distance of $2 \mu\text{m}$. In transmission contrast (upper left) the cells are invisible. The colorbar here indicates the total integrated number of photons collected at the detector per scan point. In dark field mode (upper right) the outline of the cells can clearly be identified. The colorbar here indicates the fraction of photons that are collected outside a pre-defined central region of the diffraction pattern. Similarly, the cells can easily be identified in differential phase contrast mode, either in vertical (lower left) or horizontal direction (lower right).

The reconstructed object phase as obtained from the ptychographic reconstruction from the short-exposure dataset is depicted in Fig. 5.3.⁴ The result is consistent with the differential phase contrast and dark-field images as well as with the optical micrographs shown in Fig. 5.1. With respect to the scanning micrographs obtained from the same dataset a significant increase in resolution and imaged details is apparent.

The maximum phase shift caused by a single cell is in the range of $0.25 - 0.3$ rad, in agreement with expected values noted above. The expected value for the amplitude attenuation is below the detection level of the experiment, leading to an overall flat experimental amplitude reconstruction with small fluctuations (not shown here).

The reconstruction shows *D. radiodurans* cells in dimeric and tetrameric form. The separation of each monomeric part of a cell into four internal subunits, which each contain

⁴All obtained phase maps are only unique up to the addition of a constant phase offset. Note here that the absolute phase is a “quantity with no physical content anyway” [105, p. 63]. Furthermore, not perfect centering of the analyzed far field diffraction patterns can cause a phase ramp in real space. As a consequence, some of the obtained phase images were multiplied with such a linear phase ramp to correct for this effect.

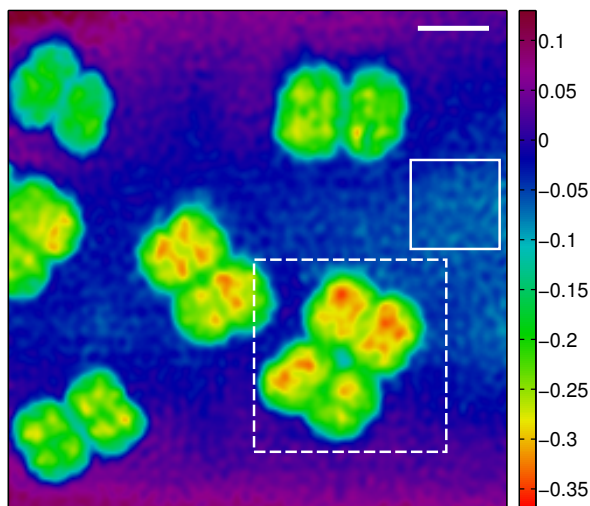


Figure 5.3: Freeze-dried *D. radiodurans* cells visualized by ptychographic Coherent X-ray Diffractive Imaging. The reconstructed phase of the object transmission function for the short exposure dataset is shown here. The depicted field of view corresponds to the conventional scanning micrographs that are depicted in Fig. 5.2. The scale bar represents a distance of 2 μm, the colorbar indicates phase values in radians. The standard deviation of the phase within the solid white rectangle is 0.012 rad. The area marked by the dashed white frame was scanned again in a subsequent scan with longer exposure time (see Fig. 5.4).

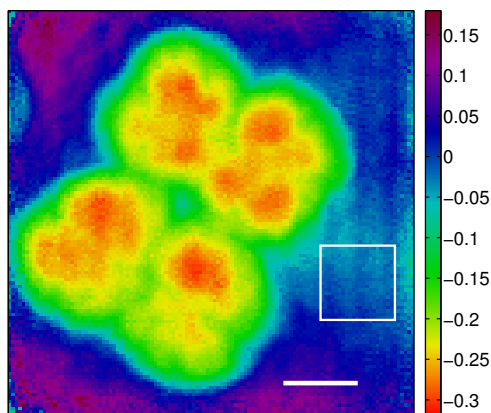


Figure 5.4: Ptychographic CDI reconstruction of a single *D. radiodurans* cell, obtained from an independent measurement with longer exposure time. The region shown here corresponds to the ROI marked by a dashed white frame in Fig. 5.3. The scale bar represents a distance of 1 μm, the colorbar indicates phase values in radians. The standard deviation of the phase within the solid white rectangle is 0.017 rad.

a single copy of the bacterium's genome [84], can be observed for a large part of the cells. Note that actively growing and separating cells were used. Therefore, the internal structure of the cells is likely to be not as uniform as for stationary-state cells [84]. In addition, it cannot be excluded that the preparation process has led to small deviations from the native structure.

An independent ptychographic reconstruction of the object phase is depicted in Fig. 5.4 for the long exposure dataset. The reconstruction is consistent with the corresponding region of the short exposure dataset, indicating that correct reconstruction parameters have been chosen. In comparing both images note that the colorbars are not identical.

5.4.2 Reconstructed diffraction patterns

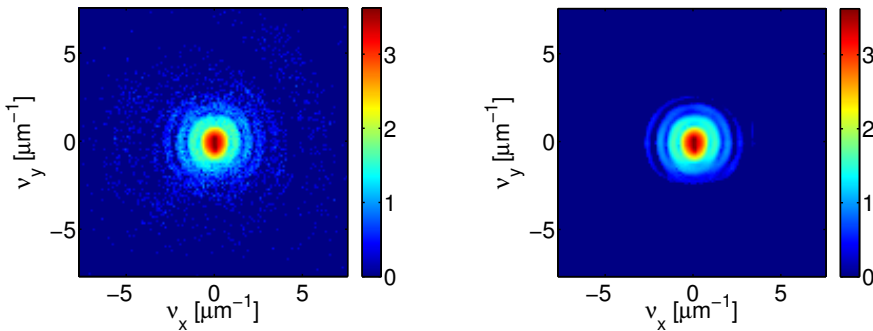


Figure 5.5: Typical measured (left) and reconstructed (right) diffraction pattern from the short-exposure dataset at a scan point where a cell was in the beam. Colorbars indicate the time integrated photon flux per pixel on a logarithmic scale.

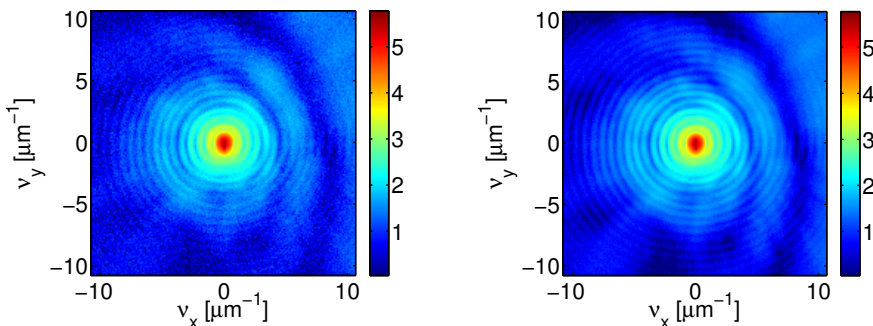


Figure 5.6: Typical measured (left) and reconstructed (right) diffraction pattern from the long-exposure dataset at a scan point where a cell was in the beam. Colorbars indicate the time integrated photon flux per pixel on a logarithmic scale. Note that the diffraction patterns cover more than 5 orders of magnitude, obtained in a single measurement.

From the reconstructed complex-valued illumination and the reconstructed object function, it is possible to generate reconstructed diffraction patterns at each scan point. A comparison of exemplary experimental and reconstructed diffraction patterns for the short and long exposure dataset is given in Fig. 5.5 and Fig. 5.6, respectively. The diffraction data shown here was obtained at scan points where cellular material was in the beam. The reconstructed diffraction patterns are very consistent with the measured ones. Signal has been reliably reconstructed to a highest spatial frequency of about $3 \mu\text{m}^{-1}$ for the short-exposure dataset and $> 10 \mu\text{m}^{-1}$ for the long-exposure dataset. The diffraction patterns are dominated by the scattering from the circular pinhole aperture that leads to the observed Airy pattern in the far field.

5.4.3 Reconstructed illumination

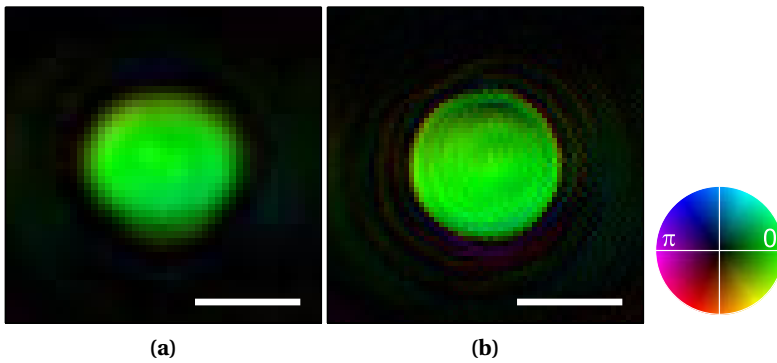


Figure 5.7: Reconstructed complex illumination functions corresponding to the short-exposure dataset (a) and the long-exposure dataset (b). Both probe functions have been back-propagated here over a distance of 1.4 mm to the exit plane of the pinhole. Scale bars indicate a distance of $1 \mu\text{m}$.

The reconstructed complex-valued illumination functions are shown for both datasets in Fig. 5.7. Both have been back-propagated to the exit plane of the pinhole. As indicated by the diffraction patterns the resolution of the reconstruction is improved by longer illumination time. The reconstructions also show that on the scale of the sample signal⁵ there is a significant deviation from the expected scattering behavior of an ideal circular and opaque mask with zero thickness. Therefore, a successful reconstruction of the sample transmission function is unlikely in the present case with a fixed and guessed illumination function (ptychographic without probe retrieval). Nevertheless, it was observed to be advantageous that the used pinhole was nearly circular and — through the fabrication process by focused ion beam milling — showed a scattering behavior close to an ideal pinhole. Therefore, it was not necessary to obtain in a first step an independent reconstruction of the illumination wave field by ptychographic imaging of a strongly scattering test pattern. A fall-back routine then could have been to use the so-obtained illumination

⁵The sample here causes a maximum phase change of about $0.03 \text{ rad} = 1.7^\circ$.

function as a seed for the reconstruction of the weakly scattering object. Nevertheless, an experiment with a strongly scattering test sample was also done here in order to justify the choice of the initial guess of an ideal circular mask [59] and to optimize the parameters for the initial guess. The distance between the pinhole and the sample was accurately known from measurements with the online optical microscope during the experiment.

5.4.4 Density maps

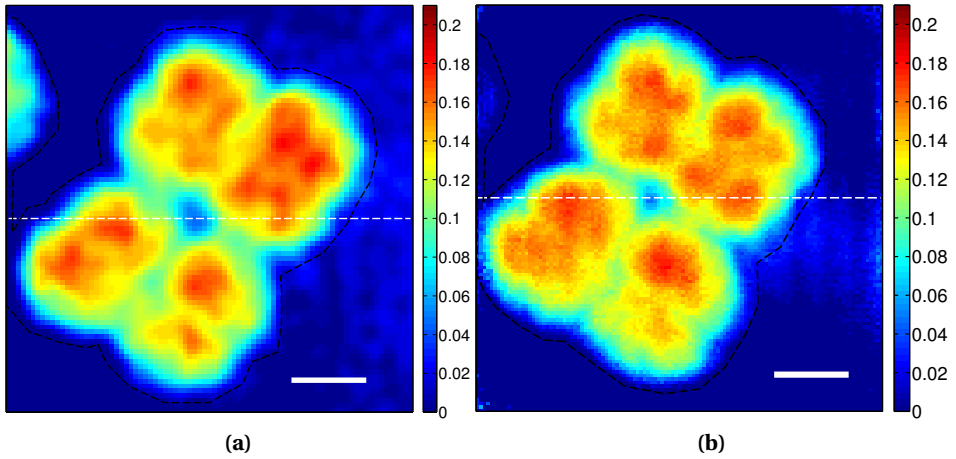


Figure 5.8: Effective projected mass density distribution of a single *D. radiodurans* cell, shown here in comparison as obtained from the short-exposure dataset (a) and the long-exposure dataset (b). Scale bars indicate a distance of 1 μm , colorbars give $\bar{\sigma}_m(x, y)$ in units mg/cm^2 . The substrate region outside the dashed black lines has been used for a determination of the background offset to define a zero reference density (see main text). Line profiles of the projected mass density along the dashed white lines are shown in Fig. 5.9.

In the present experiment all photons reaching the detector have been recorded quantitatively. In particular, no beamstop had to be used to block the direct beam. As a consequence, the reconstructed phase maps can be analyzed quantitatively. As outlined in Secs. 3.2.1 and 3.2.2 the obtained phase map is linearly related to the real part of the refractive index, as long as the projection approximation can be applied. With a cell thickness certainly below 5 μm in the present experiment and a photon energy of 6.2 keV the projection approximation remains valid down to a lateral resolution of about (see Eq. 3.136) 30 nm which is beyond the values that were reached here (see below). Eqs. (3.123) and (3.148) then yield

$$\varphi(x, y) = -r_e \lambda_0 \sigma_e(x, y) \quad (5.1)$$

where $\varphi(x, y)$ denotes the phase distribution of the object transmission function and

$$\sigma_e(x, y) := \bar{\rho}_e(x, y) \quad (5.2)$$

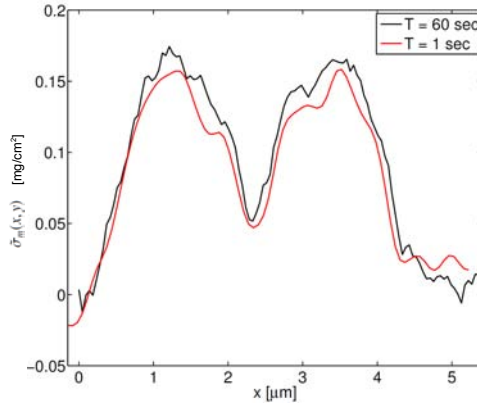


Figure 5.9: Line profiles of the projected mass density obtained from the mass density maps shown in Fig. 5.8. The profiles are shown as obtained from the short ($T = 1$ sec) and long ($T = 60$ sec) exposure dataset.

the electron density distribution, integrated over the sample volume along the direction of the optical axis. It thus becomes possible to rescale the obtained phase map linearly into a projected electron density distribution. With Eq. (3.125) one further obtains

$$\sigma_e(x, y) = \left(\frac{\bar{Z}}{u\bar{A}} \right) \sigma_m(x, y) \quad (5.3)$$

where $\sigma_m(x, y)$ denotes the projected mass density of the sample. \bar{A} and \bar{Z} are the atomic weight and charge number in the material, averaged over all molar fractions. For unstained biological objects such as the cells that have been imaged here one can approximate $\bar{A}/\bar{Z} \approx 2$. One can then define an ‘effective’ mass density via

$$\tilde{\sigma}_m(x, y) := \frac{2\bar{Z}}{\bar{A}} \sigma_m(x, y). \quad (5.4)$$

The prefactor relating the true and ‘effective’ mass density is close to 1. For a the biological model material used in the simulation (see above) one obtains $2\bar{Z}/\bar{A} \approx 1.065$. As a result, the obtained phase maps can be rescaled into an effective projected mass density map via

$$\tilde{\sigma}_m(x, y) = - \left(\frac{2u}{\lambda_0 r_e} \right) \varphi(x, y). \quad (5.5)$$

For biological material this effective mass density can be expected to deviate from the true mass density by less than 10%.

Reconstructed mass density distributions of the same cell, imaged at two different illumination times, are shown in Fig. 5.8. The substrate regions circumvented by black dashed lines in the images have been used to define an offset density that was subtracted from the rescaled phase maps. Due to fluctuations in the substrate region there is a remaining

inaccuracy in this process and an additional offset of 0.02 mg/cm^2 was subtracted from the density map obtained for the long-exposure dataset in order to make the density maps obtained from both reconstructions comparable.

Horizontal line profiles as depicted in Fig. 5.9 show a good coincidence between the two entirely independent reconstructions of the same cell.

5.4.5 Reconstructions from simulated data

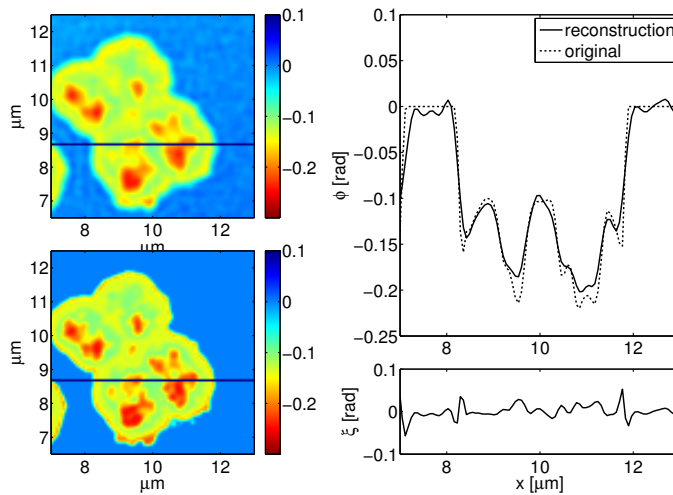


Figure 5.10: (Lower Left) Subregion of a phantom phase distribution used for simulation of a ptychographic dataset corresponding to the experimental short-exposure dataset. The colorbar indicates the phase in radians. (Upper left) Corresponding region of the reconstructed phase distribution as obtained from the simulated dataset. (Upper right) Line profiles of the phase along the horizontal dark blue lines shown in the images on the left. (Lower right) Residuals of the line profiles.

Fig. 5.10 summarizes results from the reconstruction of the simulated short exposure dataset. A visual comparison of the simulated and reconstructed phase in a subregion of the total simulated object transmission function indicates an accurate reconstruction of the phantom phase distribution. A slight blurring can be observed in the reconstructed phase map which can be attributed to the finite amount of simulated photons scattered from the sample, limiting the obtainable resolution. The standard deviation of the phase difference in the cellular area that is depicted in the images was determined to be around 0.017 rad , giving a measure of the average error in the reconstruction. Line profiles through the simulated and reconstructed phase map along with their residuals (see Fig. 5.10) give an alternative view on the accuracy of the reconstruction.

The result of an analogous analysis is depicted in Fig. 5.11 for the simulated long exposure dataset. Evidently, the reconstruction of phantom image is more accurate compared to the short-exposure dataset. In addition, the blurring of the reconstructed phase map is weaker here which can best be observed by a comparison of the line profiles. The

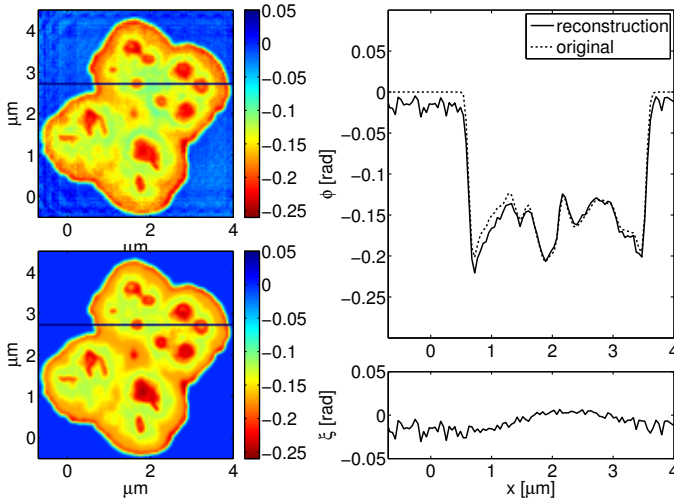


Figure 5.11: (Lower Left) Subregion of a phantom phase distribution used for simulation of a ptychographic dataset corresponding to the experimental long-exposure dataset. The colorbar indicates the phase in radians. (Upper left) Corresponding region of the reconstructed phase distribution as obtained from the simulated dataset. (Upper right) Line profiles of the phase along the horizontal dark blue lines shown in the images on the left. (Lower right) Residuals of the line profiles.

higher reconstruction accuracy can be quantified by the standard deviation of the difference between the simulated and reconstructed phase in the cellular area, given here as 0.012 rad.

5.4.6 Resolution

An assessment of the resolution of the obtained reconstructions is not straightforward, as the biological objects that have been imaged here exhibit no sharp features which could be used to obtain a line spread function, for example. In far field coherent diffractive imaging, the phase retrieval transfer function (see Section 4.5) has now become a quasi-standard to determine the obtained resolution [103, 127, 132, 142]. Therefore, this approach was also followed here.

As the diffraction patterns contain many zeros here, the angular-averaged PRTF has been calculated according to

$$\text{PRTF}(k_r) := \frac{\langle |\mathcal{F}[\bar{\psi}](\mathbf{k}_\perp)| \rangle}{\langle \sqrt{I(\mathbf{k}_\perp)} \rangle}. \quad (5.6)$$

Here k_r denotes the radial reciprocal space variable; it is related to the radial spatial frequency variable ν_r via $\nu_r = k_r/2\pi$. In other words, the angular average $\langle \cdot \rangle$ has been performed prior to forming the ratio, as also described in [136]. Averaging before division can be expected to give the same result compared to division and subsequent averaging, if

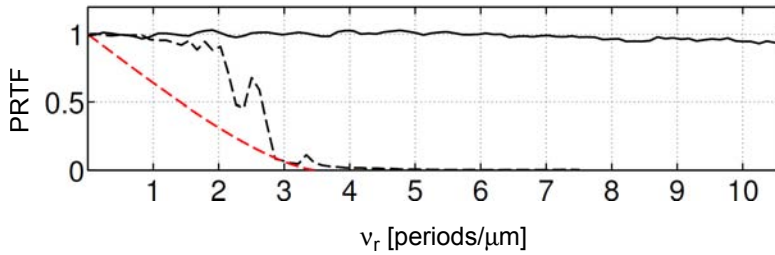


Figure 5.12: Typical phase retrieval transfer functions for a scan point where cellular material was illuminated. Curves are shown here for the short (black dashed line) and long exposure dataset (black solid line). For comparison, the red dashed line shows an ideal modulation transfer function with a cutoff frequency of $3.5 \mu\text{m}^{-1}$.

the diffraction pattern is nearly isotropic. This is nearly the case for the present experiment. Division before averaging is problematic here due to many zeros in the recorded diffraction pattern.

PRTF curves for scan points, where cellular material was in the beam, are shown in Fig. 5.12 for the short and long-exposure dataset. For comparison, an ideal optical (here also modulation) transfer function for incoherent illumination and a circular exit pupil with a cutoff frequency of $3.5 \mu\text{m}^{-1}$ is shown⁶ [61]. The PRTF of the short exposure dataset decreases to zero at about $3.5 \mu\text{m}^{-1}$, corresponding to a real space half-period length of about 150 nm. There is no unique relation of the PRTF to a resolution number in the literature. Usually, one selects the spatial frequency corresponding to a certain decay value of the PRTF, e.g. 0.1 [127]. The PRTF of the long-exposure dataset stays at a value of 1 up to the highest spatial frequency of the selected field of view on the detector. This indicates that the exit wave has been consistently phased down to a half-period resolution of about 50 nm, the real space pixel width.

A difficulty that arises in the resolution assessment of ptychographic reconstructions becomes apparent here. The diffraction patterns used above to evaluate the resolution contain a convolution of the far field diffraction pattern of the sample with that of the illumination. The values obtained above thus give an indication for the resolution of the entire exit wave reconstruction at the corresponding scan point. In general the PRTF obtained from a single reconstructed scan point thus only sets a lower (best) limit to both the resolution of the illumination and the object reconstruction.

In the present case the diffraction patterns are dominated by scattering contributions from the pinhole. In accordance with this observation, resolutions as estimated above are in agreement with the reconstructed illumination functions shown in Fig. 5.7. A visual inspection of the reconstructed object functions indicates that for the long-exposure dataset the resolution value estimated by the PRTF is too high.

⁶The functional form of this modulation transfer function is $2/\pi[\arccos(\tilde{v}_r) - \tilde{v}_r\sqrt{1 - \tilde{v}_r^2}]$ with $\tilde{v}_r = v_r/v_{\text{max}}$ and $v_{\text{max}} = 3.5 \mu\text{m}^{-1}$.

An alternative estimate of the resolution was thus made based on the reconstructed object transmission function only. Experimental and theoretical evidence [72] indicates that for biological objects illuminated by a plane wave the far field intensity decays with a power law behavior with respect to spatial frequency. Reported exponents vary from about -3 to -6 [72]. For plane wave illumination the far field intensity can be interpreted as the power spectral density (PSD) of the object transmission function. In the present case, the *reconstructed* object transmission (here its phase distribution) was thus used to calculate a power spectrum. As for the plane wave diffraction pattern, a decay in a straight line is expected, until the PSD reaches a plateau region, which is dominated by contributions of noise in the image.

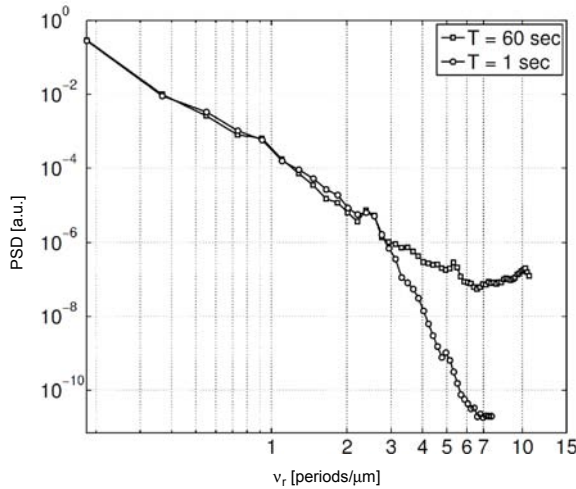


Figure 5.13: Angular averaged power spectral density of the projected mass density distributions as shown in Fig. 5.8. Both axes are on a logarithmic scale.

Fig. 5.13 shows angular averaged PSD curves as obtained from the reconstructed mass density distributions⁷ shown in Fig. 5.8. Up to a spatial frequency of $2.5 \mu\text{m}^{-1}$ both curves follow the same expected decay line, which can be described by a power law decay with exponent -4.4 .⁸ The PSD curve for the long-exposure dataset enters the noise plateau region at a spatial frequency of about $6 \mu\text{m}^{-1}$, corresponding to a real space half-period length around 85 nm. Note, however, that this value can only be regarded as a lower (best) limit to the resolution. The PSD curve indicates the information content in the image with respect to spatial frequency, but it does not provide information on the accuracy of this information with respect to the measured data [136].

⁷These are proportional to the reconstructed phase maps.

⁸Note that in [59] the PSD was calculated directly from the reconstructed object, here it has been obtained from the reconstructed mass density maps. In addition, in the present analysis a Kaiser-Bessel window was applied to the images before forming the PSD, in order to avoid high-frequency artifacts. This procedure can, however, affect the power value of the decay line.

The PSD curve for the short-exposure dataset deviates from the expected behavior: At $\nu_r \approx 2.5 \mu\text{m}^{-1}$ the exponent of the decay decreases significantly before the curve enters a plateau region at about $6.5 \mu\text{m}^{-1}$. The region for frequencies larger than $2.5 \mu\text{m}^{-1}$, where the PSD curve deviates from the initial decay behavior, might thus be attributed to information that is not contained in the data. Taking the end of the expected decay behavior as a lower (best) limit to the resolution then yields a value of about 200 nm.

Assuming a material composition as used in the simulations the dose applied to the sample in both scans can be estimated based on Eq. (4.102). For the short exposure scan this yields a dose of $D_1 \approx 1.8 \times 10^3$ Gy, for the long exposure scan $D_2 \approx 1.2 \times 10^5$ Gy. Both are well below the feature destroying limit at the resolutions that have been estimated here. Note that the present data has been taken using a beam that was not highly focused.

5.4.7 Experimental error

In view of the quantitative reconstructions we would like to give a measure of their experimental uncertainty. It was determined here from the phase fluctuations in flat regions of the substrate as well as from comparisons of the simulated phase distributions with their reconstructions.

Fluctuations in flat substrate regions of experimental reconstructions have been determined to 0.012 rad (standard deviation) for the short exposure dataset and 0.017 rad for the long exposure dataset. The increased fluence here thus does not lead to a decay in phase fluctuations in regions where a uniform phase is expected. This indicates that remaining systematic fluctuations add to the phase uncertainty here. These can partly be attributed to the Cartesian grid, on which the scan points are located, which may lead, for weakly scattering objects, to remaining artifacts in the reconstruction [34]. A way to circumvent possible contributions from the raster grid ambiguity is to locate the scanning positions on a non-Cartesian grid as shown in [34].

The standard deviation of the residuals between simulated and reconstructed phase in the cellular area shown in Fig. 5.11 (long exposure dataset) is 0.012 rad. For the simulated short exposure dataset (see Fig. 5.10) the value is 0.017 rad. Phase deviations smaller than these values cannot be expected to be reconstructed reliably any more. For both datasets deviations generally stay below 0.03 rad which can be regarded as an estimate for the phase reconstruction error in the present experiment.

The conversion of the obtained phase maps into area mass density implies the subtraction of a constant offset from the phase map and a rescaling in units of mass density. With Eq. (5.5) an estimate in the error for the mass density is thus given as

$$\Delta\bar{\sigma}_m = \left(\frac{2u}{\lambda_0 r_e} \right) \sqrt{\Delta\varphi_{\text{sim}}^2 + \Delta\varphi_{\text{bg}}^2} \quad (5.7)$$

where $\Delta\varphi_{\text{sim}}$ denotes the statistical phase error as obtained from the simulations (see above) and $\Delta\varphi_{\text{bg}}$ the statistical error of the phase offset used to define a zero projected density. Based on these calculations, the total error in density is obtained as 0.018 mg/cm^2 for the long-exposure dataset and 0.029 mg/cm^2 for the short-exposure dataset. As the long-exposure dataset contains only a relatively small substrate region, the overall uncertainty in the determination of the offset value is higher than for the short-exposure dataset,

for which a small subregion from a larger substrate area was selected for the mass density analysis.

5.5 Discussion and Conclusion

In conclusion, it was demonstrated here that ptychographic (hard) x-ray coherent diffractive imaging can be applied to unstained biological cells in a quantitative manner. The required high phase sensitivity of the method is on the order of 0.03 rad and becomes possible through an accurate simultaneous reconstruction of the illumination and object function.

Estimating the resolution of the reconstructed images is difficult for ptychographic reconstructions of weakly scattering samples, as the contributions to the diffraction patterns are not equally separated between the opaque mask causing the Airy pattern and the weakly scattering sample. The values estimated here can only be regarded as lower (best) limits.⁹ Note also that the applied dose is at a very low level, compared to high-resolution plane wave CDI studies [103, 132]. If one would like to optimize the experiment for high resolution, one could replace the pinhole by a focusing device, such as a Fresnel zone plate.

Due to the simple interaction process of the cells with the coherent hard x-ray beam (projection approximation) and the quantitative collection of all photons reaching the detector (no beamstop), the reconstructed phase maps could be rescaled into projected electron (or, with certain restrictions, mass) density maps.

The reconstructed density distributions of the *D. radiodurans* cells are characterized by relatively high projected density in the regions where the bacterial nucleoid is located. A majority of cells contain three to four of those regions 400 to 600 nm in diameter with higher projected density. In cryo transmission electron micrographs of vitrified sections these regions of compactified plasmid DNA exhibit slightly less absorption compared to their ribosome rich surrounding [39]. For the x-ray images tomographic reconstructions are needed to assign a volume density to the reconstructed phase maps, as it is generally not known, if the higher projected density arises due to larger thickness or higher volume density. In addition, artifacts from the preparation process might contribute in the present case to non-natural density distributions, so that a full comparison to the EM images should only be made with cryo-fixated specimens. Nevertheless, it remains an interesting question to what extent absorption contrast in EM images of biological specimens can be reproduced or complemented here by quantitative density contrast from x-ray images. Certainly, the interaction process with x-rays is much simpler for thin specimens and high photon energies (> 5 keV) compared to the multiple scattering interaction of electrons with the specimen.

⁹It is noted that for a heavy element test pattern with much higher scattering power than that of the unstained cells, lines and spaces with a half period down to about 50 nm could be resolved quantitatively [59] with the same setup that was used here, applying a similar fluence of about 5.1×10^6 ph/ μm^2 .

6 Ptychographic soft x-ray microscopy

Lens-based soft x-ray microscopy has been applied with great success in the co-called water window range of energies [81, 151]. This is the photon energy range between the K-absorption edge of carbon ($E \approx 280$ eV) and oxygen ($E \approx 530$ eV). As lens-based soft x-ray microscopy mainly exploits the absorption contrast, this energy range is particularly suited to achieve high absorption contrast of biological samples against their aqueous environment. Ptychographic coherent diffractive imaging, on the other hand, has been limited to the hard x-ray [33, 34, 59, 77, 120, 130, 131, 141] or optical [13, 90, 118, 139] wavelength range in experimental demonstrations so far with the exception of a precursor to the method that is based on “Wigner-deconvolution” [18]. With its strengths in terms of specimen and wave field characterization, ptychographic CDI could also represent a very valuable tool in the soft x-ray range. The experiment described in the following¹ therefore aimed at an extension of ptychographic CDI to this photon energy range. Here a photon energy of 517 eV or wavelength of $\lambda_0 \approx 2.4$ nm was chosen.

6.1 Experiment

6.1.1 Fossil diatom

In the present experiment a fossil diatom was imaged using a pinhole as the beam confining optical element. Diatoms are a very abundant microorganisms that can be found as a major component of plankton in all sea waters on earth [32]. Their silicified cell walls form a complex 3D structure, the frustule, which exhibits features in the range of several hundred nanometers to microns. In the fossil form only the frustule is left which can be used as a test object in soft x-ray microscopy [7].

For preparation an aqueous suspension of fossil diatoms was spread onto a 100 nm-thick silicon-nitride membrane (Silson, UK) and air-dried.² Note that the polyimide foil sample support used for the hard x-ray experiments cannot be applied at these photon energies: the intensity transmission of a 10 μm -thick polyimide layer at a photon energy of 517 eV is around 4×10^{-7} [67].

The long wavelength and thus very small soft x-ray penetration depth in air under ambient pressure requires the complete beam path from the source to the detector to be set under vacuum. For the present experiment, which was carried out at the undulator

¹Contents of this chapter have been published in [55].

²The preparation was performed by the group of Dr. Axel Rosenhahn at the University of Heidelberg, Germany.

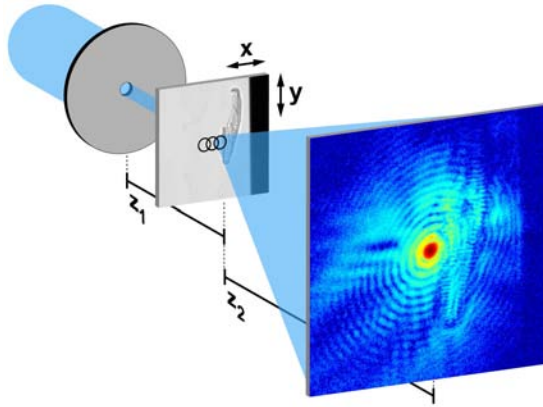


Figure 6.1: *Experimental setup for ptychographic coherent x-ray diffractive imaging of a fossil diatom: The illuminating wave field is confined by a small pinhole with a diameter on the order of $2\ \mu\text{m}$, before it impinges onto the sample after propagating over a distance $z_1 \approx 1\ \text{mm}$. The sample, a diatom on a silicon nitride membrane, is scanned laterally through the beam on a rectangular grid while at each scan point a diffraction pattern is collected on a two-dimensional CCD detector placed at a distance $z_2 \approx 0.49\ \text{m}$ away from the sample. The same setup and measurement principle was then used in a second experiment to image a test pattern structured by nano-lithography. Figure from [55].*

beamline UE52-SGM of the Berlin electron storage ring Bessy II, a dedicated experimental vacuum chamber [91] was used that has been developed by the group of Dr. Axel Rosenhahn at the University of Heidelberg. The incident beam was focused by mirrors and/or confined by slits to a size of about $17.4(\text{hrz.}) \times 100(\text{vrt.})\ \mu\text{m}^2$. After passing the pinhole (stainless steel, thickness ca. $13\ \mu\text{m}$, diameter³ on the order of $2\ \mu\text{m}$, Edmund Optics, Germany) positioned into the beam focus and free-space propagation over a distance of $z_1 \approx 1 - 1.4\ \text{mm}$, the Fresnel-diffracted beam reached the sample, which was then scanned laterally through the beam on a rectangular grid with a small enough grid period to allow for sufficient overlap between illuminated areas of adjacent scan points. A schematic of the experiment is depicted in Fig. 6.1. To assure high positioning accuracy, closed-loop piezoelectric positioning stages (Physik Instrumente, Germany) were used for scanning the sample through the beam. The resulting diffraction patterns were recorded at a distance $z_2 = 0.49\ \text{m}$ away from the sample on a back-illuminated, peltier-cooled CCD detector (DX436, Andor Technology, UK) with a pixel width of $13.5\ \mu\text{m}$ in horizontal and vertical direction and a total number of 2048×2048 pixels.

Ptychographic CDI of the diatom sample was carried out as follows. The sample was translated at a distance of about $1\ \text{mm}$ downstream of the pinhole in a plane perpendicular to the optical axis on a Cartesian grid with a spacing of $800\ \text{nm}$ in both directions and $14(\text{hrz.}) \times 24(\text{vrt.})$ scan points. Without using a beamstop, diffraction patterns were collected with $0.18\ \text{s}$ exposure time at each scan point, making use of the full dynamic

³The pinhole actually had a slightly elliptical shape with largest (smallest) diameter of about $2\ \mu\text{m}$ ($1.5\ \mu\text{m}$).

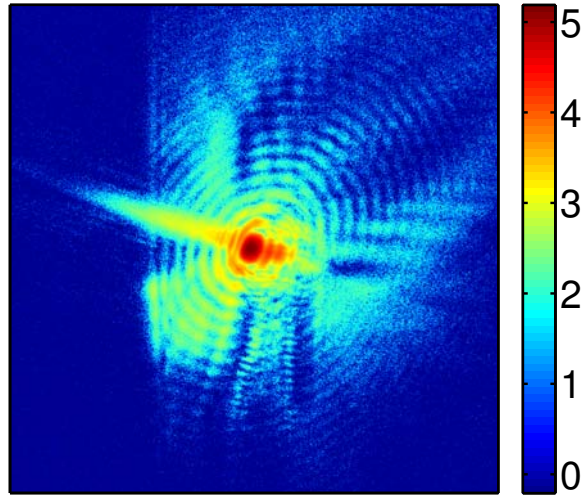


Figure 6.2: Single dark-field corrected and binned diffraction pattern from the diatom dataset. The color bar indicates the corrected signal on a logarithmic scale (to basis 10), covering more than 5 orders of magnitude. The area shown here corresponds to 1920×1920 pixels on the detector. The shadowed region on the left corresponds to an edge of the silicon nitride window that is used as a sample support. Figure adapted from [55].

range ($16 \text{ bit} \approx 10^{4.8}$) of the CCD. To minimize effects of thermal drift of the vacuum scanning stages the total scan time had to be kept at a minimum. Therefore a fast readout mode of the detector was used, leading to a significant readout noise contribution in the diffraction patterns. To correct for this and other noise contributions a dark image (with closed shutter) with exposure time 0.18 s was collected immediately after the scan. Relatively independent of exposure time, the mean value of the dark noise was on the order of 795 counts/pixel. The corrected detector signal was then calculated for each pixel as

$$I_{\text{corr}} = \max\{I_{\text{meas}} - (1 + 2\sigma)I_{\text{dark}}, 0\} \quad (6.1)$$

with I_{meas} denoting the measured signal, I_{dark} the dark signal and $\sigma \lesssim 0.01$ denoting the standard deviation of the dark image, relative to its mean. By application of Eq. (6.1) remaining camera readout noise contributions to I_{corr} could be strongly inhibited.

For reconstruction, a CCD region of 1920×1920 pixels was selected. Using a pinhole diameter of $2 \mu\text{m}$ as a reference diameter of the exit wave in the sample plane, the detector distance corresponds to a Fresnel number $F \approx 0.003$. Neglecting low intensity contributions due to the sidelobes of the pinhole wave field at the sample (see below) the detector was thus placed into the far field of the exit wave, leading with Eq. (3.80) to a real space pixel size of 45 nm in the exit plane. The 336 diffraction patterns, each containing 1920×1920 pixels, result in rather high computational demands. Therefore, the diffraction patterns were binned down by a factor of 2 along the horizontal and vertical direction, so that each

pixel value of the binned diffraction equals the sum of four neighboring pixel values of the unbinned diffraction pattern.

A typical dark-field corrected diffraction pattern from the ptychographic dataset is shown in Fig. 6.2. As visible in the pattern, the diffracted intensity is composed of three contributions: The far field diffraction pattern of the pinhole (concentric rings), the far field diffraction pattern from an edge of the diatom sample (streak that extends into the empty region on the left) and finally a near field diffraction pattern of the diatom sample (vertical stripes of low intensity in the lower half of the image). The empty region on the left is due to the absorbing frame of the silicon nitride window that is used as a sample support. Note that the different contributions to the diffraction pattern are generally not additive. For a further interpretation of the diffraction pattern see the discussion section.

6.1.2 Siemens star

As a second specimen, a Siemens star test pattern (model ATN/XRESO-50HC, NTT-AT, Japan) consisting of a 500-nm-thick nanostructured tantalum layer on a transparent membrane (Ru(20 nm)/SiC(200 nm)/SiN(50 nm)) was translated at a distance of $z_1 \approx 1.4$ mm from the pinhole on a rectangular grid with the same spacing as used before. To minimize the effect of drift in the positioning stages only a subregion of the total scanned area was selected for reconstruction, consisting of 9×7 scan points. 10 exposures with a duration of 0.22 s each were collected at every scan point, accumulated, and corrected by subtraction of an equivalent sum of dark images. The combination of several exposures lead to an increased dynamic range of the diffraction patterns used for reconstruction. As for the first dataset, data from a detector region of 1920×1920 pixels was selected and binned by a factor of 2 along each dimension.

A typical diffraction pattern from the Siemens star dataset is depicted in Fig. 6.3. The pattern which was recorded near the center of the Siemens star is strongly dominated by the near and far field diffraction signal due to the sample, with the signal from the pinhole strongly suppressed.

6.2 Reconstruction

6.2.1 Diatom dataset

For reconstruction the algorithm described in section 4.4.5.2 and [139, 141] was used and iterated for 200 iterations. Start of the algorithm was initiated by a random complex object field containing pixel values $(0.95 + 0.05Z) \times \exp(i(2\pi Z - \pi)/20)$ where Z denotes an evenly distributed (pseudo) random variable between 0 and 1. Larger random amplitudes were found to increase transient times very strongly. The initial illumination was constructed by near field propagation of a binary pinhole mask, using an elliptical pinhole shape with major axes $1.35 \mu\text{m}$ and $1.55 \mu\text{m}$, rotated by 55 degrees with respect to the coordinate axes. The simultaneous retrieval of the illumination function (see Eq. 4.72) was initiated here at iteration 2.

The evolution of the difference map error as defined in Eq. (4.78) is shown in Fig. 6.4. To average out remaining fluctuations the final complex object and probe reconstruction

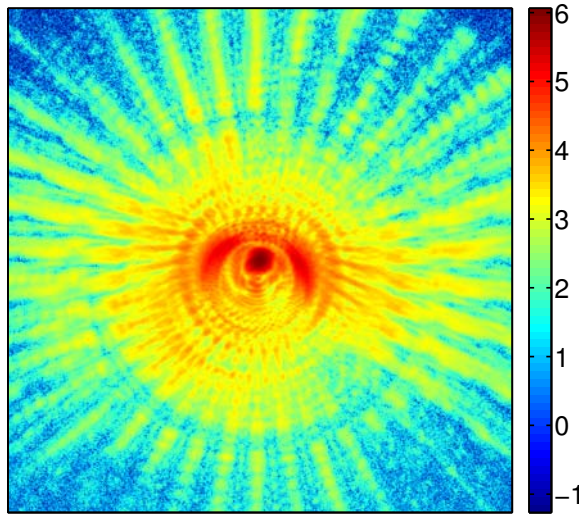


Figure 6.3: Single dark-field corrected diffraction pattern from the Siemens star dataset. The color bar indicates the corrected signal on a logarithmic scale. Figure adapted from [55].

were obtained as a mean over the last 50 iterations. One may argue that the difference map error still decreases by a very small amount during the last 50 iterations. By visual comparison of reconstruction results after 150 and 200 iterations, however, which can hardly be distinguished visually in the object region (see Fig. 6.5), it was decided to stop after 200 iterations and use the last 50 iterates for complex averaging.⁴

As noted before (see Sec. 4.4.6), the separation of the views $\psi_j(\mathbf{r})$ of the ptychographic dataset into an object function $O(\mathbf{r})$ and a translated illumination function $P(\mathbf{r} - \mathbf{r}_j)$ involves a scaling ambiguity with equivalent solutions $f(\mathbf{r})O(\mathbf{r})$ and $f^{-1}(\mathbf{r})P(\mathbf{r})$ with a scalar function $f(\mathbf{r})$ that is periodic with respect to the lattice period of the Cartesian scanning grid. In practice, $f(\mathbf{r})$ generally reduces to a scalar factor for specimens with relatively strong scattering signal, such as the diatom imaged at soft x-ray wavelengths. This scalar factor, however, can lead to unphysical amplification of the object or illumination amplitude. For the present dataset this was found to be a problem at regions where the illumination function was weak. To prevent the unphysical object amplitude amplification, additional constraints on the probe function were introduced. More specifically, a window (or mask)

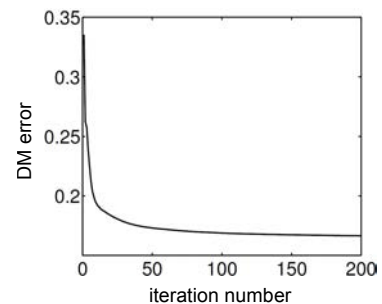


Figure 6.4: Difference map error, see Eq. (4.78), versus iteration number.

⁴200 iterations lasted 21 hours on an eight-CPU-core workstation running at 3.0 GHz under Matlab using built-in multicore processing routines for the evaluation of fft operations.

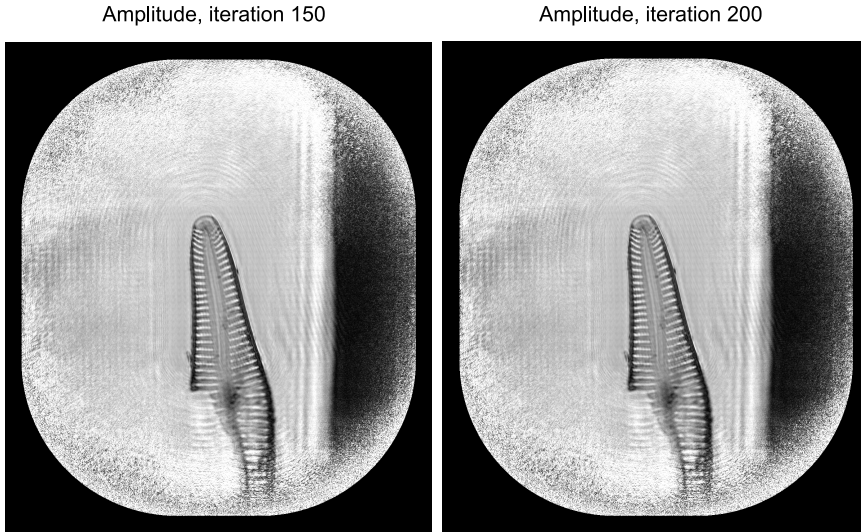


Figure 6.5: Comparison of the object amplitude after 150 and after 200 iterations. The dark region around at the edge of the FOV is caused by a circular mask that was applied on the illumination function.

function described by a Heaviside step function $\Theta(r_0 - r)$ with radial coordinate r was multiplied with the illumination function during each iteration of illumination retrieval, i.e. after each evaluation of Eq. (4.72). By application of the mask the illumination was set to zero outside a circular region with a diameter of $2r_0 = 0.9D_1$ and left unchanged inside the circular region. D_1 here is equal to the width of the numerical FOV of the illumination function in the sample plane. It is related to the wavelength λ_0 , the propagation distance z_2 between sample and detector and the detector pixel width $\Delta x'$ via $D_1 = \lambda_0 z_1 / \Delta x'$. In addition, the object amplitude was bounded by a maximum value of 1, enforced after each iteration of Eq. (4.71).

Noise in the reconstruction was treated by application of the modified modulus constraint operator as defined in Eq. (4.87). The corrected detector signal I_{corr} which taken as an input to the algorithm cannot be identified directly with the integrated photon flux as e.g. for the Pilatus detector. As a consequence, the noise statistics are not truly Poissonian. The modified Fourier constraint operator still gave convincing results, if the parameter D was tuned for optimum reconstruction results. A value of $D = 1.25$ was finally used here.

6.2.2 Siemens star

For the reconstruction of the Siemens star dataset the algorithm was iterated for 400 iterations with an equally constructed initial guess as for the diatom dataset⁵. An additional real space constraint was applied here on the object function, exploiting the essentially binary amplitude due to the test object: As a first additional constraint, the object amplitude transmission $|O|$ was confined to $T_{\min} < |O| < T_{\max} = 1.0$ with $T_{\min} = 0.0114$ and $T_{\max} = 1.0$ denoting the minimum and maximum theoretical amplitude transmission of the sample, respectively. Secondly, beginning at iteration 152, the object amplitude was set equal to the expected value T_{\min} (500 nm Ta at 517 eV photon energy [67]) at every fourth iteration, but only if $|O| < 0.25$.

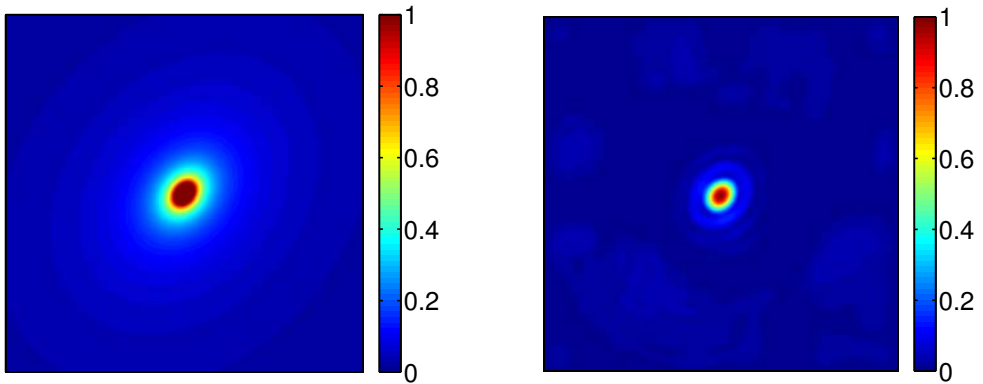


Figure 6.6: (Left) “Hat”-function used as an upper bound to the normalized amplitude of the illumination function in the exit plane. For further description, see main text. (Right) Final reconstructed and normalized amplitude of the illumination function in the exit plane on a linear scale. Both fields are shown here over the whole field of view (1920×1920 pixels).

The scaling ambiguity between the object and illumination function here also had to be circumvented by an additional “mask” constraint on the illumination function. A binary mask as it has been used for the reconstruction of the diatom dataset was found to give unsatisfactory reconstruction results. Therefore, a different constraint on the illumination was devised here. A “hat”-function of the form $(ax_r^2 + by_r^2)^{-c}$ with $a, b, c \in \mathbb{R}$, $c > 1$ and (x_r, y_r) denoting sample plane coordinates in a system rotated with respect to the one used for reconstruction was used as an upper bound for the normalized illumination amplitude. a, b and c were adjusted using the probe reconstruction from the diatom dataset, while an emphasis was put on minimally restricting possible solutions. The “hat”-function that was used here is depicted together with the final reconstructed and normalized illumination amplitude in Fig. 6.6.

Furthermore, a normalization condition for the illumination function was introduced after each evaluation of Eq. (4.72). This condition is briefly discussed here. For every view

⁵Except the assumed propagation distance z_1 between the elliptical pinhole mask and the sample.

ψ_j the overall object intensity transmission is given as

$$T_j := \|O_j\|^2 = \frac{\|\psi_j\|^2}{\|P\|^2} \quad (6.2)$$

with the norm as defined in Eq. (4.34). If $M := \max_j \{\|\psi_j\|^2\}$, then

$$T_j \cdot \|P\|^2 \stackrel{!}{\leq} M \quad \forall j. \quad (6.3)$$

As a consequence, a conditional normalization was introduced as

$$P \rightarrow \sqrt{\frac{M}{T_j}} \cdot \frac{P}{\|P\|}, \quad \text{if } \|P\|^2 > \frac{M}{T_j}. \quad (6.4)$$

For the updated illumination then $\|P\|^2 = M/T_j$. The expected average transmission of the object was set here equal to 0.2. This is an additional constraint helping to prevent P from growing without bound.



Figure 6.7: (Left) Initial binary mask applied to the illumination function, back propagated to the aperture plane. (Right) Final mask as obtained after several iterations of the Shrink-Wrap procedure, see main text. The scale bars indicate $2 \mu\text{m}$.

As an additional step, the illumination wave field was restricted in the plane of the aperture by back propagation of the current illumination estimate to the pinhole plane, multiplication with a binary elliptical mask outlining the support region defined by the pinhole, and subsequent propagation to the sample plane. The binary mask in the pinhole plane was determined by a shrink-wrap mechanism [93] with very loose constraints in order to not over-restrict the problem: Starting with a circular mask with a diameter of $3.2 \mu\text{m}$ the mask was refined at iterations 10, 30, 50 and 70 by setting all values of the mask to one, for which the back-propagated probe amplitude, convoluted with a Gaussian of σ -half-width of 3 pixels, was above 10% of the maximum amplitude value. All other pixels

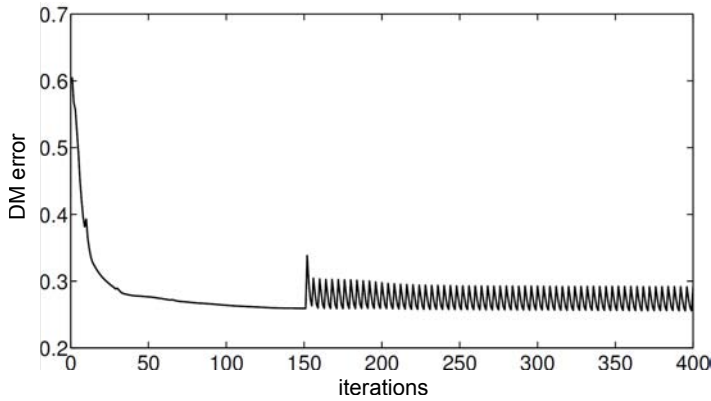


Figure 6.8: *Difference map error against iteration for the Siemens star reconstruction.*

of the mask were set to zero. For a comparison of the initial aperture plane mask with the final mask that was used from iteration 70 on, see Fig. 6.7.

The corresponding difference map error is shown in Fig. 6.8. The fluctuations at in the second half are due to the additional object constraint described above. The parameter for the treatment of noise (see above) was optimized to $D = 3$.

6.3 Results

6.3.1 Fossil diatom

An overview of the reconstructed complex object transmission function for the diatom sample is depicted in Fig. 6.9B. Note that the reconstructed area shown here is much larger than the area of the scanning grid which is covered by the central and most intensive part of the beam. Even the edge of the silicon nitride window supporting the sample becomes visible on the left side. This large reconstructed area is caused by the relatively slowly decaying illumination field in the object plane (see also section 6.4). The reconstruction is consistent with an optical micrograph of the same sample which is shown on the left in Fig. 6.9A.

A magnified inset of the object reconstruction is shown in Fig. 6.10A. The area corresponds the region that has been covered by the central part of the probe during the scan, i.e. approximately the region of the raster grid shown in Fig. 6.9B. Details of the ornamental perforations in the frustule are depicted in subfigures 6.10B (phase) and 6.10D (amplitude). Note that in Fig. 6.9B and 6.10A phase values are shown modulo 2π . As the physical phase extends an interval of length 2π for the diatom object, phase jumps occur, e.g. on the left edge of the diatom. For the small subregion shown in subfigure Fig. 6.10B unphysical phase discontinuities in horizontal direction have been removed using the Matlab-built-in one-dimensional phase unwrapping routine `unwrap.m`. The function recognizes phase jumps larger than a pre-defined tolerance value $\Delta\varphi$ along the vertical

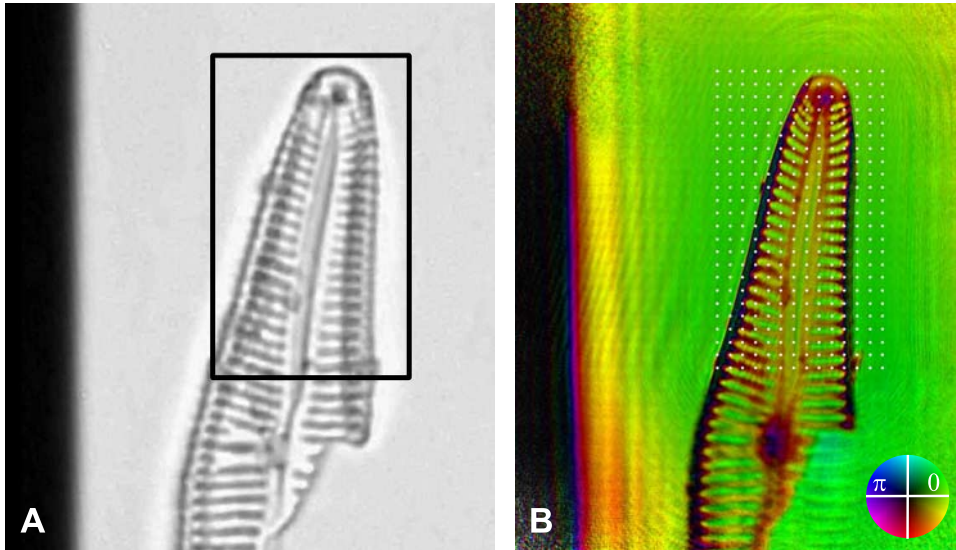


Figure 6.9: (A) Optical micrograph of the fossil diatom sample. The area scanned by the x-ray beam is marked by a black frame. The dark stripe on the left side of the image corresponds to the edge of the silicon-nitride window. (B) Complex-valued ptychographic reconstruction of the object transmission function from the same diatom sample as shown in subfigure A. Color encodes phase (modulo 2π), brightness the amplitude as indicated by the colorwheel on the lower right. The positions at which the illuminating wave field (the probe) was centered during the scan are marked by white dots covering an area of $10.4(\text{h}) \times 18.4(\text{v}) \mu\text{m}^2$. Note that also here the edge of the silicon nitride window can be seen: Although the extension of the probe was on the order of $2 \mu\text{m}$ according to the full width at half maximum (FWHM) of the amplitude, the object is reconstructed far beyond the scanned area as marked by the scan positions. This is due to the relatively slow decay of the probe amplitude in the object plane (see Section 6.4). Figure from [55].

direction of a wrapped two-dimensional phase array. To unwrap the phase jumps here, the tolerance has been set to $\Delta\varphi = 1.1\pi$ with the array being transposed before applying the unwrapping routine, so that effectively phase jumps along the horizontal direction in the original array were unwrapped. After the operation, the array was transposed again. The result is a continuous phase distribution.

To a good approximation, the fossil diatom can be considered to be composed of silicon-dioxide with a uniform density. Assuming a silicon dioxide mass density of 2.2 g/cm^3 [67] one arrives at a phase shift of around 1π rad and amplitude transmission of $T = 0.58$ per $1 \mu\text{m}$ projected thickness [67], leading here to a maximum thickness on the order of $2 - 3 \mu\text{m}$. If the exact composition were known and characterized by a single real refractive index component δ , one could actually very precisely rescale the phase map into a depth map $\Delta z(x, y)$ of the object using Eq. (3.148) and $\bar{\delta} = \delta \Delta z(x, y)$.

Note that the obtained phase map (Fig. 6.10B) shows much less fluctuations, compared to the amplitude map (Fig. 6.10D). This superiority of the phase versus the amplitude

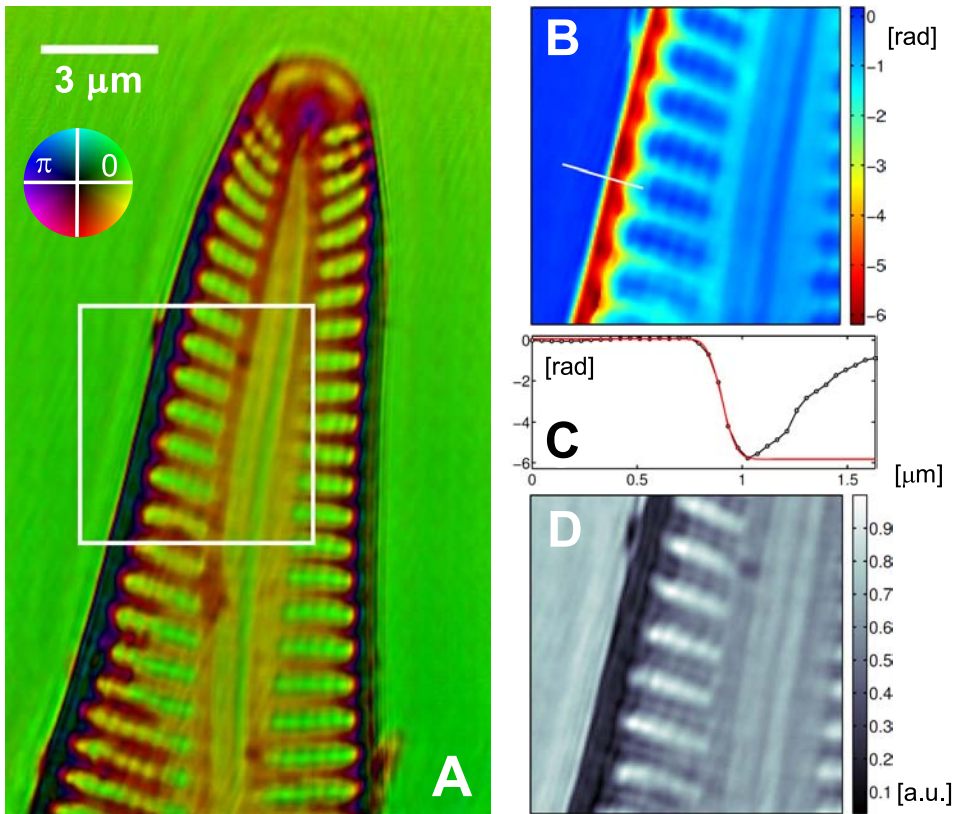


Figure 6.10: (A) Complex-valued object reconstruction (phase values modulo 2π) within the area that has been covered by the central and most intensive part of the probe wave field during the scan, roughly corresponding to the extension of the grid of scan points shown in Fig. 6.9B. (B) and (D) Detailed view of the amplitude (B) and phase (D) of the reconstructed object transmission corresponding to the marked square (side length $6\ \mu\text{m}$) in subfigure A. For the subregion shown here the phase has been unwrapped, i.e. it is shown without non-physical phase jumps due to wrapping phase values into an interval of width 2π . (C) Line profile of the phase perpendicular to the edge of the sample as marked by the white line in subfigure B. The red line marks a fit to the phase step with an error-function. Figure from [55].

reconstruction has very advantageously been utilized before [33] and can be considered as a remarkable prospect of coherent imaging methods which enable simultaneous reconstruction of the phase and amplitude.

Biological objects usually do not exhibit edges with a known sharpness. As a consequence, an exact determination of the obtained resolution from the reconstruction alone is difficult. Nevertheless, a fit of an error-function to the sharp boundary of the diatom

(see Fig. 6.10C) was used here to give an estimate on the obtained resolution. The edge smoothness of the fitted error function was obtained as 129 nm (FWHM).

6.3.2 Siemens star test pattern

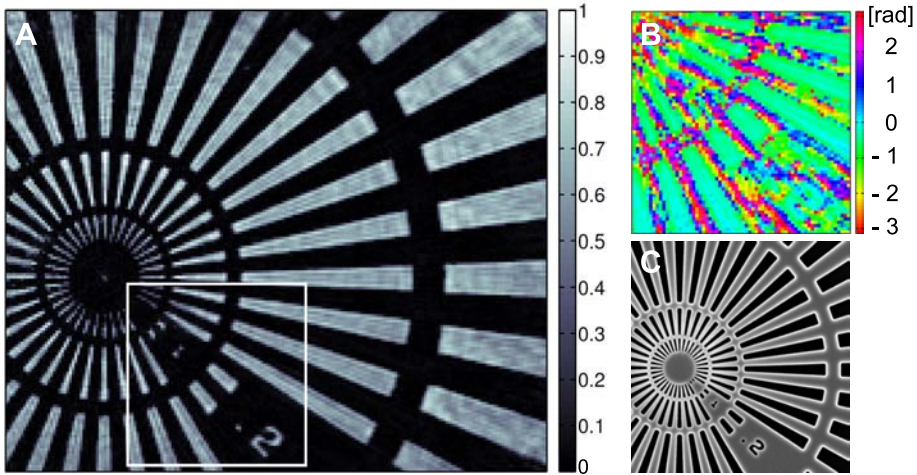


Figure 6.11: (A) Reconstructed amplitude of the Siemens star object transmission function, the pixel width here is ≈ 45 nm. Towards the center the void areas in the innermost ring of the test pattern reach a width of 50 nm in angular direction and many of them can be separated from the filled stripes along their whole radial extension. (B) Reconstructed phase (in radians) of the area indicated by a square (side length $3 \mu\text{m}$) in subfigure A. (C) Scanning electron micrograph of roughly the same region as imaged in the experiment. On the innermost side of each segmented ring the void stripes reach an angular width of $0.2 \mu\text{m}$ (third ring from center), $0.1 \mu\text{m}$ (second ring from center) and $0.05 \mu\text{m}$ (innermost ring). Figure from [55].

The reconstructed object transmission amplitude due to the Siemens star test object is shown in Fig. 6.11A. Details down to a half-period resolution on the order of 50 nm, i.e. the smallest lateral width of the void stripes of the innermost ring, are visualized.

As visible in Fig. 6.11B the phase is only reconstructed uniformly in the void segments, exhibiting random fluctuations in the filled regions. Qualitatively this can be understood in view of the low minimum intensity transmission of $T_{\min}^2 = 1.3 \cdot 10^{-4}$ leading to insufficient transmission for a reliable phase reconstruction. With an average background-corrected accumulated count number of $2 \cdot 10^9$ analog-to-digital units (“counts”) on the detector for each scan point the average “fluence” at the sample is around $1.2 \cdot 10^8$ counts/ μm^2 or $2.6 \cdot 10^5$ counts per pixel. This allows for a relative error in intensity transmission of $1/\sqrt{2.6 \cdot 10^5} = 2 \cdot 10^{-3}$ which is however insufficient to reliably detect a transmission of $T^2 = 1.3 \cdot 10^{-4}$ as expected for the tantalum material. Instead of the expected value of about 88, the average relative amplitude transmission between void and filled regions is around 22. The value has been determined from Gaussian fits to the distribution of amplitude

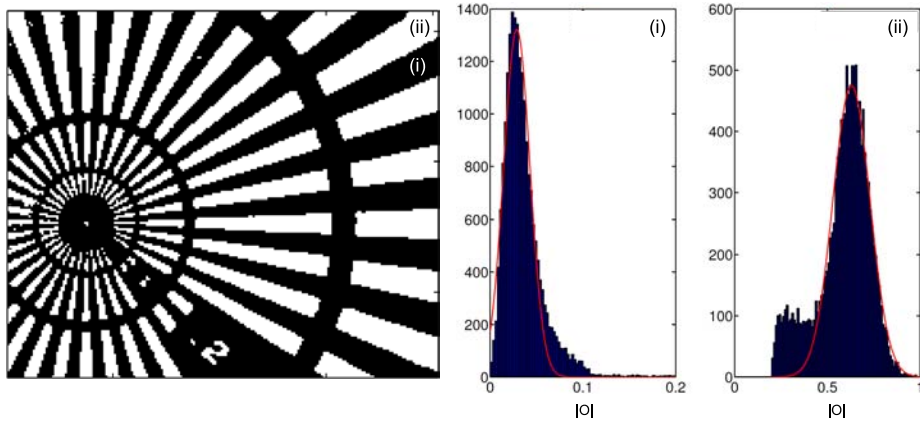


Figure 6.12: (Left) Binary mask that was used to determine the distribution of amplitude values in the low and high density regions. Mask values were set to one at all pixels where the reconstructed object amplitude exceeds a value of 0.2, other mask pixel values were set to zero. (Right) Histograms along with Gaussian fits of object amplitude values in regions (i) and (ii) as indicated in the mask on the left.

values in the object region as depicted in Fig. 6.12. Further reasons for the non-quantitative object reconstruction are discussed in Sec. 6.4.

6.3.3 Reconstructed illumination functions

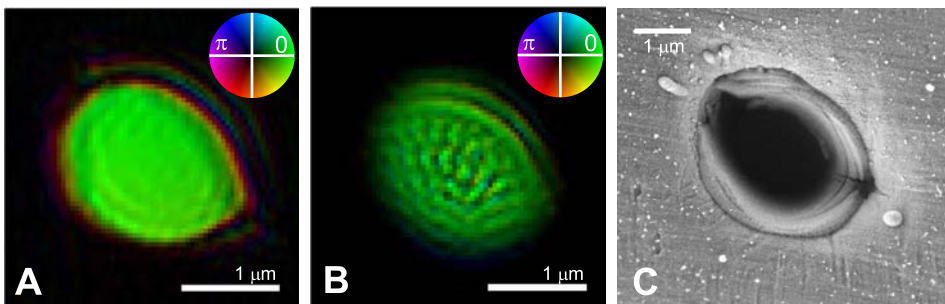


Figure 6.13: (A) Reconstructed complex illumination function (diatom dataset), back propagated over a distance of 1.08 mm to pinhole exit plane. (B) Reconstructed complex illumination function (Siemens star dataset), back propagated over a distance of 1.36 mm to pinhole plane. (C) Scanning electron micrograph of the pinhole that was used for beam confinement. Figure adapted from [55].

The reconstructed complex illumination functions, as obtained from the diatom and Siemens star datasets, are depicted in Fig. 6.13A and B, respectively. Both wave fields have been back propagated to the plane of the aperture. Starting from an approximate experimental value of the distance z_1 between aperture and sample, the propagation

distance was optimized for both samples to yield a flat and sharply bounded illumination. Thus, an accurate distance measurement between pinhole and sample becomes possible. The pinhole structure as visualized in a scanning electron micrograph (see 6.13C) is in overall agreement with the reconstructed wave fields. Notably, the reconstruction obtained from the diatom sample, a much weaker scatterer compared to the Siemens star, shows a flat amplitude and phase inside the elliptical aperture. The reconstruction obtained from the Siemens star dataset, on the other hand, shows considerable high-frequency distortions in amplitude and phase which can most likely be interpreted as artifacts from the reconstruction process (see Sec. 6.4). Note for example, that a typical diffraction pattern due to the diatom (see Fig. 6.2) is dominated by pinhole scattering whereas a typical Siemens star diffraction pattern is strongly dominated by scattering from the sample which totally suppresses the signal from the aperture (see Fig. 6.3).

6.4 Discussion

Despite additional constraints in the reconstruction process, especially for the Siemens star dataset, several artifacts remain in the reconstructed object and probe functions of both datasets which shall be discussed in the following. In both cases, the imaging geometry is crucial for an understanding of image formation via reconstruction: Note that the present setup can be used in two extreme imaging geometries (see Fig. 6.14 A and B) which both have been described before in Secs. 4.3.1 and 4.3.2.

For small distances z_1 between pinhole and sample, i.e. large Fresnel numbers $F = a^2 / \lambda_0 z_1$ (with pinhole diameter a), the illumination at the sample plane is sharply confined in amplitude and nearly flat in phase. In this geometry which is closest to conventional plane wave CDI the diffraction pattern after further propagation over a distance z_2 from the sample to the detector is similar to the squared modulus of a Fourier transform of the object transmission function and has no resemblance to the object function.

For large z_1 , i.e. small Fresnel numbers $F = a^2 / \lambda_0 z_1$, the illuminating wave field due to the pinhole is given as product of a spherical phase term (with radius of curvature equal to z_1) and the Fourier transform of the aperture exit wave field. Stated differently, the sample is placed into the far field of the pinhole exit wave. Within the small-angle approximation the propagation of the sample exit wave over the distance z_2 to the detector can then be described in an equivalent plane wave geometry (see Sec. 3.1.4), with the spherical part of the exit wave being removed. The propagation distance in the equivalent geometry is equal to z_2 / M with the geometrical magnification factor $M = (z_1 + z_2) / z_1$. The extension of the sample plane field of view (FOV) in either coordinate direction for a single exit wave in a ptychographic experiment is then given as $D'_1 = D_2 / M$ with D_2 denoting the corresponding field of view in the detection plane. In contrast to the previously described case, the diffraction pattern at the detector is now approximately given as the modulus of the object transmission function propagated into the geometrical *near* field. As a consequence, the diffraction pattern shows considerable resemblance to the object transmission function (see e.g. the diatom diffraction pattern depicted in Fig. 6.2).

Generally, ptychographic reconstructions are obtained by illuminating the sample with a rather flat and well-confined wavefront [34, 59, 77, 130, 141], as illustrated in Fig.

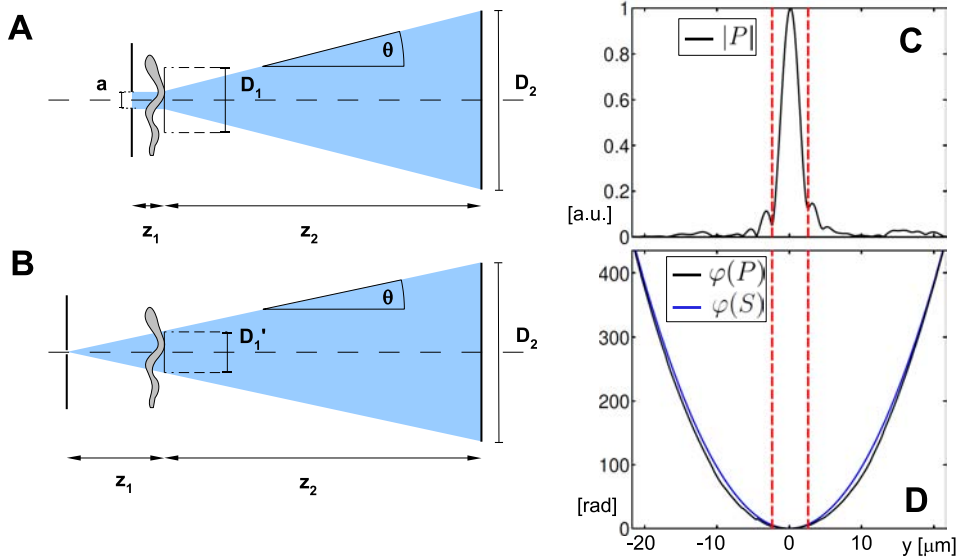


Figure 6.14: (A) Far-field geometry: For Fresnel numbers $F = a^2 / (\lambda z_1) \gg 1$ (with pinhole diameter a) the wavefront impinging on the sample is almost flat and the amplitude of the exit wave field well-confined. The field distribution at the detector in the far field shows no resemblance with the exit wave. There is no geometrical magnification of the exit wave field behind the sample and the width D_1 of the exit wave's FOV in the reconstruction plane is not related to the lateral size of the detector, but inversely proportional to its pixel width. (B) Effective near field geometry: For Fresnel numbers $F \ll 1$ the illumination at the sample is nearly spherical and less well-confined in amplitude. This leads to a diffracted amplitude which can be interpreted as magnified near field propagated object function (with the spherical part of the illumination removed). The extension $D'_1 = D_2 / M$ of the FOV in the sample plane is now proportional to the FOV width in the detector plane. (C) Vertical slice through the normalized reconstructed illumination amplitude $|P|$ for the Siemens star dataset. Red vertical lines mark the positions of the first side minima, within which 98 % of the intensity is located. (D) Vertical slice through the unwrapped reconstructed phase $\varphi(P)$ of the illumination function and the phase $\varphi(S)$ of an ideal spherical wave S in paraxial approximation, emanating from the center of the pinhole and propagated over a distance z_1 . Figure from [55].

6.14A. This can be achieved by placing the sample into the focal plane of a strongly focused wave field [77, 130, 141], or very close to an opaque mask such as a pinhole [34, 59]. By these means a “substantially” localized illumination function as required in [118] can be generated. Otherwise, sufficient (over)sampling of the single diffraction patterns is not guaranteed.

In the present experiment, however, where $F \approx 1$, none of the two extreme (and ideal) cases illustrated in Fig. 6.14A and B adequately represents the experimental geometry. To understand this, consider the vertical slices through the amplitude and phase part of the reconstructed sample plane illumination function for the Siemens star dataset, as depicted in Figs. 6.14C and D: Here 78% of the total amplitude (98% of the intensity) is concentrated

within the first side minima, a region with a relatively flat phase, with variations up to 1.5π rad. This strongest part of the beam leads to the dominating effects in the detector wave field, visible as far field diffraction patterns of the illuminated sample area. On the other hand, the remaining part of the illuminating wave field, possesses a phase curvature almost as high as that of a spherical wave with radius z_1 (see Fig. 6.14D). Consequently, this contribution to the beam generates a weaker, near field propagated image of a relatively large part of the sample on the detector.

Beyond these effects, the side maxima far away from the center in the reconstructed illumination amplitude (see Fig. 6.14C) are most probably an artifact caused by the previously described product ambiguity between illumination and object amplitude. These sidelobes correspond to the high-frequency ripples visible in the back-propagated illumination of the Siemens star dataset (see Fig. 6.13B). In the reconstructed and back-propagated wave field due to the diatom dataset the high frequency ripples are much weaker.

It has been shown before that high-curvature beams can be used advantageously for coherent diffractive imaging [see e.g. 154] and, more specifically, also for ptychographic CDI [148]. In these so-called Fresnel CDI experiments the complex illumination actually has to be reconstructed independently from a diffraction pattern of the empty beam alone [113].

Having focused on the reconstruction of the illumination function so far, let us now examine typical observed diffraction patterns of the diatom and the Siemens star datasets in a qualitative manner (see Figs. 6.2 and 6.3). In both cases, the diffraction patterns contain contributions from a near-field propagated *direct* image of the sample as well as a far-field propagated *reciprocal* space pattern. Such a mixture of optical regimes is typically also found in diffraction patterns observed in Fresnel CDI [e.g. 154]. Due to the large lateral extension of the Siemens star sample over dozens of microns in either coordinate direction, here the near-field propagated direct image always covers the full detector area. The direct (or holographic) image is produced by the outer parts of the relatively far propagated pinhole beam, leading to an extraordinary broad mix of lengthscales: The beam center with a relatively flat phase, high intensity and a diameter of about $2\ \mu\text{m}$ impinges on the center of the Siemens star with smallest length scales down to 50 nm, producing reciprocal space signals extending to the edges of the detector. Simultaneously, the weaker and highly curved outer parts of the illumination extend over a sample area with a maximum extension of $D'_1 \approx 72\ \mu\text{m}$ (assuming an ideal paraxial spherical wave emanating from the pinhole), producing the previously discussed direct image of very large sample structures on the detector. As a consequence, both signals—which are in fact characterized by similar spatial patterns for this specific sample—are entangled in a complicated way in the outer regions of the detector. An additional source of possible artifacts is thus given by the chance of an algorithmic misinterpretation of direct low-frequency signal as high-frequency reciprocal space signal. Generally, the reconstruction of the diatom dataset showed a much better convergence compared to the Siemens star dataset. This can mostly be attributed to the smaller total extension of the sample, producing a less dominant and less extended holographic (direct) image of the sample on the detector.

Lastly, it is noted that binning of detector pixels can be a further cause of artifacts in the present experimental situation: The computationally relevant FOV in the sample area is equal to D_1 rather than D'_1 as the data is *not* translated to the effective plane-wave

geometry for ptychographic reconstruction. Binning by a factor of $B = 2$, as used here, corresponds to $D_1 \approx 43 \mu\text{m}$. As a consequence, some weak direct (holographic) signal at the outer regions of the detector will either not be reconstructed or cause reconstruction artifacts due to miss-interpretation as high-frequency reciprocal space signal. On the other hand, tests on the Siemens star dataset with $B = 1$ (scaling up computation time by a factor of 4) showed that the direct signal at the outer parts of the detector is generally too weak to be reconstructed as a direct near field propagated signal. Based on this observation, the effect of shorter computation time was preferred.

The question remains which level of illumination curvature and extension can be tolerated for ptychographic CDI. The reconstruction of much larger areas than covered by the vast majority of the optical power that is applied to the sample indicates a smooth transition between a well-confined and oversampled illumination and one that is too extended. The overdetermination of the *whole* ptychographic dataset might also lead to a slight reduction of the oversampling requirements on a single diffraction pattern. If one has the choice, the reconstruction should be confined to a smaller area than in the present experiment. Here this was not possible due to the intolerable danger of collision between the pinhole and the sample inside the vacuum chamber. This certainly is a parameter that can be better controlled in future experiments. Another option would be to use a larger pinhole. In the present experiment, however, the detector would have been overilluminated even for smallest exposure times allowed by the fast shutter, making the use of a beamstop necessary.

Finally, note that diffraction fringes are visible on the edges of the diatom in the reconstructed transmission function (see Fig. 6.10A), indicating a possible breakdown of the projection approximation. A coarse criterion for the neglect of diffraction effects during propagation through the sample, i.e. for the validity of the projection approximation, has been given based on the angle of total external reflection due to a lateral refractive index gradient [21]: The approximation is valid as long as the lateral resolution r obeys $r > a_1 = \sqrt{2\delta\Delta z}$ where δ is the refractive index difference along a lateral resolution element and Δz the propagation distance through the sample. In addition, Eq. (3.137) has to be obeyed, i.e. the resolution has to fulfill $\Delta r > a_2 = \sqrt{\lambda\Delta t}$ in order to avoid Fresnel diffraction effects within the sample. Assuming $\delta = 0.0012$ and a thickness of $2 \mu\text{m}$ in the present example one arrives at $a_1 \approx 100 \text{ nm}$ and $a_2 \approx 69 \text{ nm}$. With a resolution in the object reconstruction close to this value it is clear that the experimental configuration is at the validity limit of the projection approximation and the sample might extend the depth of focus at certain points. As a consequence, there is no global focal plane any more, in which the object function can be focused. This effect is well-known from plane wave CDI at soft x-ray wavelengths [103, 132].

6.5 Conclusion

The extension of iterative ptychographic CDI to soft x-ray wavelengths has been demonstrated by imaging a fossil diatom. The reconstructed complex-valued object function allows for a comparison of its structure in amplitude and phase contrast. For the given example the phase contrast image shows less fluctuations, enabled partly by the fact that the phase is linearly related to the projected material density, whereas the amplitude has a logarithmic dependence. A resolution on the order of 130 nm was estimated for the Diatom dataset.

The reconstructed object function of a strongly scattering tantalum test pattern indicates a resolution on the order of 50 nm. Considering a typical diffraction pattern which shows scattered signal to the edge of the detector higher resolutions can be obtained for larger detector areas. An evaluation of the obtained amplitude transmission values and comparison with the expected values for the test pattern of known composition indicates a non-quantitative reconstruction. This can be partly explained by the insufficient amplitude transmission of the Ta material at the given photon energy.

The complex-valued illumination functions obtained for both datasets are in overall agreement. Back-propagation to the pinhole exit plane shows typical features of the used pinhole as determined from an SEM micrograph.

Complications arising from the relatively large photon wavelength have been discussed. The pinhole size and its distance to the sample, nearly identical to those of the hard x-ray ptychography experiment presented in Chapter 5, here lead to a relatively high phase curvature of the illumination at the sample. As a consequence, the diffraction pattern shows far field components, resulting from small sample features as well as direct space 'holographic' components resulting from larger sample features. The reconstructed object area becomes much larger than the scanning area as estimated from the diameter of the pinhole. In this respect the used illumination is at the limit of a 'substantially' localized illumination needed for ptychography [118]. This is also reflected by additional constraints that were introduced on the illumination and object functions for reconstruction. Possible artifacts resulting from these complications and other sources (e.g. the sample thickness) have been carefully discussed.

In summary, it has been shown that ptychographic CDI can be used also in the soft x-ray range to measure both, complex-valued wave fields and objects. The pinhole illumination used in the present experiment is simple and allows large fields of view to be scanned in relatively short scan time.

For future experiments it is recommended to test also a focused illumination which exhibits a flat wave front at the sample. This strongly simplifies the reconstruction procedure. On the other hand, the scanning time for the same field of view and dose is increased, mainly due to the required higher number of CCD measurements which suffer from relatively long readout times. This in turn increases the demands for stability.

7 Waveguide based x-ray propagation microscopy of eukaryotic cells

X-ray propagation imaging using coherent plane wave illumination is a relatively new, but now routine tool for quantitative imaging [105, and references therein] in 2 and 3D. Using plane wave illumination the resolution of the technique is usually limited to the pixel size of the detector which can reach — for systems using an x-ray/visible light converter combined with optical magnification optics and a CCD — smallest sizes down to 0.3 μm [24].

As outlined in Section 4.3.3 higher resolution requires the use of a cone beam illumination that is produced by a small source size. Unless sample scattering outside the illumination cone is considered, the resolution is then roughly limited to the lateral extension of this source (see below). As a consequence, small source sizes are needed for the microscopic imaging of single cells. In the hard x-ray regime x-ray waveguides have been proved to produce lateral source diameters well below 20 nm [80] and are thus well-suited optics for cone beam propagation microscopy. If the waveguide exit wave is modeled as a Gaussian (diffraction-limited) beam, the lateral coherence length at the sample in the far field of the source is roughly as large as the beam diameter at the sample (see Section 4.7.2 and [123]). This coherence length at the sample even applies if the exit wave is not fully coherent, as long as the exit wave intensity distribution can be approximately described as Gaussian. A Gaussian exit wave intensity distribution is a very good model for single-mode waveguides [47] and often still a rather good approximation for multimodal waveguides. As a consequence, it is concluded that the coherence requirements for near-field propagation imaging are generally well-obeyed for waveguide-based imaging, merely because of the high lateral confinement of the exit wave. The required coherence length for near-field imaging is on the order of $\sqrt{\lambda_0 z}$, the maximum lateral length scale for diffraction effects [21]. In addition, waveguides act as spatial filters [see e.g. 47] and can thus largely improve the quality of the illumination for imaging applications, especially, if the guiding core dimensions and the photon wavelength are chosen such that only a single mode is allowed to propagate within the waveguide. The experimentally observed far field can then be well-described by a Gaussian beam [see e.g. 47, 48].

In this chapter waveguide based x-ray coherent propagation microscopy of single, unstained cells is presented.¹

¹The work presented here has been published before in shorter form in [57].

7.1 Setup, experimental procedure and treatment of raw data

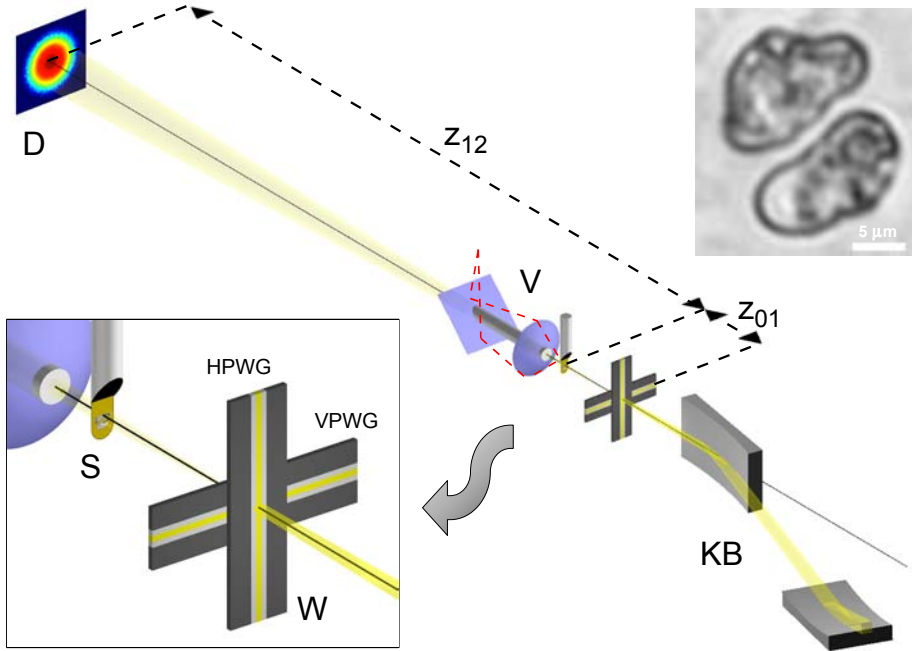


Figure 7.1: Sketch of the experimental setup for waveguide-based quantitative near field imaging. The x-ray beam is focused by two Kirkpatrick-Baez (KB) mirrors in horizontal and in vertical direction onto a system of two planar one-dimensional waveguides (W) mounted in a crossed geometry. The horizontally confining planar waveguide (HPWG) is placed upstream, while the vertically confining waveguide (VPWG) is placed downstream. The resulting divergent exit wave propagates onto the sample (S) at a distance $z_{01} = 8.83$ mm. The freeze-dried cells were attached to a several microns thick polyimide foil. For an optical micrograph of the sample cells see the inset on the upper right (Z1 Observer, Zeiss, Germany). Visual feedback on the sample in the setup for x-ray imaging is possible by using an optical video microscope (V) with a drilled lens to allow the passage of the diffracted x-ray beam. The area detector (D) is placed at distance $z_{12} = 3.09$ m from the sample exit plane. Figure from [57]. Copyright (2011) by the American Physical Society.

The experiment (for a sketch see Fig. 7.1) was performed at the ID22-NI endstation of the European Synchrotron Radiation Facility (ESRF). The pink-beam undulator radiation with a photon energy of $E_{\text{ph}} = 17.5$ keV ($\Delta E_{\text{ph}}/E \simeq 0.02$) was pre-focused by a system of two KB mirrors down two lateral dimensions of about 129×166 nm² (horz.) \times (vert.) intensity FWHM, as determined by translation of an Au stripe and measuring the fluorescence signal with respect to lateral position of the stripe.

A system of two one-dimensionally confining waveguides was placed into the KB focus in order to further confine the x-ray beam [47]. The waveguide system that was used

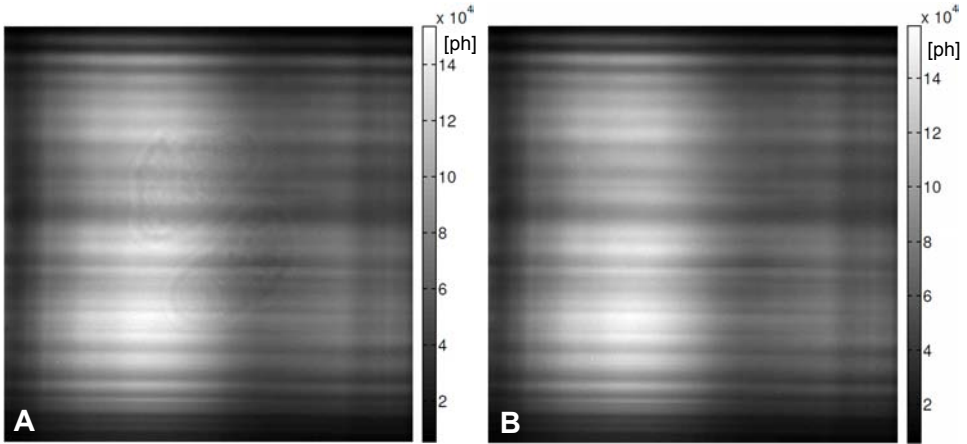


Figure 7.2: Cumulated flatfield-corrected diffraction patterns $\sum_n I_s^{(n)}$ with the sample in the beam (A) and $\sum_n I_0^{(n)}$ without the sample in the beam (B). The near field diffracted sample signal is visible as a small perturbation on the background. (Linear) colorbars indicate the integrated photon flux per pixel. Both fields span a used field of view of 242×242 pixels with a pixel area of $55 \times 55 \mu\text{m}^2$. The net accumulation time for each image was 90.2 s.

here consisted of two one-dimensionally confining planar waveguides, glued on top of each other in a crossed geometry. A detailed description of the waveguide system and the corresponding beam confinement is given in [80]. Each planar waveguide consisted of a layered structure with a guiding core width of 35 nm, leading to a lateral beam confinement significantly below this value [80]. Even with a certain astigmatism that is introduced by the system of two planar waveguides placed after one another into the beam (over a total depth of $607 \mu\text{m}$) the sample at a distance $z_{01} = 8.83 \text{ mm}$ was placed well into the far field of the resulting source exit wave, as long as only radiation from the guiding cores is concerned. Parasitic transmitted intensity outside the guiding cores can lead to an increase of the effective source size, however, on an intensity level several orders of magnitude below the center intensity.

The freeze-dried *D. discoideum* cells on polyimide film had a thickness of $\Delta z \lesssim 5 \mu\text{m}$. The two-dimensional detector, a Maxipix [111] single-photon counting detector without readout noise and a pixel width of $55 \mu\text{m}$ in horizontal and vertical direction, was placed at a distance $z_{12} = 3.09 \text{ m}$ away from the sample.

The setup thus corresponds to the experimental situation depicted in Fig. 4.7 and is described here in the effective near field geometry outlined in Section 4.3.3. The sample transmission function will only be reconstructed on length scales much larger than the wavelength, so that the necessary condition of paraxiality is assumed to be fulfilled (see Section 3.1.2).

In the effective near field geometry and under the assumption that the object and illumination can be factorized the amplitude of the propagated object transmission function

is given by Eq. (4.29), restated here for easy reference²:

$$\left|O\left(\frac{r_2}{M}; z_{\text{eff}}\right)\right|^2 = \frac{|\psi(r_2; z_{12})|^2}{|P(r_2; z_{12})|^2}. \quad (7.1)$$

$$\begin{aligned} &= \frac{I_s(r_2; z_{12})}{I_0(r_2; z_{12})} \\ &= \bar{I}(r_2; z_{12}). \end{aligned} \quad (7.2)$$

Here $I_s(r_2; z_{12})$ and $I_0(r_2; z_{12})$ denote the intensity measured in the detector plane at lateral position $r_2 = (x_2, y_2)$ with and without the sample in the beam, respectively. \bar{I} then denotes the normalized intensity.

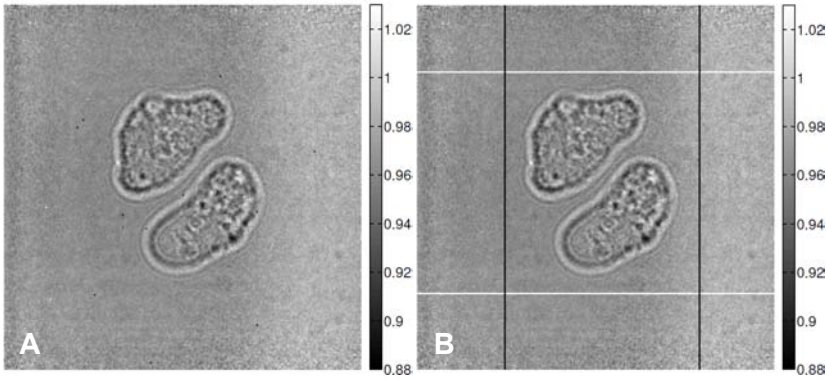


Figure 7.3: (A) Normalized intensity formed by division of the summed sample and empty field shown in Fig. 7.2A and B. Some outliers due to false pixel responses can be clearly identified. (B) Normalized field with outliers corrected, i.e. replaced by the mean values of their neighbors. A residual low-frequency variation of the background in horizontal and vertical direction can be well described by summing rows and columns, respectively, outside the center area where the diffraction pattern of the cells is located.

In the experiment, the waveguide beam showed a significant decrease in overall intensity on timescales of minutes. As an approach to circumvent the problem of normalizing two non-stationary fields here the diffraction patterns $I_s(r_1, z_{12})$ and $I_0(r_1, z_{12})$ were collected in a sequence $(I_s^{(1)}, I_0^{(1)}, I_s^{(2)}, I_0^{(2)}, \dots, I_s^{(N)}, I_0^{(N)})$ with $N = 451$ and a short illumination time of 0.2 s per image, so that the summed sample and empty beam intensity were measured over the same time span, with approximately equal cumulated intensity. The resulting flat-field corrected cumulated intensity distributions are shown in Fig. 7.2. The normalized intensity $\bar{I}(r_1, z_{12})$ was then calculated as $\bar{I} = I_s/I_0 = \sum_n I_s^{(n)} / \sum_n I_0^{(n)}$ with $I_s = \sum_n I_s^{(n)}$ and $I_0 = \sum_n I_0^{(n)}$. The total integrated photon flux collected at the detector during this procedure was about 4×10^9 photons, with and without the very weakly absorbing sample in the beam, corresponding to a fluence of about 2.8×10^6 ph/ μm^2 at the sample. With Eq. (4.102) and assuming a material composition as described in [71] this

²Again we use $r_i := \mathbf{r}_\perp^{(i)} = (x_i, y_i)$ and thus $(r_i, z) = (\mathbf{r}_\perp^{(i)}; z)$ here to assign lateral coordinates in plane Σ_i .

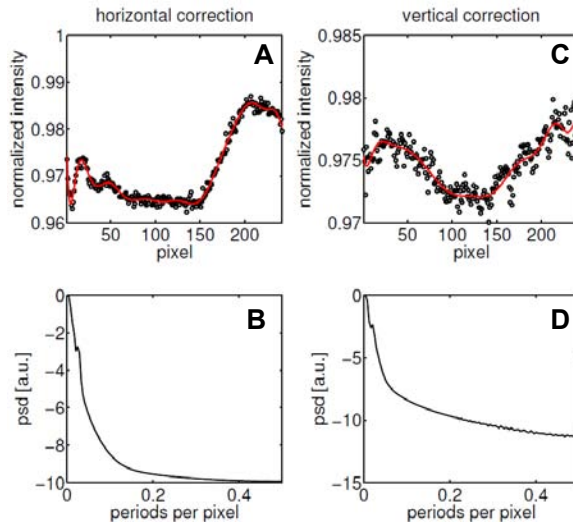


Figure 7.4: (A) Experimental background profile (circles) along the horizontal direction summed over rows above the upper and below the lower white line shown in Fig. 7.2B. An empirical model curve describing this profile is indicated by the red line. (B) Normalized power spectral density of the model curve from subfigure A. As indicated by the curve, there are no significant high-frequency components in the model curve. As for the 2D-PSD shown in Fig. 7.6 a Kaiser-Bessel-window was multiplied here with the profile to suppress cutting artifacts in the DFT-generated spectrum. (C/D) Analogous quantities are shown here for the vertical direction.

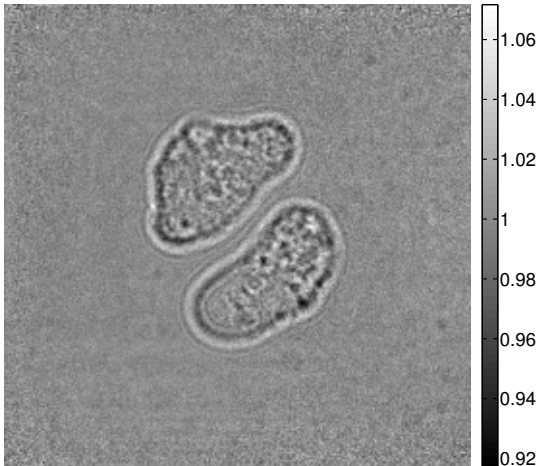


Figure 7.5: Final normalized and corrected near field diffraction pattern of the cells. The pattern can be described as the intensity $|O(\mathbf{r}_{\text{eff}}; z_{\text{eff}})|^2$ of the object transmission function, propagated over an effective distance z_{eff} , and observed in an effective lateral coordinate system $\mathbf{r}_{\text{eff}} = \mathbf{r}_2 / M$. With a detector pixel width Δ_2 the effective pixel width in the near field geometry is thus given as Δ_2 / M . Figure adapted from [57].

corresponds to a dose of 0.8×10^3 Gy. Note that this dose is within a factor of three of that applied in the short exposure experiment described in Chapter 5.

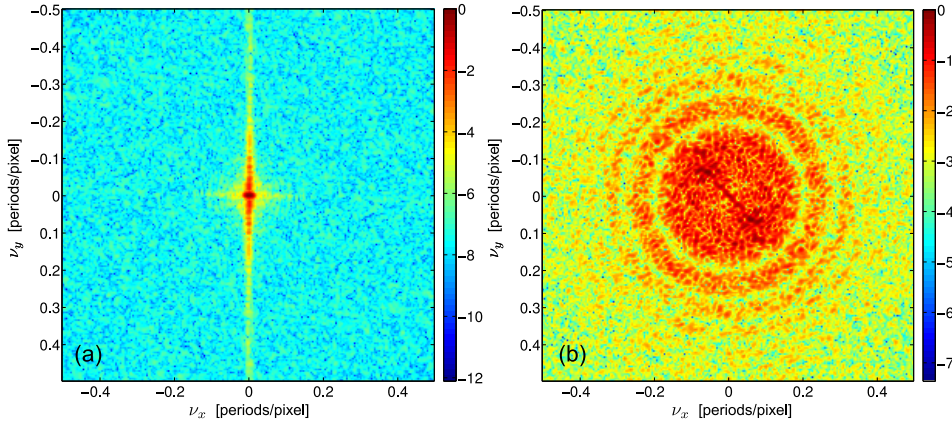


Figure 7.6: (a) Power spectral density of the cumulated empty waveguide far field, shown on logarithmic scale. The intensity was weighted with a two-dimensional Kaiser-Bessel-window [14] prior to forming the power spectral density by a DFT-operation. The highly anisotropic structure in the far field becomes apparent here, with most features in the vertical direction. The PSD is normalized to its maximum value with the colorbar indicating the fraction of the maximum on a logarithmic scale. (b) Angular averaged PSD of the diffraction pattern shown in Fig. 7.5. Also here a Kaiser-Bessel window was applied prior to forming the PSD.

The resulting normalized intensity distribution is shown in Fig. 7.3A. 20 pixels were visually identified as outliers and their values replaced by the mean of their 8 neighbors. The result is shown in Fig. 7.3B. A remaining low-frequency variation in the area where no cellular material was present had to be corrected in order to make the iterative analysis procedure (see below) more precise. As variations are solely oriented in horizontal and vertical direction, the following correction procedure was applied: For correction of horizontal variations rows below the lower white and above the upper white line in Fig. 7.3B were summed and the resulting profile fitted to a non-noisy model profile (see Fig. 7.4A).³ The model profile filling a single row was then copied into all rows of a correction array which was then used to normalize the experimental array. An indication that no artificial high-frequency content is introduced to the image, which could affect the later reconstruction process in the near field, is given by the PSD of the model profile shown in Fig. 7.4B. The same procedure was also used for the correction of vertical variations.

The resulting final normalized intensity distribution is shown in Fig. 7.5. According to Eq. (4.29) it is equal to the intensity $|O(\mathbf{r}_{\text{eff}}; z_{\text{eff}})|^2$ of the object transmission function, propagated over an effective distance z_{eff} , and observed in an effective lateral coordinate system $\mathbf{r}_{\text{eff}} = \mathbf{r}_2/M$. The effective detector pixel width is thus given as $\Delta_{\text{eff}} = \Delta_2/M \approx 157$ nm for the present experiment with $M \approx 351$.

³The model used here was a Fourier series with eight frequency components with the largest period not restricted to the profile length, but taken as a free parameter. What model curve is used, is not important as long as no high frequency-components are introduced within the near-field diffraction pattern of the cells.

As outlined in Section 4.3.3 the application of Eq. (7.1) requires the propagation of the object wave to be independent from the propagation of the illumination. If the illumination is an ideal paraxial spherical wave and if the detector is illuminated homogeneously, this condition is obeyed. The present experimental situation comes close to this ideal, there are, however, remaining intensity variations in the empty beam, visible as characteristic horizontal (and, with a larger period length, vertical) stripes. Note that a structured illumination is an experimental difficulty which is not limited to the use of x-ray waveguides. For example, coherently illuminated x-ray mirrors and/or monochromator crystals produce significant structure in the empty beam which has to be normalized out in the same way as it is done here [21]. It cannot be excluded that these intensity variations have an influence on the normalized diffraction pattern of the cells, other than changing locally the noise amplitude of the normalized diffraction pattern.

A good experimental test, however, to study the influence of the variations on the normalized diffraction pattern, is to compare the power spectral densities of the normalized diffraction pattern and of the empty beam. Both are depicted in Fig. 7.6. While the PSD of the empty beam diffraction pattern has a very characteristic streak in the vertical direction, there is no sign of this structure in the PSD of the normalized cell diffraction pattern.

Noise statistics of the normalized intensity

For the iterative reconstruction of the complex object transmission function $O(r_{\text{eff}}; 0)$ in the exit plane of the sample it is necessary to evaluate the noise statistics of the normalized detector intensity $\bar{I}(r_2; z_{12}) = I_s(r_2; z_{12})/I_0(r_2; z_{12})$. As both, $I_s(r_2; z_{12})$ and $I_0(r_2; z_{12})$ are characterized by high measured photon counts around $N_{\text{ph}} \approx 10^5$, they can be well described by Gaussian statistics with means $\langle I_s(r_2) \rangle$ and $\langle I_0(r_2) \rangle$ and approximately equal variances $\sigma^2(r_2) = \langle I_0(r_2) \rangle$ at every point r_2 on the detector⁴. If one assumes error propagation of Gaussian random variables one obtains for the the variance of the normalized intensity $\bar{I}(r_2)$

$$\langle (\bar{I} - \langle \bar{I} \rangle)^2 \rangle = \frac{\sigma^2}{\langle I_s \rangle^2} + \sigma^2 \frac{\langle I_s \rangle^2}{\langle I_0 \rangle^4} \quad (7.3)$$

$$\approx \frac{1}{\langle I_0 \rangle} + \frac{1}{\langle I_0 \rangle} \quad (7.4)$$

$$= \frac{2}{\langle I_0 \rangle} \quad (7.5)$$

which is true for every point r_2 on the detector. In an experiment we cannot obtain the expectation value $\langle I_0(r_2) \rangle$ at every r_2 , however we can form the sum over all pixels N_p at locations $r_2^{(j)}$

$$\frac{1}{N_p} \sum_{j=1}^{N_p} \frac{2}{I_0(r_2^{(j)})} \rightarrow \frac{1}{N_p} \sum_{j=1}^{N_p} \frac{2}{\langle I_0 \rangle(r_2^{(j)})} = \frac{2}{\langle I_0 \rangle}. \quad (7.6)$$

⁴As intensities are only considered in the detector plane we dropped the z -dependence here for notational convenience.

For high count rates and nearly equal expectation values $\langle I_0 \rangle (r_2^{(j)})$ at every pixel this sum approaches the variance of the normalized intensity according to Eq. (7.5).

The above predictions were tested on the experimental normalized intensity. The normalized intensity in the region free of diffraction signal from the sample can be described by Gaussian statistics reasonably well (see Fig. 7.7). The resulting standard deviation of a Gaussian fit to the histogram of intensity values in this region is given as $\sigma_{\text{Gaussian}} = 0.0067$. Alternatively, the sum on the left-hand side of Eq. (7.6) yields a value of $\sigma = 0.0064$, which is in good agreement with the Gaussian fit to the histogram. This value can be obtained from the empty beam alone, even if there are no empty regions in the normalized diffraction pattern.

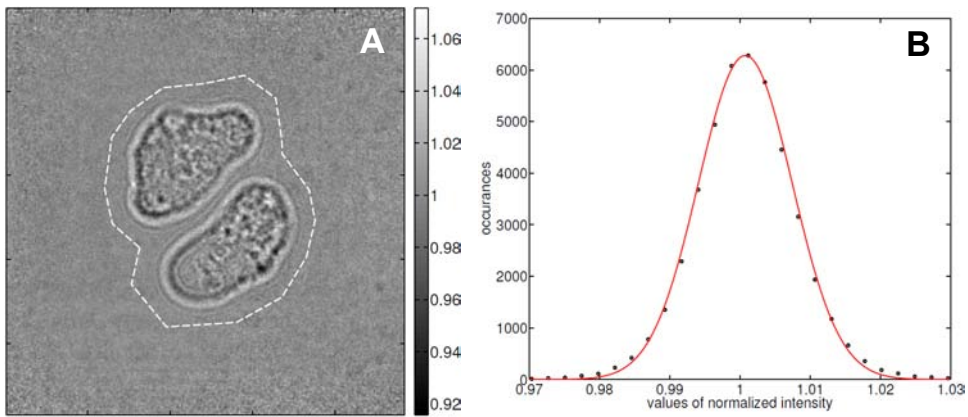


Figure 7.7: A histogram of the photon count values per pixel in the area outside the dashed line in subfigure A is shown in subfigure B. A Gaussian fit (solid red line) yields a reasonable agreement with the observed form of the histogram.

7.2 Simulations

Simulations were carried out to optimize algorithmic parameters for the reconstruction of the experimental data and to assess possible reconstruction errors, but also the possible range of the achievable experimental resolution.

The simulated experiments are based on the same geometry as described above. The illumination wave field $P(\mathbf{r})$ generated by the waveguide was modeled as a Gaussian beam⁵ [133]

$$P(\mathbf{r}) = \frac{\exp(i(kz' - \zeta(z'))) }{w(z')} \exp\left(-\frac{x^2 + y^2}{w(z')^2} + ik\frac{x^2 + y^2}{2R(z)}\right) \quad (7.7)$$

⁵This representation of the Gaussian beam has no special normalization, as the illumination at the sample was finally normalized to a certain integrated photon flux.

with $z' = z + z_{01}$. The sample exit plane here corresponds to $z = 0$ (see Fig. 4.7). Here the $1/e$ -decay half-width is defined as

$$w(z') = w_0 \sqrt{1 + \frac{z'^2}{z_r^2}}$$

with the Rayleigh length

$$z_R = \pi w_0^2 / \lambda_0.$$

$\zeta(z')$ is defined as

$$\zeta(z') = \arctan\left(\frac{z'}{z_R}\right)$$

and the beam radius of curvature as

$$R(z') = z' + \frac{z_R^2}{z'}.$$

The only free parameter of this beam is the beam waist radius w_0 , i.e. the $1/e$ -decay half width of the field amplitude at the plane $z' = 0$, the waveguide exit plane. w_0 was chosen here such that the intensity FWHM in the WG exit plane equals 10 nm, roughly corresponding to the experimental value [80]. w_0 and the intensity FWHM are connected via $w_0 = \text{FWHM}_0 / \sqrt{2 \ln 2}$.

The Gaussian beam is a solution to the paraxial approximation of the Helmholtz equation [133]. As a consequence, the transition to the effective geometry can be made for the present simulated experiment. For the simulations, which were carried out in the effective geometry, the planar part of the illumination in the sample plane $z = 0$ was formed according to Eq. (3.36) as

$$P(x, y, 0)^{(P)} = P(x, y, 0) \exp\left(\frac{-ik(x_1^2 + y_1^2)}{2z_{01}}\right). \quad (7.8)$$

and normalized to the required total integrated photon flux. z_{01} was always chosen⁶ such that $z_{01} \gg z_R$, so that, apart from a global phase factor, the Gaussian beam is approximately equal to a product of a real Gaussian amplitude with $1/e$ -half width $w(z')$ and an imaginary phase factor corresponding to the paraxial approximation of a spherical wave phase factor. For $z_{01} \gg z_r$ this phase factor is canceled by the one in Eq. (7.8), so that the illumination at the sample comes close to a plane wave with a Gaussian amplitude distribution and $1/e$ amplitude decay half width $w(z_{01})$.

An object transmission function corresponding to simulated phantom cells was generated as described in Section 3.2.3. The sample exit wave was formed as the product $P(x, y, 0)^{(P)} O(x, y)$ and propagated over an effective propagation distance $z_{\text{eff}} = z_{01} z_{12} / (z_{01} + z_{12})$ to yield the simulated near field diffraction pattern by forming the squared modulus of the wave field. For numerical propagation, the paraxial propagator defined in Eq. (3.79) was used. An independent propagation of the illumination $P(x, y, 0)^{(P)}$ was

⁶At a photon energy of 17.5 keV the resulting Rayleigh length of the Gaussian beam was 3.2 μm .

carried out for normalization of the near field diffraction pattern. Before normalization Poissonian noise was added to the data.

Quadratic pixels of sidelength $\Delta x_{\text{eff}} = \Delta x' / M$ were assumed with $\Delta x' = 55 \mu\text{m}$ denoting the experimental detector pixel width. The magnification factor $M = (z_{01} + z_{12}) / z_{01}$ was adjusted according to the geometry of the experiment. To increase the numerical accuracy of the near field diffraction patterns, the near field propagation was usually carried out with a smaller pixel width $\Delta x_{\text{eff}} / \alpha$ with $\alpha \in \mathbb{N}$. Accurate sampling of the phase chirp functions in the near field propagator was assured by using a large enough simulation array (cf. Eq. 3.85). If $\alpha > 1$, the exit waves with and without a sample in the beam, were rebinned after propagation to the detector plane to a pixel width of Δx_{eff} . Afterwards, the central numerical array corresponding in size to the experimental situation was selected from the total simulated array. Subsequently, diffraction patterns were generated by forming the squared modulus of the propagated fields, and finally the normalized near field diffraction pattern was calculated according to Eq. (7.1).

7.2.1 Cells

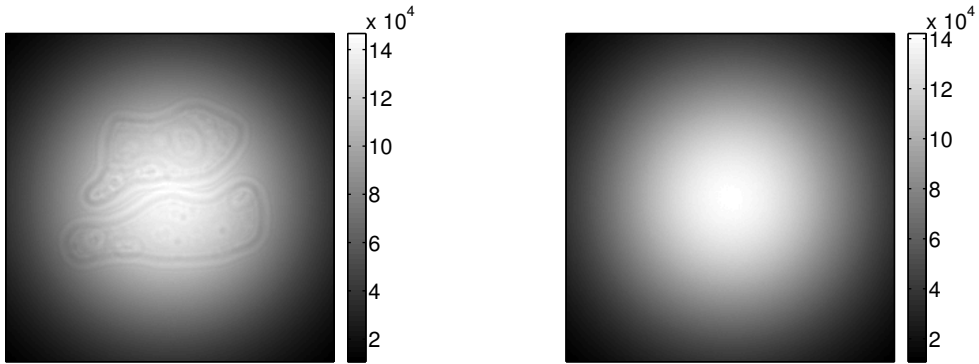


Figure 7.8: Simulated waveguide far field diffraction patterns, with (left) and without (right) cells in the beam. The detector field of view shown here was equal to that used in the experiment, namely 242×242 quadratic pixels of width $55 \mu\text{m}$. Colorbars indicate photons per pixel.

The experiment on the *D. discoideum* cells was simulated with the same photon energy, setup geometry, detector pixels size, integrated photon flux etc. as used in the real experiment. The cells were assumed to be composed of protein material with the empiric composition $\text{H}_{50}\text{C}_{30}\text{N}_9\text{O}_{10}\text{S}_1$ and mass density of 1.35 g/cm^3 , as used before. The maximum cell thickness was assumed to be $1.5 \mu\text{m}$, leading to a maximum amplitude attenuation and phase change of $A = 1.04 \times 10^{-4}$ and $\Delta\varphi = 0.13 \text{ rad}$, respectively. As a consequence, the cells can be treated as pure phase shifting objects. The simulated phase distribution of the phantom objects is shown in Fig. 7.9 (a).

Simulated near field diffraction patterns at the detector are shown in Fig. 7.8, with and without the cells in the beam. The signal due to the cells is visible as a small modulation of the overall intensity distribution, just as in the experimental diffraction pattern. The

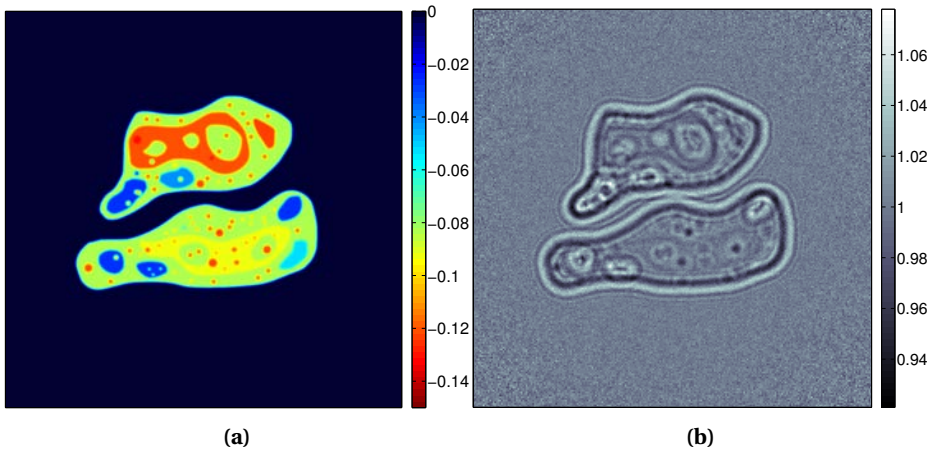


Figure 7.9: (a) Simulated phase map of an unstained biological cell. The pixel width used for the simulation is smaller by a factor of $\alpha = 4$ compared to the experimental width which was finally used for reconstruction (see main text). The sidelength of the simulated array is $13.3 \times 13.3 \text{ mm} / M^2 = 38 \times 38 \mu\text{m}^2$ with $M \approx 351$. The colorbar indicates phase in rad. Figure adapted from [57]. (b) Normalized effective near field diffraction pattern, corresponding to the patterns shown in Fig. 7.8. Just as there the FOV on the detector is $13.3 \times 13.3 \text{ mm}$. In the effective geometry the FOV corresponds to that of the simulated phase distribution on the left. The colorbar indicates intensity per pixel, normalized by the empty beam intensity in that pixel.

corresponding normalized diffraction pattern is shown in Fig. 7.9. The standard deviation of the normalized intensity as defined in the previous section here has a value of $\sigma = 0.0063$, well in agreement with the experimental value.

7.2.2 High resolution test objects

7.2.2.1 Resolution provided by the waveguide beam

Although the intensity distribution at the detector can be interpreted as a near field distribution, the detector plane is usually well in the far field of the exit wave at the sample exit plane. With a squared detector that collects data up to a numerical aperture NA, the Rayleigh resolution of the experiment is thus limited to $\Delta r_R = \lambda_0 / (2NA)$, as described in Section 4.5.

A practical resolution limit for the present analysis is given, however, by the numerical aperture of the waveguide beam itself. If the detector collects data up to much higher numerical aperture than the waveguide beam can provide, the normalization expressed in Eq. (7.1) is no longer possible, as the empty beam intensity outside the central cone decreases to zero and causes singularities in the normalized intensity. In this case the non-normalized diffraction pattern has to be analyzed with different methods from those presented here. At a certain point also the paraxial approximation can no longer be used, and one has to analyze the data in the physical geometry of the experiment. ‘Fresnel

Coherent X-ray Diffractive Imaging' [154], a technique for iterative reconstruction of highly curved wave fields, could in principle also be applied here.

An estimation of the resolution provided by the waveguide beam is based on the numerical aperture of a Gaussian beam. If the $1/e$ decay half width w_0 of the field amplitude is assumed as a measure for the half width of the beam, its numerical aperture is given approximately as [133]

$$\text{NA}_{\text{Gaussian}} = \frac{\lambda_0}{\pi w_0}. \quad (7.9)$$

Substituting this numerical aperture into the Rayleigh resolution equation of the detector yields

$$\begin{aligned} \Delta r_R &= \frac{\pi}{2} w_0 \\ &= \frac{\pi}{2} \sqrt{2 \ln 2} \cdot \text{FWHM}_0 \\ &\approx 1.33 \cdot \text{FWHM}_0. \end{aligned} \quad (7.10)$$

Here FWHM_0 denotes the intensity full width at half maximum of the waveguide exit wave. As a consequence, the resolution that is provided within the waveguide cone itself is close to the FWHM of the intensity in the exit plane of the waveguide. The exact value depends on the exact definition of the beam width in the detector plane and the resolution criterion that is applied.

Ultimately, the resolution is limited by the angle to which scattering from the sample can be observed, just as in plane wave CDI.

7.2.2.2 Test pattern simulation

For the simulation of the cell dataset geometrical parameters were chosen equal to the experimental ones, yielding an effective pixel size of about 157 nm. This is clearly above the resolution that can be achieved with the simulated waveguide system, based on an exit wave intensity FWHM of 10 nm. The situation is equal for the experimental WG system with an estimated exit wave FWHM below 15 nm [80].

Due to instrumentation constraints the geometrical magnification could not be increased significantly beyond the applied value during the experiment at the beamline. Nevertheless, an assessment of the used experimental system in terms of its resolving power is possible based on a simulated experiments. To this end a second phantom object was generated, with a shape corresponding to the well known Siemens star design. A pure phase shifting object was assumed with alternating phase values of about -0.1 rad and -0.13 rad and a maximum phase shift comparable to that of the studied biological objects. The resulting simulated phase map is depicted in Fig. 7.10 (a).

All physical parameters of the simulation were kept the same as in the previous simulation and the experiment, except the distance z_{01} between the WG exit plane and the sample. It was decreased here by a factor of 9. As for $z_{01} \ll z_{12}$ the magnification is approximately given as $M \approx z_{12}/z_{01}$ this leads to an increase of the geometrical magnification by the same factor, leading to $M \approx 3151$. Notably, the fluence at the sample increases quadratically with the magnification here, so that with the same integrated flux an average fluence of

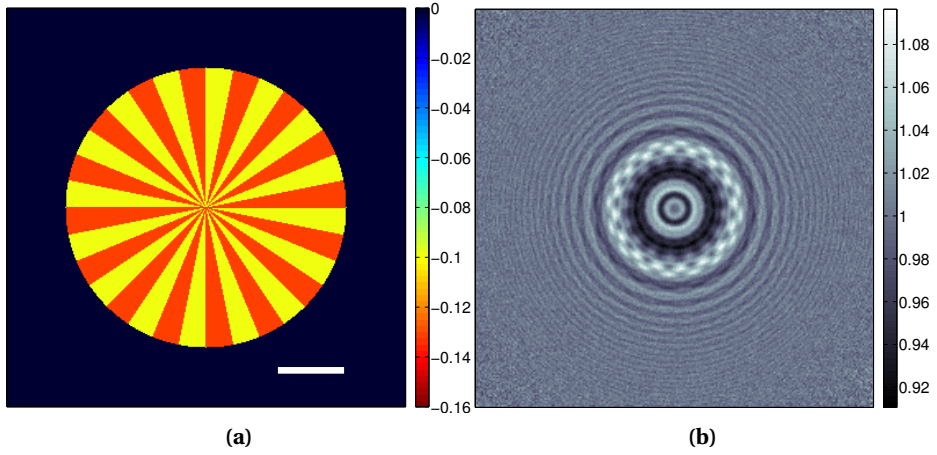


Figure 7.10: (a) Simulated phase map of a Siemens star test object. The pixel width used for the simulation is smaller by a factor of $\alpha = 4$ compared to the experimental width which was finally used for reconstruction (see main text). The scale bar indicates a length of 250 nm. The colorbar indicates phase in rad. Figure adapted from [57]. (b) Normalized diffraction pattern corresponding to the phase map on the left. The FOV on the detector is 13.3×13.3 mm, corresponding here to an effective FOV of 13.3×13.3 mm/ M^2 with $M \approx 3151$. The colorbar indicates intensity per pixel, normalized by the empty beam intensity in that pixel.

2.2×10^8 ph/ μm^2 is obtained in the simulation. Experimentally, this allows for a simple increase in fluence by moving the sample closer to the waveguide, without an increase in total illumination time. For high resolution applications, which require high fluence, this is an important experimental relief compared to illumination with an unfocused plane wave.

7.3 Reconstruction

Reconstructions were obtained in three ways. Firstly, holographic reconstructions were carried out by simple near field back propagation of the experimental and simulated normalized diffraction patterns (see Section 4.4.2.1). Secondly, the Gerchberg-Saxton algorithm was applied as described in Section 4.4.3, i.e. assuming an amplitude transmission of 1 in the sample plane. Lastly, the modified Hybrid-Input-Output scheme was applied in the same manner as described in Section 4.4.3. In the present case, however, the noise in the diffraction patterns was explicitly accounted for by application of a modified detection plane modulus replacement operator, similar to the one described in Section 4.6. More precisely, the ‘output’ object function at iteration n was formed as

$$O'_n = D_{-z_{\text{eff}}} \left[|\tilde{O}'_n| \cdot \frac{\tilde{O}_n}{|\tilde{O}_n|} \right] \quad (7.11)$$

with

$$|\tilde{O}'_n| = \left[\left(1 - \frac{D}{d} \right) \bar{I} + \frac{D}{d} |\tilde{O}_n|^2 \right]^{1/2} \text{ for } d > D. \quad (7.12)$$

$\tilde{O}_n = D_{z_{\text{eff}}}[O_n]$ here denotes the object function, propagated over the distance z_{eff} . d is the RMS deviation of the estimated and measured normalized intensity distribution at iteration n , i.e.

$$d = \left[\frac{1}{N} \sum_{(x,y)} (|\tilde{O}_n(x,y)|^2 - \bar{I}(x,y))^2 \right]^{1/2}. \quad (7.13)$$

with N denoting the number of entries in array O_n . D is the expected value of d which can be determined from the noise statistics of the experiment. Identifying the detection plane intensity estimate $|\tilde{O}_n|^2$ at iteration n with the expected intensity $\langle \bar{I} \rangle$ in Eq. (7.3) one obtains $D_{\text{th}} \approx 2/\langle I_0 \rangle$ as an estimate for the relaxation parameter D , as outlined in at the beginning of this chapter. If $d \leq D$, the update operation equals the identity operator and the algorithm is stopped. The update (7.12) thus operates on the detection plane intensities rather than the amplitudes, as the one described in Section 4.6 does.⁷

The modified HIO algorithm was initialized with a random object function

$$O_0(x,y) = \begin{cases} 1 + a_0 Z_J \exp(i\varphi_0 Z_J) & \text{if } (x,y) \notin S, \\ 1 + a_0 Z_J \exp(i(\varphi_0 Z_J - 0.1)) & \text{else,} \end{cases} \quad (7.14)$$

assigned to each entry of the object array at position (x,y) . The parameters a_0 and ψ_0 were chosen as $a_0 = \varphi_0 = 0.2$ and equally distributed pseudo-random numbers on the interval $Z_J = [-0.5, 0.5]$ were used for Z_J . The GS algorithm was initialized with an array of unit amplitude and zero phase.

The algorithmic feedback parameters β and δ in Eqs. (4.55) and (4.57) were optimized within the interval $[0, 1]$ using the data from the simulated cell phantom dataset: For this example the algorithm yielded best reconstruction results for small values of β and γ , as measured by the RMS deviation of the reconstructed and simulated phase distribution within the support area. On the other hand, smaller values for β and γ here also led to an increase in the required number of iterations, until the stopping criterion $d \leq D$ was obeyed. In the end, a compromise between the required number of iterations and the RMS error of the reconstruction was formed, yielding values of $\beta = \gamma = 0.2$. The reconstructed phase maps for different values of β and γ are shown in Section A.5 for the simulated and the experimental dataset(s). The threshold parameter was adjusted to $D = 1.06D_{\text{th}}$, i.e. to a value 6% larger than the expected relaxation parameter. Reconstructions with $D < 1.06D_{\text{th}}$ were found to be generally non-converging with respect to the above stopping criterion within less than 5000 iterations. The same algorithmic parameters $\beta = \gamma = 0.2$ and $D = 1.06D_{\text{th}}$ were used for all modified HIO reconstructions shown in this chapter. For each set of algorithmic parameters, the modified HIO algorithm was run 25 times with 25 independent randomly generated initial guesses. The final result was then formed as a complex average of the 25 independent solutions.

⁷It is noted that the relaxed *amplitude* operator can equally be applied here. d then becomes a metric on the complex search space of all possible complex arrays ψ with N entries.

7.4 Results

7.4.1 Experimental cell dataset

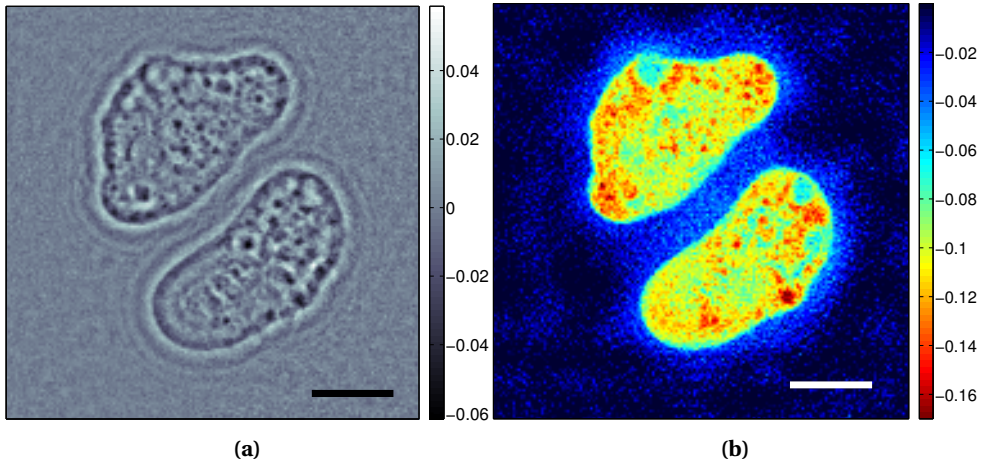


Figure 7.11: (a) Phase of the holographic reconstruction obtained by free-space back propagation of the normalized intensity over the distance z_{eff} . (b) Phase of the iterative reconstruction obtained with a Gerchberg-Saxton algorithm after 200 iterations. Colorbars indicate phase in rad, scale bars indicate a distance of $5 \mu\text{m}$. Figure adapted from [57].

The phase of the holographic reconstruction of the experimental dataset is shown in Fig. 7.11 (a). The cell rim as well as internal structures are well-recognizable. Phase values vary nearly symmetrically around zero and can thus not be considered as a quantitative representation of the true phase map due to the cells. The bright halos surrounding the cells are formed by the defocused twin image.

The phase map obtained by the Gerchberg-Saxton algorithm (see Fig. 7.11 (b)) already proceeds into the right direction: No twin image is observable, and phase values do not extend in two directions with respect to the zero phase value of the substrate. On the other hand, noise from the normalized diffraction pattern significantly distorts the reconstruction here. Note that for the GS algorithm only ideal modulus replacement operators have been used.

The reconstruction is significantly improved by application of the modified HIO algorithm as described above (see Fig. 7.12). The improvement can be attributed to the use of a modified modulus replacement operator in the detection plane⁸ as well as to the global optimization scheme that is applied in the algorithm.

⁸This also could have been used for the GS algorithm. As in this algorithm the sample and detection plane, however, are treated equally, one would also need a modified propagator in the sample plane. This requires an estimate for the relaxation parameter D also in the sample plane.

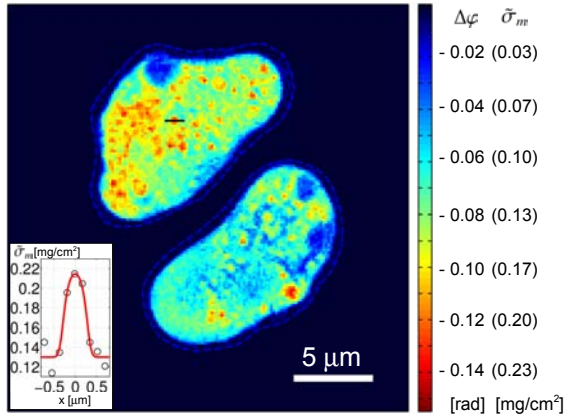


Figure 7.12: Reconstructed phase map obtained with the modified HIO algorithm as obtained in the main text. The dashed blue line indicates the rim of the support region used in the reconstruction. The colorbar is shown in two scalings, the phase shift $\Delta\varphi$ and the effective projected mass density $\bar{\sigma}_m$ as given in Eq. (5.5). The inset on the lower left shows the projected density along the black line in the upper cell (open circles), along with a model projected density (red line, see main text). Figure adapted from [57].

The reconstructed phase map can be rescaled into projected effective mass density as given in Eq. (5.5). The overall density is in the same range as obtained in the ptychographic reconstruction of bacterial cells, obtained in a completely independent way. Given the fact that a similar thickness in the range between 1 and 3 μm can be assumed for the *D. discoideum* and the *D. radiodurans* cells, the observed consistency confirms both rather different approaches to phase retrieval.

Note the globular features several pixels in diameter which are apparent in the reconstruction. They are attributed here to mitochondria, i.e. cell organelles that provide chemical energy for the cell, especially in the motile state during which the cells were fixated. The data for an exemplary object (see Fig. 7.12) can be described by a very simplistic model, assuming a spherical shape with a mass density of 1.35 g/cm^3 . This is in coarse agreement with a reported value of 1.315 g/cm^3 for the dry density from rat liver mitochondria [89]. For the object marked in Fig. 7.12 a sphere diameter of $0.64 \mu\text{m}$ was assumed. To account for the finite experimental resolution, the corresponding one-dimensional projected density profile was convolved with a normal distribution with a FWHM equal to the pixel size of 157 nm .

Blue regions, especially in the lower cell, can probably attributed to defects arising from the freeze-drying process. In addition, the lower cell appears to be of overall lower density compared to the upper one. It cannot be excluded that this is an artifact arising from the oscillatory phase contrast transfer function of near field propagation (see Section 4.3.2).

The angular averaged power spectral density of the phase reconstruction shown in Fig. 7.12 is depicted in Fig. 7.13. The expected PSD scaling behavior for a biological object with

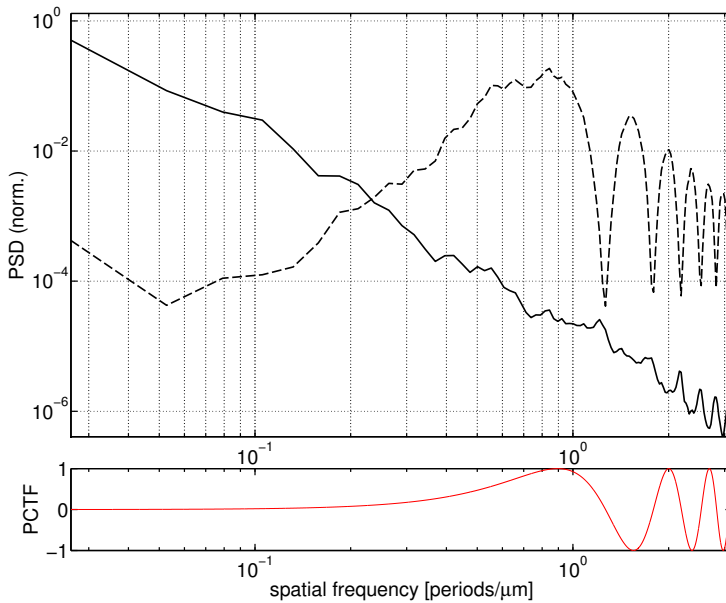


Figure 7.13: Angular averaged, normalized power spectral densities of the reconstructed phase distribution. While in the holographic reconstruction the zeros of the phase contrast transfer function appear as minima (dashed line), they appear as maxima in the iterative reconstruction based on a modified HIO algorithm (solid line). For comparison, the phase contrast transfer function corresponding to the experimental geometry is shown (lower graph).

structure on all imaged length scales is a power law decay in a straight line [72]. Globally, such a decay can also be observed in the PSD of the iterative HIO reconstruction. There are, however, deviations in form of local maxima at most of the zero frequencies in the phase contrast transfer function. They appear as minima in the PSD of the holographic reconstruction. The phase at these frequencies is unconstrained by the data and can therefore evolve with more freedom during the reconstruction process than the phase at other frequencies, leading to the maxima in the PSD of the iterative reconstruction. Maxima become more pronounced for increasing spatial frequencies, and the first three zeros in the PCTF have been quite successfully overcome by the iterative algorithm, compared to the holographic reconstruction. In real space, the corresponding unconstrained modes can lead to reconstruction errors. Note, however, that the strongest last four maxima observed in the experimental PSD fall into a frequency region corresponding to half-period lengths of 250 nm and below. In the reconstruction shown in Fig. 7.12 this corresponds to distances of less than two pixel widths.

Based on the reconstructed PSD and given the sharp rim of the cells, the interval between one and two pixel widths is also the range of the spatial resolution in the present experiment, i.e. between 150 and 300 nm. This should be considered in view of the low dose of about 0.8×10^3 Gy applied to the cells. Notably, the dose-resolution combination estimated here is in the same range as that obtained from the short exposure dataset in the

ptychographic CDI experiment (see Chapter 5).

7.4.2 Simulated cell dataset

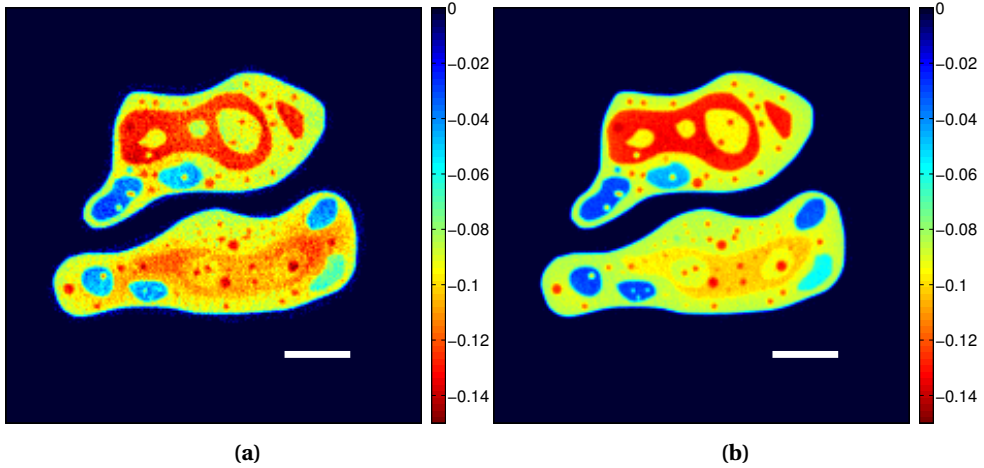


Figure 7.14: (a) Phase map reconstructed from the simulated cell dataset using the modified HIO scheme. The corresponding simulated phase distribution is shown in Fig. 7.9 (a). Experimental and algorithmic parameters were adjusted as for the experimental dataset. Figure adapted from [57]. (b) Same as (a), but with an increase in the simulated fluence by a factor of 10. Colorbars indicate phase in rad, scale bars a distance of $5 \mu\text{m}$.

A reconstructed phase map as obtained with the modified HIO algorithm from the simulated cell dataset is shown in Fig. 7.14 (a). Here experimental and algorithmic parameters were chosen equal to those of the experimental dataset and its reconstruction. There is a strong agreement with the simulated phase map shown in Fig. 7.9 (a): The RMS deviation between the simulated and reconstructed phantom phase within the support area was 0.012 rad with a largest absolute phase deviation of 0.038 rad . These values are significantly above the standard deviation of the reconstructed phase in each pixel, taken over the ensemble of 25 reconstructed object transmission functions, from which the final result was generated as the mean.

The reconstruction is improved by investing higher fluence: The reconstruction shown in Fig. 7.14 (b) was obtained from a dataset that was simulated with 10 times increase in fluence. Here the RMS deviation of simulation and reconstruction is 0.006 rad , with a maximum deviation of 0.018 rad .

The improvement in the reconstruction for an increased fluence (dose) can also be observed in the angular averaged power spectral densities of the reconstructions, shown in Fig. 7.15. The maxima that appear here just as in the PSD of the experimental reconstruction (see Fig. 7.13) at the zeros of the phase contrast transfer function are suppressed by an increased fluence. In fact, the PSD of the high fluence reconstruction shows no maxima at

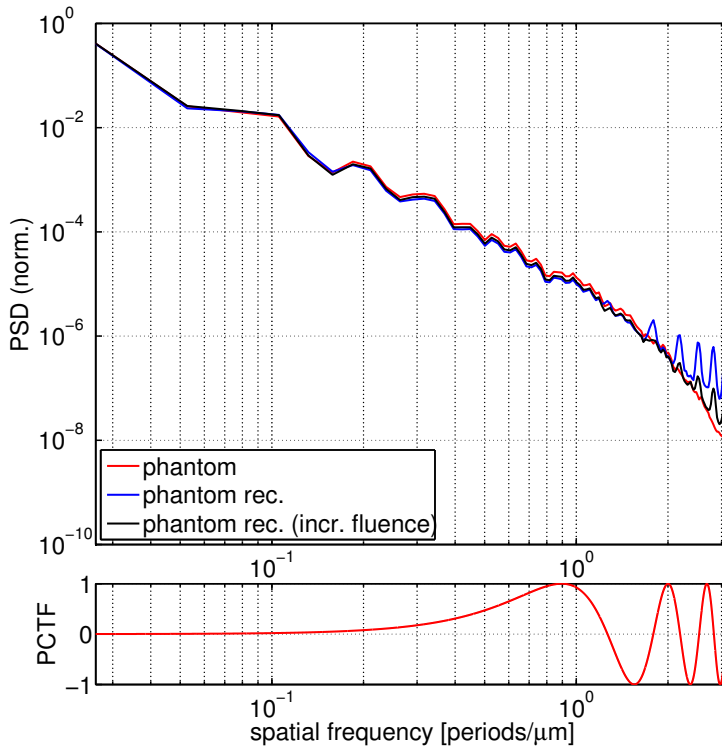


Figure 7.15: Angular averaged and normalized power spectral densities of the simulated cell phase distribution, the modified HIO reconstruction from the simulated dataset with experimental fluence, and from the simulated dataset with increased fluence. For comparison, the phase contrast transfer function corresponding to the experimental geometry is shown (lower graph). Figure adapted from [57].

all at the first three zeros of the PCTF. The trend observed here indicates that artifacts due to the oscillatory contrast transfer function in the Fresnel regime can be fully suppressed, if high enough fluence is applied.

7.4.3 Simulated Siemens star dataset

Fig. 7.16 shows a comparison of the reconstructed phase maps from the simulated Siemens star dataset, as obtained by holographic and iterative reconstruction using the modified HIO scheme. Within the area covered by the Siemens star the RMS deviation between the iteratively reconstructed phase map and the phantom phase distribution is 0.008 rad. Compared to the phantom holographic reconstruction is severely distorted, especially at frequencies corresponding to zeros in the PCTF (see Fig. 7.17.). On the other hand, the iteratively reconstructed phase, obtained here with the same algorithmic parameters as used for the experimental data, is free of such artifacts and gives a quantitative reconstruction

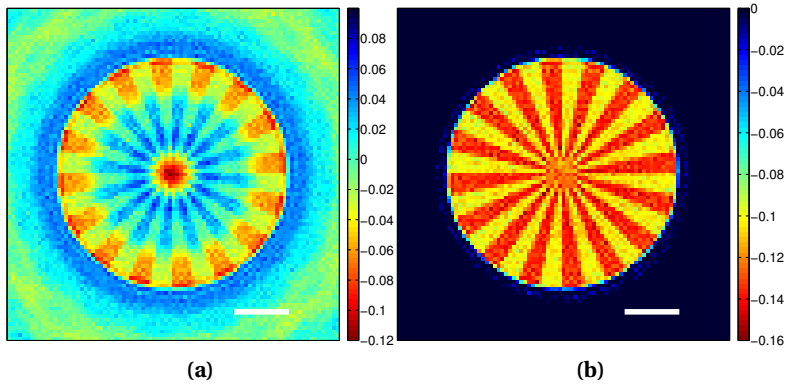


Figure 7.16: (a) Holographic phase reconstruction corresponding to the simulated phase distribution shown in Fig. 7.10 (a). (b) Iterative phase reconstruction as obtained with the modified HIO algorithm. Colorbars indicate phase in rad, scale bars indicate a distance of 250 nm, the pixel width is ≈ 17 nm. Figures adapted from [57].

of the phantom. A reconstruction (half-period) resolution close to the pixel size (17.5 nm) is indicated by a comparison of the power spectral densities of the phantom object phase map and the its iterative reconstruction (see Fig. 7.17).

Lastly, note that the simulated phase map shown in Fig. 7.10 corresponds to an object with two distinct thicknesses, if the same overall refractive index is assumed. In particular, lateral length scales are uncoupled from the depth length scale. This cannot generally be expected for a biological object. In this respect the phase distribution simulated here is an ideal case. As a consequence, a similar resolution in the reconstruction of a real biological cell can be expected to require higher fluence, but is certainly not prevented any by fundamental physical constraints.

7.5 Conclusion

The feasibility of waveguide-based x-ray microscopy applied to unstained biological cells was demonstrated. The method takes advantage of a new generation of crossed high-transmission planar waveguides allowing for a lateral beam confinement below 15 nm. Different reconstruction schemes have been used and compared. A modified HIO algorithm, adapted for pure phase objects and taking experimental noise into account, was observed to have best reconstruction performance, yielding phase reconstructions in agreement with expected values for biological cells.

It was shown that the well-known problem of unconstrained frequency components due to the oscillatory phase contrast transfer function in the Fresnel regime can be largely circumvented by the used reconstruction scheme. Experimentally, the possible resolution range has not been exploited yet. However, it is indicated by simulations that resolutions in the range of the WG exit wave diameter are possible, even for rather weakly scattering

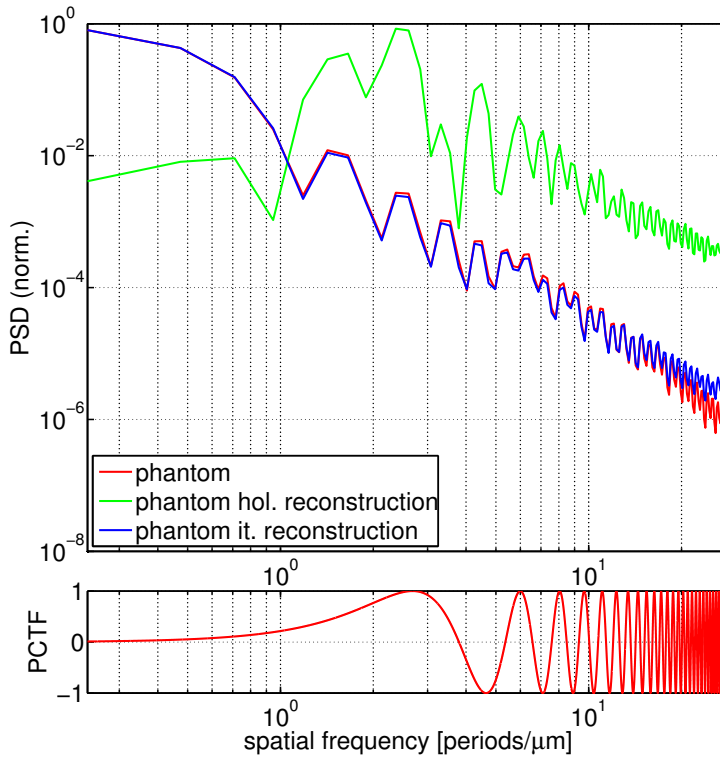


Figure 7.17: Angular averaged and normalized power spectral densities of the simulated Siemens star phase distribution, as well as its holographic and its modified HIO reconstruction. For comparison, the phase contrast transfer function corresponding to the experimental geometry is shown (lower graph). Figure adapted from [57].

samples. The required higher imaging dose can simply be obtained by moving the sample closer to the waveguide.

The reconstruction scheme that has been proposed and demonstrated here requires only one holographic image and no detailed knowledge about the complex illumination, as long as this can be approximated by a paraxial spherical wave with a smooth and nearly constant amplitude envelope in the area covered by the sample. The method offers a wide application range in propagation-based hard x-ray imaging of biological objects.

8 Summary

The main goal of the present thesis was to extend new methods in coherent x-ray microscopy to single unstained biological cells. A special emphasis was placed on applications in the hard x-ray range where the interaction process of the wave field with the sample is especially simple. As a consequence, the sensitivity limits of the methods had to be explored and it was shown that it is possible to extract quantitative phase maps from single unstained cells using illumination with a hard x-ray wave field.

As a prerequisite, a sample environment was implemented which allows for imaging of freeze-dried biological cells in the hard x-ray regime and which is also compatible with observation under cryogenic sample temperatures. For the experiments shown in this thesis two different types of cells have been prepared by freeze-drying, eukaryotic *Dictyostelium discoideum* and bacterial *Deinococcus radiodurans* cells.

In a first experiment, it was shown that ptychographic coherent x-ray diffraction microscopy can be applied successfully to weakly scattering single cells. A pinhole was used here to define the illumination on the sample. As a key prerequisite for the extension of ptychography to weakly scattering specimens the complex-valued illumination function was reconstructed together with the object function. The resolution of this first experiment which was carried out in the low dose limit, can be increased in the future by investing more fluence, e.g. by a focused illumination. Quantitative phase maps of the cells have been obtained with small and quantified errors. Experimental reconstructions were corroborated by reconstructions from simulated data. Due to the simple interaction process of the thin biological material with the hard x-ray wave field, the phase maps can be rescaled into projected electron density maps and, with restrictions, also mass density maps. The obtained values are in the range expected for unstained biological material. For the specific case of the *D. radiodurans* cells that were imaged here, subcellular density variations were observed with increased (projected) density in regions where the bacterial nucleoid is located.

In the second experiment, the extension of ptychographic CDI to the soft x-ray energy range was demonstrated. Absorption and phase contrast images have been obtained for a fossil diatom sample, showing highest image quality phase contrast. In addition, a heavy element test pattern has been imaged down to a line/space half-period width of 50 nm. For the smaller photon energy applied here the used pinhole illumination exhibits a significant lateral extension and phase curvature at the sample. In the object function this allows for a reconstruction of much larger areas than covered by the central part of the beam. On the other hand, the large extension of the illumination at the sample makes a reconstruction

more difficult. In this respect the experiment is a limiting case of ptychographic CDI.

The third experiment presented in this thesis demonstrates imaging of single unstained cells by waveguide-based hard x-ray propagation microscopy. A magnified near field diffraction pattern of two *Dictyostelium discoideum* cells was recorded in the simple geometry of in-line holography. The twin image of holographic reconstruction was successfully removed by application of an iterative reconstruction procedure that was specifically devised for the present experimental case. It was shown that the proposed reconstruction scheme, which takes into account the noise statistics of the normalized hologram, allows for a partial removal of unconstrained-frequency artifacts, well known in near field propagation microscopy. The degree to which the effects can be suppressed, scales with the invested fluence, as shown by simulations. For a simulated structure observed in the high fluence and magnification limit remaining artifacts are negligible. The resolution is limited here by the modest magnification and low dose. For this setup using a cone beam illumination, the dose can easily be increased by moving the sample closer to the source, leading also to a higher geometrical magnification and to possible resolutions near 20 nm, as indicated by a simulation for a moderately scattering test structure. The experimentally obtained phase map of the cells was analyzed in a quantitative manner, similar to the one obtained for hard x-ray ptychography. The obtained density values are in the same range, confirming the validity of the two different experimental approaches.

The hard x-ray imaging schemes presented here are characterized by a simple and quantitative¹ contrast mechanism. With the high demonstrated phase resolution they offer a unique way to determine density maps of unstained internal cellular structures with high spatial and density resolution in a single experiment. Especially in the hard x-ray range, the high penetrating power of x rays allows for investigation of unsliced and relatively large specimens and has the potential to provide quantitative 3D density distributions of unsliced, unstained and vitrified cells.

¹In the case of ptychographic CDI on cells the contrast is fully quantitative, for the demonstrated near field reconstruction scheme used in waveguide-based cellular imaging, the presented simulations indicate the quantitiveness to be dependent on the invested fluence, but also to be scalable to very high accuracy, with realistic experimental parameters.

A Appendix

A.1 List of abbreviations

AMP	Adenosine Monophosphate
ACTF	Amplitude Contrast Transfer Function
CCD	Charge Coupled Device
C(X)DI	Coherent (X-ray) Diffractive Imaging
DF	Dark Field
DFT	Discrete Fourier Transform
DIC	Differential Interference Contrast
DM	Difference Map (algorithm)
DPC	Differential Interference Contrast
EM	Electron Microscopy
ER	Error Reduction (algorithm)
ESRF	European Synchrotron Radiation Facility
FFT	Fast Fourier Transform
FOV	Field of View
FT	Fourier Transform
FWHM	Full Width at Half Maximum
GS	Gerchberg-Saxton (algorithm)
HGW	Hyperquenched Glassy Water
HIO	Hybrid-Input-Output (algorithm)
IDFT	Inverse DFT
IFFT	Inverse FFT
KB	Kirkpatrick-Baez (mirrors)
PCDI	Ptychographic Coherent Diffractive Imaging
PCTF	Phase Contrast Transfer Function
PIE	Ptychographic Iterative Engine
PRTF	Phase Retrieval Transfer Function
PSD	Power Spectral Density
RMS	Root Mean Square

ROI	Region of Interest
SNR	Signal-to-Noise (ratio)
SW	Shrink-Wrap (algorithm)
UHV	Ultra High Vacuum
WG	Waveguide
XM	X-ray Microscopy

A.2 Graphical representation of complex-valued images

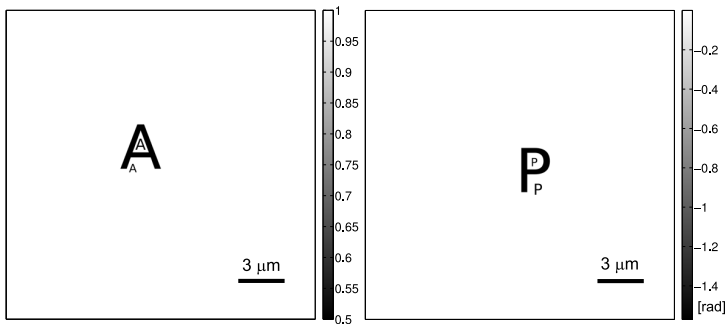


Figure A.1: A two-dimensional complex transmission function. The amplitude is shown on the left, the phase on the right.

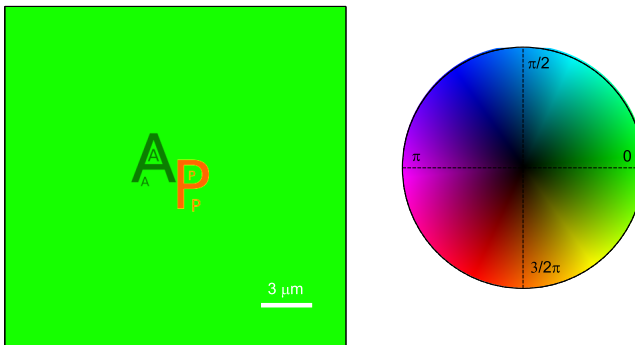


Figure A.2: The same transmission function as shown in Fig. A.1 is shown here in complex representation. The phase is encoded as hue, the amplitude as brightness, according to the colorwheel on the right. Phase is shown here modulo 2π , so that values between $-\pi$ and 0 are mapped into the interval from π to 2π .

The graphical representation of phase and amplitude in a single image is a common way of depicting two-dimensional complex functions and is used also within this thesis.

Here the phase is encoded in the color and the amplitude in brightness. In the hue-saturation-value (hsv) colorspace, the phase (modulo 2π) corresponds to hue, and the amplitude to value. The saturation value is not used and equal to 1 everywhere. In a colorwheel which fills the unit circle in the complex plane (see as Fig. A.2, right) all combinations of phase (modulo 2π) and amplitude (within 0 and 1) are encoded.

As an illustrative example a phantom transmission function is shown in the conventional way in Fig. A.1, i.e. with amplitude and phase depicted in separate images. For comparison, the representation of the same complex transmission function in a single image is shown in Fig. A.2. The phase and amplitude at each point can be determined from the colorwheel in Fig. A.2.

Note that a rotation of the colorwheel by a certain angle corresponds to the addition of a global phase offset. A reconstructed transmission function is usually only unique up to the addition of such an arbitrary offset.

A.3 Kaiser-Bessel-window

For the calculation of the 2D power spectral density of an image, within this thesis usually a multiplicative Kaiser-Bessel-window was applied before the Fourier transform operation. More specifically, a window function as defined in [14, p. 97] has been applied, corresponding to the form

$$w(n_x, n_y) = \begin{cases} \frac{I_0(\beta\sqrt{1-(2r/N)^2})}{I_0(\beta)} & r \leq N/2 \\ 0 & \text{else} \end{cases} \quad (\text{A.1})$$

with $r = \sqrt{n_x^2 + n_y^2}$, $-N/2 \leq n_x, n_y \leq N/2 - 1$ and I_0 denoting the modified Bessel function of the first kind. For simplicity, N has been assumed to be even here. $\beta = 8$ was a usual choice of the parameter β .

The purpose of the window function is to minimize errors in the PSD originating from truncation of the real space image at the edges. The rapid decay of the Kaiser-Bessel window in Fourier space facilitates the identification of weak frequency components of the signal [see e.g. 14].

A.4 PCDI of bacterial cells: Reconstructions for different values of the relaxation parameter

In the following, reconstructions are shown for the simulated and experimental datasets for different values of the Fourier constraint relaxation parameter D as described in Sec. 4.6.

A.4.1 Short exposure dataset

For the reconstruction of the simulated and experimental short exposure dataset the algorithm was iterated for 1100 iterations. To increase the reproducibility of the result, the final reconstruction was formed as a complex average over the last 101 iterations (see also Sec. 4.4.6).

The reconstructed and simulated object phase and complex illumination for the short exposure dataset are depicted in Figs. A.3 and A.4. Note that the complex illumination function is reconstructed accurately in spite of the inaccurate initial guess for the distance between aperture and sample plane.¹ Furthermore, the overall phase distribution in the reconstructed object and probe functions is largely independent of the relaxation parameter D . On closer inspection, the object reconstructions differ more than the probe reconstructions for different values of D . For $D \rightarrow 0$, the modified Fourier projector (see Eq. (4.87)) enforces strong agreement with the noisy experimental data, leading to increased variations in the reconstructions of subsequent iterates. As a consequence, the final averaged reconstruction is characterized by a high reproducibility, but a rather low spatial

¹To simulate an imperfect knowledge of the illumination function in the experiment for the simulated short-exposure dataset, the initial probe for the reconstruction was calculated based on a propagation distance of 1.2 mm instead of 1.4 mm between the pinhole and the sample.

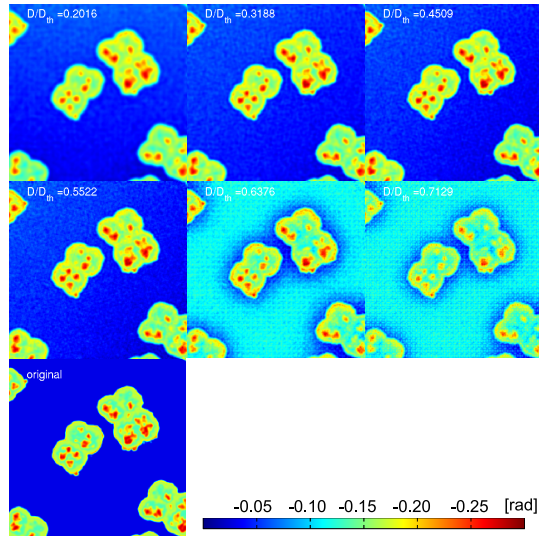


Figure A.3: Reconstructed phase of the simulated short-exposure dataset for different values of the relaxation parameter D which is given here in units of the expected value D_{th} . For comparison, the corresponding ROI of the simulated phase distribution is shown ('original').

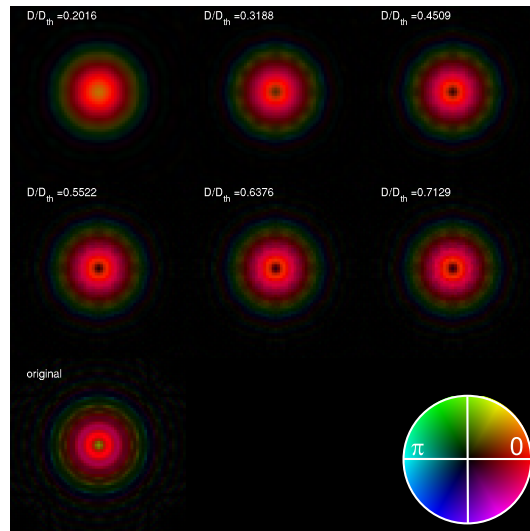


Figure A.4: Reconstructed complex illumination of the simulated short-exposure dataset for different values of the relaxation parameter D . The simulated illumination function is also shown ('original').

resolution. On the other hand, $D \rightarrow D_{th}$ here leads to reconstruction artifacts and causes the algorithm to stagnate. Generally, residual fluctuations in the phase reconstruction

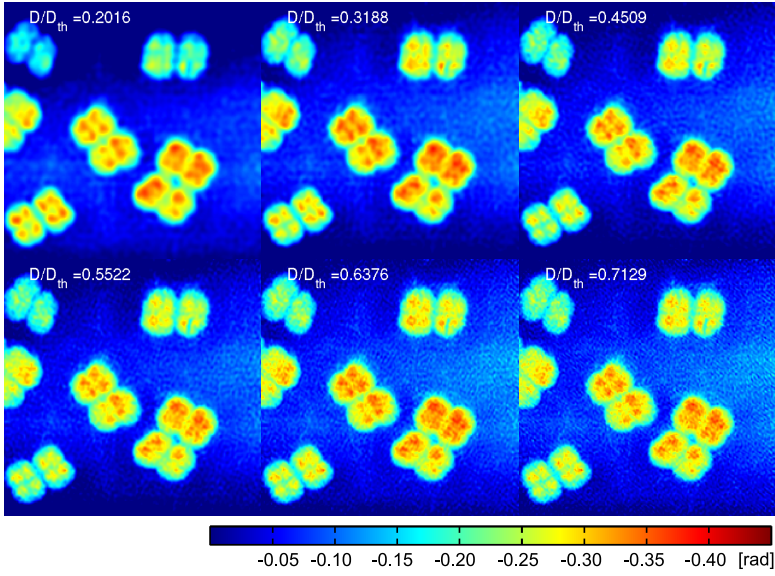


Figure A.5: Reconstructed phase of the experimental short-exposure dataset for different values of the relaxation parameter D .

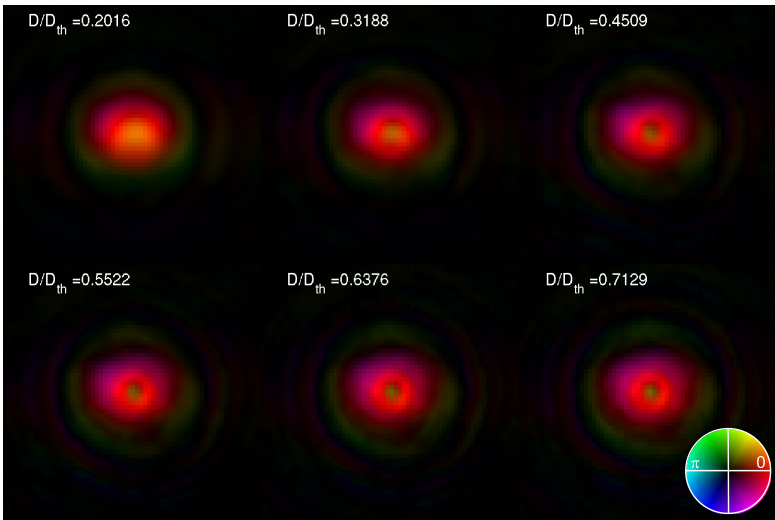


Figure A.6: Reconstructed complex illumination of the experimental short-exposure dataset for different values of the relaxation parameter D .

remain for all tested values of D , especially in background regions with no sample. For

$D \ll D_{th}$, however, they are smoothed out more and more.

The overall observations made here are similar, at least in a qualitative way, to those for the reconstructions from the corresponding experimental dataset (see Figs. A.5 and A.6), for equal values of D . The final (optimum) value ($D = 0.32D_{th}$) of the relaxation parameter for the current experimental conditions was chosen based on a comparison of the experimental with the ‘simulated’ reconstructions as well as of the simulated reconstructions with the phantom phase distribution.² The reconstruction shown in Fig. 5.3 was obtained with this value for D .

A.4.2 Long exposure dataset

In a subsequent step, the simulated and the experimental long exposure dataset was reconstructed. Here 2500 iterations were used, with the final complex average of the object and illumination function formed from the last 101 iterates.

Illumination and object (phase) reconstructions for the simulated dataset are shown in Figs. A.7 and A.8, respectively. Compared to the (simulated) short exposure dataset, the reconstructions are generally less dependent on the value of the relaxation parameter. This can be explained by the higher signal from the object that is acquired over the longer accumulation time. Accurate reconstructions are generally achieved for a value of D near the expected value D_{th} .

The reconstructions of the experimental long exposure dataset are shown in Figs. A.9 and A.10, respectively. The general dependence on the relaxation parameter D is similar to that of the simulated reconstructions. The optimum parameter $D = 1.25D_{th}$ was chosen based on two main criteria: firstly, the comparison with simulated reconstructions and, secondly, the degree of consistency with the reconstructions from the experimental short exposure dataset which covers the field of view of the long exposure dataset as a subregion.

²The exact values selected here were chosen initially with respect to a different definition of the relaxation parameter that was used in an earlier version of the algorithm. The dependence on the relaxation parameter is weak enough, so that the tested values cover the whole range of possible results around the correct solution.

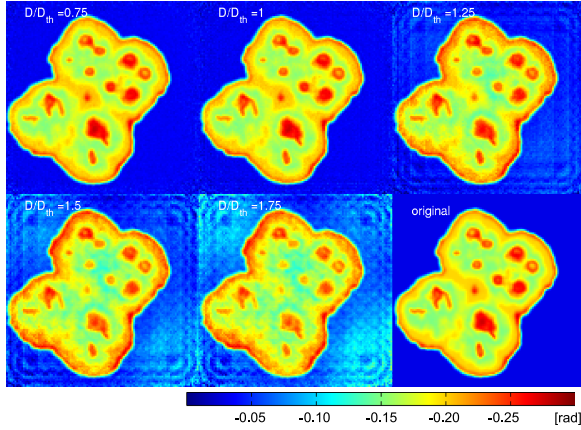


Figure A.7: Reconstructed phase of the simulated long-exposure dataset for different values of the relaxation parameter D . For comparison the corresponding ROI of the simulated phase distribution is shown ('original').

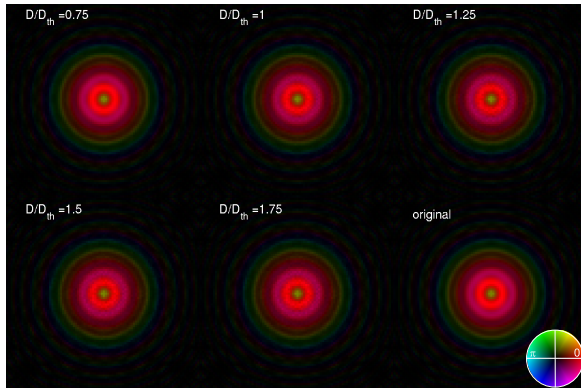


Figure A.8: Reconstructed complex illumination of the simulated long-exposure dataset for different values of the relaxation parameter D . The simulated illumination function is also shown ('original').

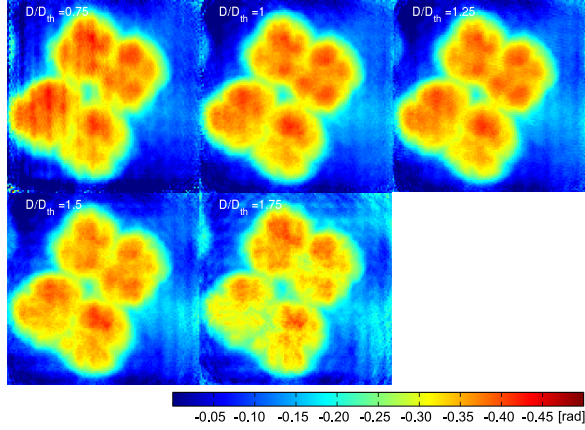


Figure A.9: Reconstructed phase of the experimental long-exposure dataset for different values of the relaxation parameter D .

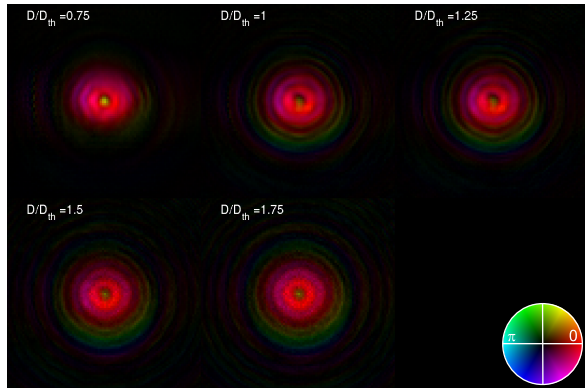


Figure A.10: Reconstructed complex illumination of the experimental long-exposure dataset for different values of the relaxation parameter D .

A.5 Waveguide based propagation microscopy: Near field reconstructions for different values of algorithmic parameters

In the following phase reconstructions are shown for different values of the feedback parameters β and γ . All reconstructions were formed as a complex average of the result after 25 reconstruction runs, initialized independently as described in Section 7.3. All reconstructions were carried out using $D = 1.06D_D$ as the relaxation parameter. The algorithm was stopped as soon as $d \leq D$, or when the number of iterations reached a value of 5000.

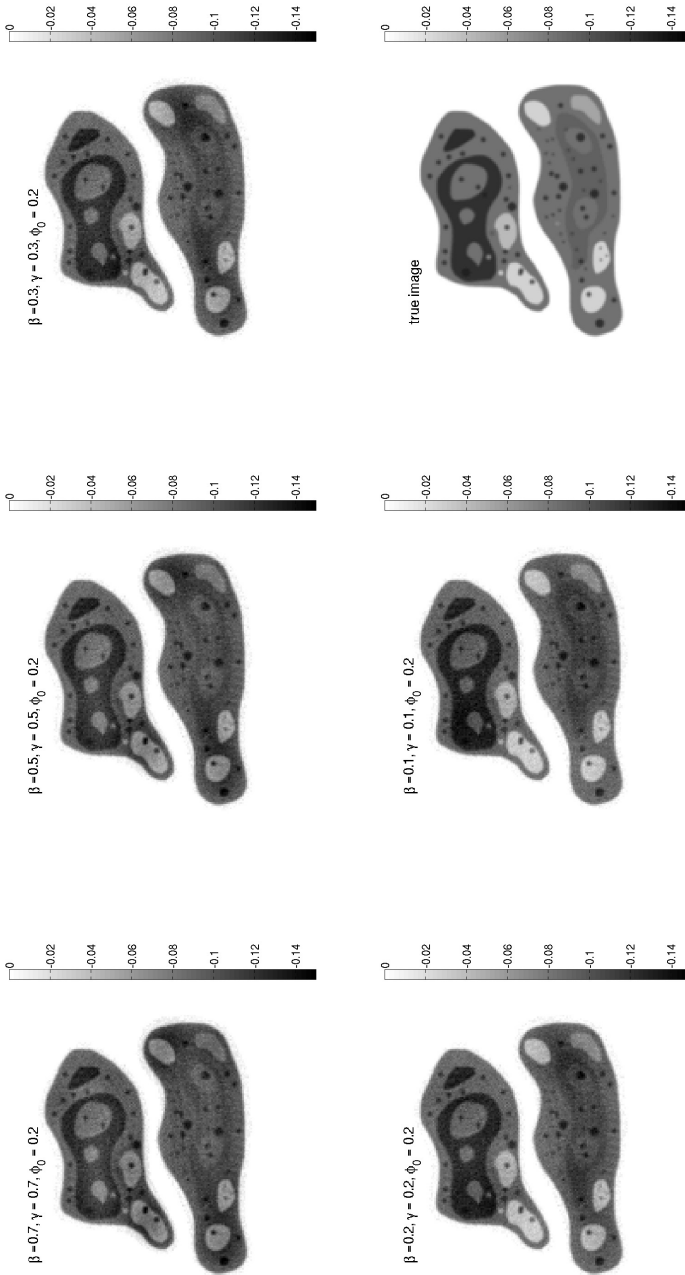


Figure A.11: Reconstructed phase maps for the simulated cell phantom dataset. For comparison the true simulated phase map is also shown. Colorbars indicate phase in rad.

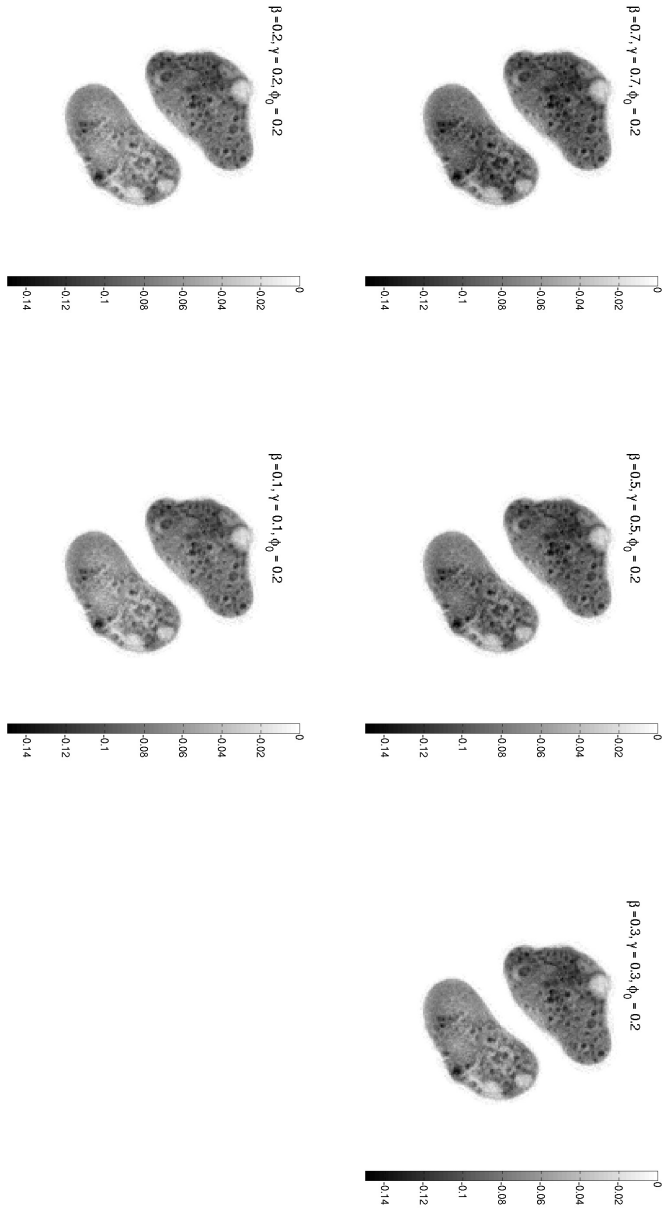


Figure A.12: Reconstructed phase maps for the experimental dataset. Colorbars indicate phase in rad.

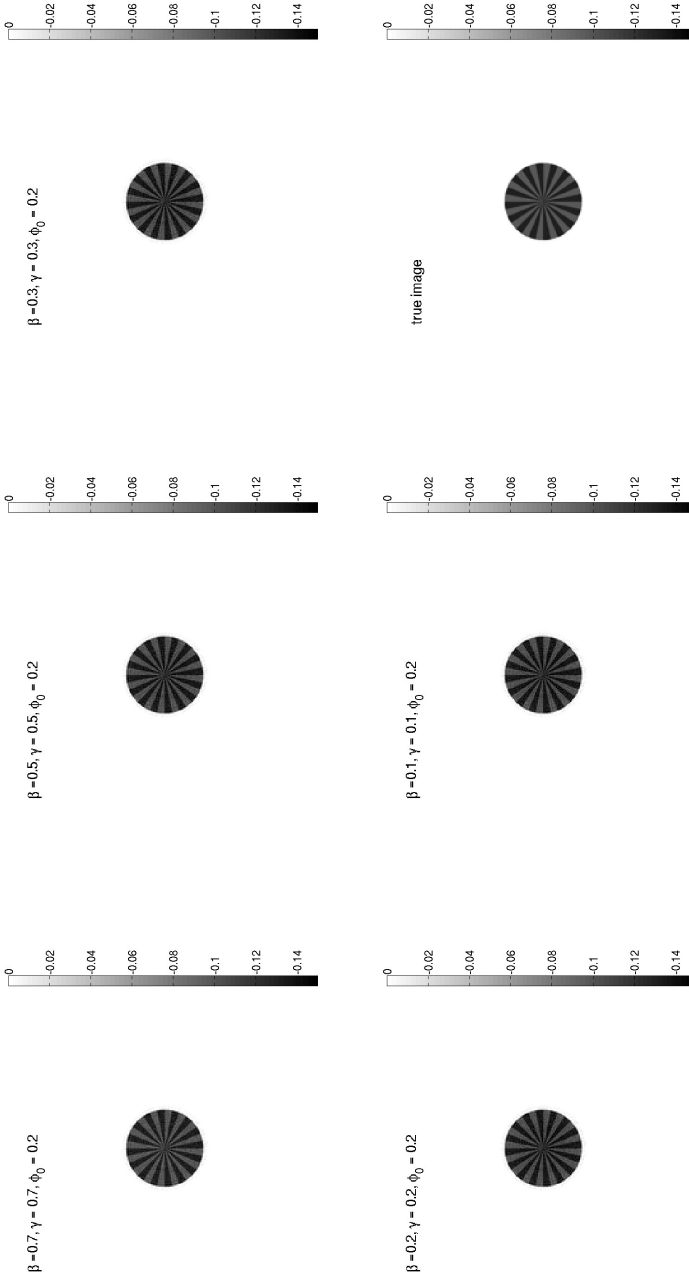


Figure A.13: Reconstructed phase maps for the simulated Siemens star dataset. For comparison the true simulated phase map is also shown. Colorbars indicate phase in rad.

Bibliography

- [1] B. Abbey, G. J. Williams, M. A. Pfeifer, J. N. Clark, C. T. Putkunz, A. Torrance, I. McNulty, T. M. Levin, A. G. Peele, and K. A. Nugent. Quantitative coherent diffractive imaging of an integrated circuit at a spatial resolution of 20 nm. *Appl. Phys. Lett.*, 93(21):214101, 2008.
- [2] J. Als-Nielsen and D. McMorrow. *Elements of Modern X-ray Physics*. Wiley, New York, 2001.
- [3] T. Arens, F. Hettlich, C. Karpfinger, U. Kockelkorn, K. Lichtenegger, and H. Stachel. *Mathematik*. Spektrum Akad. Verl., Heidelberg, 2010.
- [4] D. T. Attwood. *Soft X-rays and extreme ultraviolet radiation: Principles and applications*. Univ. Press, 2000.
- [5] R. H. T. Bates. Fourier phase problems are uniquely solvable in more than one dimension. I: Underlying theory. *Optik (Stuttgart)*, 61(3):247, 1982.
- [6] T. Beetz, M. Howells, C. Jacobsen, C.-C. Kao, J. Kirz, E. Lima, T. Mentes, H. Miao, C. Sanchez-Hanke, D. Sayre, and D. Shapiro. Apparatus for X-ray diffraction microscopy and tomography of cryo specimens. *Nuclear Instrum. Meth. A*, 545(1-2):459, 2005.
- [7] M. Bertilson, O. von Hofsten, U. Vogt, A. Holmberg, and H. M. Hertz. High-resolution computed tomography with a compact soft x-ray microscope. *Opt. Express*, 17(13):11057, 2009.
- [8] P. Bleuet, P. Cloetens, P. Gergaud, D. Mariolle, N. Chevalier, R. Tucoulou, J. Susini, and A. Chabli. A hard x-ray nanoprobe for scanning and projection nanotomography. *Rev. Sci. Instrum.*, 80(5):056101, 2009.
- [9] M. Born and E. Wolf. *Principles of optics: Electromagnetic theory of propagation, interference and diffraction of light*. Cambridge Univ. Press, 2006.
- [10] W. L. Briggs and V. E. Henson. *The DFT: An owner's manual for the discrete Fourier transform*. Soc. for Industrial and Applied Math., Philadelphia, 1995.
- [11] E. O. Brigham. *The Fast Fourier Transform and its applications*. Prentice Hall, Englewood Cliffs, NJ (USA), 1988.

- [12] C. Broennimann, E. F. Eikenberry, B. Henrich, R. Horisberger, G. Huelsen, E. Pohl, B. Schmitt, C. Schulze-Briese, M. Suzuki, T. Tomizaki, H. Toyokawa, and A. Wagner. The PILATUS 1M detector. *J. Synchrotron Radiat.*, 13(2):120, 2006.
- [13] O. Bunk, M. Dierolf, S. Kynde, I. Johnson, O. Marti, and F. Pfeiffer. Influence of the overlap parameter on the convergence of the ptychographical iterative engine. *Ultramicroscopy*, 108(5):481, 2008.
- [14] T. Butz. *Fouriertransformation für Fußgänger*. Teubner, Wiesbaden, 3rd edition, 2003.
- [15] L. D. Caro, C. Giannini, A. Cedola, S. Lagomarsino, and I. Bukreeva. X-ray point- and line-projection microscopy and diffraction. *Opt. Commun.*, 265(1):18, 2006.
- [16] D. C. Champeney. *Fourier transforms and their physical applications*. Techniques of physics 1. Academic Press, London, 1973.
- [17] W. Chao, B. D. Harteneck, J. A. Liddle, E. H. Anderson, and D. T. Attwood. Soft X-ray microscopy at a spatial resolution better than 15 nm. *Nature*, 435(7046):1210, 2005.
- [18] H. N. Chapman. Phase-retrieval X-ray microscopy by Wigner-distribution deconvolution. *Ultramicroscopy*, 66(3-4):153, 1996.
- [19] H. N. Chapman, A. Barty, S. Marchesini, A. Noy, S. P. Hau-Riege, C. Cui, M. R. Howells, R. Rosen, H. He, J. C. H. Spence, U. Weierstall, T. Beetz, C. Jacobsen, and D. Shapiro. High-resolution ab initio three-dimensional x-ray diffraction microscopy. *J. Opt. Soc. Am. A*, 23(5):1179, 2006.
- [20] E. Chu. *Discrete and continuous fourier transforms. Analysis, applications and fast algorithms*. CRC Press, Boca Raton, Fla., 2008.
- [21] P. Cloetens. *Contribution to Phase Contrast Imaging, Reconstruction and Tomography with Hard Synchrotron Radiation*. PhD thesis, Vrije Universiteit Brussel, 1999.
- [22] P. Cloetens, R. Barrett, J. Baruchel, J.-P. Guigay, and M. Schlenker. Phase objects in synchrotron radiation hard x-ray imaging. *J. Phys. D. Appl. Phys.*, 29(1):133, 1996.
- [23] P. Cloetens, W. Ludwig, J. Baruchel, D. V. Dyck, J. V. Landuyt, J. P. Guigay, and M. Schlenker. Holotomography: Quantitative phase tomography with micrometer resolution using hard synchrotron radiation x rays. *Appl. Phys. Lett.*, 75(19):2912, 1999.
- [24] P. Cloetens, R. Mache, M. Schlenker, and S. Lerbs-Mache. Quantitative phase tomography of arabidopsis seeds reveals intercellular void network. *P. Natl. Acad. Sci. USA*, 103(39):14626, 2006.
- [25] P. Cloetens, M. Pateyron-Salome, J. Y. Buffiere, G. Peix, J. Baruchel, F. Peyrin, and M. Schlenker. Observation of microstructure and damage in materials by phase sensitive radiography and tomography. *J. Appl. Phys.*, 81(9):5878, 1997.

- [26] J. W. Cooley and J. W. Tukey. An Algorithm for the Machine Calculation of Complex Fourier Series. *Math. Comput.*, 19(90):297, 1965.
- [27] M. M. Cox and J. R. Battista. *Deinococcus radiodurans* – the consummate survivor. *Nat. Rev. Micro.*, 3(11):882, 2005.
- [28] V. Čížek and J. Jirát. *Discrete Fourier transforms and their applications*. Hilger, Bristol, 1986.
- [29] Data has been obtained from the beamline website <http://www.psi.ch/sls/csaxs/> on 26.12.2010.
- [30] M. D. de Jonge, B. Hornberger, C. Holzner, D. Legnini, D. Paterson, I. McNulty, C. Jacobsen, and S. Vogt. Quantitative Phase Imaging with a Scanning Transmission X-Ray Microscope. *Phys. Rev. Lett.*, 100(16):163902, 2008.
- [31] P. G. Debenedetti. Supercooled and glassy water. *J. Phys. Cond. Matt.*, 15(45):R1669, 2003.
- [32] Diatom. Retrieved from Encyclopedia Britannica Online under <http://www.britannica.com/EBchecked/topic/161817/diatom> on 3.12.2010.
- [33] M. Dierolf, A. Menzel, P. Thibault, P. Schneider, C. M. Kewish, R. Wepf, O. Bunk, and F. Pfeiffer. Ptychographic X-ray computed tomography at the nanoscale. *Nature*, 467:436, 2010.
- [34] M. Dierolf, P. Thibault, A. Menzel, C. M. Kewish, K. Jefimovs, I. Schlichting, K. von König, O. Bunk, and F. Pfeiffer. Ptychographic coherent diffractive imaging of weakly scattering specimens. *New J. Phys.*, 12(3):035017, 2010.
- [35] J. Dubochet. The Physics of Rapid Cooling and Its Implications for Cryoimmobilization of Cells. *Method. Cell Biol.*, 79:7, 2007.
- [36] J. Dubochet, M. Adrian, J.-J. Chang, J.-C. Homo, J. Lepault, A. W. McDowell, and P. Schultz. Cryo-Electron microscopy of vitrified specimens. *Q. Rev. Biophys.*, 21(2):129, 1988.
- [37] S. Eisebitt, J. Luning, W. F. Schlotter, M. Lorgen, O. Hellwig, W. Eberhardt, and J. Stohr. Lensless imaging of magnetic nanostructures by x-ray spectro-holography. *Nature*, 432:885, 2004.
- [38] V. Elser. Phase retrieval by iterated projections. *J. Opt. Soc. Am. A*, 20:40, 2003.
- [39] M. Eltsov and J. Dubochet. Fine Structure of the *Deinococcus radiodurans* Nucleoid Revealed by Cryoelectron Microscopy of Vitreous Sections. *J. Bacteriol.*, 187(23):8047, 2005.
- [40] M. Eltsov and J. Dubochet. Rebuttal: Ring-Like Nucleoids and DNA Repair in *Deinococcus radiodurans*. *J. Bacteriol.*, 188(17):6052, 2006.

- [41] M. Eltsov and J. Dubochet. Study of the *Deinococcus radiodurans* Nucleoid by Cryo-electron Microscopy of Vitreous Sections: Supplementary Comments. *J. Bacteriol.*, 188(17):6053, 2006.
- [42] Y. M. Engelberg and S. Ruschin. Fast method for physical optics propagation of high-numerical-aperture beams. *J. Opt. Soc. Am. A*, 21(11):2135, 2004.
- [43] M. Feser, T. Beetz, C. Jacobsen, J. Kirz, S. Wirick, A. Stein, and T. Schäfer. Scanning transmission soft x-ray microscopy at beamline X-1A at the NSLS – advances in instrumentation and selected applications. In D. A. Tichenor and J. A. Folta, editors, *Soft X-ray and EUV Imaging Systems II*, volume 4506 of *Proc. SPIE*, pages 146–153, 2001.
- [44] J. R. Fienup. Reconstruction of an object from the modulus of its Fourier transform. *Opt. Lett.*, 3(1):27, 1978.
- [45] J. R. Fienup. Phase retrieval algorithms: A comparison. *Appl. Opt.*, 21(15):2758, 1982.
- [46] J. R. Fienup, T. R. Crimmins, and W. Holsztynski. Reconstruction of the support of an object from the support of its autocorrelation. *J. Opt. Soc. Am.*, 72(5):610, 1982.
- [47] C. Fuhse. *X-ray waveguides and waveguide-based lensless imaging*. PhD thesis, University of Göttingen, 2006.
- [48] C. Fuhse, C. Ollinger, and T. Salditt. Waveguide-Based Off-Axis Holography with Hard X Rays. *Phys. Rev. Lett.*, 97(25):254801, 2006.
- [49] D. Gabor. A New Microscopic Principle. *Nature*, 161:777, 1948.
- [50] J. Garcia, D. Mas, and R. G. Dorsch. Fractional-Fourier-transform calculation through the fast-Fourier-transform algorithm. *Appl. Opt.*, 35(35):7013, 1996.
- [51] E. F. Garman and R. L. Owen. Cryocooling and radiation damage in macromolecular crystallography. *Acta Cryst. D*, 62(1):32, 2006.
- [52] R. Gens. Two-dimensional phase unwrapping for radar interferometry: Developments and new challenges. *Int. J. Remote Sens.*, 24(4):703, 2003.
- [53] R. W. Gerchberg and W. O. Saxton. A Practical Algorithm for the Determination of Phase from Image and Diffraction Plane Pictures. *Optik (Jena)*, 35:237, 1972.
- [54] D. C. Ghiglia and M. D. Pritt. *Two-dimensional phase unwrapping: Theory, algorithms, and software*. Wiley, New York, NY, 1998.
- [55] K. Giewekemeyer, M. Beckers, T. Gorniak, M. Grunze, T. Salditt, and A. Rosenhahn. Ptychographic coherent x-ray diffractive imaging in the water window. *Opt. Express*, 19(2):1037, 2011.
- [56] K. Giewekemeyer, M. Hantke, C. Beta, R. Tucoulou, and T. Salditt. Fluorescence imaging of *Dictyostelium discoideum* with a hard X-ray nanoprobe. *J. Phys. Conf. Ser.*, 186:012086, 2009.

- [57] K. Giewekemeyer, S. P. Krüger, S. Kalbfleisch, M. Bartels, C. Beta, and T. Salditt. X-ray propagation microscopy of biological cells using waveguides as a quasipoint source. *Phys. Rev. A*, 83(2):023804, 2011.
- [58] K. Giewekemeyer and T. Salditt. Counterion distribution near a monolayer of variable charge density. *Europhys. Lett.*, 79(1):18003, 2007.
- [59] K. Giewekemeyer, P. Thibault, S. Kalbfleisch, A. Beerlink, C. M. Kewish, M. Dierolf, F. Pfeiffer, and T. Salditt. Quantitative biological imaging by ptychographic x-ray diffraction microscopy. *P. Natl. Acad. Sci. USA*, 107(2):529, 2010.
- [60] J. W. Goodman. *Introduction to Fourier Optics*. Roberts & Company: Englewood, Colorado, 2005.
- [61] H. Gross, H. Zügge, M. Peschka, and F. Blechinger. *Aberration Theory and Correction of Optical Systems*, volume 3 of *Handbook of Optical Systems*. Wiley-VCH, Weinheim, 2007.
- [62] M. Guizar-Sicairos and J. R. Fienup. Phase retrieval with transverse translation diversity: A nonlinear optimization approach. *Opt. Express*, 16(10):7264, 2008.
- [63] T. E. Gureyev. Composite techniques for phase retrieval in the fresnel region. *Opt. Commun.*, 220(1-3):49, 2003.
- [64] M. Hantke. Optimierung der Probenumgebung für linsenlose Cryoröntgenmikroskopie an prokaryotischen Zellen. Bachelor's thesis, Georg-August-Universität Göttingen, October 2008.
- [65] M. A. Hayat, editor. *Principles and techniques of electron microscopy: biological applications*. Cambridge University Press, 4th edition, 2000.
- [66] R. Hegerl and W. Hoppe. Dynamische Theorie der Kristallstrukturanalyse durch Elektronenbeugung im inhomogenen Primärstrahlwellenfeld. *Berich. Bunsen Gesell.*, 74:1148, 1970.
- [67] B. L. Henke, E. M. Gullikson, and J. C. Davis. X-ray interactions: Photoabsorption, scattering, transmission, and reflection at $E = 50\text{-}30,000$ eV, $Z = 1\text{-}92$. *Atomic Data and Nuclear Data Tables*, 54(2):181–342, 1993.
- [68] G. T. Herman. *Image reconstruction from projections: The fundamentals of computerized tomography*. Acad. Press, New York, 1980.
- [69] M. Heydt, A. Rosenhahn, M. Grunze, M. Pettitt, M. E. Callow, and J. A. Callow. Digital In-Line Holography as a Three-Dimensional Tool to Study Motile Marine Organisms During Their Exploration of Surfaces. *J. Adhes.*, 83(5):417, 2007.
- [70] W. Hoppe. Beugung im inhomogenen Primärstrahlwellenfeld. I. Prinzip einer Phasenmessung von Elektronenbeugungsinterferenzen. *Acta Crystallogr. A*, 25(4):495, 1969.

- [71] M. Howells, T. Beetz, H. Chapman, C. Cui, J. Holton, C. Jacobsen, J. Kirz, E. Lima, S. Marchesini, H. Miao, D. Sayre, D. Shapiro, J. Spence, and D. Starodub. An assessment of the resolution limitation due to radiation-damage in x-ray diffraction microscopy. *Journal of Electron Spectroscopy and Related Phenomena*, 170(1-3):4, 2009.
- [72] X. Huang, H. Miao, J. Steinbrener, J. Nelson, D. Shapiro, A. Stewart, J. Turner, and C. Jacobsen. Signal-to-noise and radiation exposure considerations in conventional and diffraction x-ray microscopy. *Opt. Express*, 17(16):13541, 2009.
- [73] X. Huang, J. Nelson, J. Kirz, E. Lima, S. Marchesini, H. Miao, A. M. Neiman, D. Shapiro, J. Steinbrener, A. Stewart, J. J. Turner, and C. Jacobsen. Soft X-Ray Diffraction Microscopy of a Frozen Hydrated Yeast Cell. *Phys. Rev. Lett.*, 103(19):198101, 2009.
- [74] J. F. James. *A Student's Guide to Fourier Transforms. With Applications in Physics and Engineering*. Cambridge Univ. Press, Cambridge, 2nd edition, 2002.
- [75] A. Jarre, C. Fuhse, C. Ollinger, J. Seeger, R. Tucoulou, and T. Salditt. Two-Dimensional Hard X-Ray Beam Compression by Combined Focusing and Waveguide Optics. *Phys. Rev. Lett.*, 94(7):074801, 2005.
- [76] R. H. Kessin. *Dictyostelium – Evolution, cell Biology, and the Development of Multicellularity*. Cambridge Univ. Press, Cambridge (UK), 2001.
- [77] C. M. Kewish, P. Thibault, M. Dierolf, O. Bunk, A. Menzel, J. Vila-Comamala, K. Jefimovs, and F. Pfeiffer. Ptychographic characterization of the wavefield in the focus of reflective hard X-ray optics. *Ultramicroscopy*, 110(4):325, 2010.
- [78] J. Kirz, C. Jacobsen, and M. Howells. Soft X-ray microscopes and their biological applications. *Q. Rev. Biophys.*, 28(1):33, 1995.
- [79] J. Kirz and H. Rarback. Soft x-ray microscopes. *Rev. Sci. Instrum.*, 56(1):1, 1985.
- [80] S. P. Krüger, K. Giewekemeyer, S. Kalbfleisch, M. Bartels, H. Neubauer, and T. Salditt. Sub-15 nm beam confinement by two crossed x-ray waveguides. *Opt. Express*, 18(13):13492, 2010.
- [81] C. A. Larabell and M. A. Le Gros. X-ray Tomography Generates 3-D Reconstructions of the Yeast, *Saccharomyces cerevisiae*, at 60-nm Resolution. *Mol. Biol. Cell*, 15(3):957, 2004.
- [82] C. A. Larabell and K. A. Nugent. Imaging cellular architecture with X-rays. *Curr. Opin. Struc. Biol.*, 20(5):623, 2010.
- [83] G. Lawrence. Optical modeling. In R. Shannon and J. Wyant, editors, *Applied Optics and Optical Engineering*, volume XI, chapter 3, pages 125–200. Acad. Press, Boston, 1992.

- [84] S. Levin-Zaidman, J. Englander, E. Shimoni, A. K. Sharma, K. W. Minton, and A. Minsky. Ringlike Structure of the *Deinococcus radiodurans* Genome: A Key to Radioreistance? *Science*, 299(5604):254, 2003.
- [85] R. A. Lewis, N. Yagi, M. J. Kitchen, M. J. Morgan, D. Paganin, K. K. W. Siu, K. Pavlov, I. Williams, K. Uesugi, M. J. Wallace, C. J. Hall, J. Whitley, and S. B. Hooper. Dynamic imaging of the lungs using x-ray phase contrast. *Physics in Medicine and Biology*, 50(21):5031, 2005.
- [86] E. Lima, L. Wiegart, P. Pernot, M. Howells, J. Timmins, F. Zontone, and A. Madsen. Cryogenic X-Ray Diffraction Microscopy for Biological Samples. *Phys. Rev. Lett.*, 103(19):198102, 2009.
- [87] H. Lodish, A. Berk, P. Matsudaira, C. A. Kaiser, M. Krieger, M. P. Scott, S. L. Zipursky, and J. Darnell. *Molecular Cell Biology*. W.H. Freeman and Company, 2004.
- [88] R. Ludwig. Die ungewöhnlichen Eigenschaften des unterkühlten und glasartigen Wassers. *Angew. Chem.*, 118:3480, 2006.
- [89] C. D. Luvé. Nobel lecture. Last retrieved from http://nobelprize.org/nobel_prizes/medicine/laureates/1974/duve-lecture.pdf on 2.8.2011.
- [90] A. M. Maiden and J. M. Rodenburg. An improved ptychographical phase retrieval algorithm for diffractive imaging. *Ultramicroscopy*, 109(10):1256, 2009.
- [91] A. P. Mancuso, T. Gorniak, F. Staier, O. M. Yefanov, R. Barth, C. Christophis, B. Reime, J. Gulden, A. Singer, M. E. Pettit, T. Nisius, T. Wilhein, C. Gutt, G. Grübel, N. Guerassimova, R. Treusch, J. Feldhaus, S. Eisebitt, E. Weckert, M. Grunze, A. Rosenhahn, and I. A. Vartanyants. Coherent imaging of biological samples with femtosecond pulses at the free-electron laser FLASH. *New J. Phys.*, 12(3):035003, 2010.
- [92] S. Marchesini. Invited article: A unified evaluation of iterative projection algorithms for phase retrieval. *Rev. Sci. Instrum.*, 78(1):011301, 2007.
- [93] S. Marchesini, H. He, H. N. Chapman, S. P. Hau-Riege, A. Noy, M. R. Howells, U. Weierstall, and J. C. H. Spence. X-ray image reconstruction from a diffraction pattern alone. *Phys. Rev. B*, 68(14):140101, 2003.
- [94] D. Mas, J. Garcia, C. Ferreira, L. M. Bernardo, and F. Marinho. Fast algorithms for free-space diffraction patterns calculation. *Opt. Commun.*, 164(4-6):233, 1999.
- [95] K. Matsushima and T. Shimobaba. Band-limited angular spectrum method for numerical simulation of free-space propagation in far and near fields. *Opt. Express*, 17(22):19662–19673, Oct. 2009.
- [96] S. Mayo, P. Miller, S. Wilkins, T. Davis, D. Gao, T. Gureyev, D. Paganin, D. Parry, A. Pogany, and A. Stevenson. Quantitative x-ray projection microscopy: Phase-contrast and multi-spectral imaging. *J. Microsc.*, 207:79, 2002.

- [97] O. Medalia, I. Weber, A. S. Frangakis, D. Nicastro, G. Gerisch, and W. Baumeister. Macromolecular Architecture in Eukaryotic Cells Visualized by Cryoelectron Tomography. *Science*, 298(5596):1209, 2002.
- [98] A. Menzel, C. Kewish, P. Kraft, B. Henrich, K. Jefimovs, J. Vila-Comamala, C. David, M. Dierolf, P. Thibault, F. Pfeiffer, and O. Bunk. Scanning transmission X-ray microscopy with a fast framing pixel detector. *Ultramicroscopy*, 110(9):1143, 2010.
- [99] J. Miao, P. Charalambous, J. Kirz, and D. Sayre. Extending the methodology of X-ray crystallography to allow imaging of micrometre-sized non-crystalline specimens. *Nature*, 400(6742):342, 1999.
- [100] J. Miao and D. Sayre. On possible extensions of X-ray crystallography through diffraction-pattern oversampling. *Acta Crystallographica Section A*, 56(6):596, 2000.
- [101] J. Miao, D. Sayre, and H. N. Chapman. Phase retrieval from the magnitude of the Fourier transforms of nonperiodic objects. *J. Opt. Soc. Am. A*, 15(6):1662, 1998.
- [102] P. D. Nellist, B. C. McCallum, and J. M. Rodenburg. Resolution beyond the ‘information limit’ in transmission electron microscopy. *Nature*, 374:630, 1995.
- [103] J. Nelson, X. Huang, J. Steinbrener, D. Shapiro, J. Kirz, S. Marchesini, A. M. Neiman, J. J. Turner, and C. Jacobsen. High-resolution x-ray diffraction microscopy of specifically labeled yeast cells. *P. Natl. Acad. Sci. USA*, 107(16):7235, 2010.
- [104] K. A. Nugent. X-ray noninterferometric phase imaging: a unified picture. *J. Opt. Soc. Am. A*, 24(2):536, 2007.
- [105] K. A. Nugent. Coherent methods in the X-ray sciences. *Advances in Physics*, 59(1):1–99, 2010.
- [106] Nyquist frequency. Last retrieved on 1.8.2011 from http://en.wikipedia.org/wiki/Nyquist_frequency.
- [107] Nyquist-Shannon sampling theorem. Last retrieved on 1.8.2011 from http://en.wikipedia.org/wiki/Sampling_theorem.
- [108] D. M. Paganin. *Coherent X-Ray Optics*. Oxford Univ. Press, Oxford (UK), 2006.
- [109] I. Pitas. *Digital image processing algorithms and applications*. Wiley, New York, 2000.
- [110] A. Pogany, D. Gao, and S. W. Wilkins. Contrast and resolution in imaging with a microfocus x-ray source. *Rev. Sci. Instrum.*, 68(7):2774, 1997.
- [111] C. Ponchut, J. Clément, J.-M. Rigal, E. Papillon, J. Vallerga, D. LaMarra, and B. Mikulec. Photon-counting X-ray imaging at kilohertz frame rates. *Nuc. Instrum. Meth. A*, 576(1):109, 2007.
- [112] H. M. Quiney, K. A. Nugent, and A. G. Peele. Iterative image reconstruction algorithms using wave-front intensity and phase variation. *Opt. Lett.*, 30(13):1638, 2005.

- [113] H. M. Quiney, A. G. Peele, Z. Cai, D. Paterson, and K. A. Nugent. Diffractive imaging of highly focused X-ray fields. *Nat. Phys.*, 2(2):101, 2006.
- [114] C. Quintana. Cryofixation, cryosubstitution, cryoembedding for ultrastructural, immunocytochemical and microanalytical studies. *Micron*, 25(1):63, 1994.
- [115] C. Quitmann, C. David, F. Nolting, F. Pfeiffer, and M. Stampanoni. 9th International Conference on X-Ray Microscopy. *J. Phys. Conf. Ser.*, 186:011001, 2009.
- [116] R. B. Ravelli and S. M. McSweeney. The ‘fingerprint’ that X-rays can leave on structures. *Structure*, 8(3):315, 2000.
- [117] J. Rodenburg. Ptychography and Related Diffractive Imaging Methods. In P. Hawkes, editor, *Advances in Imaging and Electron Physics*, volume 150, pages 87–184. Elsevier, 2008.
- [118] J. Rodenburg, A. Hurst, and A. Cullis. Transmission microscopy without lenses for objects of unlimited size. *Ultramicroscopy*, 107(2-3):227, 2007.
- [119] J. M. Rodenburg and H. M. L. Faulkner. A phase retrieval algorithm for shifting illumination. *Appl. Phys. Lett.*, 85(20):4795, 2004.
- [120] J. M. Rodenburg, A. C. Hurst, A. G. Cullis, B. R. Dobson, F. Pfeiffer, O. Bunk, C. David, K. Jefimovs, and I. Johnson. Hard-X-Ray Lensless Imaging of Extended Objects. *Phys. Rev. Lett.*, 98(3):034801, 2007.
- [121] A. Rosenhahn, R. Barth, F. Staier, T. Simpson, S. Mittler, S. Eisebitt, and M. Grunze. Digital in-line soft x-ray holography with element contrast. *J. Opt. Soc. Am. A*, 25(2):416, 2008.
- [122] K. P. Ryan. Cryofixation of tissues for electron microscopy: A review of plunge cooling methods. *Scanning Microscopy*, 6:715, 1992.
- [123] T. Salditt, K. Giewekemeyer, C. Fuhse, S. P. Krüger, R. Tucoulou, and P. Cloetens. Projection phase contrast microscopy with a hard x-ray nanofocused beam: Defocus and contrast transfer. *Phys. Rev. B*, 79(18):184112, 2009.
- [124] D. Sayre. Some implications of a theorem due to Shannon. *Acta Cryst.*, 5(6):843, 1952.
- [125] D. Sayre. X-Ray Crystallography: The Past and Present of the Phase Problem. *Struct. Chem.*, 13:81, 2002. 10.1023/A:1013477415486.
- [126] G. Schneider, P. Guttmann, S. Heim, S. Rehbein, F. Mueller, K. Nagashima, J. B. Heymann, W. G. Muller, and J. G. McNally. Three-dimensional cellular ultrastructure resolved by X-ray microscopy. *Nat. Meth.*, 7(12):985, 2010.
- [127] C. G. Schroer, P. Boye, J. M. Feldkamp, J. Patommel, A. Schropp, A. Schwab, S. Stephan, M. Burghammer, S. Schoder, and C. Riekkel. Coherent x-ray diffraction imaging with nanofocused illumination. *Phys. Rev. Lett.*, 101(9):090801, 2008.

- [128] C. G. Schroer, O. Kurapova, J. Patommel, P. Boye, J. Feldkamp, B. Lengeler, M. Burghammer, C. Riekkel, L. Vincze, A. van der Hart, and M. Kuchler. Hard x-ray nanoprobe based on refractive x-ray lenses. *Appl. Phys. Lett.*, 87(12):124103, 2005.
- [129] A. Schropp. *Experimental Coherent X-Ray Diffractive Imaging: Capabilities and Limitations of the Technique*. PhD thesis, Universität Hamburg, 2008.
- [130] A. Schropp, P. Boye, J. M. Feldkamp, R. Hoppe, J. Patommel, D. Samberg, S. Stephan, K. Giewekemeyer, R. N. Wilke, T. Salditt, J. Gulden, A. P. Mancuso, I. A. Vartanyants, E. Weckert, S. Schoder, M. Burghammer, and C. G. Schroer. Hard x-ray nanobeam characterization by coherent diffraction microscopy. *Appl. Phys. Lett.*, 96(9):091102, 2010.
- [131] A. Schropp, P. Boye, A. Goldschmidt, S. Hönig, R. Hoppe, J. Patommel, C. Rakete, D. Samberg, S. Stephan, S. Schöder, M. Burghammer, and C. Schroer. Non-destructive and quantitative imaging of a nano-structured microchip by ptychographic hard X-ray scanning microscopy. *J. Microsc. Oxford*, page 9, 2010.
- [132] D. Shapiro, P. Thibault, T. Beetz, V. Elser, M. Howells, C. Jacobsen, J. Kirz, E. Lima, H. Miao, A. M. Neiman, and D. Sayre. Biological imaging by soft x-ray diffraction microscopy. *P. Natl. Acad. Sci. USA*, 102(43):15343, 2005.
- [133] A. E. Siegman. *Lasers*. Univ. Science Books, Mill Valley, California, 1986.
- [134] A. Snigirev, I. Snigireva, V. Kohn, S. Kuznetsov, and I. Schelokov. On the possibilities of x-ray phase contrast microimaging by coherent high-energy synchrotron radiation. *Rev. Sci. Instrum.*, 66(12):5486, 1995.
- [135] J. Steinbrener, J. Nelson, X. Huang, S. Marchesini, D. Shapiro, J. J. Turner, and C. Jacobsen. Data preparation and evaluation techniques for x-ray diffraction microscopy. *Opt. Express*, 18(18):18598, 2010.
- [136] J. F. Steinbrener. *X-ray Diffraction Microscopy: Computational Methods and Scanning-type Experiments*. PhD thesis, Stony Brook University, 2010.
- [137] P. Tafforeau, R. Boistel, E. Boller, A. Bravin, M. Brunet, Y. Chaimanee, P. Cloetens, M. Feist, J. Hozzowska, J.-J. Jaeger, R. Kay, V. Lazzari, L. Marivaux, A. Nel, C. Nemoz, X. Thibault, P. Vignaud, and S. Zabler. Applications of X-ray synchrotron microtomography for non-destructive 3D studies of paleontological specimens. *Appl. Phys. A - Mater.*, 83:195, 2006.
- [138] P. Thibault. *Algorithmic methods in diffraction microscopy*. PhD thesis, Cornell University, 2007.
- [139] P. Thibault, M. Dierolf, O. Bunk, A. Menzel, and F. Pfeiffer. Probe retrieval in ptychographic coherent diffractive imaging. *Ultramicroscopy*, 109(4):338, 2009.

- [140] P. Thibault, M. Dierolf, C. M. Kewish, A. Menzel, O. Bunk, and F. Pfeiffer. Contrast mechanisms in scanning transmission x-ray microscopy. *Phys. Rev. A*, 80(4):043813, 2009.
- [141] P. Thibault, M. Dierolf, A. Menzel, O. Bunk, C. David, and F. Pfeiffer. High-Resolution Scanning X-ray Diffraction Microscopy. *Science*, 321(5887):379, 2008.
- [142] P. Thibault and V. Elser. X-ray diffraction microscopy. *Annu. Rev. Cond. Matter Phys.*, 1(1):237, 2010.
- [143] P. Thibault, V. Elser, C. Jacobsen, D. Shapiro, and D. Sayre. Reconstruction of a yeast cell from x-ray diffraction data. *Acta Cryst. A*, 62(4):248, 2006.
- [144] R. E. Thorne, Z. Stum, J. Kmetko, K. O'Neill, and R. Gillilan. Microfabricated mounts for high-throughput macromolecular cryocrystallography. *J. Appl. Crystallogr.*, 36(6):1455, 2003.
- [145] T. Tuohimaa, M. Otendal, and H. M. Hertz. Phase-contrast x-ray imaging with a liquid-metal-jet-anode microfocus source. *Appl. Phys. Lett.*, 91(7):074104, 2007.
- [146] F. van der Veen and F. Pfeiffer. Coherent x-ray scattering. *J. Phys. Condens. Matt.*, 16(28):5003, 2004.
- [147] I. A. Vartanyants and I. K. Robinson. Partial coherence effects on the imaging of small crystals using coherent x-ray diffraction. *Journal of Physics: Condensed Matter*, 13(47):10593, 2001.
- [148] D. J. Vine, G. J. Williams, B. Abbey, M. A. Pfeifer, J. N. Clark, M. D. de Jonge, I. McNulty, A. G. Peele, and K. A. Nugent. Ptychographic Fresnel coherent diffractive imaging. *Phys. Rev. A*, 80(6):063823, 2009.
- [149] D. G. Voelz and M. C. Roggemann. Digital simulation of scalar optical diffraction: revisiting chirp function sampling criteria and consequences. *Appl. Opt.*, 48(32):6132, 2009.
- [150] M. Warkentin, V. Berejnov, N. S. Hussein, and R. E. Thorne. Hyperquenching for protein cryocrystallography. *J. Appl. Crystallogr.*, 39(6):805, 2006.
- [151] D. Weiss, G. Schneider, B. Niemann, P. Guttmann, D. Rudolph, and G. Schmahl. Computed tomography of cryogenic biological specimens based on x-ray microscopic images. *Ultramicroscopy*, 84(3-4):185, 2000.
- [152] S. W. Wilkins, T. E. Gureyev, D. Gao, A. Pogany, and A. W. Stevenson. Phase-contrast imaging using polychromatic hard X-rays. *Nature*, 384(6607):335, 1996.
- [153] G. Williams, M. Pfeifer, I. Vartanyants, and I. Robinson. Effectiveness of iterative algorithms in recovering phase in the presence of noise. *Acta Cryst. A*, 63(1):36, 2007.

-
- [154] G. J. Williams, H. M. Quiney, B. B. Dhal, C. Q. Tran, K. A. Nugent, A. G. Peele, D. Paterson, and M. D. de Jonge. Fresnel Coherent Diffractive Imaging. *Physical Review Letters*, 97(2):025506, 2006.
- [155] E. Wolf. *Introduction to the Theory of Coherence and Polarization of Light*. Cambridge Univ. Press, Cambridge, 2007.
- [156] L. Yang, R. McRae, M. M. Henary, R. Patel, B. Lai, S. Vogt, and C. J. Fahrni. Imaging of the intracellular topography of copper with a fluorescent sensor and by synchrotron x-ray fluorescence microscopy. *P. Natl. Acad. Sci. USA*, 102(32):11179, 2005.

Publications

- Nováková, E., Giewekemeyer, K., and Salditt, T.: *Structure of two-component lipid membranes on solid support: An x-ray reflectivity study*, Phys. Rev. E **74**, 051911 (2006).
- Koelsch, P., Viswanath, P., Motschmann, H., Shapovalov, V.L., Brezesinski, G., Möhwald, H., Horinek, D., Netz, R.R., Giewekemeyer, K., Salditt, T., Schollmeyer, H., von Klitzing, R., Daillant, J., and Guenoun, P.: *Specific ion effects in physicochemical and biological systems: Simulations, theory and experiments*, Colloids and Surfaces A: Physicochemical and Engineering Aspects **303**, 110 (2007).
- Giewekemeyer, K., and Salditt, T.: *Counterion distribution near a monolayer of variable charge density*, Europhysics Lett. **79**, 18003 (2007).
- Hohage, T., Giewekemeyer, K., and Salditt, T.: *Iterative reconstruction of a refractive-index profile from x-ray or neutron reflectivity measurements*, Phys. Rev. E **77**, 051604 (2008).
- Enders, B., Giewekemeyer, K., Kurz, T., Podorov, S., and Salditt, T.: *Non-iterative coherent diffractive imaging using a phase-shifting reference frame*, New Journal of Physics **11**, 043021 (2009).
- Salditt, T., Giewekemeyer, K., Fuhse, C., Krüger, S.P., Tucoulou, R., and Cloetens, P.: *Projection phase contrast microscopy with a hard x-ray nanofocused beam: Defocus and contrast transfer*, Phys. Rev. B **79**, 184112 (2009).
- Giewekemeyer, K., Hantke, M., Beta, C., Tucoulou, R., and Salditt, T.: *Fluorescence imaging of Dictyostelium discoideum with a hard x-ray nanoprobe*, Journal of Physics: Conference Series **186** (2009).
- Giewekemeyer, K., Thibault, P., Kalbfleisch, S., Beerlink, A., Kewish, C.M., Dierolf, M., Pfeiffer, F., and Salditt, T.: *Quantitative biological imaging by ptychographic x-ray diffraction microscopy*, Proceedings of the National Academy of Sciences of the USA **107**, 529 (2010).
- Schropp, A., Boye, P., Feldkamp, J.M., Hoppe, R., Patommel, J., Samberg, D., Stephan, S., Giewekemeyer, K., Wilke, R.N., Salditt, T., Gulden, J., Mancuso, A.P., Vartanyants, I.A., Weckert, E., Schöder, S., Burghammer, M., and Schroer, C.G.: *Hard x-ray*

nanobeam characterization by coherent diffraction microscopy, Applied Physics Letters **96**, 091102 (2010).

- Giewekemeyer, K., Neubauer, H., Kalbfleisch, S., Krüger, S.P., and Salditt, T.: *Holographic and diffractive x-ray imaging using waveguides as quasi-point sources* New Journal of Physics **12**, 035008 (2010).
- Krüger, S.P., Giewekemeyer, K., Kalbfleisch, S., Bartels, M., Neubauer, H., and Salditt, T.: *Sub-15 nm beam confinement by two crossed x-ray waveguides* Optics Express **18**, 13492 (2010).
- Kalbfleisch, S., Osterhoff, M., Giewekemeyer, K., Neubauer, H., Krüger, S.P., Hartmann, B., Bartels, M., Sprung, M., Leupold, O., Siewert, F., and Salditt, T.: *The holography endstation of beamline P10 at PETRA III* AIP. Conf. Proc. **1234**, 433 (2010).
- Giewekemeyer, K., Beckers, M., Gorniak, T., Grunze, M., Salditt, T., and Rosenhahn, A.: *Ptychographic coherent x-ray diffractive imaging in the water window*, Optics Express **19**, 1037 (2011).
- Giewekemeyer, K., Krüger, S.P., Kalbfleisch, S., Bartels, M., Beta, C. Salditt, T.: *X-ray propagation microscopy of biological cells using waveguides as a quasi-point source*, Physical Review A **83**, 023804 (2011).

Acknowledgements

First of all, I would like to thank my supervisor Prof. Dr. Tim Salditt for giving me the opportunity to enter the fascinating field of coherent x-ray science. I am deeply grateful for his never-ending support, encouragement and motivation that he has given me during the time of my thesis.

I also would like to thank Prof. Dr. Stefan W. Hell who has agreed to co-referee the thesis.

The team work is certainly one of the most enjoyable experiences of synchrotron experiments, and I am happy to have been part of the imaging team at the IRP. In particular, I would like to thank Sven Krüger who has designed the waveguides for our cell experiment. I very much enjoyed our many fruitful discussions during the last months of this thesis work. I also want to thank Sebastian Kalbfleisch, our master of instrumentation and André Beerlink for being great team members during our beamtimes.

I thank Dr. Tanja Ducic for her help with sample preparation and an introduction to cell culturing. I enjoyed very much working with Max Hantke, who has contributed in many ways to the further refinement of the preparation process and has allowed me to use some of his graphs on the preparation process. I thank Robin Wilke for many fruitful discussions about numerics and algorithms.

Bastian Hartman is thanked for his outstanding support in designing and building the instrumentation for the beamtimes. I also would like to thank Jochen Herbst, Thorsten Gronemann, Carsten Wulf, and Peter Nieschalk for excellent experimental preparation and workshop support.

Many other people outside the IRP have helped to make this work possible. Most of all, I would like to thank Dr. Pierre Thibault for allowing me to use an example version of his ptychography code and for his willingness to share his ideas on the treatment of noisy data. I thank Prof. Dr. Franz Pfeiffer for giving me the opportunity to spend a month as a guest in his group and I would like to thank Dr. Cameron Kewish for outstanding support during the cSAXS beamtime.

I thank Dr. Axel Rosenhahn, Mike Beckers and Thomas Gorniak for sharing their resources and expertise in experimental soft x-ray imaging and for a very enjoyable beamtime experience.

I thank Prof. Dr. Carsten Beta and Prof. Dr. Eberhard Bodenschatz for providing the Dictyostelium cells. Prof. Dr. Holger Stark is thanked for introducing me to the plunge-freezing technique.

I thank Dr. Remi Tucoulou for his support during the beamtime at the ESRF.

Beyond that, I thank many other people in the IRP, for many discussions, not only about physics and for making the IRP an enjoyable place to work: In particular I would like to thank Sven Krüger, Dr. Simon Castorph, Sebastian Kalbfleisch, and Dr. Eva Novakova.

I would like to thank Sven Krüger, Dr. Olha Ivanyshyn, and Ulf Seemann for proof-reading parts of the manuscript.

Von ganzem Herzen danke ich meinen Eltern und vor allem meiner Frau Antonia für ihre immerwährende Unterstützung und Geduld.

This work has been supported financially by the DFG Collaborative Research Center SFB 755 “Nanoscale Photonic Imaging”, the Helmholtz society in the framework of the Virtual Institute VI-203, and the German Ministry of Education and Research under Grant No. 05KS7MGA.

Lebenslauf

Klaus Giewekemeyer
Geboren am 7. Januar 1981 in Sögel.
Staatsangehörigkeit: deutsch.

Wissenschaftlicher Werdegang

- | | |
|-----------------|--|
| 7/2000 | Erlangung der Allgemeinen Hochschulreife, Hümmling-Gymnasium Sögel |
| 10/2000–7/2003 | Studium der Physik an der Georg-August-Universität Göttingen |
| 09/2003–6/2004 | Studium der Physik an der University of California, San Diego |
| 10/2004–11/2006 | Studium der Physik an der Georg-August-Universität Göttingen |
| 11/2006 | Diplom in Physik, Titel der Arbeit: "A study of the counterion distribution near a planar charged wall by resonant x-ray reflectivity", Institut für Röntgenphysik, Georg-August-Universität Göttingen |
| seit 01/2007 | wissenschaftlicher Mitarbeiter am Institut für Röntgenphysik, Georg-August-Universität Göttingen |

The use of coherent x rays for microscopic imaging has seen a rapid and on-going development within the past decade, driven by an increasing availability of highly brilliant and coherent sources worldwide. Accordingly, novel methods have been developed, which replace the microscope's objective lens by a numerical reconstruction scheme. The aim of the present work is to study how very recent experimental and algorithmic developments in the field can be implemented towards a highly sensitive and fully quantitative microscopy method for imaging of biological cells. To this end, different experimental approaches are studied, based on coherent far-field as well as near-field diffraction. At first, an application of the novel ptychographic imaging method to single biological cells is presented. In particular, it is demonstrated how weakly scattering biological specimens can be imaged with fully quantitative density contrast. Alongside, a successful extension of the method towards soft x-ray energies is described. In the second part of the work it is shown how x-ray waveguides can be used as a point source for propagation-based microscopy of single cells in the hard x-ray regime. The specifically devised iterative reconstruction scheme allows for full quantitativity and high sensitivity and thus enables an application to single biological cells. The work contains a thorough introduction into the x-ray optical methods applied and aims at a useful and self-contained overview on aspects of signal and Fourier theory relevant for the used numerical propagation schemes.



ISBN 978-3-86395-023-1
ISSN 2191-9860

Universitätsverlag Göttingen